Manifestations of the Roton in Dipolar Bose-Einstein Condensates

by

Ryan M. Wilson

B.S., Saint Louis University, 2006

M.S., University of Colorado, 2010

A thesis submitted to the
Faculty of the Graduate School of the
University of Colorado in partial fulfillment
of the requirements for the degree of
Doctor of Philosophy
Department of Physics
2011

This thesis entitled:
Manifestations of the Roton in Dipolar Bose-Einstein Condensates
written by Ryan M. Wilson
has been approved for the Department of Physics

John L. Bohn

Chris H. Greene

Date

The final copy of this thesis has been examined by the signatories, and we find that both the content and the form meet acceptable presentation standards of scholarly work in the above mentioned discipline.

Wilson, Ryan M. (Ph.D., Physics)

Manifestations of the Roton in Dipolar Bose-Einstein Condensates

Thesis directed by Prof. John L. Bohn

Today, sixteen years after the realization of the first Bose-Einstein condensate (BEC), the field of ultracold many-body physics is booming. In particular, much excitement has been generated by the prospect of creating a degenerate quantum gas of dipolar atoms or molecules. Already, some experimental groups have succeeded in Bose-condensing atomic ^{52}Cr and ^{164}Dy, while other groups have made significant progress towards achieving degeneracy of heteronuclear molecules, such as fermionic ^{40}K^{87}Rb and bosonic ^{87}Rb^{133}Cs, where the strength of the dipolar interaction promises to be much greater than that of the already rich ^{52}Cr condensate. Just as the creation of BEC launched a whole new field of research, dipolar BECs are likely to do the same. However, such systems present a theoretical challenge due to the long-range, anisotropic nature of the dipolar interaction. In this thesis, I present a theoretical investigation of ultracold Bose gases with dipolar interactions.

The first part of this thesis is dedicated to the field theoretical treatment of a quantum Bose fluid with dipolar interactions in the ultracold, dilute regime, where the system is well-described by a classical condensate field with quasiparticle excitations. The set of nonlinear integrodifferential equations that describe these objects are derived and novel methods for solving them are presented that, in general, require intricate numerical treatment. Of particular importance is the emergence of a roton mode, reminiscent of that in superfluid ^{4}He. In the second part of this thesis, I show how the roton plays a critical role in the ground state structure and dynamics of a dipolar BEC. Full numerical simulations show that the roton can, for example, be seen in the radial density profile of a quantized vortex state or in the angular collapse and explosion of a dipolar BEC. Additionally, I show the crucial role that this roton plays in determining the transition to superfluidity in these systems. Thus, a set of novel phenomena in ultracold dipolar Bose gases is explained by the presence of the roton, and experimental signatures of these phenomena are made clear.

Dedication

To my parents, for their endless dedication and encouragement.

Acknowledgements

First and foremost, I would like to acknowledge and thank my advisor, John. If I have any success as a theorist, I owe it to him. Among a million other things, he has taught me how to think critically about physical problems and how put my work into a context that is beneficial both to me and to the scientific community at large. Perhaps more importantly, he has made my experience as a graduate student a great one. Not only is he an incredible scientist, but he is a good person. In five years, I never heard a negative word leave his mouth. He inspires with encouragement instead of criticism. For that, his place as a role model in my life transcends the realm of scientific research.

I would also like to extend a deep thanks to Shai Ronen. Shai's mentoring in the early days of my career as a graduate student was indispensable. His mind is full of creativity and brilliance. If I managed to absorb any of that during my time working with him, I have benefited greatly.

Of course, the rest of the "Bohn group" deserves a hearty thanks for being productive colleagues and good friends. Thanks to Danielle Bortolotti, Manual Lara, Ed Meyer, Goulven Quéméner, Michael Mayle, Brandon Ruzic and John Corson. I hope that I have made a sufficiently good impression so that one of them will hire me some day.

I owe a special thanks to Chris Ticknor, Seth Rittenhouse, Hossein Sadeghpour and Eddy Timmermans for extending generous invitations and hosting me on scholarly visits. These visits have been incredibly beneficial to me and have highlighted my (hopefully) young career. Lobster rolls and blue enchiladas were a big plus. Also, thanks to Han Pu for his fruitful collaboration and open communication. I was lucky to have the opportunity to collaborate with such an intuitive and intelligent researcher, and I hope to have the opportunity to do so again in the future. In this vein, I would also like to thank Ben Lev and his talented group for their open communication and collaboration.

Thanks to Tilman Pfau, Jonas Metz and Juliette Billy from the Stuttgart ^{52}Cr experiment for all of their useful input and discourse regarding their work.

Also, I feel incredibly lucky to have spent my graduate years at JILA and the University of Colorado. Outside of my research group, I would like to thank a number of other students, postdocs and faculty who have enlightened and inspired me. This includes, but is certainly not limited to, Victor Gurarie, Chris Greene, Murray Holland, Ana Maria Rey, Eric Cornell, Debbie Jin, Dominic Meiser, Jami Kinnunen, Kaden Hazzard, Jia Wang, Shu-Ming Li, Charlie Sievers, Adam Scheer, Brian Neyenhuis, Zhaochuan Shen, and Ron Pepino.

Thanks to Philippe Verkerk and the other Les Houches INTERCAN and IFRAF predoctoral school organizers for two memorable and fruitful weeks of study.

Before coming to graduate school, I received a great deal of support and inspiration as an undergraduate at Saint Louis University and as an REU student at Columbia University. From Columbia, I would like to thank Rafeal Galea, Jeremy Dodd and my fellow students Eli Visbal, Colin Beal and Stephen Poprocki. From Saint Louis University, I would like to thank Ian Redmount, Bill Thacker, Greg Comer, Thalanayar Santhanam, Larry Stacey, Les Benofy, Vijai Dixit, Jean Potvin, Fr. Mike May, Kent Staley, Brody Johnson and my partner in chips, salsa and E&M, Ben Hurst.

Outside of the Physics world, I have developed an interest in the ceramic arts. Thanks to Scott Chamberlin and Jeanne Quinn for supporting my clay habit.

Thanks to my family. Though I know that I am inspired to learn and research out of pure interest, the entirety of my inspiration has much deeper roots. My family has always made a point to tell me that they were proud of me. The impact of that on my career and life is immeasurable.

Thanks to my brother, for, whether he knows it or not, teaching me to be good.

Finally, I would like thank Lindsay Pichaske for her love and support. She inspires a joy and a confidence that penetrates deeply into my life.

Contents

Chapter

Appendix

Tables

Table

Figures

Figure

Chapter 1

Introduction

The experimental realization of a Bose-Einstein condensate (BEC) of alkali atoms at JILA, MIT and Rice University in 1995 [1, 2, 3] opened the door to a vast, interdisciplinary field full of opportunity and potential. The BEC, first theorized by A. Einstein in 1925 [4], was the coldest sample of matter known in the universe, and was the fruitful result of years of experimental and theoretical progress in the field of optical and magnetic cooling and trapping [5]. The BEC did, and still does, offer a tool with which to study a plethora of ultracold phenomena, including superfluidity and its manifestations in quantum matter. Additionally, the realization of ultracold temperatures allows for atoms and molecules to be trapped by purely optical means, which facilitates experimental control over the magnetic substates of these systems and allows for trapping in optical lattice potentials. Atoms and molecules in optical lattices can be used, for example, for quantum computing purposes or to study more complicated condensed matter systems in a clean, controllable environment [6, 7, 8].

The presence of dipolar interactions in the Bose-Einstein condensate enhances much of the physics in ultracold quantum systems. The dipole-dipole interaction (ddi) is long-range, proportional to the inverse cube of the distance between two dipoles, and anisotropic. As such, the ddi can introduce inter-site couplings in optical lattice systems in one- and two-dimensions (1D and 2D), and anisotropic couplings in three-dimensional (3D) lattices [8]. In fermionic systems, this feature can result in a transition to superfluidity as the attractive part of the ddi leads to pairing between sites [9, 10, 11]. Additionally, in 2D geometries, the presence of the ddi in a Bose gas is predicted to lead to a self-ordered crystalline state, or Wigner crystal, for sufficiently large densities [12, 13]. Experimentally, BECs of atomic ^{52}Cr [14, 15, 16] and ^{164}Dy [17] have been achieved, where the atoms possess significant permanent magnetic dipole moments, being 6 and 10 Bohr magnetons, respectively. By comparison, the magnetic dipole moment of ^{87}Rb is only 1 Bohr magneton. While comparatively small, however, the ddi has been shown to play an crucial role in the physics of the ^{87}Rb $F = 1$ spinor BEC [18, 19, 20].

While the first report from the ^{164}Dy BEC experiment has already demonstrated strong dipolar effects, the ^{52}Cr experiments in the group of Tilman Pfau in Stuttgart have demonstrated that the ddi plays a strong role in the stability [21] and dynamics [22] of a BEC. Additionally, this group demonstrated that the s-wave scattering length of the ^{52}Cr atoms could be tuned to zero, thus creating a *purely* dipolar BEC [23]. While the dipole moments of these atoms are indeed sufficiently large to observe (and predict) some interesting dipolar effects, recent experimental advances in the production, trapping and cooling of heteronuclear molecules inspires great promise that such molecules will be brought to quantum degeneracy in the near future. Such molecules can possess very large, tunable electric dipole moments when polarized in an external field, on the order of a Debye, which is about two orders of magnitude larger than a Bohr magneton when the two quantities are expressed in the same system of units. Already, experimentalists have managed to produce cold samples of heteronuclear molecules in their rovibrational ground state [24, 25, 26], and the JILA group recently demonstrated long-lifetime trapping of fermionic KRb molecules in a 3D optical lattice geometry [27]. Such progress inspires encouragement that a BEC of polar molecules is realizable in the near future.

In addition to the novel physics that has been predicted in, for example, optical lattice and spinor systems, the ddi has been predicted to lead to the rotonization of a dipolar BEC in a trapped geometry [28, 29, 30]. The roton, being a local minimum at finite wave number in the quasiparticle dispersion relation of an ultracold Bose gas, was first predicted and seen in the superfluid ^{4}He system [31, 32, 33], though the origin of the two rotons are very different. The ^{4}He system is very dense, and the roton therein is related to the structure factor of the liquid at the interatomic level, signifying a tendency for crystalline ordering in the system. The roton in the dipolar BEC, however, is present even in the dilute, gaseous state and derives from the momentum dependence of the ddi in a trapped geometry. The most transparent example of this is the so-called quasi-2D dipolar BEC, where the system is harmonically trapped in the direction of the dipole polarization and the dipoles exhibit zero-point motion in this direction. Indeed, the demonstrated control that experimentalists have over the trapping geometry and interactions in a dipolar BEC suggests that this system is ideal for studying the physics of the roton. In this dissertation, we tackle this idea head on and present a comprehensive, detailed theoretical account of the role that the roton plays in the physics of the dipolar BEC.

Because the dipolar BECs that have been created in the laboratory setting are quite dilute, they are well-described by a mean-field theory that provides a relatively simple theoretical treatment of these systems. The mean-field theory of dipoles, however, is not without its own set of challenges. Whereas short-range interactions of ultracold atoms and molecules can be well-described by a delta-function pseudopotential, the ddi admits no such simplification and must be handled explicitly. For example, the mean-field theory that we employ in this work presents a series of direct and exchange interaction terms that require the calculation of convolution integrals (see chapter 5). While the delta-function pseudo-potential trivializes these integrals, the ddi does not and the convolutions must be calculated as given. Additionally, we consider fully-trapped systems in this work that generate hard numerical problems, both when calculating the condensate field and its set of quantum fluctuations. In this dissertation, we develop and present methods for overcoming these difficulties. The key results of this work include a set of methods and algorithms that turn the theoretical treatment of a fully trapped dipolar BEC into a tractable one. We then apply these results and predict a set of novel phenomena related to the roton in the trapped dipolar BEC. To make the results presented in this dissertation as relevant as possible to the scientific community, we have made a point to associate all of our results with current experiments, or experiments that are realizable in the foreseeable future.

In chapter 2 of this thesis, we give a short background of the history of low-temperature physics. This includes a discussion of the early experiments and thoughts on superfluid ^{4}He. Indeed, it was this early scientific discourse that laid the groundwork for our understanding of superfluidity and its manifestation in matter through, for example, quantized vortices and, most fundamentally, long-range order. We also discuss some of the more recent experimental advances in the field, including the basic physics behind the optical and magnetic cooling and trapping methods that led to the first experimental realization of a BEC and the first, most fundamental results that laid the foundation for the modern study of the ultracold physics of bosons. To give the reader an idea of how the Bose-Einstein condensate phase emerges statistically as a function of temperature, we also discuss the phenomenon of BEC in a trapped, non-interacting (ideal) gas of bosons.

In chapter 3, we start from a second-quantized description of a quantum many-body system of interacting bosons and systematically derive the set of mean-field equations that describe the condensate field and the quantum fluctuations of the dilute, interacting Bose gas at zero-temperature, being the Gross-Pitaevskii equation and the Bogoliubov de Gennes equations, respectively. Additionally, we motivate the use of a pseudo-potential for the short-range two-body interactions in the ultracold gas and discuss the treatment of the ddi, where non-trivial convolution integrals must be calculated. To treat the ddi, we employ the convolution theorem and handle the integrals in momentum-space, moving to and from real space via Fourier transformation.

In chapter 4, we apply the mean-field theory to the homogeneous 3D and quasi-2D dipolar BECs. We investigate the energetics and quantum fluctuations of these systems, where the quantum fluctuations take the form of quasiparticles in the Bogoliubov theory, and thereby map their stability in parameter space. In the quasi-2D case, an effective ddi is derived, which leads to the emergence of the roton quasiparticle in Bogoliubov theory. Interestingly, the roton can lead the quasi-2D dipolar BEC to collapse that is both density dependent and local, having character that opposes the usual phonon, or energetic instability in the 3D dipolar BEC or the BEC with attractive contact interactions. Original work from this chapter is published in [34].

We move on to treat the fully-trapped dipolar BEC in chapter 5. To simplify the problem at hand, we consider a cylindrically symmetric harmonic trap with the dipoles polarized along the trap axis of symmetry, so the system as a whole possesses such symmetry. In this case, the problem is reduced from a 3D to a 2D problem in the axial and radial coordinates where the angular dependence of the relevant functions, being the condensate wave function and the quasiparticle modes, is included in an angular factor $e^{ik\varphi}$. A discrete Hankel transform is usedt o handle the transforms in the radial direction (see appendix D), where the Hankel transform expands the relevant function in terms of Bessel functions of order k. Thus, condensate modes and quasiparticle modes with arbitrary vorticity are handled by simply choosing a Hankel transform of the appropriate order. We use this algorithm to study rotationless dipolar BECs and dipolar BECs with singly- and doubly-quantized vortices by employing a conjugate gradient algorithm for efficient minimization of the Gross-Pitaevskii energy functional. We calculate the quasiparticle modes by solving the Bogoliubov de Gennes equations via an iterative Arnoldi diagonalization scheme. Our results reveal that dipolar BECs with maximum densities in a ring about the center of the trap, such as dipolar BECs with singly-quantized vortices and rotationless dipolar BECs with biconcave structure [30], become dynamically unstable due to the softening of discrete roton-like modes with angular nodal structure. Thus, the roton manifests with angular character in these systems. Additionally, we find regions in parameter space where the dipolar BEC with a singly-quantized vortex exhibits radial density oscillations. We attribute such structure to the static manifestation of a discrete radial roton mode in the ground state due to the "perturbation" of the vortex core by applying a perturbation theory to the Gross-Pitaevskii equation. Original work from this chapter is published in [35] and [36].

In chapter 6, we apply a 4th order Runge-Kutta algorithm to the time-dependent Gross-Pitaevskii equation to show that the angular roton instability of the rotationless dipolar BEC with biconcave structure results in an angular collapse and subsequent angular expansion when the trap is turned off and the condensate is allowed to expand in free space. Imaging of the expanded cloud with angular nodal structure would then provide a measurement of the angular collapse and, thus, an indirect measurement of the presence of biconcave structure in the stable ground state of the system. Original work from this chapter is published in [37].

We move on to study the superfluid properties of the dipolar BEC in chapter 7. For the fully trapped system, we calculate a "discrete" dispersion relation, or quasiparticle energy as a function of momentum, which allows us to apply the Landau criterion for superfluidity to the trapped system to get an estimate of its superfluid critical velocity, or flow velocity below which flow is dissipationless. The presence of the discrete roton serves to lower the Landau critical velocity as a function of ddi strength or condensate density, which is confirmed via direct numeric simulation of a weak blue-detuned laser moving through the condensate with varying velocity. Indeed, these results support the Landau criterion, but reveal finite size effects. These effects grow as the strength and size of the laser are increased. Indeed, if the laser is sufficiently strong so as to create a hard boundary on a length scale on the order of the healing length of the condensate, vortices are nucleated in the gas instead of quasiparticles being produced above the critical velocity. The critical velocity for vortex nucleation, however, is much lower than the critical velocity for quasiparticle production. We proceed by considering a quasi-2D dipolar BEC where the polarization is now allowed to point in any direction, not just in the direction of the axial confinement. In this case, the interactions take on anisotropic character and, for a certain ddi strength and "tilt" angle, the dispersion relation of the system possesses a roton in the direction perpendicular to the dipole tilt and only phonon character in the parallel direction. This, in turn, predicts an anisotropic critical velocity for the system via the Landau criterion. We perform numeric simulations of both weak and strong blue-detuned lasers moving through this quasi-2D system and find that the superfluid critical velocity for both quasiparticle production and vortex nucleation is anisotropic, and the quasi-2D dipolar BEC with a tilted polarization field is thus an anisotropic superfluid. Original work from this chapter is published in [38] and [39].

In chapter 8, we consider again a dipolar BEC with cylindrical symmetry, but now loaded in a 1D lattice. For the case of an infinite lattice, we find a significant simplification of the mean-field interaction terms, as long as the axial wave function has an analytic form. We thus employ a separable ansatz to the BECs at each site where the radial part of the condensate wave function is sampled on a numeric grid, as before, and the axial part of the wave function (in the lattice direction) is given by a linear combination of the 0^{th} and 2^{nd} order Hermite polynomials. For the case of a single dipolar BEC, this ansatz gives excellent qualitative agreement and good quantitative agreement with the results of the full numeric treatment given in chapter 5. Thus, the Gross-Pitaevskii equation for the infinite 1D lattice becomes an equation for a single dipolar BEC but with a modified interaction potential. We study the structure and stability of this system as a function of lattice spacing, lattice site geometry and ddi strength. We find wildly modified roton stability in the lattice, where the system is highly destabilized for small lattice spacings due to the attractive part of the ddi. We also find "islands" in the parameter space where biconcave structure is present that would not be present in the absence of the lattice. Thus, we predict emergent biconcave structure in the dipolar BEC in the infinite 1D lattice. As a check, we treat an experimentally realistic system of nine lattice sites with varying condensate number exactly on a very large numeric grid, and find that the emergent biconcave structure persists in the finite lattice. Original work from this chapter is published in [40].

We summarize this dissertation in chapter 9.

Chapter 2

Background: Theory and Experiment

In this chapter, we discuss some of the important points in the history of low-temperature physics that lead up to the discovery of Bose-Einstein condensation in a dilute alkali vapor, wherein there are some excellent demonstrations of the advancement of scientific knowledge through the interplay of experiment and theory. Regarding the more recent history, we discuss the experimental advances that have occurred in the past two decades, as these are key not only to understanding the work presented in this thesis, but also to understanding the advances that went into making the "ultracold" regime an experimental reality. Additionally, we discuss some of the more relevant experimental results on dilute Bose-Einstein condensates, and motivate the exploration of the role that the dipole-dipole interaction (ddi) plays in these systems.

2.1 A Brief History

Motivated by Satyendra Nath Bose's work on the statistics of photons, Albert Einstein formulated the first theory for the statistics of massive bosons in 1924 [4]. He predicted that, below a critical temperature T_c, the lowest energy state of a quantum many-body system of bosons would become macroscopically occupied. This idea stemmed from two basic concepts, one being the indistinguishability of quantum particles and the other being the simple fact that bosons, as opposed to fermions, obey statistical laws such that two or more identical bosons can occupy the same quantum mechanical state, whereas identical fermions are forbidden to do so. As it turns out, this behavior of fermions is responsible for, among other things, the structure of electronic orbitals in atoms and the quantum degeneracy pressure that results in the stabilization of neutron stars, as electrons and neutrons are both fermions.

As we will see, Einstein's prediction was correct and the phenomenon that is now known as Bose-Einstein condensation does indeed occur in a system of bosons at sufficiently low temperature (as long as the bosons do not solidify). Additionally, the scientific community has come to understand that there are many interesting physical phenomena associated with this novel state of matter, the Bose-Einstein condensate (BEC). Perhaps the most important consequence of Bose-Einstein condensation is the emergence of superfluidity, though the connection between BEC and superfluidity was not immediately drawn in the earlier days of its study. In fact, this connection is still being investigated today, as we discuss further in section 2.3.2.

The word "superfluid" was first used by P. Kapitza in [41] to describe the non-classical nature of liquid ^{4}He that was observed at temperatures below $\sim 2.2\,\mathrm{K}$ [42], where the use of the prefix "super" was inspired by the already observed phenomenon of superconductivity in solid mercury in 1911 [43]. The strange, non-classical, "super" behavior to which Kapitza referred was the observation of a discontinuity of the specific heat of liquid ^{4}He around this temperature, the graph of which resembled the Greek character "λ" and was thus termed the "lambda-point." This was not the first time, however, that non-classical behavior was observed in liquid ^{4}He. For example, experiments using a torsion pendulum showed that the viscosity of liquid ^{4}He drops significantly when its temperature is dropped below the lambda-point [44], that is, the flow in liquid helium was observed to be non-dissipative. Inspired by the accumulating body of experimental evidence for the superfluid behavior of ^{4}He below a critical temperature, by the earlier theoretical work of Einstein, and by the fact that such phenomena were not observed in ^{3}He (a fermionic isotope) at the same temperatures, Fritz London proposed in 1938 that the unusual behavior of liquid ^{4}He was due to the phenomenon of BEC manifesting in the cold fluid [45]. Not long thereafter, the work of other talented theorists, namely L. Tisza and L. Landau, showed that a BEC-like superfluid fraction of the system was likely present and responsible for the unique non-dissipative behavior of liquid ^{4}He, supporting F. London's earlier hypothesis.

2.1.1 Phonons and Rotons

Both Tisza [46] and Landau [31, 47] proposed two-fluid models to describe liquid ^{4}He, where one fluid corresponded to the superfluid component and the other to the "normal," or non-superfluid component. Landau's insight was particularly brilliant in that he interpreted the normal component as a set of occupied excited states consisting of phonons and *localized* quantized vortices, dubbed "rotons" due to the rotational nature of such vortices. While the phonons disperse linearly, Landau predicted that the rotons experience a quadratic dispersion,

$$\omega(k) = \Delta + \frac{k - k_{\mathrm{roton}}^2}{2M_{\mathrm{roton}}}, \tag{2.1}$$

where $\hbar k_{\mathrm{roton}}$ is the roton momentum, on the order of the inverse atomic spacing in the liquid, M_{roton} is the effective roton mass and Δ is the roton energy gap. Landau was able to estimate the values of these parameters by matching his theory to the observed thermodynamical behavior of liquid ^{4}He. From this fitted dispersion, Landau developed a hard criterion for the existence of superfluidity in ^{4}He, being that superfluid, or dissipationless flow only exists below a critical velocity, the so-called "Landau critical velocity," or superfluid critical velocity. The Landau criterion for superfluidity can be derived simply by applying arguments for the conservation of energy and momentum of a phonon or roton excitation in a Galilean frame of reference, which we present in section 7.1. For ^{4}He, the predicted Landau critical velocity is set by the roton minimum, giving a velocity of $v_c \simeq \Delta/k_{\mathrm{roton}} \approx 60\,\mathrm{m/s}$.

In 1957, Cohen and Feynman proposed that the Landau phonon-roton dispersion could be measured by inelastically scattering neutrons off of a liquid ^{4}He sample [32]. This experiment was carried out soon thereafter, where excellent agreement was found with Landau's theory [33, 48]. Thus, strong evidence was obtained in support of Landau's prediction for the phonon-roton dispersion, though the explicit connection between superfluidity and a critical velocity was still not made. It is worth noting, though, that whether rotons are associated with vorticity is inconclusive in these experiments, and as a result rotons should not necessarily be thought to have a vortical nature. The measured phonon-roton dispersion from Ref. [33] is shown in figure 2.1. Indeed, we

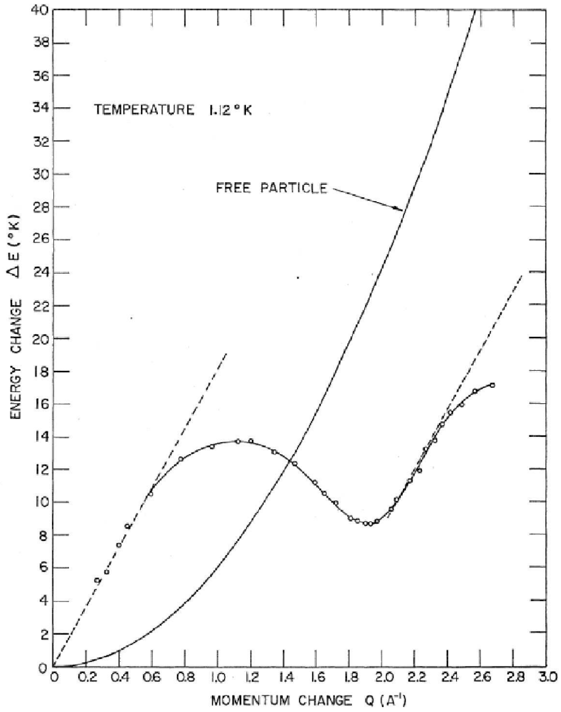

Figure 2.1: Measured quasiparticle dispersion of liquid ^{4}He at a temperature of 1.12 K. The circles show the neutron-scattering data from Ref. [33] and the solid line shows the free-particle dispersion. The phonons are seen in the linear dispersion at small momentum, and the roton is seen at the local minimum at the momentum $\sim 2.0\mathring{A}^{-1}$. Figure taken from Ref. [33].

return with strong interest to this roton feature in the ^{4}He dispersion in chapter 4, where we show that a similar feature emerges in the trapped dipolar BEC.

2.1.2 Vortices

While the neutron scattering experiments were able to measure the phonon-roton dispersion in superfluid ^{4}He, such techniques could not be applied to test the Landau criterion for superfluidity, or to measure the superfluid critical velocity in ^{4}He. For such measurements, a relative macroscopic flow velocity between the superfluid component and a “perturber” is required, the magnitude of which must be at least as great as the critical velocity of the superfluid. Such flow was realized in 1985 by forcing superfluid ^{4}He through a small aperture (less than 1 μm) [49]. The observed critical velocity in this experiment, however, was much lower than that predicted by the Landau criterion, suggesting that the excitation of rotons is not the relevant mechanism for dissipation in this superfluid system. Instead, the observed critical velocity is associated with dissipation into *quantized* vortex lines, where the vortices have quantized circulation $2\pi n\hbar/M$, where M is the mass of a particle in the fluid and n is an integer. Thus, having $n = 0$ implies no vorticity, while $n = 1$ corresponds to a singly quantized vortex, $n = 2$ corresponds to a doubly-quantized vortex, and so on. The existence of such vortex lines was first predicted by Feynman in 1955 [50], where he proposed that a critical flow velocity is necessary to nucleate such a quantized vortex state, just as is the case for a phonon or roton. He predicted that the critical velocity for the formation of a singly-quantized vortex of radius a in a cylinder of radius d should be given by

$$v_c = \frac{\hbar}{Md} \ln \left[\frac{d}{a}\right]. \tag{2.2}$$

In the experiment [49], a series of critical velocities were measured, corresponding to dissipation into vortex lines of various quantization, the lowest of which is in good agreement with Feynman's prediction (2.2). We note that the breaking of superfluid flow due to the excitation of rotons was observed, as well, by drifting negative ions through superfluid ^{4}He at sub-critical and super-critical velocities. The ions, unlike the hard wall of the aperture, were not sufficiently intrusive so as to nucleate free vortices. The mechanism for dissipation, though, is believed to be the excitation of a pair of rotons instead of a single roton above the Landau critical velocity [51].

While quantized vorticity does not exist in classical fluids, it is known to exist in single-particle quantum mechanical systems, for example, in the atom where the electrons have quantized angular momentum. The existence of quantized vortices in a superfluid suggests that the superfluid state may indeed be intimately connected with the phenomenon of Bose-Einstein condensation, where a macroscopic number of bosons occupy the ground *single* particle state. As we will see, quantized vortices manifest in BECs due to the single-particle nature of the condensed state, and are intimately related to the presence of superfluidity in cold Bose gases. Indeed, such phenomena are used as a “smoking gun” of superfluidity in these systems.

2.1.3 Superfluidity and Bose-Einstein Condensation

In 1956, Roger Penrose and Lars Onsager devised what remains today as perhaps the most fundamental theoretical criterion for superfluidity and Bose-Einstein condensation, linking the two in a before unseen way. They noticed that every such system must possess long-range order [52], that is, the single-particle density matrix or one-body correlation function $\rho^{(1)}(\mathbf{x}, \mathbf{x}')$ of the superfluid must not vanish in the limit $|\mathbf{x} - \mathbf{x}'| \to \infty$, and instead approach a finite value

$$\lim_{|\mathbf{x}-\mathbf{x}'|\to\infty} \rho^{(1)}(\mathbf{x}, \mathbf{x}') = \rho_c, \tag{2.3}$$

where ρ_c is the condensate number density of the system. This criterion is equivalent to saying that a macroscopic number of bosons in the fluid occupy the momentum state with $\hbar\mathbf{k} = 0$, corresponding to the lowest energy state of homogeneous space. Thus, the criterion for superfluidity proposed by Penrose and Onsager is simply that a finite fraction of the fluid be Bose-condensed. When introducing the methods we use to treat the BEC in this thesis (in chapters 3 and 4), we return to this point and show that the criterion for long-range order is satisfied by these methods.

Today, much of the physics of superfluid ^{4}He remains elusive, due primarily to its very high densities ($\rho \sim 2 \times 10^{22}\,\mathrm{cm}^{-3}$) and strong interactions, resulting in very small condensate fractions $\rho_c/\rho \sim 0.1$ and large depleted fractions. However, significant scientific advances in the more recent decades have provided the scientific community with a clean, reproducible and controllable tool with which to study superfluidity and other phenomena in ultracold matter. Specifically, the advent of laser and magnetic cooling and trapping, together with other cooling techniques (evaporative cooling) allowed scientists at JILA at the University of Colorado and NIST [1] and at MIT [2] to realize Bose-Einstein condensation of dilute alkali atom vapors for the first time in 1995. While interesting in and of themselves, as they were the coldest known samples of matter to exist in the universe, these dilute BECs have since proven to be useful tools from which much can be gained regarding the knowledge of cold matter. In section 2.3, we discuss some of the basic physics behind such cooling and trapping techniques, and present some key results that are relevant for the work in this thesis. First, we discuss in more detail the phenomenon of Bose-Einstein condensation in an ideal, non-interacting Bose gas, pointing out some finite-size effects that are associated with putting the system with finite particle number into a trap. While the theory formulated in chapter 3 is meant to describe a zero-temperature Bose gas, the following treatment of an ideal gas at finite temperatures gives insight into the nature of the phenomenon of Bose-Einstein condensation and motivates the pursuit of the ultracold regime by showing clear, analytic results for the temperature dependence of this phenomenon.

2.2 The Ideal Bose Gas

An ideal gas of non-interacting bosons is just an ensemble of non-interacting one-body systems. For the case at hand, we consider an ideal gas of N bosons with mass M in a harmonic trapping, or external potential $U(\mathbf{x})$,

$$U(\mathbf{x}) = \frac{1}{2}M\left(\omega_x^2 x^2 + \omega_y^2 y^2 + \omega_z^2 z^2\right). \tag{2.4}$$

We discuss how such a potential can be realized for a sample of atoms or molecules in section 2.3.1. The energy spectrum of a single-particle in this harmonic potential is well-known to be

$$\epsilon_{n_x n_y n_z} = \hbar\left(n_x\omega_x + n_y\omega_y + n_z\omega_z\right) + \epsilon_0, \tag{2.5}$$

where n_i are integers specifying the energy level in the i^{th} coordinate and $\epsilon_0 = \frac{1}{2}\hbar(\omega_x + \omega_y + \omega_z)$ is the ground state energy. For simplicity, we take $\omega_x = \omega_y = \omega_z = \omega$, so the trap is spherical, and define and state vector $\vec{l} = (n_x, n_y, n_z)$, so $\vec{l}$ describes a direction and magnitude in the discrete Hilbert space of a single particle in a three-dimensional (3D) harmonic oscillator. Now, the energy eigenvalues for this system can be written as $\epsilon_{\vec{l}} = \hbar\omega\mathrm{Tr}[\vec{l}] + \epsilon_0$. With the degeneracy factor $g_l = \frac{1}{2}(l+1)(l+2)$ of the spherical harmonic trap, meaning that there are g_l ways that a single particle can achieve the energy ϵ_l, the canonical partition function for this system can be written as

$$Z_N(T, N) = \sum_{\vec{l}} \exp\left[-\beta\sum_l g_l\epsilon_l n_l\right], \tag{2.6}$$

where $\beta = 1/k_BT$, k_B is the Boltzmann constant and the total particle number is given by $N = \sum_l n_l$, where n_l is the state occupation number, corresponding to n_l bosons occupying a state with energy ϵ_l. This restriction on the total particle number N makes calculating any physical observables or thermodynamic quantities with (2.6) very difficult, and motivates the introduction of the grand canonical ensemble, where the constraint of fixed particle number is replaced by the constraint of fixed chemical potential, μ. This means that the system under consideration stays in thermal equilibrium with a surrounding environment at the cost of exchanging particles with the environment [53], that is, the system is in chemical equilibrium.

The grand canonical partition function is calculated by taking the Laplace transform of the canonical partition function (2.6),

$$\Xi(T,\mu) = \sum_{N=0}^{\infty} e^{\beta\mu N} Z_N(T,N) = \prod_{l=0}^{\infty} \left(1 - e^{\beta(\mu-\epsilon_l)}\right)^{-g_l}, \tag{2.7}$$

from which the grand canonical potential can be calculated,

$$\Pi(T,\mu) = -k_BT \ln \Xi(T,\mu) = k_BT \sum_{l=0}^{\infty} g_l \ln\left[1 - e^{\beta(\mu-\epsilon_l)}\right]. \tag{2.8}$$

From this grand canonical potential, the average particle number in the non-interacting thermal Bose gas can be calculated by taking the partial derivative of (2.8) with respect to the chemical potential at fixed temperature,

$$\langle N \rangle = \left(\frac{\partial \Pi(T,\mu)}{\partial \mu}\right)_T = \sum_{l=0}^{\infty} \frac{g_l}{e^{\beta(\epsilon_l-\mu)} - 1}. \tag{2.9}$$

It is easy to identify the occupation number $\langle n_l \rangle = g_l(e^{\beta(\epsilon_l-\mu)} - 1)^{-1}$ from this result, which is just the Bose-Einstein distribution [4] weighted by the degeneracy factor g_l. For this result to be physical, we restrict $\mu \leq \epsilon_0$, so that the occupation numbers can not take on negative values. Thus, the chemical potential must be less than or equal to the ground state energy in the non-interacting Bose gas. Also, notice that as $\mu \to \epsilon_0$, the ground state occupancy n_0 becomes arbitrarily large, implying that this is suitable criteria for the emergence of a condensate. So, we expect that $\mu \to \epsilon_0$ corresponds to $T \to T_c$, where T_c is the critical temperature for Bose-Einstein condensation.

We can calculate this critical temperature T_c by considering the number of excited, non-condensed bosons in the system, given by taking the sum over all $l > 0$ in Eq. (2.9). To simplify this process, we go to the thermodynamic limit where the energy level spacing becomes very small and the degeneracy becomes large and can thus be approximated by $g_l \simeq l^2/2$. Additionally, we rescale the ground state energy to be zero. Transforming the sum in Eq. (2.9) into an integral, we see that the number of excited bosons is given by

$$N - N_0 = N_{ex} = \frac{1}{2} \int \frac{l^2 dl}{e^{\beta(\epsilon_l - \mu)} - 1}. \tag{2.10}$$

From our criteria discussed above, the critical temperature is determined by setting $\mu = 0$ and $N_{ex} = N$, giving

$$\frac{k_B T_c}{\hbar\omega} = \left(\frac{N}{\zeta(3)}\right)^{\frac{1}{3}}, \tag{2.11}$$

where $\zeta(x)$ is the Riemann-Zeta function [54] and $\zeta(3) \approx 1.2$. This result (2.11) can be used in Eq. (2.10) to show how the condensate fraction scales as a function of temperature [55]

$$\frac{N_0}{N} = 1 - \left(\frac{T}{T_c}\right)^3. \tag{2.12}$$

Thus, we see that the condensate fraction grows with an inverse cubic behavior as a function of temperature below the critical temperature T_c. The condensate fraction is plotted in figure 2.2 as a function of temperature, shown by the black dashed line. The thermodynamic limit result tells us that for $T > T_c$, there is a negligible fraction of the bosons occupying the ground state, and no condensate exists. However, for $T < T_c$ there is a macroscopic, non-negligible ground state occupation corresponding to the presence of a condensate. As forementioned, this was precisely the prediction that Einstein made in 1925 [4].

The effect of indistinguishability in Bose-Einstein condensation can be seen in a clever way. Recall that the thermal de Broglie wavelength of any massive body at temperature T is given by

$$\lambda_{\mathrm{dB}} = \sqrt{\frac{2\pi\hbar^2}{M k_B T}}. \tag{2.13}$$

We can define the phase space density ν as the number of bosons occupying the volume element λ_{dB}^3, $\nu = n\lambda_{\mathrm{dB}}^3$, where n is the real-space number density. For a thermal gas, this phase space

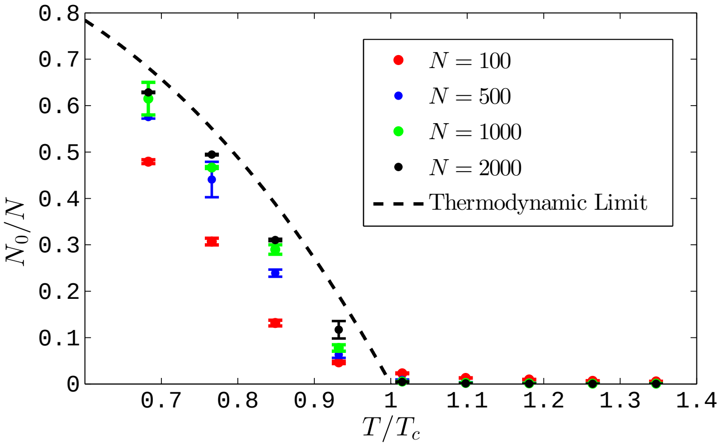

Figure 2.2: The condensate fraction N_0/N as a function of temperature for the ideal Bose gas in a spherically symmetric harmonic trap. The black dashed line is the thermodynamic limit result, and the dots are results from the Metropolis Monte Carlo algorithm for various particle numbers, as indicated in the legend. Notice that larger particle numbers in the Monte Carlo simulations exhibit better agreement with the thermodynamic limit result.

density is small as the characteristic de Broglie wavelengths of the bosons are much smaller than their average spacing. However, for an ultracold gas, we expect this phase space density to become large and correspond to the BEC transition when $\nu \sim 1$. Indeed, for a homogeneous Bose gas in a box, the BEC transition occurs when $\nu = \zeta(3/2) \approx 2.612$ [55]. Thus, below the critical temperature for BEC the wave functions of the bosons in the thermal system are sufficiently large that they become comparable to the average interparticle spacing, corresponding to the formation of a BEC. This perspective on the BEC phase transition clarifies why the critical temperature T_c is greater for higher densities. It is also interesting to note that the phase transition to BEC is purely statistical and not energetic, like the superfluid to Mott insulator transition of atoms on an optical lattice [56].

To obtain an estimate for the critical temperature of a dilute BEC, consider $N = 50 \times 10^3$ bosons in a spherical trap with frequencies $\omega = 2\pi \times 200\,\mathrm{Hz}$. These are numbers that, as we will see in section 2.3.1, are typical for modern BEC experiments. Such system parameters result in, from Eq. (2.11), a critical temperature of $T_c \simeq 330\,\mathrm{nK}$, which is about a factor of 6×10^{-8} *smaller* than the critical temperature (lambda-point) of liquid helium.

Before proceeding to discuss the techniques that led to the realization of the ultracold regime and the Bose-Einstein condensation of a dilute Bose gas, it is important to note the "finite size" corrections that are present in the real physical system, which is not well-represented by the thermodynamic limit. To investigate the effects that finite size has on the condensate fraction and the critical temperature of a Bose gas, we compute the harmonic oscillator state occupations exactly in the canonical ensemble (Eq. (2.6)) using the Metropolis Monte Carlo method for particle numbers of $N = 100, 500, 1000, 2000$. For details on this Monte Carlo algorithm, we refer the reader to [57]. As one expects, the finite size effects are more pronounced for smaller particle numbers, for example, $N = 100$, though the condensate fraction for $N = 2000$ is very close to the analytic thermodynamic limit results. Finite size effects were also studied in [58], where a first order correction in finite size predicts precisely what the Monte Carlo results show, that the condensate fraction and the critical temperature are decreased in finite systems. The role of interactions in the Bose-Einstein condensation of a trapped, finite sample was first considered in [59] where repulsive (attractive) interactions were found to decrease (increase) the condensate fraction and the critical temperature for condensation. Indeed, the presence of a trapping potential and repulsive interactions makes the realization of a BEC more difficult, as lower temperatures must be reached for these cases.

2.3 Bose-Einstein Condensation of Trapped Gases

To reach the ultracold nK regime that is necessary for the Bose-Einstein condensation of dilute gases, a variety of experimental techniques were developed and employed that utilized the nature of the atom's interactions with magnetic and optical fields. In this section, we discuss some of these techniques and the underlying physics that is involved. For a more detailed account, we refer the reader to [60] and [61]. Additionally, we discuss a few early experimental and theoretical results that are important for the work presented in this thesis, particularly, the realization of Bose-Einstein condensation in a trap and the demonstration of quantized vortex states in BECs.

2.3.1 Experimental Techniques

The cooling of a gaseous atomic sample typically begins in a Zeeman slower, where cooling from hundreds of Kelvin down to the μ-Kelvin range is possible. The Zeeman slower relies on the Doppler effect that is present in a sample of atoms moving relative to a beam of laser light. If the laser frequency ω is tuned properly, the atoms moving opposite the direction of the laser light in a certain range of velocities will absorb more photons, as the light is more "blue" for these atoms. By conservation of momentum, this slows the atoms down and, upon spontaneous emission, the atoms end up slower, and thus cooler, on average. A problem encountered with this technique is that the cooling is limited as the atoms slow to a certain velocity, below which photon absorption is critically suppressed. To counter this problem, a Zeeman slower uses an inhomogeneous magnetic field along the direction of the laser propagation in order to shift the resonant frequency of the atom as a function of space via the linear Zeeman effect, making the laser cooling process more efficient. This allows the atoms to slow to very small velocities and still "see" laser light that is resonant with the atomic transition. The laser cooling technique was developed and demonstrated successfully by William D. Phillips and others, for which they shared the Nobel Prize in Physics in 1997 [5, 62].

While laser cooling can produce a very cold, μK sample of atoms, sub-μK temperatures are necessary to achieve BEC, as was discussed in the previous section. To achieve these temperatures, experimentalists developed evaporative cooling methods for trapped atoms. The basic idea of evaporative cooling is to effectively lower the walls of the trap at higher energies that correspond to atoms at super-critical temperatures, so that these atoms can leave the trap and only the cooler atoms remain. This can be achieved, for example, in magnetic traps by flipping the spin of high-energy atoms with an RF pulse. Indeed, evaporative cooling allowed experimentalists to lower the temperature of their atomic samples sufficiently to achieve BEC. For a review of evaporative cooling, see [63].

As suggested, the linear Zeeman effect describes the interaction of an atom with an applied magnetic field and the linear Hamiltonian of the interaction can be written as

$$H_i'(\mathbf{x}) = -\boldsymbol{\mu}_i \cdot \mathbf{B}(\mathbf{x}) \tag{2.14}$$

where $\boldsymbol{\mu}_i$ is the magnetic moment of the atom in state i and $\mathbf{B}(\mathbf{x})$ is the applied magnetic field that, in general, can vary throughout space. The magnetic moment can be nontrivial to calculate and depends on both electronic and nuclear structure. We leave out a detailed discussion here, and instead direct the reader to [64] or [60], but note that the result of such an interaction is the splitting of the hyperfine levels of the atom (used in the Zeeman slower). Additionally, if $\mathbf{B}(\mathbf{x})$ is not homogeneous in space, the linear Zeeman shift results in a spatially varying potential for the atoms. Such a potential can be used to trap atoms if the magnetic field $\mathbf{B}(\mathbf{x})$ possesses a potential maximum or minimum in space. However, there are two important considerations related to such trapping, one being that the achievable magnetic fields in a laboratory are typically much less than a Tesla and the magnetic moment of an atom is typically on the order of 1-10 Bohr magnetons, $\mu_B = e\hbar/2M_e$, resulting in maximum trap depths of less than a Kelvin. The other important consideration is that a magnetic field can not possess a local maximum in a current-free region [65], so only "low field seeking states" with $\mu_i > 0$ can be magnetically trapped.

Magnetic trapping has other limitations as well. For example, magnetic traps, by their nature, distinguish between magnetic substates and shift their energy levels, effectively trapping the different states in different potentials. However, it is possible to trap atoms (and molecules) in purely optical fields where all Zeeman substates "feel" the same trapping potential. Such optical potentials allow for the investigation of the spin or magnetic degrees of freedom in a quantum gas because the potential is effectively the same for all corresponding substates. The optical trapping of atoms utilizes the AC Stark shift, which describes the energy shift of an atom in an oscillating time-dependent field. In the dipole approximation (valid when the wavelength of the laser is much greater than the size of the atom, which is automatic for optical transitions), the AC Stark shift of the atom in its *ground* state is given in second-order perturbation theory by

$$V_g(\mathbf{x}) = -\frac{1}{2}\mathrm{Re}\left[\alpha(\omega)\right] \left|\langle \mathcal{E}(\mathbf{x},t)\rangle_t\right|^2 \tag{2.15}$$

where ω is the laser frequency, $\mathcal{E}(\mathbf{x},t)$ is the magnitude of the electric field as a function of space and time and $\alpha(\omega)$ is the electric polarizability [55],

$$\alpha(\omega) = 2\sum_e \frac{E_e - E_g}{(E_e - E_g)^2 - (\hbar\omega)^2}|\langle e|\mathbf{d}\cdot\hat{\epsilon}|g\rangle|^2. \tag{2.16}$$

Here, the sum is over all excited states e with energies E_e, $\langle e|\mathbf{d}\cdot\hat{\epsilon}|g\rangle$ are the dipole matrix elements between the ground and excited states and $\hat{\epsilon}$ is a unit vector in the direction of the electric field $\mathcal{E}$. If the laser frequency ω is tuned near the resonance $E_e - E_g$, all other excited states in the sum in (2.16) can be neglected to a good approximation. In this case, we can define the dipole matrix element $d = \langle e|\mathbf{d}\cdot\hat{\epsilon}|g\rangle$ and the splitting $\Delta = (E_e - E_g) - \hbar\omega$, where the term $1/\Delta$ dominates the expansion of the energy-dependent coefficient in (2.16) when the laser is tuned near resonance, and write

$$\alpha \approx \frac{d^2}{\Delta}. \tag{2.17}$$

For $\Delta < 0$, corresponding to a laser that is "blue" detuned from the dipole transition, the potential energy shift (2.15) has a maximum where the optical field has a maximum intensity. For $\Delta > 0$, corresponding to a laser that is "red" detuned from the dipole transition, the potential energy shift has a *minimum* where the optical field has a maximum intensity. Thus, focusing laser light to achieve an intensity maximum can be used to attract (red-detuned) or repel (blue-detuned) atoms from the high intensity region.

Regarding the time averaging of the field in Eq. (2.15), there are two important cases to consider, one where there is a single propagating laser and one where there is a laser reflected back onto itself, or a retro-reflected laser. Without loss of generality, we consider a laser that propagates in the z-direction. The electric field of the single propagating laser can be written as

$$\mathcal{E}(\mathbf{x},t) = \mathcal{E}_0(\boldsymbol{\rho})e^{ikz}e^{-i\omega t}, \tag{2.18}$$

which has the time averaged intensity $|\langle\mathcal{E}(\mathbf{x},t)\rangle_t|^2 = |\mathcal{E}_0(\boldsymbol{\rho})|^2$. If we assume that the laser has a Gaussian beam profile in the radial direction, then $|\mathcal{E}_0(\boldsymbol{\rho})|^2$ is Gaussian, as well. Thus, we see that proper focusing of laser light can result in intensity maxima with Gaussian profiles that can trap or repel atoms. We can write the field for the retro-reflected laser as

$$\mathcal{E}(\mathbf{x},t) = \mathcal{E}_0(\boldsymbol{\rho})e^{ikz}e^{-i\omega t} + \mathcal{E}_0^\star(\boldsymbol{\rho})e^{-ikz}e^{i\omega t}, \tag{2.19}$$

This field has the time-averaged intensity $|\langle\mathcal{E}(\mathbf{x},t)\rangle_t|^2 = \mathcal{E}_0^2(\boldsymbol{\rho})\cos^2 kx$, taking the form of a standing wave pattern, or a one-dimensional (1D) lattice with spacing $2\pi/k$. This result is easily extended to both two-dimensions (2D) and three-dimensions (3D), correspond to 2D and 3D optical lattice potentials. While the relevant optical lattice geometry for the work in this thesis is 1D (see chapter 8), there is much interest in the 2D and 3D geometries, as well, for studying quantum degenerate systems. For a review of the physics of ultracold bosons in optical lattices, see [6] and for a review of dipolar bosons in optical lattices, see [8].

The typical depths of optical traps that utilize the AC Stark shift are $\sim \mu$K, and are thus much more shallow than typical magnetic traps. However, this depth is still much greater than the characteristic critical temperatures for BEC, so such optical traps can still hold condensates and atoms and molecules that are pre-cooled to the sub-μK range. As a result, optical traps for dilute BECs are well-approximated by harmonic traps of the form (2.4). Trapping by purely optical means has proven particularly useful in recent experiments on "spinor" BECs, where homogeneous applied magnetic fields split the degeneracy of the magnetic sublevels and spin-exchange interactions lead to novel spin-density phases of these quantum gases. Such experiments have been performed on $F = 1$ ^{87}Rb and $F = 1$ ^{23}Na (both with 3 spin components), and more recently on $F = 3$ ^{52}Cr in Paris [66] (with 7 spin components). Additionally, purely optical traps are important when using Fano-Feshbach resonances to control the strength of the short-range interactions in BECs, as these resonances can exhibit strong magnetic field dependence. We discuss such resonances further in section 6.1, as they are directly relevant to the results presented therein.

2.3.2 Key Results

As mentioned in section 2.1.3, the cooling and trapping techniques described above allowed researchers at JILA [1] and MIT [2] to achieve nearly pure Bose-Einstein condensates for the first

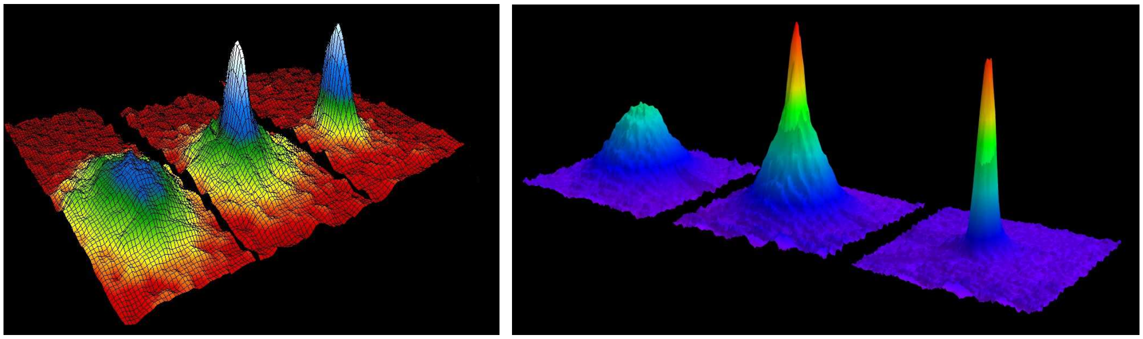

Figure 2.3: Images from the first BEC experiments of ^{87}Rb at JILA (left) and ^{23}Na at MIT (right). From left to right in each image, surface plots are shown of velocity distributions and real-space distrubutions, respectively, at temperatures just above, at, and below the critical temperature for BEC. The sharpening of the distribution below the critical temperature provides evidence BEC formation. Figures used with permission of E. A. Cornell from [67] (left) and W. Ketterle from [68] (right).

time in 1995. Images of the emergence of the BECs at JILA and MIT are shown in figure 2.3. The JILA image on the left shows the velocity distribution of the Bose gas as a function of temperature, and the MIT image on the right shows the real-space distribution of the Bose gas as a function of temperature. One clearly sees a peak in the right-most image in both cases, signifying the macroscopically occupied Bose-Einstein condensate.

The realization of BEC, together with novel trapping techniques and methods to control two-body interactions, which we discuss in detail later, gave both experimentalists and theorists a tool with which to study a seemingly endless field of ultracold phenomena and quantum matter. While this field is still growing today as researchers are working towards, for example, the creation of degenerate molecular gases and degenerate quantum gases with novel interactions, such as the dipole-dipole interaction discussed for the remainder of this thesis, it is important to first note a couple of very important results that demonstrated, for the first time, the novel superfluid nature of the dilute BEC.

Recall from the discussion in section 2.1.2 that quantized vortices are direct signatures of superfluidity. Thus, the observation of quantized vortex states in a dilute BEC provides direct evidence of superfluidity in this system. This is precisely what was done, for the first time, by the

JILA group in 1999 [69]. By clever spatial and temporal control of the optical pumping of ^{87}Rb between two spin states, angular momentum was imparted to the BEC in order to nucleate a vortex state. Images from this experiment are shown in the top part of figure 2.4, where the vortex is present in one spin component in (a) and has been transfered to the other spin component, and is thus no longer seen in (c). The presence of vorticity implies the presence of angular momentum, or circulation, which is characterized by a phase wrapping of a quantum mechanical wave function. For quantized vorticity, the phase wrapping $\Delta\phi$ must occur in integer units of 2π, $\Delta\phi = 2\pi n$ where n is an integer. In the experiment [69], phase interference was used to confirm the presence of the singly-quantized vortex

In 2001, the MIT group succeeded in realizing and imaging multiple vortex states in a dilute BEC, where the vortex density was sufficiently high to create a vortex *lattice*, showing for the first time the presence of bulk vortex matter in a quantum degenerate system, with a lifetime of tens of seconds [70]. To impart angular momentum to their BEC, the group used two blue-detuned lasers, which form repulsive Gaussian potentials via the AC Stark shift, and rotated them through the cloud. Images from this experiment are shown in the bottom part of figure 2.4, where the images from left to right show an increase in the laser precession frequency and thus more vortices in the BEC. Beyond the fact that the vortices (with the same circulation) form a lattice, it is interesting that many singly-quantized vortices form instead of one or a few multiply-quantized vortices. Indeed, multiply-quantized vortices can be, depending on the shape and interaction strength in the BEC, dynamically unstable to the formation of multiple singly-quantized vortices. This point was demonstrated by the JILA group in [71], where a blue-detuned laser was used to create a density minimum in a BEC with vortex matter, wherein the vortices combined to a multiply-quantized state, then decayed back into the lattice of singly-quantized vortices.

We have just pointed out a couple of the more interesting, relevant results from the early BEC experiments here, though many more exist [72, 73, 67, 68]. Having seen that nearly pure Bose-Einstein condensates of dilute atomic vapors are realizable in the laboratory setting and that their superfluid properties have been demonstrated, we now turn our attention to the presence of

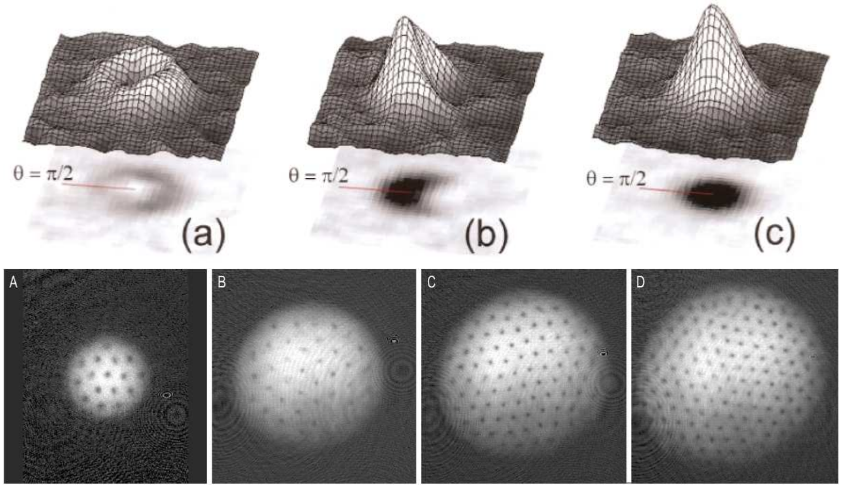

Figure 2.4: *Top image*: Image of a singly-quantized vortex in a single spin component of a ^{87}Rb BEC at JILA. In (a), the vortex is present, in (b) it is being transfered to the other spin component, and in (c) it absent, having been transfered to the other spin component. Figure reprinted with permission from [69]. *Bottom image*: Images of vortex lattice structures in the ^{23}Na BEC at MIT. The leftmost (rightmost) images correspond to less (more) angular momentum transfered to the BEC, resulting in fewer (more) vortices in the BEC. Figure reprinted with permission from [70]. Both images are from experiments that played a key role in demonstrating the superfluid nature of the dilute BEC.

interactions in these systems, in particular, the dipole-dipole interaction.

2.4 Dipolar Interactions in Ultracold Bose Gases

Since the first BEC experiments, many other atomic species have been Bose condensed, including hydrogen [74], lithium [3], potassium [75], cesium [76], ytterbium [77], calcium [78], strontium [79], chromium [14] and most recently, dysprosium [17]. The latter two species, unlike the others, have significant permanent magnetic dipole moments, as indicated in table 2.1. While there is a plethora of rich physics that exists, and presumably has yet to be discovered, in quantum degenerate gases of the other atomic species, the presence of large dipole moments in Cr and Dy sparks particular interest, as interactions between such dipoles have been predicted to lead to new physics related to, for example, novel states of quantum matter and quantum phase transitions [8].

Additionally, there has recently been a strong push towards the realization of a quantum degenerate gas of heteronuclear molecules. A significant achievement in this line of research was marked when the Jin/Ye collaboration at JILA managed to create a motionally ultracold gas of fermionic KRb molecules in their ground rovibrational state via the novel STIRAP process [24], though quantum degeneracy (marked by the Fermi temperature) has remained elusive. For more information on the STIRAP process, we refer the reader to [80]. Other groups have adopted this technology, and researchers now have a cold sample of bosonic KRb molecules [26] in their rovibrational ground state, and bosonic RbCs is promisingly close [81]. Heteronuclear polar molecules, unlike dipolar atoms with permanent magnetic dipole moments, are electrically polarizable and can develop very large electric dipole moments when polarized in an applied field. This polarizabilty, actually, is given by the zero-frequency value of the AC polarizability $\alpha(0)$ from Equation (2.16). The zero-frequency behavior of the AC Stark shift is referred to, appropriately, as the DC Stark shift. These molecules, however, saturate at sufficiently large fields to a maximally attainable dipole moment d_{max}. Maximum dipole moments for some heteronuclear molecules are given in table 2.1. For a review of the physics related to ultracold polar molecules, see [7].

Besides having potentially large dipole moments, which can induce, for example, long-range coupling in optical lattice models, polar molecules have other important characteristics that allow them to be used for studying other rich, more complicated systems with a high level of control. For example, recent work has proposed using polar molecules to simulate quantum magnetism, where the rotational degrees of freedom map into spin degrees of freedom [82]. Additionally, it has been theorized that, at large enough densities and in reduced dimensions, dipolar quantum gases can be used to realize and study self-assembled crystals [83] (see section 4.2.5 for more details). Also, because some heteronuclear polar molecules are chemically reactive, the high level of quantum state control and ultracold temperatures allow for the study of ultracold, highly controlled atom-molecule and molecule-molecule chemical reactions [7]. It has also been proposed that cold polar molecules could be used as qubits in quantum computing algorithms [84].

In this work, we are most concerned with the effect of the dipole-dipole interaction in a Bose-Einstein condensate of dipolar constituents. For two permanent dipoles with dipole moments $\mathbf{d}_1$

Species	Dipole Moment	a_{dd} (a_0)	Reactive?	Reference
^{87}Rb	1 μ_B	0.71	N	[85]
^{52}Cr	6 μ_B	15.36	N	[85]
^{164}Dy	10 μ_B	134.57	N	[85]
^{41}K^{87}Rb	0.57 Debye	3.940×10^3	Y	[86]
^{87}Rb^{133}Cs	1.25 Debye	3.257×10^4	N	[87, 88]
^{232}Th^{16}O	3.89 Debye	3.556×10^5	N	[89, 90]

Table 2.1: Dipole moments, characteristic dipole lengths of candidate atomic and molecular species. For the molecules, the dipole moment specifies the maximum achievable dipole moment. Because ^{41}K^{87}Rb is chemically reactive, it is labeled as such.

and $\mathbf{d}_2$ at positions $\mathbf{x}_1$ and $\mathbf{x}_2$, respectively, the interaction potential is given by (in cgs units) [91]

$$V_d(\mathbf{x}_1, \mathbf{x}_2) = V_d(\mathbf{x}_1 - \mathbf{x}_2) = \frac{\mathbf{d}_1 \cdot \mathbf{d}_2 - 3(\mathbf{n} \cdot \mathbf{d}_1)(\mathbf{n} \cdot \mathbf{d}_2)}{|\mathbf{x}_1 - \mathbf{x}_2|^3}, \tag{2.20}$$

where $\mathbf{n}$ is the unit vector in the direction of $\mathbf{x}_1 - \mathbf{x}_2$. The dipole-dipole interaction (ddi) is anisotropic and long-range, the explicit meaning of which is explained in section 3.4.2. Thus, the interaction potential changes magnitude and sign depending on the relative orientation of the dipoles. As we will see, this feature plays a very important role in the physics of BECs with dipolar interactions, or dipolar BECs, leading to new, novel physics even when the BEC is dilute. Though the interaction potential (2.20) is proportional to the product of the dipole moments, the theory that we formulate in the next two chapters shows that the strength of the ddi is actually characterized by the dipole "coupling," $g_d = 4\pi\hbar^2 a_{dd}/M$, where M is the mass of a dipolar atom or molecule and a_{dd} is the characteristic dipole length of a species with dipole moment d,

$$a_{dd} = \frac{Md^2}{3\hbar^2}. \tag{2.21}$$

Dipole lengths for various atomic and molecular species are given in table 2.1. For highly dipolar molecules, such as RbCs, the maximum achievable dipole lengths are on the order of tens of thousands of Bohr radii. We motivate the definition of this dipole length (with the factor of 3 in the denominator) in chapter 4.

As forementioned, experimental groups have succeeded in creating Bose-Einstein condensates of atomic Cr (in Tilman Pfau's group in Stuttgart and in Oliver Gorceix's group in Paris) and atomic

Dy (in Benjamin Lev's group at the University of Illinois and Stanford), and strong dipolar effects have been demonstrated in all experiments. In the following two chapters, we develop a working theory for dipolar BECs, and motivate the introduction of relevant physical parameters therein, such as the condensate wave function, or order parameter of the ultracold Bose gas. Once this object, and others, are better motivated and understood, we return to discuss recent experimental results on dipolar BECs in detail. Now, having gained an appreciation for the physics of ultracold Bose gases and BECs, as well and the motivation for understanding the role that the ddi plays in the Bose condensed state, we turn our attention to the characterization of an ultracold Bose gas in the presence of interparticle interactions, in particular, dipole-dipole interactions.

Chapter 3

Zero-Temperature Field Theory for Bosons

3.1 Second-Quantized Field Theory

The goal of this chapter is to derive a working theory for a gas of interacting dipolar bosons at zero temperature ($T = 0$). A common and fruitful approach to such an end (for finite temperature, as well), involves the language of second-quantization. In this framework, one describes a many-body system by keeping track of single-particle state occupations instead of a full many-body wave function $\Phi_N(\{\mathbf{x}_i\})$. Thus, the theory is quantized "twice" if the full many-body wave function, which obeys the many-body Schrödinger equation $\hat{H}_N \Phi_N(\{\mathbf{x}_i\}) = E\Phi_N(\{\mathbf{x}_i\})$, is considered to be quantized "once". Here, $\hat{H}_N$ is the Hamiltonian describing $N = \sum_i N_i$ interacting particles at coordinates $\{\mathbf{x}_i\} = \{\mathbf{x}_0, \mathbf{x}_1, \ldots\}$.

To motivate the definition of a quantized field, consider the separable coordinate representation of the many-body wave function Φ for a system of bosons,

$$\Phi_N(\{\mathbf{x}_i\}) = \sqrt{\frac{N_0! N_1! \ldots}{N!}} \sum_{\mathrm{P}} \phi_0(\mathbf{x}_0)\phi_1(\mathbf{x}_1)\ldots \tag{3.1}$$

where there are N_i bosons occupying the state $\phi_i(\mathbf{x})$ and $\sum_{\mathrm{P}}$ indicates that the sum should be taken over all possible permutations of the product of single-particle wave functions $\phi_i(\mathbf{x})$ [92]. The set of single-particle wave functions $\{\phi_i\}$ is assumed to be complete and orthonormal so that $\int d\mathbf{x} \phi_i^\star(\mathbf{x})\phi_j(\mathbf{x}) = \delta_{ij}$ and $\sum_i \phi_i(\mathbf{x})\phi_i^\star(\mathbf{x}') = \delta(\mathbf{x} - \mathbf{x}')$. Because we are dealing with bosons, the wave function (3.1) is symmetric with respect to all permutations P. Now, consider the matrix elements of the operator $\hat{\mathcal{O}} = \sum_i \hat{o}_i$ where $\hat{o}_i$ operates only on functions of the coordinate $\mathbf{x}_i$. The only non-zero matrix elements of this operator are those corresponding to all $N_i \to N_i$ (diagonal) or those corresponding to the occupation of some state i being decreased by unity while the occupation of some state j is increased by unity, or $N_i \to N_i - 1$ while simultaneously $N_j \to N_j + 1$ so the total particle number $N = \sum_i N_i$ is conserved [93].

Such behavior can be captured by introducing the Bose creation and annihilation operators, $\hat{a}_i^\dagger$ and $\hat{a}_i$, respectively. These operators are defined by their their action on a many-body state in the occupation number, or Fock representation, $|\Phi_N\rangle = |N_0, N_1, \ldots, N_i, \ldots\rangle$, corresponding to N_0 particles occupying state $\phi_0(\mathbf{x})$, N_1 particles in the state $\phi_1(\mathbf{x})$, and so on, and by their commutation algebra. These many-body occupation number states are defined to be orthonormal so that $\langle\Phi_{N'}|\Phi_N\rangle = \delta_{N'N}$. The action of the annihilation operator $\hat{a}_i$ on $|\Phi_N\rangle$ reduces the occupation of the state $\phi_i(\mathbf{x})$ by unity,

$$\hat{a}_i|N_0, N_1, \ldots, N_i, \ldots\rangle = \sqrt{N_i}|N_0, N_1, \ldots, N_i - 1, \ldots\rangle, \tag{3.2}$$

and the action of the creation operator $\hat{a}_i^\dagger$ on $|\Phi_N\rangle$ increases the occupation of the state $\phi_i(\mathbf{x})$ by unity,

$$\hat{a}_i^\dagger|N_0, N_1, \ldots, N_i, \ldots\rangle = \sqrt{N_i + 1}|N_0, N_1, \ldots, N_i + 1, \ldots\rangle. \tag{3.3}$$

The factors of $\sqrt{N_i}$ and $\sqrt{N_i + 1}$ are defined so that the annihilation of a particle from state $\phi_i(\mathbf{x})$ with occupation number $N_i = 0$ gives the result $\hat{a}_i|\ldots, N_i = 0, \ldots\rangle = 0$ and does not allow for unphysical negative occupation numbers. Additionally, it is straightforward to see that the number operator $\hat{N}_i$ is diagonal in the occupation number basis and has eigenvalue N_i. The number operator is expressed in terms of the creation and annihilation operators as $\hat{N}_i = \hat{a}_i^\dagger\hat{a}_i$,

$$\begin{aligned} \hat{a}_i^\dagger\hat{a}_i|N_0, N_1, \ldots, N_i, \ldots\rangle &= \hat{a}_i^\dagger\sqrt{N_i}|N_0, N_1, \ldots, N_i - 1, \ldots\rangle \\ &= \sqrt{(N_i - 1) + 1}\sqrt{N_i}|N_0, N_1, \ldots, (N_i - 1) + 1, \ldots\rangle \\ &= N_i|N_0, N_1, \ldots, N_i, \ldots\rangle, \end{aligned} \tag{3.4}$$

so the occupation number of the state $\phi_i(\mathbf{x})$ is just given by $\langle\Phi_N|\hat{N}_i|\Phi_N\rangle = N_i$.

The Bose creation and annihilation operators satisfy the commutation relations

$$\left[\hat{a}_i, \hat{a}_j^\dagger\right] = \delta_{ij} \tag{3.5}$$

$$\left[\hat{a}_i, \hat{a}_j\right] = \left[\hat{a}_i^\dagger, \hat{a}_j^\dagger\right] = 0, \tag{3.6}$$

so the many-body states are properly symmetrized. At this point, we introduce the vacuum field of our occupation number basis, $|0\rangle$, which is defined so that $\hat{a}_i|0\rangle = 0$ for all i. Starting with this vacuum state, we can create a state with a given configuration by successive application of appropriate creation operators,

$$|\Phi_N\rangle = \frac{1}{\sqrt{N_0! N_1! \dots N_i! \dots}} \left(a_0^\dagger\right)^{N_0} \left(a_1^\dagger\right)^{N_1} \dots \left(a_i^\dagger\right)^{N_i} \dots |0\rangle. \tag{3.7}$$

While the use of creation and annihilation operators in the occupation number representation provides a clean and natural toolset to work with many-body systems, it is often advantageous to work in the coordinate representation when the objects of interest are related to, for example, the spatial density of the system. A direct connection between the occupation number representation and the coordinate representation can be made by defining the Bose field operators,

$$\hat{\psi}(\mathbf{x}) = \sum_i \phi_i(\mathbf{x}) \hat{a}_i \tag{3.8}$$

$$\hat{\psi}^\dagger(\mathbf{x}) = \sum_i \phi_i^\star(\mathbf{x}) \hat{a}_i^\dagger, \tag{3.9}$$

where, again, $\{\phi_i(\mathbf{x})\}$ is a complete, orthonormal set of single particle wave functions. By multiplying Eq. (3.8) by $\phi_j^\star(\mathbf{x})$ and Eq. (3.9) by $\phi_j(\mathbf{x})$ and integrating over all $\mathbf{x}$, we arrive at the inverse relations

$$\hat{a}_i = \int d\mathbf{x}\, \hat{\psi}(\mathbf{x}) \phi_i^\star(\mathbf{x}) \tag{3.10}$$

$$\hat{a}_i^\dagger = \int d\mathbf{x}\, \hat{\psi}^\dagger(\mathbf{x}) \phi_i(\mathbf{x}). \tag{3.11}$$

Using these inverse relations, the commutators of the field operators are found to be

$$\left[\hat{\psi}(\mathbf{x}), \hat{\psi}^\dagger(\mathbf{x}')\right] = \delta(\mathbf{x} - \mathbf{x}') \tag{3.12}$$

$$\left[\hat{\psi}(\mathbf{x}), \hat{\psi}(\mathbf{x}')\right] = \left[\hat{\psi}^\dagger(\mathbf{x}), \hat{\psi}^\dagger(\mathbf{x}')\right] = 0. \tag{3.13}$$

The number operator for the *total* number of particles in the system, $\hat{N} = \sum_i \hat{N}_i$ can be written in terms of the field operators,

$$\hat{N} = \int d\mathbf{x} \hat{\psi}^\dagger(\mathbf{x})\hat{\psi}(\mathbf{x}), \tag{3.14}$$

where we have used the completeness of the set $\{\phi_i(\mathbf{x})\}$ to arrive at this result. Unlike the annihilation and creation operators which annihilate and create a particle in a well defined single-particle state, the field operators (3.8) and (3.9) annihilate and create, respectively, a particle at position $\mathbf{x}$.

3.1.1 Many-Body Hamiltonian in Second-Quantization

Recall that the system under consideration is an ultracold, *dilute* gas of interacting bosons. The dilute character of the gas allows us to truncate the interactions at the two-body, or binary level due to the fact that the probability of two particles interacting in a dilute gas overwhelms the probably of three particles doing so. Thus, in terms of the Bose field operators, the many-body Hamiltonian can be expressed as

$$\hat{H} = \int d\mathbf{x} \hat{\psi}^\dagger(\mathbf{x}) \hat{H}^{(1)}(\mathbf{x}) \hat{\psi}(\mathbf{x}) + \frac{1}{2}\int d\mathbf{x} \int d\mathbf{x}' \hat{\psi}^\dagger(\mathbf{x})\hat{\psi}^\dagger(\mathbf{x}') V(\mathbf{x}-\mathbf{x}')\hat{\psi}(\mathbf{x}')\hat{\psi}(\mathbf{x}), \tag{3.15}$$

where $V(\mathbf{x}-\mathbf{x}')$ is the two-body interaction potential and $\hat{H}^{(1)}(\mathbf{x})$ is the single particle Hamiltonian

$$\hat{H}^{(1)}(\mathbf{x}) = -\frac{\hbar^2}{2M}\nabla^2 + U(\mathbf{x}), \tag{3.16}$$

where M is the mass of a single boson and $U(\mathbf{x})$ is the external, or trapping potential. The factor of $1/2$ in the interaction term corrects for a double counting that is inherent in the integration. This Hamiltonian operator (3.15) can be expressed in terms of the creation and annihilation operators by substituting Eqs. (3.8) and (3.9) in for the Bose field operators, giving

$$\hat{H} = \sum_{i,j} \hat{a}_i^\dagger H_{ij}^{(1)} \hat{a}_j + \frac{1}{2}\sum_{i,j,k,l} \hat{a}_i^\dagger \hat{a}_j^\dagger V_{ijkl} \hat{a}_k \hat{a}_l, \tag{3.17}$$

where $H_{ij}^{(1)}$ are the matrix elements of the single particle Hamiltonian

$$H_{ij}^{(1)} = \int d\mathbf{x} \phi_i^\star(\mathbf{x}) \hat{H}^{(1)}(\mathbf{x}) \phi_j(\mathbf{x}) \tag{3.18}$$

and V_{ijkl} are the interaction matrix elements

$$V_{ijkl} = \int d\mathbf{x} \int d\mathbf{x}' \phi_i^\star(\mathbf{x}) \phi_j^\star(\mathbf{x}') V(\mathbf{x}-\mathbf{x}') \phi_k(\mathbf{x}') \phi_l(\mathbf{x}). \tag{3.19}$$

3.2 The Bogoliubov Approximation

The diagonalization of the Hamiltonians (3.15) and (3.17) is quite difficult as they are written in full generality. However, a significant simplification can be made by restricting the system of bosons that these Hamiltonians describe to the ultracold regime. Here, ultracold refers to temperatures $T \ll T_c$, where T_c is the critical temperature for Bose-Einstein condensation. In this regime, the number of bosons occupying the condensed state $\phi_0(\mathbf{x})$ is macroscopic and overwhelms the occupation of any excited states corresponding to $\phi_i(\mathbf{x})$ with $i \neq 0$, that is, the condensate fraction $n_0 \equiv N_0/N \sim 1$ and the excited fraction $n_{\text{ex}} \equiv \sum_{i\neq 0} N_i/N \ll 1$. To a good approximation, we can treat the condensate part of the field operator as a c-number and write the field operator as

$$\hat{\Psi}(\mathbf{x}) \simeq \langle \hat{\Psi}(\mathbf{x}) \rangle + \hat{\varphi}(\mathbf{x}) = \sqrt{N_0}\phi_0(\mathbf{x}) + \hat{\varphi}(\mathbf{x}) \tag{3.20}$$

where $\langle \hat{\Psi}(\mathbf{x}) \rangle$ is a low-temperature ensemble average of the field operator and $\hat{\varphi}(\mathbf{x})$ corresponds to the excited, non-condensed states, or the so-called quantum fluctuations

$$\hat{\varphi}(\mathbf{x}) = \sum_{i \neq 0} \phi_i(\mathbf{x}) \hat{a}_i. \tag{3.21}$$

This decomposition of the field operator was first proposed by Bogoliubov [94], and amounts to replacing the creation and annihilation operators of the condensate field by the root of the condensate occupation number $\hat{a}_0 = \hat{a}_0^\dagger = \sqrt{N_0}$. An important consequence of this Bogoliubov approximation is that the number operator $\hat{N}$ no longer commutes with the Hamiltonian (3.15) and particle number is no longer conserved. This motivates the introduction of the grand-canonical Hamiltonian $\hat{K} = \hat{H} - \mu \hat{N}$ where μ is the chemical potential of the system and acts as a Lagrange multiplier to conserve particle number on average [53].

Using the Bogoliubov decomposition (3.20), we express the grand-canonical Hamiltonian $\hat{K}$ perturbatively in orders of the condensate occupation N_0 as $\hat{K} = K_0 + \hat{K}_1 + \hat{K}_2 + \ldots$ where $\hat{K}_i$ contains the terms that are i^{th} order in the quantum fluctuations $\hat{\varphi}(\mathbf{x})$. The zeroth order term K_0 is given by

$$\frac{K_0}{N_0} = \int d\mathbf{x}\phi_0^\star(\mathbf{x}) \left\{ \hat{H}^{(1)}(\mathbf{x}) - \mu \right\} \phi_0(\mathbf{x}) + \frac{N_0}{2} \int d\mathbf{x} \int d\mathbf{x}' \phi_0^\star(\mathbf{x})\phi_0^\star(\mathbf{x}')V(\mathbf{x}-\mathbf{x}')\phi_0(\mathbf{x}')\phi_0(\mathbf{x}). \quad (3.22)$$

An equation governing the chemical potential and the condensate field $\phi_0(\mathbf{x})$ is derived by enforcing that K_0 be a minimized with respect to small variations in the condensate field $\phi_0^\star(\mathbf{x})$. This ensures that $\hat{K}_1$ vanishes and results in the equation

$$\mu\phi_0(\mathbf{x}) = \left\{ \hat{H}^{(1)}(\mathbf{x}) + N_0 \int d\mathbf{x}' \phi_0^\star(\mathbf{x}')V(\mathbf{x}-\mathbf{x}')\phi_0(\mathbf{x}') \right\} \phi_0(\mathbf{x}). \quad (3.23)$$

This Eq. (3.23) is the non-local Gross-Pitaevskii equation (GPE) and is the governing equation for the condensate field $\phi_0(\mathbf{x})$, commonly referred to as the condensate wave function. The second term on the RHS of the GPE is the mean-field potential, $U_{\text{mf}}(\mathbf{x})$. It emerges by taking the mean-field $\langle\hat{\Psi}(\mathbf{x})\rangle$ in the Bogoliubov approximation (3.20), and has the form of a classical potential that is felt by all particles in the system, both condensed and excited, due to the presence of the condensate.

The GPE (3.23) was derived independently by Gross [95] and Pitaevskii [96] in 1961. It provides a self-contained and fruitful description for the fully condensed, zero temperature state of a system of dilute bosons. While the chemical potential μ is given by the condensate wave function $\phi_0(\mathbf{x})$ through the GPE, the stationary condensate wave function itself must be calculated by minimizing the zeroth order part of the Hamiltonian (3.15),

$$\frac{E_0}{N} = \int d\mathbf{x}\phi_0^\star(\mathbf{x})\hat{H}^{(1)}(\mathbf{x})\phi_0(\mathbf{x}) + \frac{N_0}{2} \int d\mathbf{x} \int d\mathbf{x}' \phi_0^\star(\mathbf{x})\phi_0^\star(\mathbf{x}')V(\mathbf{x}-\mathbf{x}')\phi_0(\mathbf{x}')\phi_0(\mathbf{x}). \quad (3.24)$$

This energy functional (3.24) is therefore known as the Gross-Pitaevskii energy functional. Minimization of (3.24) corresponds to the minimization of (3.22), the only difference between the two being a global shift by the chemical potential μ. Additionally, it is important to note that the GPE and the energy functional (3.24) remain unchanged by any global phase shift of the condensate wave function $\phi_0(\mathbf{x})$, so we see that this system possesses a $U(1)$ symmetry that is spontaneously broken in the BEC phase. It was pointed out by Goldstone [97, 98] that systems with such symmetry, here corresponding to a rotation of the condensate phase, necessarily possess some long-wavelength, arbitrarily low-energy mode known as the Goldstone boson (i.e., the theory must have a gapless excitation spectrum). We will see that the theoretical formulation of quantum fluctuations presented here is consistent with Goldstone's theorem and results in a gapless excitation spectrum.

The next non-zero term in the expansion of $\hat{K}$ is the second order term $\hat{K}_2$, given by

$$\begin{aligned}\hat{K}_2 = &\int d\mathbf{x}\hat{\varphi}^\dagger(\mathbf{x})\left\{\hat{H}^{(1)}(\mathbf{x})-\mu\right\}\hat{\varphi}(\mathbf{x}) + \frac{N_0}{2}\int d\mathbf{x}\int d\mathbf{x}' V(\mathbf{x}-\mathbf{x}')\\ &\times\left\{\hat{\varphi}^\dagger(\mathbf{x})\hat{\varphi}^\dagger(\mathbf{x}')\phi_0(\mathbf{x}')\phi_0(\mathbf{x}) + \hat{\varphi}^\dagger(\mathbf{x})\phi_0^\star(\mathbf{x}')\hat{\varphi}(\mathbf{x}')\phi_0(\mathbf{x}) + \hat{\varphi}^\dagger(\mathbf{x})\phi_0^\star(\mathbf{x}')\phi_0(\mathbf{x}')\hat{\varphi}(\mathbf{x})\right.\\ &\left.+\,\phi_0^\star(\mathbf{x})\hat{\varphi}^\dagger(\mathbf{x}')\phi_0(\mathbf{x}')\hat{\varphi}(\mathbf{x}) + \phi_0^\star(\mathbf{x})\phi^\star(\mathbf{x}')\hat{\varphi}(\mathbf{x}')\hat{\varphi}(\mathbf{x}) + \phi_0^\star(\mathbf{x})\hat{\varphi}^\dagger(\mathbf{x}')\hat{\varphi}(\mathbf{x}')\phi_0(\mathbf{x})\right\}\\ = &\int d\mathbf{x}\hat{\varphi}^\dagger(\mathbf{x})\hat{H}_{\mathrm{GP}}(\mathbf{x})\hat{\varphi}(\mathbf{x}) + \frac{N_0}{2}\int d\mathbf{x}\int d\mathbf{x}' V(\mathbf{x}-\mathbf{x}')\\ &\times\left\{\hat{\varphi}^\dagger(\mathbf{x})\hat{\varphi}^\dagger(\mathbf{x}')\phi_0(\mathbf{x}')\phi_0(\mathbf{x}) + 2\hat{\varphi}^\dagger(\mathbf{x})\hat{\varphi}(\mathbf{x}')\phi_0^\star(\mathbf{x}')\phi_0(\mathbf{x}) + \hat{\varphi}(\mathbf{x})\hat{\varphi}(\mathbf{x}')\phi_0^\star(\mathbf{x}')\phi_0^\star(\mathbf{x})\right\},\end{aligned} \tag{3.25}$$

where $\hat{H}_{\mathrm{GP}}(\mathbf{x})$ is defined so that $\hat{H}_{\mathrm{GP}}(\mathbf{x})\phi_0(\mathbf{x}) = 0$ (see Eq. (3.23)) and we have assumed that that the interaction potential $V(\mathbf{x}-\mathbf{x}')$ has the even symmetry $V(\mathbf{x}-\mathbf{x}') = V(\mathbf{x}'-\mathbf{x})$. Note that $\hat{K}_2$ is not diagonal in the quantum fluctuation operators $\hat{\varphi}(\mathbf{x})$. However, this expression can be diagonalized by transforming these operators [99],

$$\hat{\varphi}(\mathbf{x}) = \sum_{i\neq 0}\left[u_i(\mathbf{x})\hat{b}_i - v_i^\star(\mathbf{x})\hat{b}_i^\dagger\right]. \tag{3.26}$$

To make the transformation canonical, the creation and annihilation operators $\hat{b}_i^\dagger$ and $\hat{b}_i$ must obey the Bose commutation relations (3.5) and (3.6), from which the normalization condition for the $u_i(\mathbf{x})$ and $v_i(\mathbf{x})$ wave functions are derived to be

$$\int d\mathbf{x}\left[u_i^\star(\mathbf{x})u_j(\mathbf{x}) - v_i^\star(\mathbf{x})v_j(\mathbf{x})\right] = \delta_{ij}. \tag{3.27}$$

Interestingly, the only constraint on these functions is that they are normalized relative to each other while their magnitudes are otherwise unconstrained. It is precisely this fact that allows the canonical Bogoliubov transformation (3.26) to diagonalize the quantum fluctuation Hamiltonian $\hat{K}_2$.

Indeed, inserting the transformation (3.26) and its conjugate into (3.25) allows us to write $\hat{K}_2$ as

$$\hat{K}_2 = \sum_{i \neq 0} \hbar\omega_i \hat{b}_i^\dagger \hat{b}_i, \tag{3.28}$$

where the energy eigenvalue ω_i is given by

$$\begin{aligned}\hbar\omega_i = \int d\mathbf{x} \Big[& u_i^\star(\mathbf{x})\hat{H}_{\mathrm{GP}}(\mathbf{x})u_i(\mathbf{x}) + v_i^\star(\mathbf{x})\hat{H}_{\mathrm{GP}}(\mathbf{x})v_i(\mathbf{x}) + N_0 \int d\mathbf{x}' V(\mathbf{x}-\mathbf{x}') \left\{ \phi_0(\mathbf{x})u_i^\star(\mathbf{x})\phi_0^\star(\mathbf{x}')u_i(\mathbf{x}') \right. \\ & + \left. \phi_0^\star(\mathbf{x})v_i^\star(\mathbf{x})\phi_0(\mathbf{x}')v_i(\mathbf{x}') + \phi_0(\mathbf{x})u_i^\star(\mathbf{x})\phi_0(\mathbf{x}')v_i(\mathbf{x}') + \phi_0^\star(\mathbf{x})v_i^\star(\mathbf{x})\phi_0^\star(\mathbf{x}')u_i(\mathbf{x}') \right\} \Big].\end{aligned} \tag{3.29}$$

Enforcing that the off-diagonal elements of $\hat{K}_2$ vanish is achieved by enforcing that the creation and annihilation operators obey the commutation relations [100]

$$\left[\hat{K}_2, \hat{b}_i\right] = -\omega_i \hat{b}_i \tag{3.30}$$

$$\left[\hat{K}_2, \hat{b}_i^\dagger\right] = \omega_i \hat{b}_i^\dagger. \tag{3.31}$$

From these relations, the functions $u_i(\mathbf{x})$ and $v_i(\mathbf{x})$ are found to obey the Bogoliubov de Gennes (BdG) equations,

$$\hbar\omega_i u_i(\mathbf{x}) = \hat{H}_{\mathrm{GP}}(\mathbf{x})u_i(\mathbf{x}) + N_0 \int d\mathbf{x}' V(\mathbf{x}-\mathbf{x}') \left\{ \phi_0^\star(\mathbf{x}')u_i(\mathbf{x}') + \phi_0(\mathbf{x}')v_i(\mathbf{x}') \right\} \phi_0(\mathbf{x}) \tag{3.32}$$

$$-\hbar\omega_i v_i(\mathbf{x}) = \hat{H}_{\mathrm{GP}}(\mathbf{x})v_i(\mathbf{x}) + N_0 \int d\mathbf{x}' V(\mathbf{x}-\mathbf{x}') \left\{ \phi_0^\star(\mathbf{x}')v_i(\mathbf{x}') + \phi_0(\mathbf{x}')u_i(\mathbf{x}') \right\} \phi_0(\mathbf{x}). \tag{3.33}$$

For a non-interacting system, solutions to Eqs. (3.32) and (3.33) correspond to the single-particle system where the ω_i are the single-particle energies and the $u_i(\mathbf{x})$ are the single-particle excited states, while $\int d\mathbf{x} v_i^\star(\mathbf{x})v_i(\mathbf{x}) = 0$. When interactions are present, however, the $v_i(\mathbf{x})$ play an important role in this theory and the the solutions no longer correspond to single-particles, but instead correspond to *quasiparticles.* The quasiparticle picture, while perhaps unintuitive, is the natural language with which to describe dilute Bose gases at low temperatures $T \sim 0$ as the Hamiltonian for the system is diagonal in this representation. The functions $u_i(\mathbf{x})$ and $v_i(\mathbf{x})$ are therefore referred to as quasiparticle wave functions.

Eqs. (3.32) and (3.33) are linear in the quasiparticle wave functions $u_i(\mathbf{x})$ and $v_i(\mathbf{x})$, and thus account for quasiparticle-condensate interactions while neglecting quasiparticle-quasiparticle

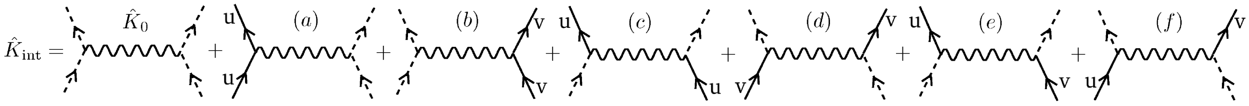

Figure 3.1: The diagrammatic representation of the interaction part of grand canonical Hamiltonian $\hat{K}_{\text{int}}$. The dashed lines represents the condensate, the solid lines represent excited quasiparticles and the squiggly lines represent interactions. The first diagram shows the 0^{th} order contribution to the interaction energy given by condensate-condensate interactions. The remaining diagrams (a)-(f) represent the next to leading order contribution to the interaction energy from quasiparticle-condensate interactions. (a) and (b) show quasiparticles scattering off of the condensate (direct terms) and (c)-(f) show interactions that absorb and expel quasiparticles from the condensate (exchange terms).

interactions. However, in a dilute gas at approximately zero temperature, the latter interactions may be neglected as the total quantum depletion (see section 3.2.3) is very small. The quasiparticle-condensate interactions, on the other hand, are non-negligible and are characterized by two types of terms. One is a "direct" term that describes a quasiparticle scattering off of the condensate, and the other term is an "exchange" term that describes a quasiparticle scattering into or out of the condensate. The interaction parts of the grand canonical Hamiltonian $\hat{K}$ are represented diagrammatically in figure 3.1 and such direct and exchange terms are identified therein.

It is convenient to write the BdG equations in the matrix form,

$$\begin{pmatrix} \hat{H}_{\text{GP}} + \hat{C} + \hat{X} & \hat{X}^{\star} \\ -\hat{X}^{\star} & -\hat{H}_{\text{GP}} - \hat{C} - \hat{X} \end{pmatrix} \begin{pmatrix} u \\ v \end{pmatrix} = \hbar\omega \begin{pmatrix} u \\ v \end{pmatrix} \tag{3.34}$$

where the $\hat{C}$ and $\hat{X}$ operators represent the direct and exchange terms, respectively, and we have neglected the spatial dependence of the operators and quasiparticle wave functions. The direct operation of $\hat{C}$ on a quasiparticle wave function $u_i(\mathbf{x})$ is given by

$$\left[\hat{C}u_i\right](\mathbf{x}) = N_0 \int d\mathbf{x}\phi_0^{\star}(\mathbf{x}')V(\mathbf{x}-\mathbf{x}')\phi_0(\mathbf{x}')u_i(\mathbf{x}), \tag{3.35}$$

and the exchange operation of $\hat{X}$ on a quasiparticle wave function $u_i(\mathbf{x})$ is given by

$$\left[\hat{X}u_i\right](\mathbf{x}) = N_0 \int d\mathbf{x}\phi_0^{\star}(\mathbf{x}')V(\mathbf{x}-\mathbf{x}')u_i(\mathbf{x}')\phi_0(\mathbf{x}). \tag{3.36}$$

Then, in practice the quasiparticle wave functions $u_i(\mathbf{x})$ and $v_i(\mathbf{x})$ can be obtained simultaneously with the energy eigenvalues ω_i via diagonalization of the 2×2 BdG Hamiltonian in Eq. (3.34).

3.2.1 Long-Range Order

Recall that in section 2.1.3 we discussed the criterion laid out by Penrose and Onsager that superfluids, and BECs, must possess long-range order, given in terms of the single-particle density matrix in Eq. (2.3). Here, we show that long-range order is indeed present in the Bogoliubov decomposition given by Eqs (3.20) and (3.26) by calculating the single-particle density matrix explicitly,

$$\begin{aligned}\rho^{(1)}(\mathbf{x},\mathbf{x}') &= \langle \hat{\Psi}^\dagger(\mathbf{x})\hat{\Psi}(\mathbf{x}')\rangle \\ &= \left\langle \left(\sqrt{N_0}\phi_0^\star(\mathbf{x}) + \hat{\varphi}^\dagger(\mathbf{x})\right)\left(\sqrt{N_0}\phi(\mathbf{x}') + \hat{\varphi}(\mathbf{x}')\right)\right\rangle \\ &= N_0\phi_0^\star(\mathbf{x})\phi_0(\mathbf{x}') + \langle \hat{\varphi}^\dagger(\mathbf{x})\hat{\varphi}(\mathbf{x}')\rangle, \end{aligned} \tag{3.37}$$

where the terms that are linear in the quantum fluctuation operators $\hat{\varphi}(\mathbf{x})$ vanish. If we consider a homogeneous system in a cubic box of volume V, we can use a plane wave basis (which we return to in the next chapter), $\phi_{\mathbf{k}}(\mathbf{x}) = 1/\sqrt{V}e^{i\mathbf{k}\cdot\mathbf{x}}$. In this case, $\lim_{|\mathbf{x}-\mathbf{x}'|\to\infty}\langle\hat{\varphi}^\dagger(\mathbf{x})\hat{\varphi}(\mathbf{x}')\rangle = 0$ and $\lim_{|\mathbf{x}-\mathbf{x}'|\to\infty}\phi_0^\star(\mathbf{x})\phi_0(\mathbf{x}') = 1/V$, so we see that

$$\lim_{|\mathbf{x}-\mathbf{x}'|\to\infty}\rho^{(1)}(\mathbf{x},\mathbf{x}') = N_0/V, \tag{3.38}$$

so the single-particle density matrix asymptotes to the condensate density in the Bogoliubov decomposition, thus satisfying the criterion of long-range order.

3.2.2 Symmetry in the Bogoliubov de Gennes Equations

Note that if we can write $\phi_0^\star(\mathbf{x}) = \phi_0(\mathbf{x})$, the BdG equations (3.34) are unchanged under the exchange of $u \leftrightarrow v^\star$ and $\omega \leftrightarrow -\omega$. Because of this symmetry, the solutions come in pairs of $(u, v^\star)^\mathsf{T}$ with eigenvalue ω, the positive-norm solution, and $(v^\star, u)^\mathsf{T}$ with eigenvalue $-\omega$, the negative-norm solution. Thus, we can transform the u and v quasiparticle wave functions $u = \frac{1}{2}(f - g)$ and

$v = \frac{1}{2}(f+g)$ and end up with an equivalent form of the BdG equations. Squaring these transformed BdG equations results in a diagonal form [101, 102],

$$\left(\hat{H}_{\mathrm{GP}} + \hat{C}\right)\left(\hat{H}_{\mathrm{GP}} + \hat{C} + 2\hat{X}\right) f = \omega^2 f \tag{3.39}$$

$$\left(\hat{H}_{\mathrm{GP}} + \hat{C} + 2\hat{X}\right)\left(\hat{H}_{\mathrm{GP}} + \hat{C}\right) g = \omega^2 g. \tag{3.40}$$

To obtain just the energy eigenvalues ω, it is sufficient to solve just one of these equations while both (3.39) and (3.40) must be solved to gain information about the quasiparticle wave functions. For example, diagonalization of (3.39) gives the eigenvalues ω and the eigenvectors f while a matrix inversion of (3.40) gives the eigenvectors g. With knowledge of both f and g, the quasiparticle wave functions u and v can be reconstructed.

3.2.3 Quantum Depletion

The Bogoliubov transformation (3.26) mixes the single-particle creation and annihilation operators, and it is therefore useful to define a new ground state (vacuum) in terms of the quasiparticle annihilation operator instead of the single-particle annihilation operator,

$$\hat{b}_i|0\rangle = 0, \tag{3.41}$$

so the state $|0\rangle$ is defined as a quasiparticle vacuum, or the state that is devoid of quasiparticles, corresponding to a pure condensate. The number of particles in this ground state can be calculated by taking the expectation value of the number operator in this state. In the Bogoliubov approximation, the number operator takes the form,

$$\hat{N} = N_0\phi_0^\star(\mathbf{x})\phi_0(\mathbf{x}) + \sqrt{N_0}\left(\phi_0^\star(\mathbf{x})\hat{\varphi}(\mathbf{x}) + \phi_0(\mathbf{x})\hat{\varphi}^\dagger(\mathbf{x})\right) + \hat{\varphi}^\dagger(\mathbf{x})\hat{\varphi}(\mathbf{x}), \tag{3.42}$$

and applying the canonical transformation (3.26) to (3.42) gives

$$\begin{aligned}\hat{N} = N_0\phi_0^\star(\mathbf{x})\phi_0(\mathbf{x}) &+ \sqrt{N_0}\sum_{i\neq 0}\left(\phi_0^\star(\mathbf{x})\left[u_i(\mathbf{x})\hat{b}_i - v_i^\star(\mathbf{x})\hat{b}_i^\dagger\right] + \phi_0(\mathbf{x})\left[u_i^\star(\mathbf{x})\hat{b}_i^\dagger - v_i(\mathbf{x})\hat{b}_I\right]\right)\\ &+ \sum_{i,j\neq 0}\left[u_i^\star(\mathbf{x})u_j(\mathbf{x})\hat{b}_i^\dagger\hat{b}_j - u_i^\star(\mathbf{x})v_j^\star(\mathbf{x})\hat{b}_i^\dagger\hat{b}_j^\dagger - u_i(\mathbf{x})v_j(\mathbf{x})\hat{b}_i\hat{b}_j + v_i(\mathbf{x})v_j^\star(\mathbf{x})\hat{b}_i\hat{b}_j^\dagger\right].\end{aligned} \tag{3.43}$$

When taking the vacuum expectation value, we use the fact that $\langle 0|0\rangle = 1$ and $\langle 0|\hat{b}_i^\dagger|0\rangle = \langle 0|\hat{b}_i|0\rangle = 0$ to arrive at the result

$$\langle 0|\hat{N}|0\rangle = N_0 + \sum_{i\neq 0}\int d\mathbf{x} v_i^\star(\mathbf{x})v_i(\mathbf{x}). \tag{3.44}$$

The second term in this expression is known as the quantum depletion. This term gives the number of particles that are forced out of the condensate at zero temperature into excited quasiparticle states, and was first calculated by Lee, Huang and Yang for a gas of bosons at $T = 0$ with hard-sphere interactions [103]. It is worth emphasizing that this is a *zero temperature* result. At finite temperature, thermal energy manifests in the occupation of excited quasiparticle states so the annihilation of a quasiparticle from a thermal many-body state does not result in zero as is the case for the ground state, defined in Eq. (3.41). Thus, terms like $\langle \hat{b}_i^\dagger \hat{b}_i\rangle \neq 0$ in a Bose gas at $T > 0$.

3.3 Time-dependent formulation

So far, we have neglected any time-dependence in the formulation of our low-temperature field theory. In general, the field-operators can be time-dependent $\hat{\Psi}(\mathbf{x}) \to \hat{\Psi}(\mathbf{x}, t)$, and their equation of motion is given in the Heisenberg picture by

$$\begin{aligned} i\hbar\partial_t\hat{\Psi}(\mathbf{x},t) &= [\hat{\Psi}(\mathbf{x},t), \hat{K}(t)] \\ &= \left\{\hat{H}^{(1)} - \mu + \int d\mathbf{x}'\hat{\Psi}^\dagger(\mathbf{x}',t)V(\mathbf{x}-\mathbf{x}')\hat{\Psi}(\mathbf{x}',t)\right\}\hat{\Psi}(\mathbf{x},t). \end{aligned} \tag{3.45}$$

The decomposition of the field operator from Eq. (3.20) can now be inserted into Eq. (3.45) to derive an equation for the condensate field $\phi_0(\mathbf{x}, t)$. At ultracold temperatures, however, we employ the perturbative approach and keep only the leading order terms in N_0, which amounts to neglecting terms that are of cubic order or greater in the quantum fluctuations. In practice, we take a $T = 0$ ensemble average of Eq. (3.45) and note that $\langle\hat{\varphi}(\mathbf{x}, t)\rangle = \langle\hat{\varphi}^\dagger(\mathbf{x}, t)\rangle = 0$ to arrive at an equation for $\phi_0(\mathbf{x}, t)$,

$$i\hbar\partial_t\phi_0(\mathbf{x},t) = \left\{-\frac{\hbar^2}{2M}\nabla^2 + U(\mathbf{x}) - \mu + N_0\int d\mathbf{x}'\phi_0^\star(\mathbf{x}',t)V(\mathbf{x}-\mathbf{x}')\phi_0(\mathbf{x}',t)\right\}\phi_0(\mathbf{x},t). \tag{3.46}$$

This equation is known as the time-dependent Gross-Pitaevskii equation, and it governs the real-time evolution of the condensate field $\phi_0(\mathbf{x}, t)$. The stationary solution to this equation corresponds to the time-independent condensate field with time-dependent phase $\phi_0(\mathbf{x})e^{-i\mu t/\hbar}$, where $\phi_0(\mathbf{x})$ obeys the GPE (3.23).

Additionally, in section 3.2 it was shown that the Hamiltonian $\hat{K}_2$ is diagonalized by the introduction of quasiparticle operators. Thus, the time evolution of the quasiparticles is given simply by their energy eigenvalues ω_i,

$$\hat{\varphi}(\mathbf{x},t) = \sum_{i\neq 0}\left[u_i(\mathbf{x})e^{-i\omega_i t/\hbar}\hat{b}_i - v_i^{\star}(\mathbf{x})e^{i\omega_i t/\hbar}\hat{b}_i^{\dagger}\right]. \tag{3.47}$$

It is easy to show that the insertion of (3.47) into the equation of motion for the field operator (3.45) results in the BdG equations (3.34). Additionally, formulating the quantum fluctuations in this time-dependent form reveals important information regarding the stability of the dilute Bose gas. Manipulation of the BdG equations (3.32) and (3.33) results in the condition

$$(\omega_i - \omega_i^{\star})\int d\mathbf{x}\,[u_i^{\star}(\mathbf{x})u_i(\mathbf{x}) - v_i^{\star}(\mathbf{x})v_i(\mathbf{x})] = 0. \tag{3.48}$$

However, the normalization condition (3.27) says that the integral part of this expression must be equal to unity, so $(\omega_i - \omega_i^{\star})$ must be zero. This is only guaranteed when ω_i is purely real. If ω_i has a non-zero imaginary part, Eq. (3.48) can not hold unless the $u_i(\mathbf{x})$ and $v_i(\mathbf{x})$ functions are not normalizable, i.e., they diverge relative to each other. Indeed, one sees directly from the time-dependent form of the quantum fluctuations in Eq. (3.47) that any $\mathrm{Im}[\omega_i] \neq 0$ results in quasiparticle wave functions whose norms diverge exponentially, signifying a dynamical instability. Thus, solutions to the BdG equations give us a criterion for dynamic stability [104],

$$\mathrm{Im}[\omega_i] = 0. \tag{3.49}$$

It was shown rigorously in reference [104] that the emergence of complex eigenvalues in the BdG equations coincides with the degeneracy between a positive-norm solution and a negative-norm solution. Ref. [105] also confirmed this claim using a two-mode approximation. At the point of degeneracy, the real parts of the positive-norm and negative-norm eigenvalues become identical as their imaginary parts emerge that are identical in magnitude and opposite in sign. This is seen explicitly in the solutions to the BdG equations that are presented in chapter 5.

3.3.1 First-Quantized Theory - Alternative Derivation

In this section we present an alternative derivation of the Gross-Pitaevskii equations, both time-independent (3.23) and time-dependent (3.46), the Gross-Pitaevskii energy functional (3.24) and the BdG equations (3.34). First, we notice that the energy functional (3.24) describes the energy of a *pure* condensate field $\phi_0(\mathbf{x})$ in the presence of two-body interactions. We can write the first-quantized Hamiltonian for a system of N such bosons as

$$\hat{H}\left(\{\mathbf{x}_i\}\right) = \sum_{i=1}^{N}\left[-\frac{\hbar^2}{2M}\nabla_i^2 + U(\mathbf{x}_i)\right] + \sum_{i<j} V(\mathbf{x}_i - \mathbf{x}_j), \tag{3.50}$$

and we can write the symmetrized wave function of the pure condensate, where every particle occupies the exact same wave function $\phi_0(\mathbf{x})$, as

$$\Psi\left(\{\mathbf{x}_i\}\right) = \prod_{i=1}^{N} \phi_0(\mathbf{x}_i). \tag{3.51}$$

Such an approximation to the zero-temperature Bose system is known as the Hartree approximation. The energy per particle of such a system is then given by the expectation value of the Hamiltonian (3.50) in the state (3.51),

$$\frac{E}{N} = \prod_{i=1}^{N} \int d\mathbf{x}_i \Psi^{\star}\left(\{\mathbf{x}_i\}\right) \hat{H}\left(\{\mathbf{x}_i\}\right) \Psi\left(\{\mathbf{x}_i\}\right). \tag{3.52}$$

Subsequent integration over the coordinates $\mathbf{x}_i$ results in an energy functional that is identical to (3.24), but with the N_0 that multiplies the mean-field interaction term replaced by $N-1$ [106, 55]. Here, N_0 and N refer to the same number, being the number of particles in the condensate. Such a result is intuitive, actually, because although such a mean-field theory is meant to describe a large number of bosons in the condensate, the limit that $N \to 1$ should produce no interactions, as a particle can not interact with itself in the way we consider here. Thus, we adopt the factor of $N-1$ for the parts of this thesis where trapped, finite Bose gases are considered. At any rate, the difference between N and $N-1$ is typically negligible for current BEC experiments, where condensate particle numbers are on the order of tens of thousands.

The time-independent Gross-Pitaevskii equation is derived in this first-quantized theory by introducing the chemical potential as a Lagrange multiplier to conserve particle number on average, in the grand canonical theory, and enforcing that $\delta E - \mu\delta N = 0$. The result is, again, identical to Eq. (3.23), but with $N_0 \to N-1$. Similarly, the time-independent Gross-Pitaevskii equation is derived by writing out the time-dependent Schrödinger for the many-body wave function Ψ, which we now generalize to the time-dependent form $\Psi(\{\mathbf{x}_i\}, t)$. Projecting out all coordinates except for one gives the time-dependent GPE, Eq. (3.46), but, again, with $N_0 \to N-1$.

In the first-quantized approach, the elementary excitations are treated as small perturbations to the ground stationary state, in this case, the condensate wave function $\phi_0(\mathbf{x})e^{-i\mu t}$. Using the time-dependent GPE, we write

$$\phi_0(\mathbf{x}, t) = \left[\phi_0(\mathbf{x}) + \delta\vartheta(\mathbf{x}, t)\right] e^{-i\mu t}, \tag{3.53}$$

where $\delta \ll 1$ and

$$\vartheta(\mathbf{x}, t) = \sum_i \left[u_i(\mathbf{x})e^{-i\omega_i t} + v_i^\star(\mathbf{x})e^{i\omega t}\right]. \tag{3.54}$$

Plugging the form (3.53) into the time-dependent GPE and linearizing about the small parameter δ results in the BdG equations (3.34), but, of course, with N_0 replaced with $N-1$. While this first-quantized method is seemingly identical to that of the second-quantized method introduced earlier in this section, the first-quantization does not allow one to easily go beyond this perturbative approach, whereas the second quantization allows for such treatment, for example, of self-consistent treatments of thermal and quantum fluctuations. An example of such methods are the Hartree-Fock Bogoliubov methods, developed by Allan Griffin [107], which have been proven fruitful in describing thermal Bose gases.

3.4 Two-body Interactions

To complete our theoretical description of an ultracold, dilute gas of interacting bosons, we now treat the two-body interactions. In the theory presented here, the effect of these interactions emerge in the interaction matrix elements V_{ijkl} given in Eq. (3.19). While we are primarily interested in the dipole-dipole interaction (ddi), which is discussed in section 3.4.2, the treatment of short-range interactions in dipolar Bose gases is necessary for a complete description of this system.

3.4.1 Pseudopotential for Short-Range Interactions

As discussed in section 2.2, the transition to BEC occurs when the thermal de-Broglie wavelengths of the bosons become comparable to their mean spacing, or when $n^{\frac{1}{3}}\lambda_{\mathrm{dB}} \sim 1$ where n is the density of the gas. To satisfy the diluteness criterion that is used to truncate the Hamiltonian (3.15) at the binary level, we enforce that the average distance between the bosons is much greater than the characteristic length scale on which they interact. For isotropic, short-range interactions (such as the Van der Waals interaction), an appropriate interaction length scale is set by the s-wave scattering length a_s. Thus, the diluteness criteria takes the form $n^{\frac{1}{3}}a_s \ll 1$. Our conditions for condensation and diluteness tell us that the ultracold, dilute Bose gas must obey the condition

$$\frac{a_s}{\lambda_{\mathrm{dB}}} \ll 1. \tag{3.55}$$

This condition can be used to greatly simplify the interaction matrix elements (3.19) if we enforce that all states exist below a certain energy cutoff E_{cut} so the characteristic wave numbers k_i of all states are such that $k_i \ll 2\pi/a_s$ [108]. Since the two-body interaction changes on a length scale much smaller than those of the condensed and low-lying quasiparticle states with energies $\hbar\omega_i < E_{\mathrm{cut}}$, which change on a length scale $\sim 2\pi/k_i$, the short-range interaction matrix elements can be simplified by using the shape-independent approximation,

$$\begin{aligned} V^{(c)}_{ijkl} &= \int d\mathbf{x} \int d\mathbf{x}' \phi^\star_i(\mathbf{x})\phi^\star_j(\mathbf{x}')V_c(\mathbf{x}-\mathbf{x}')\phi_k(\mathbf{x}')\phi_l(\mathbf{x}) \\ &\approx g \int d\mathbf{x}\phi^\star_i(\mathbf{x})\phi^\star_j(\mathbf{x})\phi_k(\mathbf{x})\phi_l(\mathbf{x}), \end{aligned} \tag{3.56}$$

where, for isotropic interactions, the two-body potential is just $V_c(|\mathbf{x}-\mathbf{x}'|)$ and

$$g \equiv \int d\mathbf{x} V_c(\mathbf{x}) = \tilde{V}(0). \tag{3.57}$$

This result motivates the introduction of a pseudopotential $V_c(\mathbf{x}-\mathbf{x}') = g\delta(\mathbf{x}-\mathbf{x}')$ for the short-range interaction. The coupling constant g can be determined by identifying the zero-energy solution of the Lippmann-Schwinger equation for the two-body wave function with the known low energy threshold result $\psi(r) = 1 - \frac{a}{r}$, where a is the s-wave scattering length. Using the Born approximation in this process allows one to identify the form of Eq. (3.57), thus g is given by $4\pi\hbar^2 a_{\mathrm{Born}}/M$ where a_{Born} is the Born approximation for the s-wave scattering length [55]. The Born approximation, however, does not take into account the high-momentum behavior of the two-body wave function in the vicinity of $|\mathbf{x}-\mathbf{x}'| \sim 0$ where the two-body potential is strong [109]. Indeed, such information is automatically lost in the many-body theory when the single-particle wave functions are assumed to have the separable form (3.1). However, this problem is overcome by replacing the Born approximation to the zero-energy T-matrix with the full T-matrix, which amounts to replacing a_{Born} with the true s-wave scattering length a_s to give the proper short-range pseudopotential

$$V_c(\mathbf{x}-\mathbf{x}') = g\delta(\mathbf{x}-\mathbf{x}') = \frac{4\pi\hbar^2 a_s}{M}\delta(\mathbf{x}-\mathbf{x}'). \tag{3.58}$$

The true s-wave scattering length can be obtained either empirically or through some calculations that treat the close-coupling of the two-body wave function. For example, an approximate analytical formula for the scattering length of atoms interacting via the Van der Waals force was derived in [110], and a delta-function pseudopotential of the form (3.58) was found to reproduce the correct scattering behavior of two bosons with hard-sphere interactions, where the scattering length is simply the radius of the hard-sphere [111, 103]. Additionally, this pseudopotential was used therein to calculate for the first time the zeroth-order (mean-field) energy, the quantum depletion and the first-order beyond mean-field energy (energy due to quantum fluctuations at zero-temperature) of a dilute BEC. However, to calculate this beyond mean-field energy (the so-called LHY energy correction) the authors used a corrected form of the pseudopotential (3.58) to first-order beyond the momentum-independent approximation (3.58), given by iterating the T-matrix solution of the Lippman-Schwinger equation to next order. This momentum-dependent pseudopotential provides a first-order account of higher energy scattering processes above the cutoff E_{cut}.

It is also interesting to note that the momentum dependent pseudopotential (3.58) is automatically on-shell ($\mathbf{k} = \mathbf{k}'$). At the mean-field Bogoliubov level that is employed in this thesis, it is sufficient to use the on-shell transition matrix elements, while higher-order theories that, for exam-

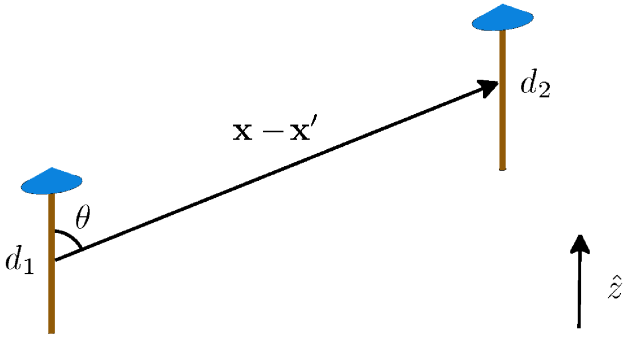

Figure 3.2: Geometry of the dipole-dipole interaction for dipoles that are polarized by an external field in the z-direction, corresponding to the interaction potential in Eq. (3.59).

ple, include quasiparticle-quasiparticle interactions, necessitate the calculation of off-shell elements. One such theory is that of Beliaev [112, 113], which uses the momentum-dependent form of the scattering amplitude to calculate the beyond mean-field corrections to the quasiparticle spectrum of a Bose gas [114]. Nevertheless, the pseudopotential (3.58) is appropriate for the dilute BEC that is discussed here.

3.4.2 Dipole-Dipole Interactions

We now turn our attention to the ddi which, unlike the interactions considered in the previous section 3.4.1, is anisotropic and long-range. In particular, we consider the interaction between two dipolar bosons that are polarized in an external field. If this polarizing field points in the z-direction and the dipole moments are given by d_1 and d_2, the two-body potential for this interaction can be written as (in cgs units)

$$V_d(\mathbf{x}-\mathbf{x}') = d_1 d_2 \frac{C_{20}(\theta,\phi)}{|\mathbf{x}-\mathbf{x}'|^3} = d_1 d_2 \frac{1-3\cos^2\theta_{\mathbf{x}-\mathbf{x}'}}{|\mathbf{x}-\mathbf{x}'|^3}, \tag{3.59}$$

where $C_{20}(\theta,\phi)$ is the reduced spherical harmonic [115] and θ is the angle between the polarizing field and the vector separating the two dipoles $\mathbf{x}-\mathbf{x}'$. This ddi potential is given by taking $\hat{d}_1 = \hat{d}_2$ in the more general expression (2.20). The geometry of the ddi given in Eq. (3.59) is shown in figure 3.2.

Unlike short-range interactions that are $\propto 1/r^6$ when they are of the Van der Waals type, the ddi goes as $\propto 1/r^3$, which gives this interaction very special properties. This can be seen by considering the long-range contribution to the low-energy threshold behavior of the elastic scattering phase shift for the l^{th} partial wave for a potential $\propto 1/r^s$ [116],

$$\tan \delta_l \propto A k^{2l+1} + B k^{s-2}. \tag{3.60}$$

The elastic cross-section is proportional to $\sin^2 \delta_l / k^2$, so for $l > 0$ and $s = 3$ (corresponding to the ddi) the first term vanishes at zero energy while the second term is constant. Thus, at low energies the scattering of dipoles is independent of k and is dominated by the $1/r^3$ part of the two-body potential for all partial waves $l > 0$. As a result of this long-range behavior of the ddi, the Born approximation works well to describe low-energy dipole-dipole scattering for non-zero partial waves [117]. For the s-wave part, a pseudopotential similar to (3.58) can be used where the s-wave scattering length is now dipole dependent, $a_s = a_s(d_1, d_2)$ [118, 119, 120, 121]. It was shown in [122] that this pseudopotential treatment of the s-wave part of the ddi is sufficient for an accurate description of low-energy dipolar collisions in a BEC, and the Born approximation works well for the $l > 0$ partial waves as long as the strength of the ddi is sufficiently weak [123].

Thus, we take our two-body interaction potential to be

$$V(\mathbf{x} - \mathbf{x}') = g\delta(\mathbf{x} - \mathbf{x}') + d^2 \frac{1 - 3\cos^2 \theta_{\mathbf{x}-\mathbf{x}'}}{|\mathbf{x} - \mathbf{x}'|^3} \tag{3.61}$$

where we have assumed that $d_1 = d_2 = d$ and a_s is the full s-wave scattering length characterizing the low-energy two-body collisions. This potential has a well-defined Fourier transform $\tilde{V}(\mathbf{k})$ [124],

$$\tilde{V}(\mathbf{k}) = g + \frac{4\pi}{3} d^2 \left(3\cos^2 \theta_k - 1\right), \tag{3.62}$$

where θ_k is the angle between the dipole polarization and the wave vector $\mathbf{k}$. We give the details of the calculation of this momentum-space ddi in Appendix B for dipoles with arbitrary spatial polarization. Indeed, the second term in this momentum-space interaction potential (3.62) describes dipole-dipole interactions for *any* uniform polarization, and not just polarization in the z-direction. We refer to the first term in this potential (3.62) as a "contact" potential due to its delta-function form in coordinate-space. The second term in this potential accounts for the long-range, anisotropic ddi that is present between two polarized dipoles. These dipoles could be either magnetic or electric in nature. Because we use cgs units, the ddi "coupling" is just d^2 in Eqs. (3.61) and (3.62). In SI units, this coupling is $d^2/4\pi\epsilon_0$ for electric dipoles and $\mu_0 d^2/4\pi$ for magnetic dipoles, where ϵ_0 is the permittivity of free space and μ_0 is the permeability of free space. In cgs units, $1/4\pi\epsilon_0 = \mu_0/4\pi = 1$ [91].

3.4.3 Mean-Field Potential

We can now write our mean-field potential $U_{\mathrm{mf}}(\mathbf{x})$ introduced in section 3.2 in terms of the contact and ddi,

$$\begin{aligned} U_{\mathrm{mf}}(\mathbf{x}) &= (N-1)\int d\mathbf{x}' V(\mathbf{x}-\mathbf{x}')|\phi_0(\mathbf{x}')|^2 \\ &= (N-1)\left[g|\phi_0(\mathbf{x})|^2 + d^2\int d\mathbf{x}' \frac{1-3\cos^2\theta_{\mathbf{x}-\mathbf{x}'}}{|\mathbf{x}-\mathbf{x}'|^3}|\phi_0(\mathbf{x}')|^2\right]. \end{aligned} \tag{3.63}$$

The delta-function form of the contact interaction eliminates the integral in the mean-field potential and leaves a term that is proportional to the square of the condensate field, or just the condensate density, while the part of the mean-field due to the ddi cannot, in general, be reduced as such and the integral needs to be handled explicitly. This is the essence of the long-range nature of the ddi, that to correctly account for the dipolar interactions at a point $\mathbf{x}$ one must convolve over the contributions from the dipoles at all other points $\mathbf{x}'$. Such a convolution can be simplified by working in momentum-space, as is explained in Appendix A.

The most important results from this chapter are the equations that govern the condensate wave function $\phi_0(\mathbf{x})$, the time-independent (3.23) and time-dependent (3.46) Gross-Pitaveskii equations, and the Bogoliubov de Gennes equations (3.34) that govern the quantum fluctuations of the system that, in the ultracold dilute Bose gas, are characterized by non-interacting quasiparticles that are excited on top of the ground condensed state. In the following chapters, we demonstrate the power of these mean-field relations by characterizing the ground condensed state and the quasiparticle excitations of trapped condensates with dipole-dipole interactions and by showing, where applicable, excellent agreement with experiment.

Chapter 4

Homogeneous Dipolar Bose-Einstein Condensates

4.1 Three-Dimensional Case

To begin investigating the role that the dipole-dipole interaction (ddi) plays in the physics of a Bose condensed gas, we first consider the simple case of an untrapped ($U(\mathbf{x}) = 0$), or homogeneous gas in the presence of both the contact and the ddi. To impose boundary conditions on the system, we consider N bosons in a cubical box of volume $V = L^3$. The homogeneous limit is then achieved by taking the volume V of the box to infinity while keeping the ratio $n = N/V$, the density of the gas, fixed. We choose a plane wave basis for our single particle states and label them by their wave vectors $\mathbf{k}$,

$$\phi_{\mathbf{k}}(\mathbf{x}) = \frac{1}{\sqrt{V}} e^{i\mathbf{k}\cdot\mathbf{x}}. \tag{4.1}$$

In this case, the two-body interactions must conserve momentum, $\mathbf{k}_i + \mathbf{k}_j = \mathbf{k}_k + \mathbf{k}_l$, and with the plane-wave free-particle energy eigenvalues $\hbar^2 k^2/2M$ the many-body Hamiltonian (3.17) can be written as

$$\hat{H} = \sum_{\mathbf{k}} \frac{\hbar^2 k^2}{2M} \hat{a}^\dagger_{\mathbf{k}} \hat{a}_{\mathbf{k}} + \frac{1}{2V} \sum_{\mathbf{k}_1,\mathbf{k}_2,\mathbf{q}} \tilde{V}(\mathbf{q}) \hat{a}^\dagger_{\mathbf{k}_1+\mathbf{q}} \hat{a}^\dagger_{\mathbf{k}_2-\mathbf{q}} \hat{a}_{\mathbf{k}_1} \hat{a}_{\mathbf{k}_2}. \tag{4.2}$$

Here, $\tilde{V}(\mathbf{q})$ is the two-body momentum-space interaction potential (3.62) that describes the transfer of momentum $\hbar\mathbf{q}$ in the scattering process. This form is obtained by calculating the interaction matrix elements V_{ijkl} in the plane-wave basis. For the contact interactions, the matrix elements are

$$
\begin{aligned}
V_c &= \frac{g}{V^2}\int d\mathbf{x}\int d\mathbf{x}' e^{-i(\mathbf{k}_1+\mathbf{q})\cdot\mathbf{x}} e^{-i(\mathbf{k}_2-\mathbf{q})\cdot\mathbf{x}'}\delta(\mathbf{x}-\mathbf{x}') e^{i\mathbf{k}_1\cdot\mathbf{x}'} e^{i\mathbf{k}_2\cdot\mathbf{x}} \\
&= \frac{g}{V^2}\int d\mathbf{x} e^{-i(\mathbf{k}_1+\mathbf{q})\cdot\mathbf{x}} e^{-i(\mathbf{k}_2-\mathbf{q})\cdot\mathbf{x}} e^{i\mathbf{k}_1\cdot\mathbf{x}} e^{i\mathbf{k}_2\cdot\mathbf{x}} \\
&= \frac{g}{V}.
\end{aligned}
\tag{4.3}
$$

For the ddi, we use the convolution theorem (see Appendix A). The momentum-space form of the ddi is taken from Eq. (3.62) and we use the fact that the momentum-space representation of a plane wave is a delta-function whose argument is just the wave number to calculate the ddi matrix elements,

$$
\begin{aligned}
V_d &= \frac{1}{V^2}\int d\mathbf{x}\int d\mathbf{x}' e^{-i(\mathbf{k}_1+\mathbf{q})\cdot\mathbf{x}} e^{-i(\mathbf{k}_2-\mathbf{q})\cdot\mathbf{x}'} V_d(\mathbf{x}-\mathbf{x}') e^{i\mathbf{k}_1\cdot\mathbf{x}'} e^{i\mathbf{k}_2\cdot\mathbf{x}} \\
&\vdots \\
&= \frac{4\pi}{3V} d^2\left(3\cos^2\theta_{\mathbf{q}}-1\right).
\end{aligned}
\tag{4.4}
$$

This result shows that while the matrix elements of the contact interaction are completely momentum independent, the matrix elements of the ddi are momentum dependent, but in homogeneous space depend only on the angle between the dipole polarization and the momentum transfer $\mathbf{q}$, $\theta_{\mathbf{q}}$, and not the magnitude of the momentum transfer. This angular dependence is to be expected, though, as the ddi itself is anisotropic.

The Hamiltonian (4.2) can be simplified by employing the Bogoliubov approximation (3.20) and separating the interaction term into parts $\propto N_0^2$ and $\propto N_0$, similar to the process that was carried out in section 3.2 for the Bose field operators. In terms of the creation and annihilation operators, the Bogoliubov approximation amounts to approximating the zero-momentum operators as c-numbers, $\hat{a}_0 = \hat{a}_0^\dagger = \sqrt{N_0}$. Note that terms $\propto N_0^{\frac{3}{2}}$ have only one excited particle operator and must vanish because the interactions must conserve momentum, and terms $\propto \sqrt{N_0}$ and $\propto 1$, which have three and four excited particle operators and describe interactions between excited particles, are ignored in the perturbative process. If we approximate $N_0 \approx N$ and define the condensate density as $n \equiv N/V$, the Hamiltonian for this system can be written in the form

$$\hat{H} = \frac{N}{2} n\tilde{V}(0) + \sum_{\mathbf{k}} \frac{\hbar^2 k^2}{2M} \hat{a}^\dagger_{\mathbf{k}} \hat{a}_{\mathbf{k}} + \frac{1}{2} n \sum_{\mathbf{k}>0} \tilde{V}(\mathbf{k}) \left\{ 2\hat{a}^\dagger_{\mathbf{k}} \hat{a}_{\mathbf{k}} + \hat{a}^\dagger_{\mathbf{k}} \hat{a}^\dagger_{-\mathbf{k}} + \hat{a}_{\mathbf{k}} \hat{a}_{-\mathbf{k}} \right\}. \tag{4.5}$$

Taking only this leading term in this Hamiltonian, corresponding to a pure condensate, gives the important result for the ground-state, or mean-field energy per particle of a homogeneous dilute Bose gas, corresponding to a pure condensate,

$$\frac{E_0}{N} = \frac{1}{2} n\tilde{V}(0). \tag{4.6}$$

The chemical potential μ is then given by $\mu = \partial E_0/\partial N = n\tilde{V}(0)$ [55].

To diagonalize the free-space Hamiltonian (4.5) we employ the Bogoliubov transformation (3.20) to the creation and annihilation operators $\hat{a}^\dagger_{\mathbf{k}}$ and $\hat{a}_{\mathbf{k}}$ [125],

$$\hat{a}_{\mathbf{k}} = u_{\mathbf{k}} \hat{b}_{\mathbf{k}} + v^\star_{-\mathbf{k}} \hat{b}^\dagger_{-\mathbf{k}} \tag{4.7}$$

$$\hat{a}^\dagger_{\mathbf{k}} = u^\star_{\mathbf{k}} \hat{b}^\dagger_{\mathbf{k}} + v_{-\mathbf{k}} \hat{b}_{-\mathbf{k}}, \tag{4.8}$$

where enforcing that the $\hat{b}_{\mathbf{k}}$ operators satisfy Bose commutation relations puts the constraint on $u_{\mathbf{k}}$ and $v_{\mathbf{k}}$, $u^\star_{\mathbf{k}} u_{\mathbf{k}'} - v^\star_{\mathbf{k}'} v_{\mathbf{k}} = \delta_{\mathbf{k}\mathbf{k}'}$, just as in Eq. (3.27). Now, a process very similar to that done for the Bose field operators in section 3.2 results in a diagonal form of the Hamiltonian (4.5)

$$\hat{H} = E_0 + \sum_{\mathbf{k}} \hbar\omega(\mathbf{k}) \hat{b}^\dagger_{\mathbf{k}} \hat{b}_{\mathbf{k}}, \tag{4.9}$$

where $\omega(\mathbf{k})$ is the Bogoliubov, or quasiparticle dispersion relation of the homogeneous Bose gas,

$$\hbar\omega(\mathbf{k}) = \sqrt{\frac{\hbar^2 k^2}{2M} \left(\frac{\hbar^2 k^2}{2M} + 2n\tilde{V}(\mathbf{k}) \right)}, \tag{4.10}$$

and the diagonal form of the Hamiltonian is made possible by the quasiparticle amplitudes $u_{\mathbf{k}}$ and $v_{\mathbf{k}}$ satisfying the relations

$$u_{\mathbf{k}}, v_{-\mathbf{k}} = \pm \sqrt{\frac{\frac{\hbar^2 k^2}{2M} + n\tilde{V}(\mathbf{k})}{2\omega(\mathbf{k})} \pm \frac{1}{2}}. \tag{4.11}$$

The dispersion (4.10), first derived by Bogoliubov in 1947 for purely contact (not dipolar) interactions [94], is a key result. It tells us that the ultracold, dilute Bose gas can be described as a condensate “reservoir” beneath a system of non-interacting quasiparticles with the spectrum $\omega(\mathbf{k})$. Additionally, the speed of sound in this system can be extracted from the phonon part of the quasiparticle dispersion, or from its small momentum behavior $\omega(\mathbf{k}) \to \hbar c(\theta_{\mathbf{k}})\mathbf{k}$, where

$$c(\theta_{\mathbf{k}}) = \lim_{k\to 0}\left[\frac{\omega(\mathbf{k})}{\hbar k}\right] = \sqrt{\frac{n\tilde{V}(\theta_{\mathbf{k}})}{M}} \tag{4.12}$$

is the speed of sound in the condensate. In (4.12), the momentum-space interaction potential is written as a function of $\theta_{\mathbf{k}}$ because the limit as $k \to 0$ only affects the magnitude of $\mathbf{k}$ and not its direction. Thus, we see that the homogeneous dipolar Bose-Einstein condensate (BEC) exhibits anisotropic sound due to the anisotropic nature of the ddi [124, 16].

At this point, it is useful to define a new coupling coefficient for the ddi. We define $g_d \equiv 4\pi\hbar^2 a_{dd}/M$, where a_{dd} is defined in Eq. (2.21). In terms of this coupling, the momentum-space interaction for the homogeneous system can be written as

$$\tilde{V}(\mathbf{k}) = \tilde{V}(\theta_{\mathbf{k}}) = g + g_d\left(3\cos^2\theta_{\mathbf{k}} - 1\right). \tag{4.13}$$

It is clear from the form of the dispersion (4.10) that phonons (small-k quasiparticles) will develop imaginary frequencies if $n\tilde{V}(\theta_{\mathbf{k}}) < 0$, and therefore trigger a dynamical phonon instability in the gas according to the condition (3.49). This can occur at different angles depending on the direction of phonon propagation and on the ratio of contact to ddi couplings, though to stabilize the gas at all angles it is necessary to have $g > g_d$. In the literature, the dipole “strength” of the gas is defined as $\epsilon_{dd} \equiv g_d/g$, so the condition for stability of the homogeneous dipolar BEC is given by

$$\epsilon_{dd} < 1. \tag{4.14}$$

It is interesting to note that the most unstable direction for phonon propagation is perpendicular to the dipolar polarization, while the most stable direction is in the direction of the dipole polarization, even though the dipoles are most attractive in this direction. This is a consequence of the shape of the density waves that correspond to phonon excitations. For phonon propagation in the direction of polarization, the regions of high and low density form sheets along which the ddi is most repulsive.

On the other hand, for phonon propagation perpendicular to the direction of polarization, these sheets lie in the plane of the dipolar polarization along which the ddi is most attractive, thus making sound propagation in this direction less stable.

As discussed in section 3.2.3, the presence of interactions in a BEC gives rise to a quantum depletion, or non-zero occupation of excited quasiparticles at zero temperature. In the homogeneous gas, the quantum depletion is given by taking the sum over the square of the Bogoliubov $v_{\mathbf{k}}$ amplitudes to an integral in the homogeneous limit (see Eq. (3.44)),

$$n_{\text{ex}} = \frac{1}{V}\sum_{\mathbf{k}\neq 0} v_{\mathbf{k}}^2 \rightarrow \int \frac{d\mathbf{k}}{(2\pi)^3} v_{\mathbf{k}}^2 = \frac{8}{3} n \mathcal{Q}_3(\epsilon_{dd}) \sqrt{\frac{n a_s^3}{\pi}} \tag{4.15}$$

where the function $\mathcal{Q}_3(\epsilon_{dd}) = \int_0^1 dx(1-\epsilon_{dd}+3\epsilon_{dd}x^2)^{\frac{3}{2}}$ comes from the integration over the angular part of the momentum-space interaction [126] and a_s is the s-wave scattering length. Interestingly, this depletion (4.15) remains finite as the dipole strength approaches the critical value for instability $\epsilon_{dd} \rightarrow 1$, indicating that the collapse of the homogeneous dipolar BEC is in fact a coherent, energetic collapse of the condensate and is *not* due to the macroscopic occupation of phonon modes. We will return to this point when discussing the collapse of dipolar BECs in trapped geometries in section 4.2. Additionally, it is interesting to note that the quantum correction to the pure mean-field density n is proportional to $\sqrt{n a_s^3}$. This term, first derived by Lee, Huang and Yang in 1957 [103], is referred to as the LHY correction, and the same proportionality governs the first-order beyond mean-field (bmf) correction to the ground state energy.

Phonon instability is also predicted to occur in a homogeneous, non-dipolar Bose gas with attractive interactions corresponding to negative scattering lengths $a_s < 0$ [125]. This is expected, though, as negative scattering lengths correspond to $g < 0$, and thus the emergence of non-zero imaginary phonon frequencies. However, these systems are stabilized by the presence of external confinement, where additional kinetic and trapping energy is added to the system. Such stabilization was first predicted by explicitly solving the GPE with attractive contact interactions in [127], and confirmed experimentally at Rice University in a BEC of ^{7}Li with attractive interactions [128]. The stabilization of an attractive BEC motivates the presence of external confinement for the dipolar Bose gas. Because the trap stabilizes the BEC with attractive contact interactions, we expect that applying a trap to a dipolar BEC in the direction of the dipole polarization and on a length scale shorter than the phonon wavelength will suppress the phonon instability in this direction and thus stabilize the condensate against energetic collapse for values of the dipolar strength $\epsilon_{dd} > 1$, presenting the possibility of creating a dominantly dipolar BEC.

The trapping of an ultracold dipolar gas is advantageous for other reasons, as well. Collisional studies of bosonic and fermionic polar molecules in reduced geometries predict that inelastic loss rates are highly reduced when the gas is squeezed in the polarization direction [129, 130, 131, 132, 133]. Such inelastic collisions correspond to chemical reactions, for example, $2\mathrm{KRb} \rightarrow \mathrm{K}_2 + \mathrm{Rb}_2$, or changes of internal molecular states that can occur at short range and result in the molecules being expelled from the trap. These results stem from the fact that the attractive head-to-tail orientation of the dipoles is highly suppressed in this squeezed geometry, and it is the classical "head-to-tail" collision pathway that allows the molecules to reach the short-range at which inelastic processes overwhelmingly occur. It is precisely this attraction that not only gives rise to the energetic collapse of the homogeneous dipolar BEC, but also results in the sharp increase of inelastic scattering of polar molecules [134] and three-body recombination in the presence of the ddi [135]. In the next section, we consider such a squeezed trapping geometry, though we assume that inelastic and three-body losses are completely absent. However, we see that the presence of such a trap significantly stabilizes the dipolar BEC, and leads to novel emergent physics in the system, namely, the emergence of the roton mode in the quasiparticle dispersion of the trapped system.

4.2 Quasi-Two-Dimensional Case

As discussed in section 2.3.1, the interaction of laser light with an atom or molecule can result in an optical force field that acts to trap the atom or molecule. In this section, we consider the case of the retro-reflected laser, where a standing optical wave is created to form an optical lattice trapping geometry. If the laser light propagates in only one direction, the resulting lattice geometry is that of a series of traps, the widths of which are set by the Gaussian width of the laser and the spacings of which are set by the wavelength of the laser. These length scales are typically rather disparate, so a series of very flat, "pancake" shaped optical traps results. We note that a BEC of ^{52}Cr has been achieved in such a geometry [136], which we will discuss further in chapter 8. For now, we consider only one site in a deep optical lattice potential and approximate it as infinitely wide, so the effective trapping potential can be written as a one-dimensional (1D) harmonic potential

$$U(\mathbf{x}) = \frac{1}{2}M\omega_z^2 z^2, \tag{4.16}$$

where ω_z is the trap frequency, and $l_z = \sqrt{\hbar M/\omega_z}$ is the corresponding harmonic oscillator length. Such a trapping geometry creates a system that is spatially homogeneous in the x-y plane, and thus has some two-dimensional (2D) character, be it pure-2D or quasi-2D.

4.2.1 Contact Interactions

In a pure-2D system, the BEC phase, characterized by long range phase coherence, occurs only at $T = 0$, as follows from Bogoliubov's k^{-2} theorem [137]. However, in 1972 Popov showed that superfluidity may exist in the absence of the pure condensate at ultracold, but non-zero temperatures due to the macroscopic occupation of finite-wavelength modes [138]. Thus, the superfluid state of a Bose fluid in 2D is characterized not by a pure condensate but by a quasi-condensate with finite size domains of phase coherence [139, 140]. Additionally, the interaction coupling for a 2D system is density dependent, $g_{\mathrm{2D}} \to g_{\mathrm{2D}}(n_{\mathrm{2D}})$, as was first predicted by Schick to zeroth-order in the 2D gas parameter $n_{\mathrm{2D}}a_c^2$ for a 2D system of hard circles [141],

$$g_{\mathrm{2D}}(n_{\mathrm{2D}}) = \frac{4\pi\hbar^2}{M}\frac{1}{|\ln n_{\mathrm{2D}}a_c^2|}, \tag{4.17}$$

where, here, a_c is the radius of the hard circle. Such a form of the 2D interaction coupling has its roots in the fact that the 2D scattering amplitude for hard-circles has the form $\propto 1/\ln ka_c$ in the limit $ka_c \to 0$, whereas the 3D scattering amplitude for hard *spheres* is momentum independent.

Historically, the study of ultracold 2D Bose fluids was motivated by experiments on monolayers of ^{4}He [142], where the size of the 1D confinement is typically smaller than the characteristic range of the interactions in the fluid. Such is not necessarily the case, however, for current experiments on dilute BECs in optical traps. Take, for example, the tight harmonic trap frequency $\omega_z \approx 2\pi \times 40$ kHz that has been achieved in the ^{52}Cr experiment [136]. The corresponding harmonic oscillator trap size for ^{52}Cr is $l_z \approx 1.3 \times 10^3\, a_0$ where a_0 is the Bohr radius. This trap size is much larger than the dipole length of chromium, $a_{dd} = 15.2\, a_0$, and is certainly much larger than scattering lengths that can be experimentally realized by using a Fano-Feshbach resonance [21] (see section 6.1). Such length scales may result in a gas with three-dimensional (3D) character. However, at very low yet experimentally accessible temperatures $T \sim 200$ nK [14], the ratio of the trapping energy to the temperature $\hbar\omega_z/k_{\mathrm{B}}T \sim 10$ is fairly large, so the character of the gas in the direction of the trap is not free and instead the particles undergo zero-point oscillations. Such character motivates the definition of, and defines the "quasi-2D" gas.

In their work [143], Petrov, Holzmann and Shlyapnikov showed that the pure BEC state is realizable in a quasi-2D Bose gas at ultracold, but non-zero temperatures $T < T_c$, where T_c is the critical temperature for BEC in the homogeneous gas. Additionally, they calculated a modified momentum-dependent interaction coupling for the quasi-2D BEC where the two-body scattering wave function has the asymptotic form $\psi(\mathbf{x}) = \chi(z)\exp\left[i\mathbf{k}\cdot\boldsymbol{\rho}\right]$,

$$g_{\mathrm{q2D}}(\mathbf{k}) = \frac{2\sqrt{2\pi}\hbar^2}{M}\frac{1}{\frac{l_z}{a_s} + \frac{1}{\sqrt{2\pi}}\ln\frac{1}{\pi k^2 l_z^2}}. \tag{4.18}$$

where $\chi(z)$ is the ground-state wave function of the potential (4.16), given by a normalized Gaussian

$$\chi(z) = \frac{1}{\sqrt{l_z}\pi^{\frac{1}{4}}}\exp\left[-\frac{z^2}{2l_z^2}\right], \tag{4.19}$$

and a_s is the 3D s-wave scattering length. In the limit $a_s \ll l_z$, the logarithmic term in (4.18) can be neglected and the coupling acquires a momentum independent form that is proportional to the ratio a_s/l_z. This is a very important result. By drawing the distinction between pure-2D and quasi-2D systems, being that the quasi-2D system permits a BEC state with long-range phase coherence [144], we can treat the quasi-2D system on the same footing as we treat the 3D system and therefore apply the results from section 4.1 directly to the quasi-2D system. The difference is that, for the quasi-2D system, we treat the condensate mode as a zero-momentum plane wave in the x-y plane with the axial wave function $\chi(z)$. Such a treatment is known as the single-mode approximation, and is valid for a dilute Bose gas when $\hbar\omega_z \gg k_B T$. In this approximation, the quasi-2D interaction coupling corresponding to the s-wave pseudopotential (3.58) can be calculated simply by integrating out the z-dependence of the interaction terms in the many-body Hamiltonian,

$$\begin{aligned} g_{\text{q2D}} &= g \int dz \int dz' \chi^\star(z)\chi^\star(z')\delta(z-z')\chi(z')\chi(z) \\ &= g \int dz \chi^\star(z)\chi^\star(z)\chi(z)\chi(z) \\ &= \frac{2\sqrt{2\pi}\hbar^2 a_s}{M l_z}. \end{aligned} \tag{4.20}$$

Thus, the quasi-2D BEC with s-wave interactions can be treated in the same way as the homogeneous 3D BEC but as a 2D system with an effective quasi-2D interaction coupling (4.20).

In the limit $a_s \gg l_z$, the relation $k^2 = 2M\mu/\hbar^2$ [92] can be used to show that the coupling (4.18) takes the pure-2D form (4.17). Thus, in this limit the gas is effectively 2D. It is interesting to note that the quasi-2D coupling (4.18) suggests not only that the character of the gas from 2D to quasi-2D can be controlled by tuning the trap frequency, but also that the strength of the interactions can be controlled by tuning the trap frequency. Indeed, a transition from attractive (negative) to repulsive (positive) occurs at a critical harmonic oscillator trap length $l_{\text{crit}} = \frac{a_s}{\sqrt{2\pi}} \ln(1/\pi k^2 l_z^2)$, corresponding to the appearance of a zero-energy bound state. Such phenomena in ultracold gases are appropriately referred to as confinement-induced resonances, and were first predicted in the quasi-1D geometry by Olshanii [145].

4.2.2 Dipole-Dipole Interactions

We now turn our attention to the case of the ddi. In pure-2D and if the dipoles are polarized in the direction of tight confinement (the z-direction if we consider the trapping potential (4.16)), the in-plane interaction is given simply by

$$V_{\text{2D}}(\boldsymbol{\rho} - \boldsymbol{\rho}') = \frac{d^2}{|\boldsymbol{\rho} - \boldsymbol{\rho}'|^3}. \tag{4.21}$$

This interaction potential has purely s-wave character and is dominated by the s-wave contribution to the scattering T-matrix at ultracold temperatures. Indeed, it was shown in [146] that the zero-energy threshold scattering behavior of two aligned dipoles interacting via the 2-body potential (4.21) is well-described by treating the dipolar interaction as a hard-wall interaction at the radius $a_s \simeq 19\, a_{dd}$. This idea is considered in [147] in the many-body context where diffusion Monte Carlo calculations were performed for a gas of bosonic dipoles in the pure-2D geometry. Therein, the authors calculate the energy per particle using the potential (4.21) and find that it agrees well with the 2D mean-field result $E_0/N = g_{2\mathrm{D}}(n_{2\mathrm{D}})n_{2\mathrm{D}}/2$ (see Eq. (4.6)) where $g_{2\mathrm{D}}(n_{2\mathrm{D}})$ is given by (4.17) for small values of the gas parameter $n_{2\mathrm{D}}a_s^2$, and $n_{2\mathrm{D}}$ is the 2D density of the gas, although small quantitative deviations exist. In the quasi-2D regime, however, this treatment of the ddi is no longer appropriate. In this regime, the zero-point oscillations reintroduce the 3D character of the ddi at a length scale $\sim l_z$, and a proper treatment of the interactions in such a system must take this into account.

To begin describing the quasi-2D dipolar BEC, we make the assumption that the dipole lengths of the bosons are sufficiently smaller than the harmonic oscillator trap length, $a_{dd} \ll l_z$ so any pure-2D character can be neglected. Then, the effective quasi-2D ddi can be calculated in the same way as is done for the contact interactions (4.20),

$$V_{\mathrm{q2D}}(\boldsymbol{\rho} - \boldsymbol{\rho}') = \int dz \int dz' \chi^\star(z)\chi^\star(z')V_d(\mathbf{x} - \mathbf{x}')\chi(z')\chi(z). \tag{4.22}$$

We handle this integral in momentum-space, and give the details of the calculation in Appendix C. For the sake of generality, we allow for the dipoles to be uniformly polarized in any direction, not just in the z-direction, at an angle α off of the z-axis. In this case, the momentum-space ddi in the quasi-2D geometry takes the elegant form [39] (Eq. (C.8))

$$\tilde{V}_{\mathrm{q2D}}(\mathbf{k}_\rho) = \frac{g_d}{\sqrt{2\pi} l_z} F\left(\frac{\mathbf{k}_\rho l_z}{\sqrt{2}}\right), \tag{4.23}$$

where the function $F(\mathbf{q}) = \cos^2 \alpha F_\perp(\mathbf{q}) + \sin^2 \alpha F_\parallel(\mathbf{q})$ has contributions from the projection of the polarization vector $\hat{d}$ onto the trap z-axis and onto the x-y plane, given in Appendix C by

Eqs. (C.6) and (C.7), respectively. Unlike the quasi-2D contact interaction potential, the quasi-2D ddi potential (4.23) depends both on the direction and magnitude of the 2D momentum $\mathbf{k}_\rho$. For the remainder of this chapter, though, we take $\alpha = 0$ so the ddi is isotropic in the x-y plane and the momentum-space form of the ddi no longer depends on the direction of $\mathbf{k}_\rho$. However, taking $\alpha \neq 0$ is crucial for the discussion in Chapter 7 and we return to the general anisotropic form of this quasi-2D ddi there. For now, including both the contact and ddi from Eqs. (4.20) and (4.23), the full quasi-2D momentum-space interaction potential takes the form

$$\tilde{V}_{\mathrm{q2D}}(\mathbf{k}_\rho) = \frac{g}{\sqrt{2\pi} l_z}\left(1 + \epsilon_{dd} F_\perp\left[\frac{\mathbf{k}_\rho l_z}{\sqrt{2}}\right]\right). \tag{4.24}$$

We note that this expression was first derived for the quasi-2D dipolar BEC in [29].

Exploring the limiting behavior of $F_\perp(q)$ illuminates interesting physics for the quasi-2D dipolar BEC,

$$\lim_{k_\rho l_z \to 0} F_\perp\left(\frac{k_\rho l_z}{\sqrt{2}}\right) = 2 \tag{4.25}$$

$$\lim_{k_\rho l_z \to \infty} F_\perp\left(\frac{k_\rho l_z}{\sqrt{2}}\right) = -1, \tag{4.26}$$

where the function is monotonically decreasing between these limits. The limit $k_\rho l_z \to 0$ in (4.25) corresponds to zero in-plane momentum. Such character describes the condensate field of the quasi-2D system, the wave function of which we write as $\phi_0(\mathbf{x}) = \sqrt{n_{\mathrm{2D}}}\chi(z)$. Thus, from this limiting behavior we can write the mean-field interaction energy of the quasi-2D dipolar BEC from Eq. (4.6),

$$\frac{E_0}{N} = \frac{1}{2}\frac{g}{\sqrt{2\pi} l_z} n_{\mathrm{2D}}\left(1 + 2\epsilon_{dd}\right), \tag{4.27}$$

where n_{2D} is the integrated 2D density of the gas, or the density obtained by integrating the full density over all z. This form suggests that in the small momentum limit, when the characteristic wavelength of a mode is much larger than the trap size, the ddi can be treated as a contact interaction with coupling $2g_d$. From Eq. (4.27), we see that for the quasi-2D BEC to be energetically stable the interaction couplings must be such that $1 + 2\epsilon_{dd} > 0$, or

$$\epsilon_{dd} > -\frac{1}{2}, \tag{4.28}$$

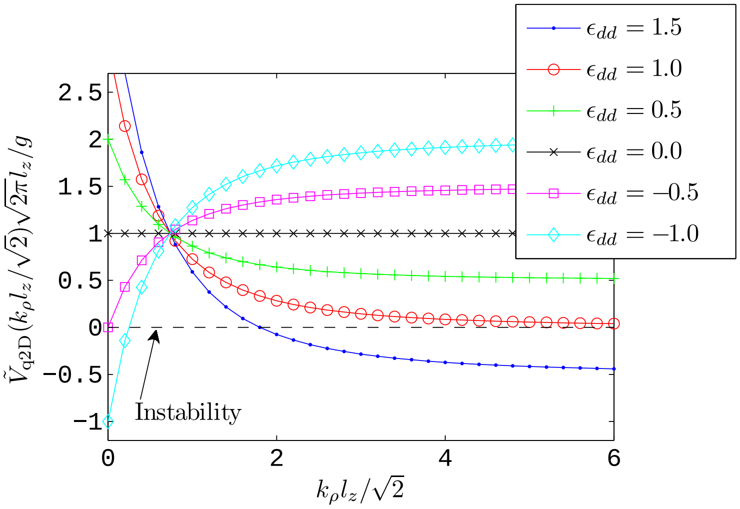

Figure 4.1: The quasi-2D momentum-space interaction potential (4.24) for fixed contact interaction coupling and various valued of the dipole interaction strength ϵ_{dd}. The black dashed line marks $\tilde{V}_{\rm q2D}(k_\rho l_z/\sqrt{2}) = 0$, below which instabilities are possible. For $\epsilon_{dd} = 0$, corresponding to no dipole interactions, the interaction is independent of momentum.

that is, quasi-2D dipolar BEC is energetically stabilized for any s-wave scattering lengths greater than minus twice the characteristic dipole length a_{dd}, or $a_s > -2a_{dd}$. This criterion shows that the quasi-2D dipolar BEC is significantly more stable than the homogeneous dipolar BEC, whose energetic stability criterion is given by Eq. (4.14).

The limit of $F_\perp(k_\rho l_z/\sqrt{2})$ as $k_\rho l_z \to \infty$ (4.26), while unphysical in the mean-field Bogoliubov picture because of our effective energy cutoff $E_{\rm cut}$ in the two-body scattering theory (see section 3.4), corresponds to a 3D character in the quasi-2D system as the characteristic wavelengths of such quasiparticles are much smaller than the trap size l_z in this limit. Indeed, taking this limit results in a quasi-2D momentum-space interaction that is proportional to $(g-g_d)$, which is the same result that is seen for quasiparticles in the 3D system that propagate perpendicular to the dipole polarization, corresponding to $\theta_k = \pi/2$ (see Eq. (4.13)). The quasi-2D momentum-space interaction potential (4.24) is plotted in figure (4.1) for different dipole interaction strengths $\epsilon_{dd} = g_d/g$. Here, phonon instability is seen as $\tilde{V}_{\rm q2D}(k_\rho l_z/\sqrt{2}) < 0$ at small $k_\rho l_z$. The case of $\epsilon_{dd} = -0.5$ is at the threshold of phonon instability, while $\epsilon_{dd} = -1.0$ is clearly unstable.

4.2.3 Bogoliubov Spectrum: Emergence of the Roton

Because the condensate is defined in the same manner in quasi-2D as in 3D (long-wavelength phase coherence [144]), the results from the 3D field theory can be used for the quasi-2D system, where the sums and integrals are now taken over momenta in the 2D plane and the effective quasi-2D interaction potentials are used. Thus, knowledge of the momentum-space interaction in the quasi-2D system permits the calculation of the quasiparticle dispersion from Eq. (4.10). Written explicitly, this dispersion takes the form

$$\hbar\omega(\mathbf{k}_\rho) = \sqrt{\frac{\hbar^2 k_\rho^2}{2M}\left[\frac{\hbar^2 k_\rho^2}{2M} + \frac{2g}{\sqrt{2\pi}l_z}n_{\mathrm{2D}}\left(1+\epsilon_{dd}F_\perp\left[\frac{k_\rho l_z}{\sqrt{2}}\right]\right)\right]}. \tag{4.29}$$

From this, we can calculate the speed of sound in the quasi-2D dipolar gas from Eq. (4.12),

$$c_{\mathrm{q2D}} = \sqrt{\frac{n_{\mathrm{2D}}\tilde{V}_{\mathrm{q2D}}(0)}{M}} = \frac{1}{(2\pi)^{\frac{1}{4}}}\sqrt{\frac{n_{\mathrm{2D}}g}{Ml_z}\left(1+2\epsilon_{dd}\right)}. \tag{4.30}$$

Unlike the case for the 3D dipolar BEC, the speed of sound in the quasi-2D dipolar BEC (when $\alpha = 0$) is isotropic. Additionally, Eq. (4.30) reveals that the speed of sound develops a non-zero imaginary part, corresponding to an imaginary phonon frequency in the quasiparticle dispersion, when $\epsilon_{dd} < -1/2$. This result is consistent with the criteria for energetic stability (4.28).

Quasiparticle dispersions are plotted for $2\sqrt{2\pi}(a_s/l_z)(n_{\mathrm{2D}}l_z^2) = 1$ and $\epsilon_{dd} = 0$ in figure 4.2 and $\epsilon_{dd} = -1$ in figure 4.3. For $\epsilon_{dd} = 0$, the system is energetically stable, as is reflected by the purely real dispersion in the corresponding figure. Therein, the free-particle (non-interacting) dispersion is plotted and the sound velocity of the interacting condensate is shown by the slope of the black dotted line. For $\epsilon_{dd} = -1$ in figure 4.3, the system is energetically unstable, as is signified by non-zero imaginary phonon frequencies. Regarding energetic stability, the criteria set by the mean-field energy (4.27) and the phonon stability predict that the quasi-2D dipolar BEC is stable for all values of $\epsilon_{dd} > -1/2$. Further investigation of the quasiparticle dispersion (4.29), however, reveals otherwise.

In the homogeneous 3D dipolar BEC, the momentum-space interaction is independent of the magnitude of $\mathbf{k}$ and instead depends only on its direction. The case for the quasi-2D dipolar BEC

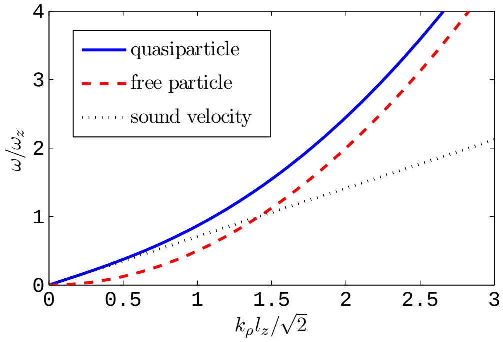

Figure 4.2: The quasiparticle dispersion (blue line) of the quasi-2D BEC with repulsive contact interactions $2\sqrt{2\pi}(a_s/l_z)(n_{2\text{D}}l_z^2) = 1$ and $\epsilon_{dd} = 0$, corresponding to no dipolar interactions. The free-particle dispersion is shown by the red dashed line and the sound velocity is given by the slope of the green dotted line.

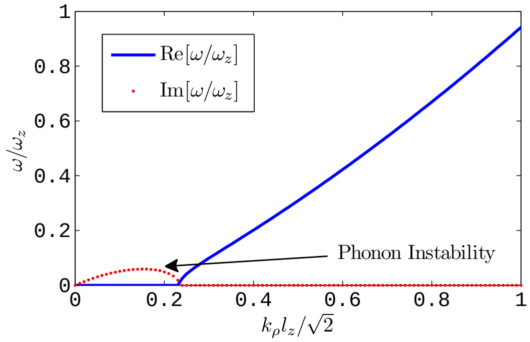

Figure 4.3: The quasiparticle dispersion (blue line) of the quasi-2D dipolar BEC with repulsive contact interactions $2\sqrt{2\pi}(a_s/l_z)(n_{2\text{D}}l_z^2) = 1$ and $\epsilon_{dd} = -1$. The red dots show the imaginary part of the dispersion at small momenta, corresponding to phonon instability for these parameters.

considered here is just the opposite, as mentioned previously, and the momentum-space interaction $\tilde{V}_{\text{q2D}}(\mathbf{k}_\rho)$ does not depend on the direction of $\mathbf{k}_\rho$ in the x-y plane but *does* depend on its magnitude k_ρ, as shown in figure 4.1. This fact can be understood qualitatively by considering that while there is no external length scale in the homogeneous 3D system, the presence of the harmonic trap sets an external length scale in the quasi-2D system. For phonons with wavelengths that are much greater than the trap size, $k_\rho l_z < 1$, the interactions have a purely repulsive 2D character. This is reflected in the fact that, for $\epsilon_{dd} > 0$, the momentum-space interaction (4.24) is positive at small wave number. However, for quasiparticles at intermediate momenta $k_\rho l_z \sim 1$, the interactions begin to take on a 3D character and the attractive part of the ddi plays an important role. This is reflected in the fact that, regardless of the value of ϵ_{dd}, the scaled momentum-space interaction (4.24) crosses through unity at $k_\rho l_z = \sqrt{2}$. Thus, the character of the quasiparticles may depend not only on its wavelength, but on the ratio of their wavelength to the harmonic oscillator length of the trap.

Indeed, for large ϵ_{dd} the interaction potential becomes sufficiently negative at intermediate wave number so that $\omega(k_{\text{roton}}) = 0$, where k_{roton} is a finite, non-zero wave number. To illustrate this fact, quasiparticle dispersions are plotted for $2\sqrt{2\pi}(a_s/l_z)(n_{2\text{D}}l_z^2) = 1$ and $\epsilon_{dd} = 3.7$ in figure 4.4 and

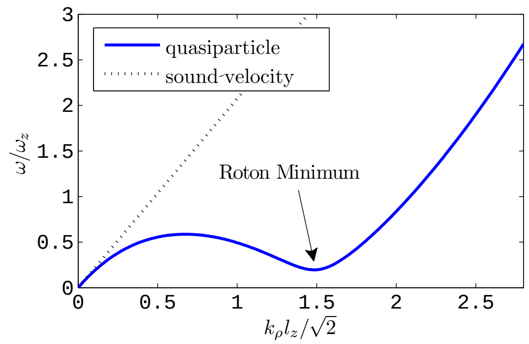

Figure 4.4: Quasiparticle dispersion of the quasi-2D dipolar BEC with repulsive contact interactions $2\sqrt{2\pi}(a_s/l_z)(n_{2\mathrm{D}}l_z^2) = 1$ and $\epsilon_{dd} = 3.7$. The sound velocity is given by the slope of the black dotted line and the roton minimum is labeled.

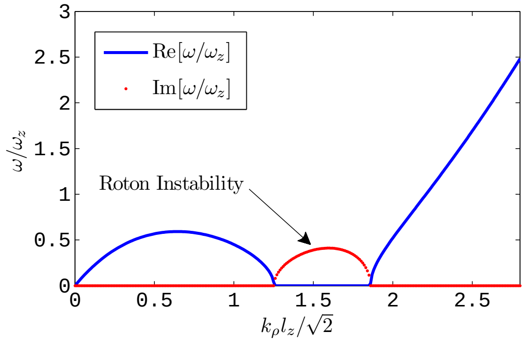

Figure 4.5: Dynamically unstable quasiparticle dispersion of the quasi-2D dipolar BEC with repulsive contact interactions $2\sqrt{2\pi}(a_s/l_z)(n_{2\mathrm{D}}l_z^2) = 1$ and $\epsilon_{dd} = 4.0$. The red dots shows the imaginary part of the dispersion at intermediate wave numbers, corresponding to a roton instability.

$\epsilon_{dd} = 4$ in figure 4.5. For $\epsilon_{dd} = 3.7$, the system is dynamically stable, but the dispersion possesses a minimum at finite wave number. This minimum is referred to as the "roton minimum," and the corresponding quasiparticle at the minimum is referred to as the roton. Similarly, the quasiparticle associated with the local maximum in the dispersion is referred to as a maxon, and the spectrum is said to have "roton-maxon" character. As ϵ_{dd} is further increased , the roton minimum drops and, at a critical value, becomes degenerate with the condensate, corresponding to $\omega(k_{\mathrm{roton}}) = 0$. This signifies a roton instability in the quasi-2D dipolar BEC, as is illustrated in figure 4.5, where the roton has a non-zero imaginary frequency for dipole strengths greater than the critical value. We plot the stability diagram of the quasi-2D dipolar BEC in figure 4.6. Therein, the phonon instability is present for all $\epsilon_{dd} < -1/2$, while the roton instability is a non-trivial function of ϵ_{dd}. This stability relation was first pointed out in [148]. We note that the roton-maxon spectrum in the trapped dipolar BEC was first pointed out in [28], and was first predicted for a dilute Bose gas in [149] where the ddi is induced in a quasi-one-dimensional BEC irradiated by a laser.

In figure 4.6, it appears as though the system stabilizes for some arbitrarily large ϵ_{dd} and some sufficiently small contact interaction coupling g. In fact, the purely dipolar (corresponding to

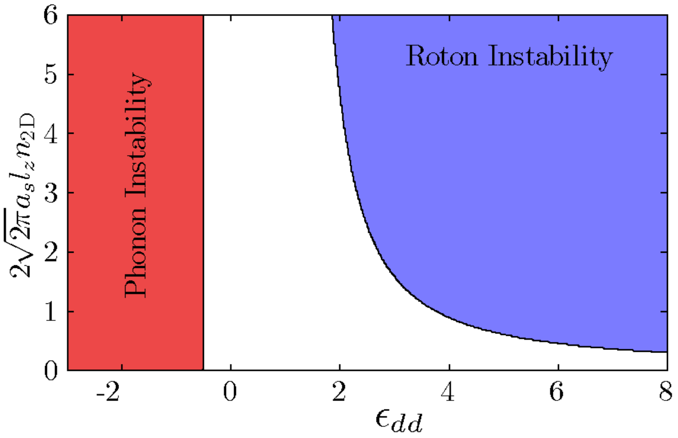

Figure 4.6: The stability diagram of the quasi-2D dipolar BEC as a function of the contact interaction coupling and the ddi strength ϵ_{dd}. The red region indicates phonon instability for all $\epsilon_{dd} < -1/2$, and the blue region indicates roton instability. The white, uncolored region corresponds to a dynamically stable system.

$g = 0$ and $g_d \neq 0$) quasi-2D BEC is dynamically stable only within a finite range of ddi couplings. We find that the the onset of the roton instability occurs for $(a_{dd}/l_z)(n_{2\mathrm{D}}l_z^2) \sim 0.34$. Thus, the threshold for roton instability can be controlled by tuning either the dipole strength, the density of the gas or the shape of the confining potential such that this value is achieved. For the ^{52}Cr system discussed earlier in this section with $\omega_z = 2\pi \times 40\,\mathrm{kHz}$ and a_s=0, a limit of the scattering length that has been achieved experimentally [21], the roton instability is predicted to occur for an integrated 2D density of $n_{2\mathrm{D}} \simeq 5 \times 10^{11}\,\mathrm{cm}^{-2}$.

There are two very important observations to be made about the roton instability. One is that the roton instability occurs at a finite density and ddi strength regardless of the size of the trapping potential, as long as the dipole length is sufficiently smaller than the harmonic oscillator length of the trap. The case of $a_{dd} > l_z$ breaks the quasi-2D criterion, and the physics of this case is discussed briefly in section 4.2.5. The other important observation to be made is that the roton instability occurs at a finite, relatively small length scale set by the size of the trap, $k_{\mathrm{roton}} \sim 1/l_z$. Thus, we find that the roton instability is density-dependent and *local*, as opposed to *global* like the phonon instability.

4.2.4 Quantum Depletion and Roton Instability

As was done for the 3D homogeneous dipolar BEC in section 4.1, it is instructive to calculate the quantum depletion for the quasi-2D dipolar BEC at the thresholds for roton and phonon instability. For simplicity, we consider the purely dipolar case with $g = 0$. In this case, recall that the depletion is given by Eq. (4.15), where we consider the system to be in a box of area $A = L^2$,

$$n_{\mathrm{ex}} = \frac{1}{A}\sum_{\mathbf{k}\neq 0} v_{\mathbf{k}_\rho}^2 \rightarrow \int \frac{d\mathbf{k}_\rho}{(2\pi)^2} v_{\mathbf{k}_\rho}^2. \tag{4.31}$$

We evaluate this integral (4.31) numerically using adaptive Gauss-Kronrod quadrature[1] and plot the results in figure 4.7. Recall that the phonon instability in the quasi-2D dipolar BEC with no contact interactions occurs for all $a_{dd} \leq 0$. Just like the case for the 3D homogeneous dipolar BEC, the quantum depletion remains finite, and in fact goes to zero at the phonon instability threshold. This confirms that the phonon instability corresponds to a coherent energetic collapse of the condensate, just as in the case for the 3D dipolar BEC.

The depletion near the roton instability, however, behaves very differently. In figure 4.7, the roton instability threshold is marked by the vertical black dashed line. As a_{dd}/l_z is increased towards this threshold, the quantum depletion grows and eventually diverges at the instability. The physical interpretation of this divergence is that the roton instability is not a coherent energetic collapse, but actually a macroscopic depletion of the condensed state that is caused by particles occupying roton modes as the roton energy becomes degenerate with the condensate, and it is thus energetically favorable for them to do so.

4.2.5 The Other Roton

It is important to draw the distinction between the roton in the dilute, quasi-2D dipolar BEC that is discussed here and the roton that was introduced in section 2.1.1 that exists in superfluid ^{4}He. The superfluid ^{4}He system exhibits roton-maxon character due to strong correlations that induce ordering at short length scales, on the order of the average interatomic spacing. In ^{4}He, the

---

[1] Available in MATLAB through the function `quadgk`

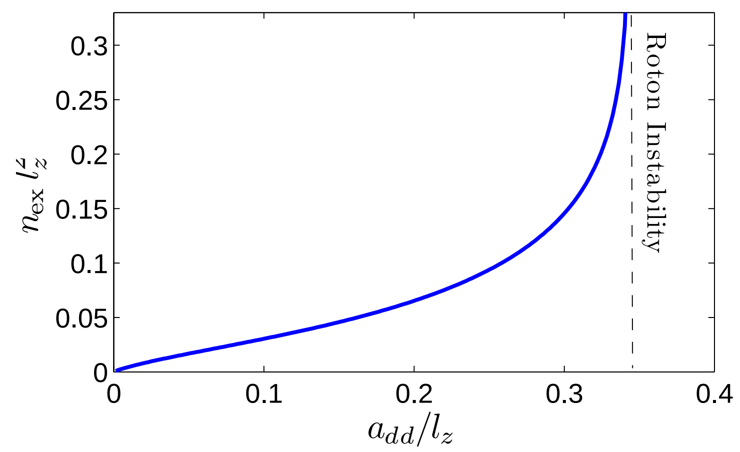

Figure 4.7: The quantum depletion, or excited quasiparticle occupation at zero temperature of the purely dipolar (no contact interactions) quasi-2D dipolar BEC. The phonon instability occurs for $a_{dd} < 0$ in this case, and the roton instability occurs for $a_{dd}/l_z \gtrsim 0.34$. The divergence of the quantum depletion at the roton instability indicates that this instability corresponds to the macroscopic depletion of the condensate into rotons.

densities are on the order $\sim 2 \times 10^{22}\,\mathrm{cm}^{-3}$ and the scattering lengths have been calculated to be $a_s \sim 8\,\mathrm{nm}$ [150], so the "gas" parameter for this system is on the order $na_s^3 \sim 10^4$. Thus, the roton is this system is intimately related with the structure of the fluid, and represents a tendency towards spatial ordering at the length scale $\sim 1/k_{\mathrm{roton}}$ which, in this system, is on the order of tens of Bohr radii, which in turn is characteristic of the lattice spacing in the solid. Thus, in ^{4}He, the roton is isotropic and arises due to the strong isotropic repulsion between the atoms in the liquid. This is in strong contrast to the roton in the quasi-2D dipolar BEC, which we present in the previous section. In this case, the condensate is dilute and thus has negligible two-body correlations and the roton instead has its roots in the momentum dependence of the interaction potential (4.24), where the momentum dependence results solely from the anisotropy of the ddi interaction at length scales $\sim l_z$.

Such is not the case, however, when the ddi is sufficiently strong (or the trap is sufficiently tight) so that $a_{dd} \gg l_z$. In this case, the anisotropy of the ddi is tuned away and the interactions become purely repulsive, taking the 2D form (4.21). This 2D system can be characterized by the

2D gas parameter $n_{\mathrm{2D}}a_{dd}^2$. Interestingly, a dispersion with roton-maxon character was predicted for this system for gas parameters $n_{\mathrm{2D}}a_{dd}^2 \gtrsim 100$ [12, 13]. Therein, quantum Monte Carlo techniques are used to demonstrate the elegant connection between the existence of superfluidity at smaller densities and the breakdown of superfluidity at larger densities as correlations become strong and superfluidity is broken, corresponding to the transition from a superfluid state to a self-ordered crystalline state. Additionally, such rotons have been predicted to play a strong role in the BKT superfluid transition in a 2D system of dipoles [151]. More, recently, the quasi-2D to 2D crossover of an ultracold dipolar Bose gas was studied using the hypernetted chain Euler-Lagrange method, wherein the crossover from the strongly interacting, ^{4}He-like roton to the quasi-2D roton was shown as the confining trap frequency was varied continuously [152].

Chapter 5

Dipolar Bose-Einstein Condensate in a Cylindrically Symmetric Trap

In the preceding chapters, we built a motivation for and a theoretical means to describe the zero-temperature dipolar Bose-Einstein condensate (dipolar BEC). Here, we proceed with this description. We solve for the condensate wave function $\phi_0(\mathbf{x})$ by minimization of the energy functional (3.24) and we calculate the chemical potential μ via the Gross-Pitaevskii equation (GPE), Eq. (3.23). Additionally, we solve the Bogoliubov de Gennes (BdG) equations (3.34) to explore the discrete quasiparticle spectrum of the trapped dipolar BEC and to study the nature of its instability. Such calculations are, in general, numerically intensive, and we handle them by introducing a novel algorithm that exploits the cylindrical symmetry of the system. Rotationless states are considered, as well and singly- and doubly-quantized vortex states. Here, we use techniques that are, within the scope of the mean-field theory, numerically exact. Thus, we are able to see novel physics that is invisible to the more simple calculations, such as the Gaussian ansatz or the Thomas-Fermi methods. This physics includes structured ground states and discrete roton-like quasiparticle excitations that play an interesting and important role in the physics of trapped dipolar BECs. Additionally we set the s-wave scattering length $a_s = 0$ in this chapter to illuminate purely dipolar effects. Indeed, this is a limit that has been achieved experimentally in a dipolar BEC of ^{52}Cr by exploiting a Fano-Feshbach resonance. We discuss this point further and discuss the physics of the Fano-Feshbach resonance in chapter 6. Original work presented in this chapter has been published in references [35], [36] and [34].

We consider a dipolar BEC in a harmonic trap with cylindrical symmetry, so $\omega_x = \omega_y = \omega_\rho$.

This trapping potential can be written as

$$U(\mathbf{x}) = \frac{1}{2} M \omega_\rho^2 \left(\rho^2 + \lambda^2 z^2\right), \tag{5.1}$$

where $\lambda = \omega_z/\omega_\rho$ is the trap aspect ratio. Small λ, or $\lambda \ll 1$, corresponds to a highly prolate, or "cigar" shaped trap while large λ, or $\lambda \gg 1$, corresponds to a highly oblate, or "pancake" shaped trap. We can consider the limit $\lambda \to \infty$ (with fixed ω_z) as a purely quasi-two dimensional (quasi-2D) system, as discussed in the previous chapter, and the limit $\lambda \to 0$ (with fixed ω_ρ) as a purely quasi-one dimensional (quasi-1D) system. Additionally, if we enforce that the dipoles be polarized in the z-direction, we can use the two-body dipole-dipole interaction (ddi) potential from Eq. (3.59) to describe the dipolar interactions. In this case, the system exhibits cylindrical symmetry, and the condensate states may be written in cylindrical coordinates as eigenstates of the orbital angular momentum projection $\hbar s$,

$$\phi_0(\mathbf{x}) = \psi(\rho, z) e^{is\varphi}. \tag{5.2}$$

Here, s is the vorticity of the condensate wave function. Thus, $s = 0$ corresponds to a rotationless condensate, $s = 1$ corresponds to a condensate with a singly-quantized vortex, $s = 2$ corresponds to a doubly-quantized vortex, and so on. Note that the form of the condensate wave function (5.2) exhibits a phase singularity at $\rho = 0$ for all $s \neq 0$.

5.1 Methods

We calculate the condensate wave function $\phi_0(\mathbf{x})$ in the form given in Eq. (5.2) by enforcing that it minimize the energy functional (3.24), which we now write explicitly in terms of the single-particle Hamiltonian $\hat{H}^{(1)}(\mathbf{x})$ and the contact and ddi potentials from Eq. (3.61),

$$\begin{aligned}\frac{E_0[\phi_0]}{N} = \int d\mathbf{x} \Bigg(& \phi_0^\star(\mathbf{x}) \left[-\frac{1}{2}\nabla^2 + \frac{1}{2}\left(\rho^2 + \lambda^2 z^2\right)\right] \phi_0(\mathbf{x}) + \frac{N-1}{2} g |\phi_0(\mathbf{x})|^4 \\ & + \frac{N-1}{2} g_d \int d\mathbf{x}' |\phi_0(\mathbf{x}')|^2 \frac{1 - 3\cos^2\theta_{\mathbf{x}-\mathbf{x}'}}{|\mathbf{x}-\mathbf{x}'|^3} |\phi_0(\mathbf{x})|^2 \Bigg),\end{aligned} \tag{5.3}$$

where we have set the number of particles in the system to be the number of particles in the condensate, $N = N_0$, and we have moved to dimensionless units where all energies are in units of

$\hbar\omega_\rho$ and all lengths are in units of the radial harmonic oscillator length, $a_{\mathrm{ho}} = a_\rho = \sqrt{\hbar/M\omega_\rho}$. We remain in these dimensionless units for the remainder of this chapter. Recall that $g = 4\pi\hbar^2 a_s/M$ where a_s is the (generally dipole-dependent) s-wave scattering length and $g_d = 4\pi\hbar^2 a_{dd}/M$ where $a_{dd} = Md^2/3\hbar^2$ is the characteristic dipole length. We also write out the explicit form of the time-independent GPE (3.23) in the dimensionless form,

$$\begin{aligned}\mu\phi_0(\mathbf{x}) = \bigg(&-\frac{1}{2}\nabla^2 + \frac{1}{2}\left(\rho^2 + \lambda^2 z^2\right) + (N-1)g|\phi_0(\mathbf{x})|^2 \\ &+ (N-1)g_d \int d\mathbf{x}'|\phi_0(\mathbf{x}')|^2 \frac{1 - 3\cos^2\theta_{\mathbf{x}-\mathbf{x}'}}{|\mathbf{x}-\mathbf{x}'|^3}\bigg)\phi_0(\mathbf{x}).\end{aligned} \tag{5.4}$$

In practice, we calculate the total energy per particle (5.3) by defining the relevant functions on a discrete spatial grid in ρ and z, with $N_\rho \times N_z$ grid points. Notice that, if $\phi_0(\mathbf{x})$ has the angular dependence $e^{is\varphi}$, a centrifugal term appears in the kinetic energy term of the energy functional and GPE that is like $\hbar^2 s^2/2M\rho^2$, which diverges at $\rho = 0$. To avoid this complication, we treat both the ddi mean-field terms and the kinetic energy terms in momentum-space in order to avoid any numerical problems that are associated with the presence of real-space divergences on the discrete numeric grid.

Recall that the kinetic energy operator has the diagonal form in momentum-space $\hat{T} = k^2/2$. Thus, we can easily calculate the kinetic energy terms in momentum-space and then represent them in real-space via Fourier transform, $-\frac{1}{2}\nabla^2\phi_0(\mathbf{x}) = \mathcal{F}^{-1}[\frac{1}{2}k^2\tilde{\phi}_0(\mathbf{k})]$, where $\mathcal{F}$ is the Fourier transform operator defined in Eqs. (A.2) and (A.3) and $\tilde{\phi}_0(\mathbf{k}) = \mathcal{F}[\phi_0(\mathbf{x})]$. If these functions are defined on appropriate numeric grids, such calculations may be carried out with great speed and accuracy via the Fast Fourier Transform (FFT) algorithm. However, the three-dimensional (3D) FFT cannot, in general, take advantage of the cylindrical symmetry of the wave function (5.2). Instead of using Fourier transforms in the radial direction, we can use Hankel transforms in the radial direction, in addition to a 1D FFT in the z-direction, where the Hankel transform of a function $f(\rho, z)e^{im\varphi}$ is given by [153]

$$\tilde{f}(k_\rho, k_\varphi, z) = 2\pi i^{-m} e^{imk_\varphi} \int_0^\infty f(\rho, z) J_m(k_\rho \rho)\rho\, d\rho, \tag{5.5}$$

where $J_m(x)$ is the Bessel function of order m. The full momentum-space representation of

$f(\rho,z)e^{im\varphi}$ is then given by $\tilde{f}(\mathbf{k}) = \mathcal{F}_z[\tilde{f}(k_\rho,k_\varphi,z)]$, where $\mathcal{F}_z$ is the Fourier transform operator in the z-direction. The inverse Hankel transform is defined analogously to the direct transform in Eq. (5.5).

Interestingly, just as the FFT algorithm computes discretized Fourier transforms with the time complexity $N\ln N$ (where here there are N grid points used to define our function), there exist Fast Hankel transforms (FHTs) and Discrete Hankel transforms (DHTs), which operate with time complexities $N\ln N$ and N^2, respectively. FHTs have been found to be numerically unstable with regards to error propagation, while DHTs have been found to be very numerically stable [102]. Thus, we employ the DHT in the radial (ρ) direction and the FFT in the axial (z) direction, resulting in an effectively 2D problem where the angular dependence is handled simply by choosing the Bessel function of the proper order. We describe the DHT algorithm in Appendix D.

As forementioned, we calculate $\phi_0(\mathbf{x})$ by enforcing that it minimize the Gross-Pitaevskii energy functional (5.3). Such a calculation was first performed for a BEC with purely contact interactions by the imaginary time propagation method [154]. Using this method, one evolves the time-dependent GPE in imaginary time, that is, $t \to it$, which turns the GPE into a dissipative equation. Thus, the norm of the condensate wave function is not preserved and one must renormalize the condensate wave function throughout the numerical process of imaginary time evolution. Convergence of the condensate wave function in imaginary time by such propagation corresponds to the condensate wave function minimizing the GP energy functional. We employed this method using the 4^{th} order Runge-Kutta algorithm[1] and found that, while robust, it was very computationally time-intensive. Instead, in this work we solve for the condensate wave function by direct minimization of the energy functional (5.3) using the conjugate gradients algorithm [155], which takes typically only a few seconds on a PC, whereas the imaginary-time evolution method takes on the order of tens of minutes, by comparison. We describe the conjugate gradients algorithm in appendix E, but note here that the DHT of a function with angular dependence $e^{ik\varphi}$ requires defining the radial grid points ρ_i in terms of the zeros of the k^{th} order Bessel function, which we refer to

---

[1] Available in MATLAB through the function `ode45`

from here on as grid of order k. Additionally, using such a radial grid allows for the application of a highly accurate quadrature-like numerical integration, which we discuss in appendix D.

Once the ground state condensate wave function is obtained, we use it in solving the BdG equations (3.34). In the trapped, cylindrically symmetric system, the Bogoliubov quasiparticles can be characterized by a definite vorticity m, just as the condensate is characterized by a vorticity s. Thus, we write

$$\begin{aligned} u_i(\mathbf{x}) &\rightarrow u_i(\rho, z)e^{im\varphi} \\ v_i^\star(\mathbf{x}) &\rightarrow v_i^\star(\rho, z)e^{-im\varphi}. \end{aligned} \tag{5.6}$$

Now, we can calculate a complete set of quasiparticle excitations (up to some energy cutoff determined by the numeric grid resolution) by specifying a set of quantum numbers m and solving the BdG equations for each of them. Written explicitly, and in the dimensionless units, these coupled BdG equations read

$$\begin{aligned} \omega_i u_i(\mathbf{x}) = \Bigg[&-\frac{1}{2}\nabla^2 + \frac{1}{2}\left(\rho^2 + \lambda^2 z^2\right) - \mu + (N-1)g|\phi_0(\mathbf{x})|^2 \\ &+ (N-1)g_d \int d\mathbf{x}' \underbrace{|\phi_0(\mathbf{x}')|^2 \frac{1 - 3\cos^2\theta_{\mathbf{x}-\mathbf{x}'}}{|\mathbf{x}-\mathbf{x}'|^3}}_{\text{a}} \Bigg] u_i(\mathbf{x}) \\ &+ (N-1)g|\phi_0(\mathbf{x})|^2 u_i(\mathbf{x}) + (N-1)g_d \int d\mathbf{x}' \underbrace{\phi_0^\star(\mathbf{x}') u_i(\mathbf{x}') \frac{1 - 3\cos^2\theta_{\mathbf{x}-\mathbf{x}'}}{|\mathbf{x}-\mathbf{x}'|^3}}_{\text{b}} \phi_0(\mathbf{x}) \\ &+ (N-1)g|\phi_0(\mathbf{x})|^2 v_i(\mathbf{x}) + (N-1)g_d \int d\mathbf{x}' \underbrace{v_i(\mathbf{x}') \phi_0(\mathbf{x}') \frac{1 - 3\cos^2\theta_{\mathbf{x}-\mathbf{x}'}}{|\mathbf{x}-\mathbf{x}'|^3}}_{\text{c}} \phi_0(\mathbf{x}), \end{aligned} \tag{5.7}$$

$$\begin{aligned}
-\omega_i v_i(\mathbf{x}) = \Bigg[&-\frac{1}{2}\nabla^2 + \frac{1}{2}\left(\rho^2 + \lambda^2 z^2\right) - \mu + (N-1)g|\phi_0(\mathbf{x})|^2 \\
&+ (N-1)g_d \int d\mathbf{x}' \, \underbrace{|\phi_0(\mathbf{x}')|^2 \frac{1 - 3\cos^2\theta_{\mathbf{x}-\mathbf{x}'}}{|\mathbf{x}-\mathbf{x}'|^3}}_{\text{d}} \Bigg] v_i(\mathbf{x}) \\
&+ (N-1)g|\phi_0(\mathbf{x})|^2 v_i(\mathbf{x}) + (N-1)g_d \int d\mathbf{x}' \, \underbrace{\phi_0(\mathbf{x}') v_i(\mathbf{x}') \frac{1 - 3\cos^2\theta_{\mathbf{x}-\mathbf{x}'}}{|\mathbf{x}-\mathbf{x}'|^3}}_{\text{e}} \, \phi_0^\star(\mathbf{x}) \\
&+ (N-1)g|\phi_0(\mathbf{x})|^2 u_i(\mathbf{x}) + (N-1)g_d \int d\mathbf{x}' \, \underbrace{u_i(\mathbf{x}') \phi_0^\star(\mathbf{x}') \frac{1 - 3\cos^2\theta_{\mathbf{x}-\mathbf{x}'}}{|\mathbf{x}-\mathbf{x}'|^3}}_{\text{f}} \, \phi_0^\star(\mathbf{x}). \qquad (5.8)
\end{aligned}$$

For a stationary condensate with $s = 0$, the only relevant phase is the global phase which, under $U(1)$ symmetry, is arbitrary. Thus, as we discussed in section 3.2, Eqs. (5.7) and (5.8) can be reduced to the form (3.34) in this case. For condensates with $s \neq 1$, however, no such reduction is possible and the BdG equations must be solved as written.

The right-hand sides of Eqs. (5.7) and (5.8) take the form of a non-sparse functional matrix operation that, for a grid of size $N_\rho \times N_z$, has $(2 \times N_\rho \times N_z)^2$ elements. To solve these equations, we employ the iterative Arnoldi diagonalization algorithm.[2] In this process, all functions must be sampled on the same spatial grid. However, because the integrands in the ddi terms have, in general, different angular dependence, interpolation to and from different radial grids must be performed in the diagonalization process. We develop a straightforward algorithm for such interpolation, which we describe in appendix F. In Eqs. (5.7) and (5.8), the ddi terms are labeled and the corresponding grid orders that are necessary to calculate the corresponding Hankel transforms are given in table 5.1. Note that, for $s = 0$, all exchange terms can be calculated on a grid of order m. In practice, we interpolate all quantities onto a grid of order m when solving the BdG equations, which is the order that is necessary to calculate the kinetic energy operations. The same technique is used when minimizing the energy functional (5.3), where all terms in are sampled on a grid of order s.

In addition to specifying quantum numbers for the projection of angular momentum of the condensate and its elementary quasiparticle excitations, we can characterize these modes as being

---

[2] Available in MATLAB through the functions `eigs`

Term	Order k ($e^{ik\varphi}$)
a	0
b	$m-s$
c	$m+s$
d	0
e	$m+s$
f	$m-s$

Table 5.1: Orders of Hankel transforms necessary to calculate the dipole-dipole interaction terms in the cylindrically symmetric Bogoliubov de Gennes equations (5.7) and (5.8).

either even or odd with respect to reflection on the $z = 0$ plane. While we find that, for all s considered here, the condensate mode possesses even symmetry (odd symmetry is always higher in energy), we can use odd and even FFT algorithms (fast sine and cosine transforms, respectively) when computing the kinetic energy and ddi energy to enforce that the excitation modes possess such symmetry. However, we find that the even excitations are always the relevant excitations to consider with regards to dynamic stability of the condensate.

5.1.1 Modified Momentum-Space Dipole-Dipole Interaction

By handling the ddi terms in momentum-space, effective "image" condensates are produced by the periodic nature of the discrete transform algorithms. One can easily see this effect by considering the basic discrete Fourier transform of a function f_n defined on a grid with N evenly spaced points indexed by $n = 1, 2, \ldots, N$,

$$\tilde{f}_m = \sum_{n=0}^{N-1} f_n e^{-2\pi i m \frac{n}{N}}. \tag{5.9}$$

It is clear from this expression that taking $n \to n + N$, equivalent to shifting the function by a grid length, leaves the transform unchanged. Thus, because the ddi is long-range, the system under consideration "feels" not only the local mean-field but also the ddi mean-fields from the unphysical image condensates.

We handle this problem by introducing a spatial cutoff to the ddi. For approximately spherical systems, the cutoff can be imposed by multiplying the real-space interaction by $\Theta(r - R)$, where

R is the radius of a sphere outside of which the ddi is set to zero and $\Theta(x)$ is the Heaviside step function of x [54]. In this case, the resulting momentum-space ddi has the analytic form [102]

$$\tilde{V}_d^R(\mathbf{k}) = \frac{4\pi}{3} d^2 \left(1 + 3\frac{\cos Rk}{R^2k^2} - 3\frac{\sin Rk}{R^3k^3}\right)\left(3\cos^2\theta_{\mathbf{k}} - 1\right). \tag{5.10}$$

For very oblate, or pancake-shaped systems, the spherical cutoff must be set by the radial size of the condensate. In this case, the axial extent of the grid must be very large to ensure there is no false periodicity in this direction. However, for these oblate systems, an axial cutoff can be imposed by multiplying the real-space interaction by $\Theta(|z| - Z)$, where Z is the cutoff length of the ddi in the z-direction. The resulting momentum-space ddi in this case has the form [102]

$$\tilde{V}_d^Z(\mathbf{k}) = \frac{4\pi}{3} d^2 \left(3\cos^2\theta_{\mathbf{k}} - 1\right) + 4\pi d^2 e^{-Zk_\rho}\left(\sin^2\theta_{\mathbf{k}}\cos Zk_z - \sin\theta_{\mathbf{k}}\cos\theta_{\mathbf{k}}\sin Zk_z\right). \tag{5.11}$$

To determine the cutoff R or Z, we consider a numeric grid in cylindrical coordinates of extent $[0, P]$ in the radial, or r-direction and $[-A, A]$ in the axial, or z-direction. Additionally, suppose that our condensate density is non-zero only for $r < r_0$ and $z < z_0$. To ensure that no *true* interactions are lost and all false interactions (from the image condensates) are eliminated, we require that $R > 2 \times \max[r_0, z_0]$ for the spherical cutoff and $Z > 2z_0$ for the axial cutoff. This also enforces that the extent of the grid be at least $A, P > 2R$ for the spherical case and $A > 2Z$ for the axial case. These rules were tested in [102], where an improvement by a factor of at least 10^{-2} in the relative error was shown in the calculation of the ddi energy over using the uncorrected ddi.

The spherical and axial cutoffs are particularly useful due to their analytic forms. A cylindrical cutoff may be used as well, though the momentum-space form of the interaction must be computed numerically in this case. In terms of the radial cutoff R and the axial cutoff Z in the cylindrical coordinates ρ and z, respectively, the momentum-space ddi takes the form [156]

$$\begin{aligned}\tilde{V}_d^C(\mathbf{k}) = {} & \frac{4\pi}{3} d^2 \left(3\cos^2\theta_k - 1\right) + 4\pi d^2 e^{-Zk_\rho}\left(sin^2\theta_{\mathbf{k}}\cos Zk_z - \sin\theta_{\mathbf{k}}\cos\theta_{\mathbf{k}}\sin Zk_z\right) \\ & - 4\pi d^2 \int_R^\infty \rho d\rho \int_0^Z dz \cos(k_z z) J_0(k_\rho \rho)\frac{\rho^2 - 2z^2}{(\rho^2 + z^2)^{\frac{5}{2}}},\end{aligned} \tag{5.12}$$

where $J_0(x)$ is the zeroth-order Bessel function. We employ such a cutoff for the calculations in chapter 8.

5.2 Rotationless ($s = 0$) Dipolar Bose-Einstein Condensate

The condensate wave function and the BdG equations were first calculated exactly (in the absence of an s-wave scattering length), in the way described in the previous section, in [102] and [30]. The key results therein are that i) for all aspect ratios, there exists a critical ddi strength beyond which the condensate becomes dynamically unstable; and ii) for certain ddi strengths and trap aspect ratios, the dipolar BEC exhibits biconcave structure where the region of maximum density exists not in the center of the trap where the trapping potential is minimum, but in a ring about the center of the trap, lying in the x-y plane. These features are shown in the structure/stability diagram in figure 5.1. The colored regions indicate dynamical stability, while the pink "islands" indicate the parameters for which biconcave structure is present. With $a_s = 0$, the dipolar BEC in the cylindrically symmetric trap is fully characterized by the trap aspect ratio λ and the dimensionless parameter D,

$$D = (N-1)\frac{Md^2}{\hbar^2 a_{\text{ho}}}. \tag{5.13}$$

An isodensity plot of a biconcave condensate at $\lambda = 8$ and $D = 35$ (showing a surface of equal density) is shown by the inset in figure 5.1. Because of its resemblance to the cellular structure, the biconcave dipolar BEC structure is sometimes referred to as a "red blood cell." While it may not be surprising that such density profiles exist in dipolar BECs, as the ddi is long-range and can force the dipoles to the edges of the trap (in the radial direction, in which the ddi is repulsive), it is quite surprising that these biconcave structures only occur in certain islands in the parameter space. We find that simulations of the ballistic expansion of a biconcave dipolar BEC show that its pronounced structure is not preserved in time-of-flight (TOF); it is however observable in other indirect ways, which we discuss in chapter 6. As an example of this, we consider a dipolar BEC with $D = 25$ in a trap with aspect ratio $\lambda = 7$, where biconcave structure is present. We perform direct numeric simulations of the time-dependent GPE (details in chapter 6), and see the biconcave feature completely vanish after the condensate is expanded in free space. Images from this simulation are shown in figure 5.2.

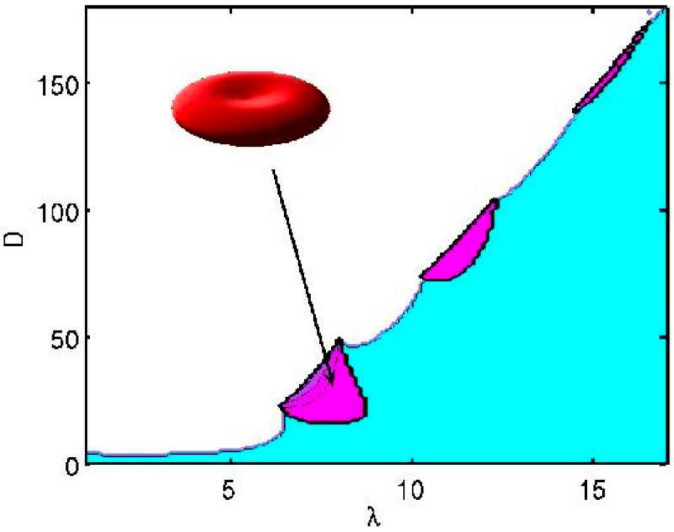

Figure 5.1: Structure/stability diagram of a dipolar BEC in a cylindrically symmetric harmonic trap as a function of trap aspect ratio λ and ddi strength D. All shaded areas are dynamically stable, while all white (unshaded areas) are dynamically unstable. The pink "island" regions show where dipolar BECs with biconcave structure are predicted to exist. An isodensity plot of a biconcave condensate is shown by the inset. Figure reprinted with permission from [30].

Regarding stability, it is also interesting to note that the biconcave islands form discontinuous cusps along the stability threshold. In fact, there exists a double instability near $\lambda = 7$, where the dipolar BEC goes unstable with increasing D, then restabilizes in the biconcave region. On a larger scale, the nature of the dipolar BEC instability changes drastically from prolate and spherical traps to oblate, pancake-shaped traps. For the former, the instability is induced by the quadruple surface mode going soft as the ddi becomes sufficiently strong so that its attractive component overwhelms all other energies in the system. The softening of this quadruple mode can be interpreted as the dipolar BEC elongating in the direction of the dipole polarization, as this configuration minimizes the energy of the ddi. Such an instability is shown schematically in figure 5.3(a), where the solid line represents a cross-section of the spherical trap in the x-z plane and the shaded region represents the condensate density. Such instability is analogous to the phonon instability in the homogeneous dipolar BEC, as discussed in section 4.1. Thus, collapse is *global* for these more prolate and spherical geometries. However, in this case it is interesting to note that while the contribution to

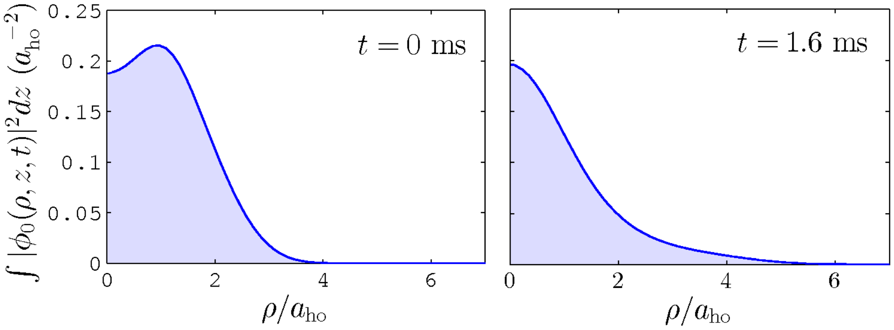

Figure 5.2: Integrated axial density of a dipolar BEC in a trap with aspect ratio $\lambda = 7$ and ddi strength $D = 25$. For the sake of example, we consider $\omega_z = 2\pi \times 100\,\text{Hz}$. The left panel shows the trapped stationary condensate with biconcave structure, and the right panel shows the condensate after it has expand in free space after 1.6 ms. The biconcave structure has clearly vanished in the ballistic expansion.

the full energy per particle from the ddi may be negative, the presence of the trap in the z-direction stabilizes the gas at small but finite D.

For pancake-shaped traps, the instability is induced by a completely different type of excitation. In this case, the instability corresponds to the softening of discrete *quasiparticle* excitations that have nodal structure on the same length scale as the free roton in the homogeneous quasi-2D dipolar BEC, with wavelengths $\sim 2\pi a_z$, where $a_z = \sqrt{\hbar/M\omega_z}$ is the axial harmonic oscillator length. Indeed, while the dipolar BEC is significantly more stabilized in pancake-shaped traps, instability still occurs for sufficiently large ddi strength, just as in the quasi-2D geometry, due to the roton mechanism. This discrete roton instability can be thought of in the following way. While the tendency for the condensate to elongate in the direction of polarization is still present in oblate traps, the strong trapping in the direction of polarization prevents such behavior. Instead, this elongation occurs *locally*, as is shown schematically in figure 5.3(c), on a length scale governed by the axial harmonic oscillator length, and in turn by the roton wavelength.

As an example of this discrete roton instability, we plot the $m = 0$ excitation spectrum of an $s = 0$ dipolar BEC in a trap with aspect ratio $\lambda = 17$ (where no biconcave structure is present at the stability threshold) in figure 5.4(a). Here, one sees a relatively high-energy mode near $D = 0$ that decreases in energy as D is increased and, at the stability threshold, softens and develops a

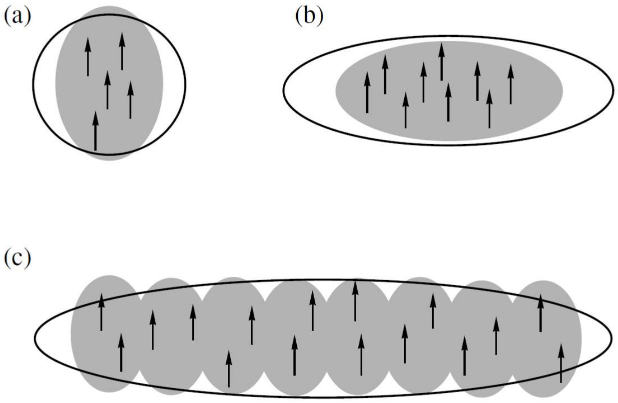

Figure 5.3: A schematic representation of the collapse of a dipolar BEC in various trap geometries. In each case, the solid black line represents the a trap isosurface, the grey shaded region represents the condensate density and the black arrows represent the dipolar polarization. In (a), the instability is due to ddi attraction as the condensate extends to a more prolate shape. In (b), the same collapse mechanism occurs, though higher densities are achievable with tighter axial confinement. In (c), or very oblate traps, the instability is due to *local* density fluctuations brought on by the softening of a roton-like mode. Figure courtesy of John Bohn.

non-zero imaginary excitation frequency as it becomes degenerate with its corresponding "negative norm" mode. In this figure, the grey region ($\omega < 0$) corresponds to the negative norm modes that, for the rotationless dipolar BEC, have energy eigenvalues that are equal and opposite of the positive-norm modes. As discussed in section 3.3, it is the degeneracy of the positive-norm and the negative-norm modes that ultimately results in the imaginary BdG energy eigenvalues, and thus the dynamic instability. Because the symmetry discussed in section 3.3 holds for the rotationless condensate, the negative norm and the positive norm modes always have equal and opposite energy eigenvalues, and can thus only become degenerate at $\omega = 0$.

We plot the radial profile of the discrete $m = 0$ roton mode near the instability threshold, marked by a red circle in figure 5.4(a), in figure 5.4(b). Here, we see clear radial oscillations with a wavelength $\sim 1.5a_{\text{ho}}$. For a trap with aspect ratio λ, the radial harmonic oscillator length can be written in terms of the axial harmonic oscillator length as $a_{\text{ho}} = a_\rho = \sqrt{\lambda}a_z$, so the discrete roton wavelength is $\sim 1.5\sqrt{17}a_z \simeq 2\pi a_z$, which is precisely the roton wavelength discussed in section 4.2. In figure 5.4(a), one also sees a mode with $\omega = 0$ for all D. This is the Goldstone mode, which is an

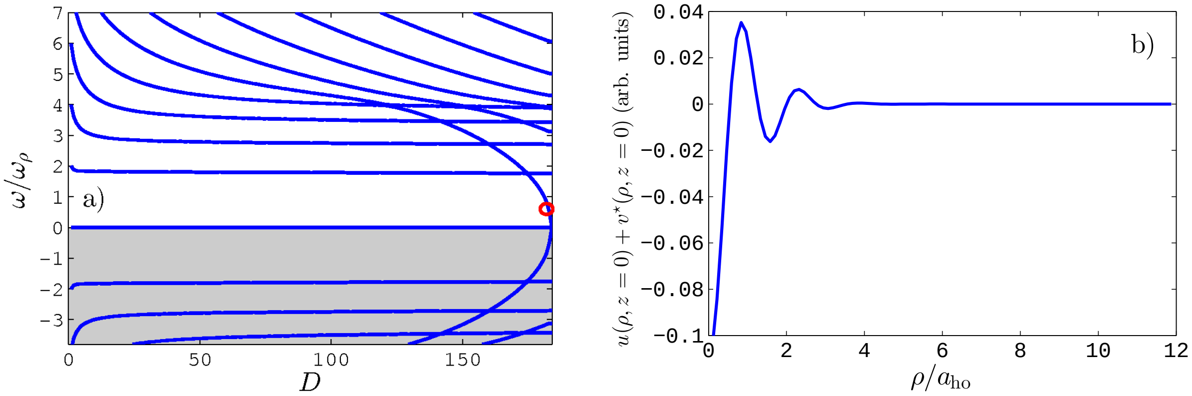

Figure 5.4: a) The real part of the Bogoliubov de Gennes spectrum of the rotationless ($s = 0$) dipolar BEC in an oblate trap with aspect ratio $\lambda = 17$. The grey region marks $\omega < 0$, where the modes have negative norm. The discrete roton is seen as the mode that decreases in energy until it softens at $D \simeq 181.2$. b) The radial profile of the discrete roton mode marked by the red circle in (a). Here, the wavelength is seen to be approximately $2\pi a_z$, which is the wavelength of the roton in the quasi-2D dipolar BEC.

unphysical, long-wavelength excitation corresponding to the condensate, and appears necessarily due to the $U(1)$ symmetry of the BEC [97, 98]. Because of its relationship to the condensate, the Goldstone mode always appears in the $m = 0$ spectrum. The radial breathing mode is also seen in this spectrum as the positive energy mode that has energy $\omega/\omega_\rho = 2$ at $D = 0$, and maintains approximately this energy for all stable values of D. Not visible in this figure is the corresponding axial breathing mode with corresponding energy $\omega = \omega_z$ at $D = 0$. Though we do not show the $m = 1$ spectrum here, the so-called Kohn mode can be seen in the $m = 1$ spectrum, corresponding to the "sloshing" of the center of mass of the condensate [157]. Thus, the Kohn mode frequency does not depend on interaction strength and has $\omega/\omega_\rho = 1$ for all D.

Recall our result from the discussion of the quasi-2D dipolar BEC, that the roton instability occurs at some critical ddi strength or, equivalently in the mean-field description, at some critical density. Thus, we expect the roton instability to originate in the region of maximum density. For dipolar BECs without biconcave structure, such as the one in the trap with $\lambda = 17$ discussed previously, this region occurs at the origin $r = 0$, and the purely radial ($m = 0$) roton is responsible for the instability. In biconcave dipolar BECs, however, the region of maximum density exists in a ring with a circumference that is typically on the order of many roton wavelengths. Indeed, the relevant mode for characterizing the instability of a biconcave dipolar BEC is a discrete *angular* roton, with $m \geq 2$ [30]. In chapter 6 we show that such angular instability translates into angular collapse in the real-time dynamics of the condensate, which in turn provides a clear experimental signature of the biconcave structure. There, we also go into more detail regarding the angular roton in the biconcave dipolar BEC.

At this point, it is instructive to compare the dipolar system to a BEC with attractive contact interactions. Consider a trapped, rotationless BEC with attractive contact interactions ($a_s < 0$) and no ddi. For such a system, there always exists a critical particle number above which the condensate goes unstable, with preference to collapse in the region of maximum density at the center of the trap [127, 128, 158]. Indeed, in the attractive, non-dipolar BEC, the instability has this global character in prolate, spherical and oblate trapping geometries. This is in stark contrast with the dipolar BEC, where the instability exhibits local character in the latter case. However, stirring the attractive condensate into a vortex state serves to stabilize the system by introducing a kinetic energy component due to angular momentum that offsets the interparticle attraction. So, in general, the vortex will sustain a larger number of particles than the non-vortex state, and is more stable.

5.3 Singly-Quantized Vortex

Now, consider the effects of the ddi on a condensate with a single vortex core, or a dipolar BEC with $s = 1$ [159]. The conditions for the generation of such a dipolar BEC vortex state are studied in Ref. [160]. In the presence of a singly-quantized vortex, the region of high density is forced away from the center of the trap due to the zero-density of the vortex core. Depending on the aspect ratio λ of the trap, this either serves to stabilize (for smaller λ) or destabilize (for larger λ) the dipolar BEC. For smaller λ, the vortex core simply breaks the prolate shape of the condensate along the direction of polarization, eliminating much of the attractive dipole-dipole interaction in this direction and thus increasing the energy due to interactions. Conversely, for larger λ the vortex increases the density in the periphery of the core and thus encourages local collapse. Just as the roton wavelength is set by the the confinement length in the direction of polarization (z), the local density fluctuations occur at the same length scale regardless of the trap geometry. Widening the trap radially while keeping the axial trapping frequency fixed makes more room for regions of density fluctuations instead of enlarging the existing regions. This marks a clear and important distinction between the dipole-dipole and contact interactions. An additional consideration relevant to the stability of dipolar BECs with a vortex are the excitations of the vortex core itself [161]. As we will see below, these excitations are unlikely to play a role in destabilizing the vortex in oblate, or even mildly prolate, traps.

The solutions of the BdG equations characterize the stability of $s = 1$ dipolar BECs. The global thermodynamical instability of $s = 1$ dipolar BECs is seen as a negative norm BdG mode with $m = 1$ and positive energy for all trap aspect ratios and dipolar interaction strengths. This mode corresponds to the system's decay into the energetically favored rotationless ground state, just as for BECs with purely contact interactions. The component of the mode with angular dependence $e^{-i(m-s)\varphi} = 1$ is in this case rotationless, capturing the symmetry of the $s = 0$ ground state. Since this mode populates the core of the vortex, it is referred to as a core mode. However, at ultracold temperatures, thermodynamical stability is less relevant in characterizing the stability of a condensate since there needs to be some thermal processes acting on the system to dissipitavely drive it into a lower energy state. We therefore disregard thermodynamical instability in the following.

The dynamically stable region where all of the BdG modes for the dipolar BEC with a singly-quantized vortex have purely real energy eigenvalues is shown by the colored portion of Figure 5.5. The dashed line in this figure marks, for a given λ, the D below which we find a local minimum of the GP energy functional by using our reduced 2D algorithm. We find that, for all λ, the D above which the GP energy functional has no minimum corresponding to an $s = 1$ ground state and the D at which the BdG spectrum begins to possess imaginary energy, denoted D_{crit}, are never equal. Indeed, dynamical instability occurs for values of D at which the GPE has a solution.

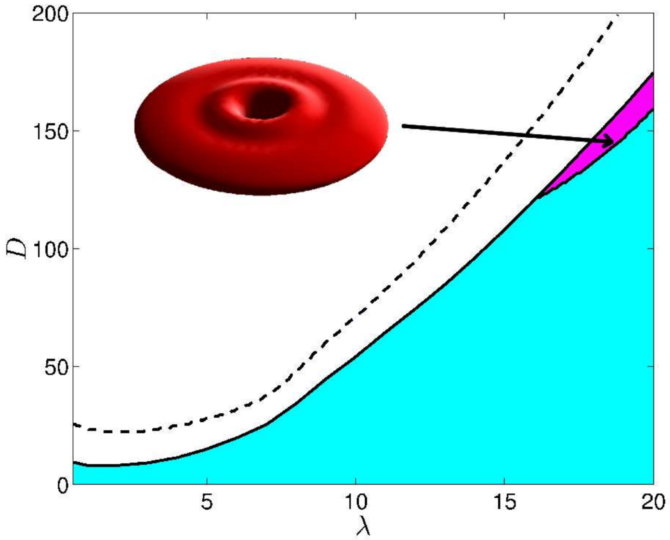

Figure 5.5: The black dashed line marks the maximum dipole strength D, for a given trap aspect ratio λ, above which the cylindrically symmetric Gross-Pitaevskii energy functional has no minimum corresponding to the $s = 1$ dipolar BEC. The solid line marks a more restrictive stability line, determined by the onset of dynamical instability, signaled by the emergence of an imaginary energy in an excitation mode. The pink (darker) region represents where radial oscillations with local minima are observed on dynamically stable states. The inset is an isodensity surface plot of an $s = 1$ dipolar BEC at the point in parameter space indicated by the arrow. The ripples in the density are explained in section 5.5.

This is because in the 2D minimization of the vortex-state energy, perturbations that break the $s = 1$ symmetry are not allowed, and are only examined later with the BdG equations. Using a fully 3D calculation, we check the accuracy of D_{crit} for various trap aspect ratios by time evolving the condensate wave function with an initial random perturbation. The D_{crit} that we calculate using the 3D algorithm, corresponding to the D at which we observe collapse under time evolution, agrees with the D_{crit} that we calculate by finding imaginary energy eigenvalues in the BdG spectrum using our 2D algorithm. The pink (darker) region in figure 5.5 represents the region where we find dynamically stable $s = 1$ ground states having radial ripples with local minima, as illustrated by the inset. The origin of such a feature is explained in detail in section 5.5.

Similar to the rotationless case, we find that $s = 1$ dipolar BECs possess imaginary energy eigenvalues in their BdG spectrum only when two modes of opposite norm are degenerate with each

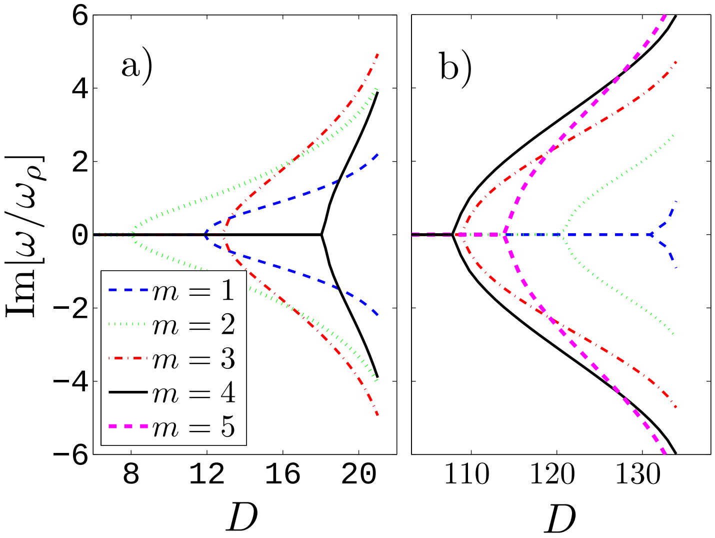

Figure 5.6: a) The imaginary part of the BdG excitation spectrum for a number of m values for a dipolar BEC in a trap with aspect ratio a) $\lambda = 2$ and b) $\lambda = 15$. For $\lambda = 2$, the $m = 2$ modes clearly develop imaginary energy eigenvalues at a D smaller than the other modes, defining $D_{\text{crit}} \simeq 8$ for this aspect ratio. For $\lambda = 15$, the $m = 4$ modes develop imaginary energy at a D smaller than the other modes, defining $D_{\text{crit}} \simeq 108$ for this aspect ratio.

other. At all aspect ratios, we observe, for some finite value of D, two modes with opposite norm approach and then go degenerate with each other at D_{crit}. At the point of degeneracy, the modes develop equal and opposite imaginary energies, signifying dynamical instability. If two modes that have the same norm approach each other, they undergo an avoided crossing instead of becoming degenerate. However, because we have $s = 1$ in this case, the energies of the positive norm and negative norm modes are not equal and opposite, as is the case for $s = 0$.

For a BEC with pure contact interactions in the $s = 1$ vortex state, the mode that defines the onset of dynamical instability is independent of the trap aspect ratio λ. Positive contact interactions ensure dynamical stability while negative contact interactions (for $\lambda \gtrsim 0.3$) bring about a dynamical instability due to an $m = 2$ mode [162]. This holds true for these systems no matter how oblate the trap. The case for a dipolar BEC, however, is quite different. Figure 5.6 illustrates the imaginary parts of the BdG spectrum for $m = 1 - 5$ for dipolar BECs in traps with aspect ratios $\lambda = 2$ and $\lambda = 15$. Where these imaginary energies are zero, from $D = 0$ to D_{crit}, the condensates are

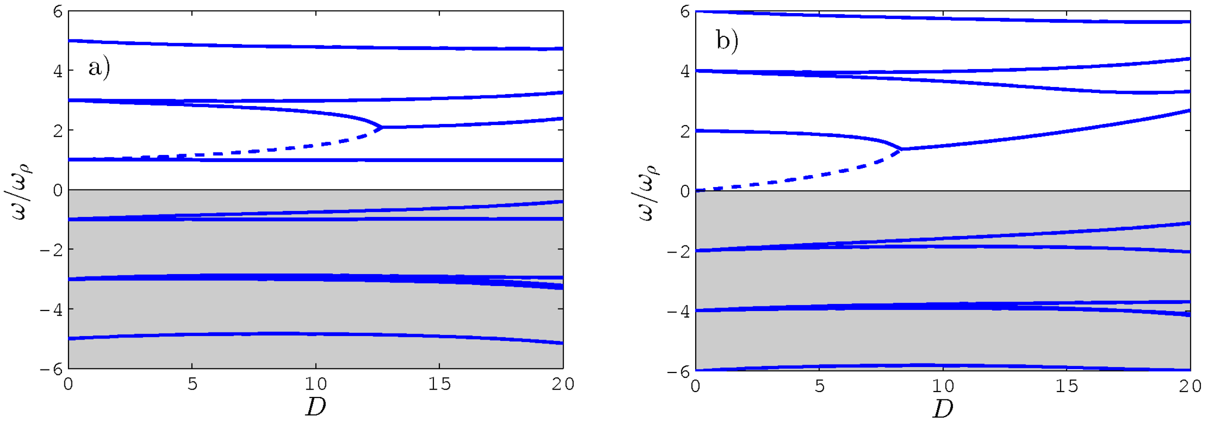

Figure 5.7: Real part of the BdG spectrum for (a) $m = 1$ and (b) $m = 2$ modes of a purely dipolar BEC in a trap with aspect ratio $\lambda = 2$. In both cases, a negative norm mode with positive energy, shown by a dashed line, goes degenerate with a positive norm mode at D_{crit}, above which the modes develop non-zero imaginary parts and the condensate is dynamically unstable. For the $m = 1$ case in (a), the negative norm mode has positive, non-zero energy for all D, signifying global thermodynamic instability of the $s = 1$ state. The Kohn mode is seen as the mode with $\omega/\omega_\rho = 1$ for all D.

dynamically stable. Notice that for $\lambda = 2$, an $m = 2$ mode develops non-zero imaginary energy at a D well below the other modes, defining D_{crit} for this aspect ratio. However, an $m = 4$ mode serves to define D_{crit} for $\lambda = 15$.

In figure 5.7, we show the real parts of the BdG spectrum for the $m = 1$ (a) and $m = 2$ (b) modes in a trap with aspect ratio $\lambda = 2$. In both cases, we see a negative norm mode (dashed line) go degenerate with a positive norm mode at D_{crit}, exactly where these modes develop non-zero imaginary energy eigenvalues. For the $m = 1$ case in figure 5.7(a), the negative norm mode has positive, non-zero energy for all D, signifying the global thermodynamic instability of the $s = 1$ state. Additionally, the Kohn mode is seen in this spectrum as the mode with $\omega/\omega_\rho = 1$ for all D. As forementioned, this Kohn mode corresponds to a "sloshing" of the center of mass of the condensate.

Unlike BECs with contact interactions, modes with different m quantum numbers serve to define D_{crit} at different aspect ratios for dipolar BECs. For moderate trap aspect ratios (such as $\lambda = 2$), an $m = 2$ mode defines D_{crit} for the dipolar BEC, similar to the case for contact interactions. However, as the trap aspect ratio is increased to more oblate shapes, modes with larger m quantum numbers develop imaginary energy eigenvalues at smaller values of D than the $m = 2$ mode. Figure 5.8(a) illustrates this by plotting the *differences* between the D's at which the BdG modes with different angular symmetries first develop imaginary energy eigenvalues, and D_{crit}, as a function of λ. Thus, for a given λ the lowest curve identifies the symmetry of the unstable mode. For $6 \lesssim \lambda \lesssim 12$, an $m = 3$ mode defines D_{crit} while for larger aspect ratios, an $m = 4$ mode defines D_{crit}. Although it is not shown here, we find that at even larger aspect ratios the vortex decays into still higher m-modes.

The relevance of the m-dependent dynamical instability is that the ddi leads a BEC to instability locally and at a fixed length scale, the wavelength of which is determined by the axial harmonic oscillator length. We find that, at the onset of imaginary energy, these modes have radial nodal spacings very similar to that of the roton in the rotationless dipolar BEC, namely $\lambda/2 \sim \pi a_z$. The angular dependence of these modes behaves in the same way. Increasing the trap aspect ratio λ decreases the ratio a_z/a_{ho}, so more radial nodes, fixed by a_z, can fit into the condensate for larger λ. In the same way, more angular nodes can fit into the condensate, therefore bringing about dynamical instability by modes with larger m quantum number, and hence more angular nodes.

All of the previously discussed BdG modes that we identify as being responsible for dynamical instability are axially symmetric and nodeless in z. Modes that break this axial symmetry can correspond to vortex excitations, where the vortex core itself may tilt or bend, and have been termed "kelvon" modes. Ref. [161] reports that, for a singly-quantized vortex in a dipolar BEC that is otherwise spatially homogeneous, the condensate is dynamically unstable to a kelvon mode when an external periodic potential is applied along the direction of the vortex. We find that, in a harmonically trapped dipolar BEC, a mode with a single node at $z = 0$ determines D_{crit} for $\lambda \lesssim 0.28$. Modes of this type might therefore correspond to a kelvon-instability in prolate traps, but we leave these considerations for future work.

As was done in Ref. [162] for self-attractive BECs in the singly-quantized vortex state, we check these BdG results for the dynamic instability by performing fully three-dimensional time-

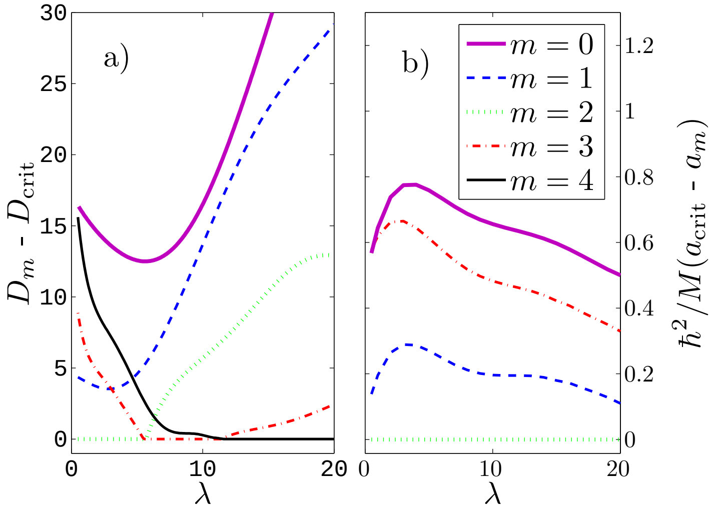

Figure 5.8: a) The difference between the D at which BdG modes with different m quantum numbers first develop imaginary energy eigenvalues and D_{crit}, the smallest D at which any mode develops an imaginary energy eigenvalue. Modes with larger m serve to define D_{crit} for more oblate traps. b) The same, but for negative contact interactions instead of dipole-dipole interactions. An $m = 2$ BdG mode is always the first to develop an imaginary energy eigenvalue for this case, except for trap aspect ratios $\lambda \lesssim 0.3$, for which an $m = 1$ mode plays this role.

dependent simulations of an $s = 1$ dipolar BEC where D is chosen to be just above D_{crit}, enabling us to go beyond the small deviations from the stationary vortex state and see the actual process of collapse. Initializing the simulations with random noise, we observe collapse, at all aspect ratios, with an angular symmetry corresponding to the m quantum number of the mode that first develops an imaginary energy eigenvalue. Our methods for such time-dependent simulation are discussed in chapter 6.

5.4 Doubly-Quantized Vortex

The dynamical instability of condensates with doubly-quantized vortices and purely contact interactions has been studied extensively [163, 164, 165, 105]. These studies report windows of positive scattering length where the BECs are dynamically unstable to an $m = 2$ BdG core mode, as well as dynamical instability for all values of negative scattering length due to an $m = 2$ mode. Knowing that the mean-field in a dipolar BEC can be engineered to be more attractive or repulsive for smaller or larger trap aspect ratios, respectively, we investigate the presence of these features in $s = 2$ dipolar BECs. When the harmonic trap is more spherical, the dipoles are free to stack vertically, resulting in an attractive interaction in this direction. However, in pancake shaped traps the dipoles create a more repulsive mean-field. Thus, for larger trap aspect ratios dipolar BECs are more self-repulsive than for smaller aspect ratios, mimicking the mean-field of condensates with repulsive contact interactions. As an example, we calculate the contribution of the dipolar mean-field to the energy of a dipolar BEC in a trap with aspect ratio $\lambda = 2$ and with $\lambda = 15$ for a fixed $D = 10$. In the $\lambda = 15$ trap, we find that this contribution is about five times larger than in the $\lambda = 2$ trap.

Indeed, for a dipolar BEC in a trap with aspect ratio $\lambda = 2$ we find that there exists an $m = 2$ mode with a complex energy eigenvalue for all values of D. However, for $\lambda = 15$ we find that there are windows in D where an $m = 2$ BdG mode has a complex energy eigenvalue, while this same mode has purely real energy outside of these windows, as illustrated in Figure 5.9. For trap aspect ratios $\lambda \lesssim 7.5$, there are no windows of dynamical stability and the condensate is dynamically unstable for all D. However, windows of dynamical stability appear for aspect ratios $\lambda \gtrsim 7.5$ and continue for larger λ. As is reported in Ref. [105], we find that there is an $m = 2$ core mode with negative norm and positive real energy that increases monotonically as it goes successively degenerate with positive norm modes as D is increased to create the windows of dynamical instability. This mode represents the $s = 2$ condensate's instability to splitting into a condensate with two singly quantized vortices. The core mode is thermodynamically unstable for all values of D and is only dynamically unstable for the windows shown in Figure 5.9.

5.5 "Perturbed" Dipolar Bose-Einstein Condensate

Here, we set out to explain the origin of the radial "ripples" seen in the density of the $s = 1$ dipolar BEC, as shown by the inset in figure 5.5. It has previously been suggested that boundaries in superfluid ^{4}He, including vortex cores, should give rise to radial density oscillations whose length scale is characteristic of the roton wavelength [166, 167, 168]. More recently, calculations

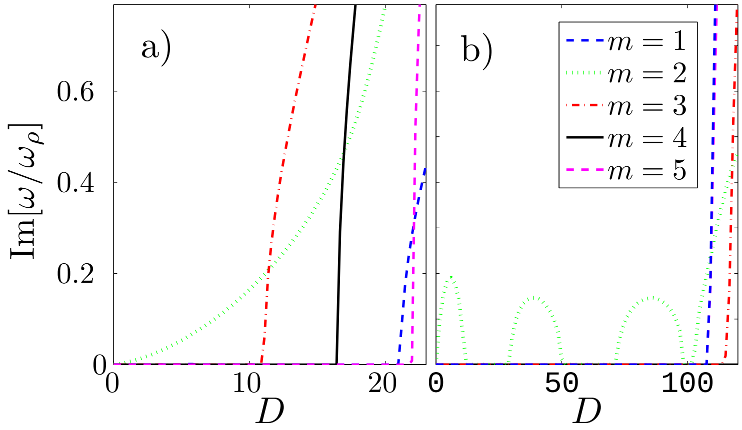

Figure 5.9: The positive imaginary part of the energy eigenvalues for a doubly quantized ($s = 2$) dipolar BEC in a trap with aspect ratio a) $\lambda = 2$ and b) $\lambda = 15$. For $\lambda = 2$, an $m = 2$ mode possesses imaginary energy for all values of D, signifying a dynamical instability for all D. However, for $\lambda = 15$ there are windows of dynamical stability as the $m = 2$ mode alternates having and not having imaginary energy for different values of D, as is the case for a purely repulsive $s = 2$ BEC.

of vortex states in a dipolar BEC in a highly oblate trap with $\lambda \sim 100$ have exhibited similar radial structures [159], raising the question of the relation between these structures and rotons in this system (progress has also been made in the understanding of the vortex state in a dipolar BEC in the Thomas-Fermi regime. However, in this regime the vortex does not exhibit a radial ripple [169, 160]).

We first note that the radial structure of the $s = 1$ vortex will be the same as that of a rotationless BEC in a trap with a central potential representing the centrifugal force. Indeed, by inserting the vortex form (5.2) into the GPE (5.4), one obtains

$$\mu\psi(\rho,z) = \left(-\frac{1}{2}\nabla_\rho^2 - \frac{1}{2}\frac{\partial^2}{\partial z^2} + \frac{s^2}{2\rho^2} + \frac{1}{2}(\rho^2+\lambda^2 z^2) \right. \\ \left. + (N-1)\int d\mathbf{x}'\psi^*(\rho',z')V(\mathbf{x}-\mathbf{x}')\psi(\rho',z')\right)\psi(\rho,z), \tag{5.14}$$

where $V(\mathbf{x}-\mathbf{x}')$ is the two-body interaction potential (3.61). Here, the centrifugal potential $s^2/2\rho^2$ is responsible for the vortex core (i.e., vanishing density at $\rho = 0$). It is natural to hypothesize that the appearance of the ripple in the vortex structure is related to a roton mode which is excited by the centrifugal potential of Eq. (5.14). This raises the interesting question, could such a ripple also be observed in the ground (non-vortex) state of a dipolar BEC perturbed by an external potential at the center of the trap? Such a perturbation may be realized experimentally by applying a blue-detuned laser along the trap axis. The origin of such a perturbing potential, being the AC Stark shift, is explained in section 2.3.1. We assume that the perturbing potential will take the form $U'(\mathbf{x}) = A\exp\left(-\rho^2/2\rho_0^2\right)$, where A is the height of the Gaussian and ρ_0 is its width. As a test case, consider a dipolar BEC of atomic ^{52}Cr that, as wee see in table 2.1, has a magnetic dipole moment $d = 6\mu_{\mathrm{B}}$. Additionally, ^{52}Cr has an optical dipole transition of 427.6 nm from its $^7S_3$ ground state to its $^7P_3$ excited state [170]. A blue-detuned laser around this transition could be used to create a repulsive potential with no significant absorption and with a minimal spatial extent of about a half-wavelength, 210 nm [61].

In sufficiently oblate traps, $s = 0$ dipolar BECs exhibit radial density oscillations in the presence of such Gaussian potentials. Fig. 5.10 illustrates the radial profiles of $s = 0$ dipolar BECs in a harmonic trap with aspect ratio $\lambda = 17$ and with a Gaussian potential having $A = \hbar\omega_\rho$ and $\rho_0 = 0.2\,a_{\mathrm{ho}}$. To give a concrete example, for ^{52}Cr atoms in a harmonic trap with radial frequency $\omega_\rho = 2\pi \times 100\,\mathrm{Hz}$, this translates to having a beam width of $\rho_0 = 280\,\mathrm{nm}$. In this trap, an interaction strength of $D = 181.2$, very near the point on instability for a $s = 0$ dipolar BEC in a trap with the above aspect ratio, may be achieved with $\sim 104,000$ ^{52}Cr atoms. It is seen that in this case even a small Gaussian perturbation makes a dramatic change in the dipolar BEC density profile. The radial oscillations near D_{crit} are much more pronounced than for a smaller dipolar BEC with $D = 100$. This is suggestive of the roton's presence in this structure, since the roton is expected to emerge with increasing dipolar interaction strength (i.e, increasing density for a fixed dipole moment) [28, 168, 102]. As was shown in the previous section, the roton mode undergoes a significant decrease in energy with increase in D until it achieves zero energy at D_{crit}, marking the point of dynamical instability for the $s = 0$ condensate. Beyond this D_{crit}, the roton energy is purely imaginary. Examining the nature of the roton itself within BdG theory tightens up its relationship with the observed structure discussed above. Additionally, we note that, for the ^{52}Cr BEC, the length scale of the radial oscillations is $\sim 2\mu$m. This is in comparison to the length scale

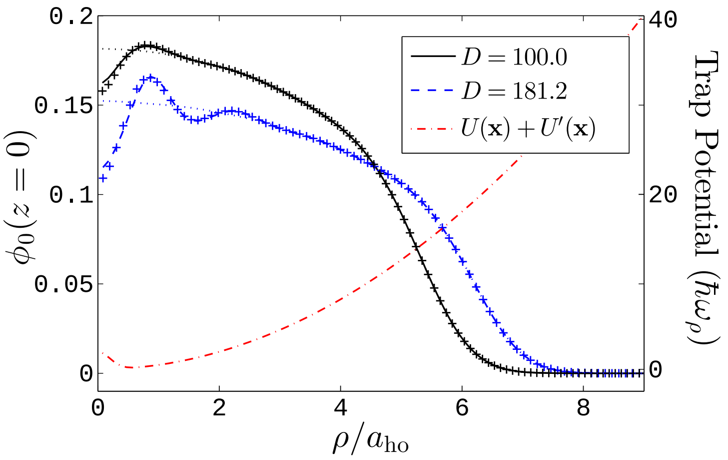

Figure 5.10: Radial profiles of the $k = 0$ dipolar BEC subject to the perturbing potential $U'(\mathbf{x}) = \hbar\omega_\rho \exp\left(-\rho^2/2(.2\,a_{\mathrm{ho}})^2\right)$ in a trap with aspect ratio $\lambda = 17$. The red dash-dotted line represents the trapping potential at $z = 0$, the black solid line represents the radial profile of the dipolar BEC at $D = 100$ and the blue dotted line represents the radial profile at $D = 181.2$, near the point of dynamic instability for the $k = 0$ dipolar BEC. The "+" signs represent the perturbation theory results and the thin dotted lines represent the unperturbed radial profiles at the corresponding dipole-dipole interaction strengths.

of the predicted ripple in the ^{4}He vortex, which is of the order of 1 Å, and has not been resolved experimentally up to now.

For an $s = 0$ condensate, we saw in section 3.2 that the coupled BdG equations reduce to two uncoupled equations, the first of which we write here as

$$\tilde{G}\tilde{F}|f\rangle = \omega^2|f\rangle, \tag{5.15}$$

where $\hat{G} = \hat{H}_{\mathrm{GP}} + \hat{C}$ and $\hat{F} = \hat{H}_{\mathrm{GP}} + \hat{C} + 2\hat{X}$, and we define $\tilde{G} = \hat{P}\hat{G}\hat{P}$ and $\tilde{F} = \hat{P}\hat{F}\hat{P}$, where $\hat{P} = \mathrm{I} - |\phi_0\rangle\langle\phi_0|$ is the projection operator into the space orthogonal to ground condensate wave function $|\phi_0\rangle$. Recall that the eigenvector $|f\rangle$ is given by $|f\rangle = |u\rangle + |v\rangle$, where $\{u, v\}$ are the Bogoliubov de Gennes eigenfunctions. In Eq. (5.15), it is understood that the linear space on which $\tilde{F}$ and $\tilde{G}$ act, and to which $|f\rangle$ belongs, is orthogonal to $|\phi_0\rangle$. Thus, by using the projection operator $\hat{P}$ we eliminate a non-physical solution to Eq. (5.15), the Goldstone mode, with eigenvalue zero [101]. The justification for working in this reduced linear space is that all *physical* excitations obey $\langle f|\phi_0\rangle = 0$ [125].

5.5.1 Perturbation Theory for the Gross-Pitaevskii Equation

As forementioned, it seems natural to assume that the roton mode dominates the structure of the perturbed dipolar BEC near instability because its energy is much lower than the energies of the other BdG modes. To explicitly demonstrate this, one needs to formulate a perturbation theory of the GPE with respect to external potential perturbation. To do so, we begin by writing a perturbation to the trapping potential as $U \to U + U'$, where U' is the small perturbation. The response of the condensate wave function to this perturbation is then $|\phi_0\rangle \to |\phi_0\rangle + |\phi_0'\rangle$. We insert these expressions into Eq. (3.23), linearize in the primed quantities, and obtain the equation

$$\tilde{F}|\phi_0'\rangle = -\hat{P}U'|\phi_0\rangle. \tag{5.16}$$

To solve Eq. (5.16), we introduce a basis defined by the eigenvalue equation

$$\tilde{F}|\varphi_n\rangle = \varepsilon_n|\varphi_n\rangle \tag{5.17}$$

and use its eigenfunction solutions to expand $|\phi_0'\rangle$ in the $|\varphi_n\rangle$ basis. Plugging these expansions back into Eq. (5.16) and working to first order gives the expression for the wave function perturbation,

$$|\phi_0'\rangle = -\sum_n \frac{\langle\varphi_n|U'|\phi_0\rangle}{\varepsilon_n}|\varphi_n\rangle. \tag{5.18}$$

This derivation involves the use of the orthogonality condition $\langle\phi_0'|\phi_0\rangle = 0$ and the fact that $\langle\varphi_n|\phi_0\rangle = 0$. The final expression (5.18) is formally identical to that of the usual perturbation theory of the linear Schrödinger equation.

The connection between the BdG roton mode and the perturbative modes is clear in the limit that the roton mode becomes degenerate with the ground state. In this limit, the roton energy ω goes to zero. In Eq. (5.15), this means that $\tilde{G}\tilde{F}$ has eigenvalue zero. Now, note that the operator $\hat{G}$ is positive semi-definite (its lowest eigenvalue is zero, with eigenfunction $|\phi_0\rangle$. This is indeed the ground state, since $|\phi_0\rangle$ is nodeless). Accordingly, the operator $\tilde{G}$ that, by definition, acts on the linear space orthogonal to $|\phi_0\rangle$, is positive definite. It then follows that any solution

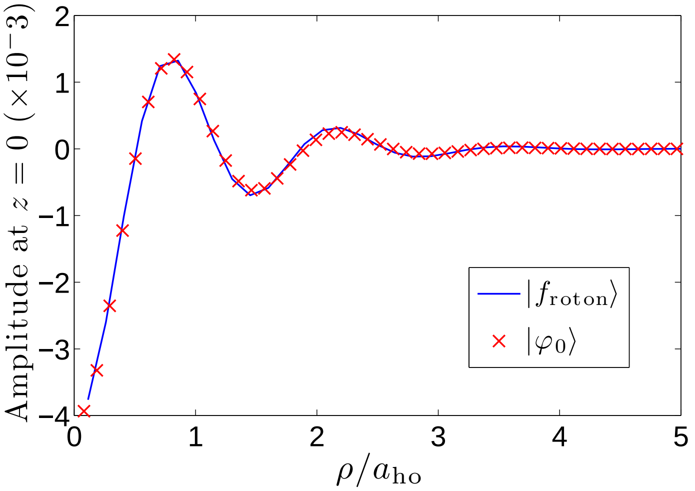

Figure 5.11: Radial profiles of excitations on a rotationless dipolar BEC with dipole strength $D = 181.2$ in a trap with aspect ratio $\lambda = 17$. The solid blue line represents the BdG roton mode while the red marks represent the $\tilde{F}$-operator eigenfunction with eigenvalue 0, $|\varphi_0\rangle$.

of $\tilde{G}\tilde{F}|f_{\text{roton}}\rangle = 0$ must also satisfy $\tilde{F}|f_{\text{roton}}\rangle = 0$. Thus, $|\varphi_0\rangle = |f_{\text{roton}}\rangle$ is a solution of Eq. (5.17) with eigenvalue $\varepsilon_0 = 0$. Since $|\phi_0'\rangle$ is written as an expansion in $|\varphi_n\rangle$ with weights proportional to $1/\varepsilon_n$, the eigenfunction $|\varphi_0\rangle$ with eigenvalue $\varepsilon_0 \sim 0$ makes a contribution to $|\phi_0'\rangle$ that strongly overwhelms the contributions of the other eigenfunctions. Thus, in the limit that the roton energy goes to zero, $|\phi_0'\rangle$ is dominated by the BdG roton mode, $|f_{\text{roton}}\rangle$.

To show that $|\varphi_0\rangle$ becomes identical to BdG roton mode $|f_{\text{roton}}\rangle$ when the roton energy goes to zero, Fig. 5.11 shows the radial profiles of both of these excited modes for a rotationless dipolar BEC with dipole strength $D = 181.2$ in a trap with aspect ratio $\lambda = 17$, which is very near the point of instability. Additionally, Fig. 5.10 illustrates the accuracy with which this perturbation theory predicts the wave function of a dipolar BEC when perturbed by a Gaussian potential, as discussed earlier in this section.

Recall that the $s = 1$ solution of the GPE gave rise to a centrifugal potential in the radial part of Eq. (5.14). This potential is constant along the trap axis and decreases quickly in the radial direction. So, just as the Gaussian potential perturbs the dipolar BEC and gives rise to ripples on its density profile, we expect similar behavior for trapped dipolar BECs with a centrifugal potential, i.e., dipolar BECs with vortex structure. To treat the centrifugal potential with our perturbation theory, we introduce a radial cutoff that is chosen to be much smaller than the spatial extent of the vortex core itself. We find that for large λ there is good agreement between our perturbation theory and the results of our exact calculations. Just as is the case for a Gaussian perturbing potential, the roton mode is responsible for the rich structure observed in the $s = 1$ vortex state of a dipolar BEC close to instability.

5.6 Conclusion

In this chapter, we introduced novel methods for calculating the ground condensate wave function $\phi_0(\mathbf{x})$ and for solving the corresponding BdG equations (3.34) for dipolar BECs in cylindrically symmetric traps and with arbitrary vorticity s. For rotationless ($s = 0$) condensates, we saw that discrete roton-like modes exist in the system, and are responsible for the dynamic instability of dipolar BECs in oblate traps. This is analogous to the roton instability in the quasi-2D system, as discussed in section 4.2. Additionally, we saw that interesting biconcave, "red blood cell" structures exist in dipolar BECs for certain islands in the parameter space defined by the trap aspect ratio λ and ddi strength D, as seen in figure 5.1. Because the region of maximum density exists in a ring about the center of the trap for the biconcave condensates, the mechanism for dynamic instability is an *angular* roton.

In addition to the rotationless dipolar BECs, we systematically map the stability and structure of dipolar BECs with a singly-quantized vortex, corresponding to $s = 1$. Because such condensates also have rings of maximum density, but here due to the zero-density vortex core, BdG modes with angular character are responsible for the dynamic instability of these dipolar BECs, as well. Additionally, for sufficiently large D and λ, we find that radial ripples exist in the dynamically stable $s = 1$ dipolar BECs near the stability threshold. To explain the origin of such structure, we developed a perturbation theory for the GPE and applied it to dipolar BECs perturbed both by thin Gaussian potentials centered on the trap axis (as may be created with a sufficiently focused blue-detuned laser) and centrifugal potentials. This theory allows us to relate the radial oscillations observed in the exact ground state profiles of perturbed dipolar BECs to the roton mode observed in the BdG spectrum of rotationless dipolar BECs.

As mentioned in section 5.2, we performed simulations of the ballistic expansion of a biconcave dipolar BEC, which demonstrate that the biconcave structure is not preserved in the expansion. In the next chapter, we revisit the biconcave dipolar BEC with the goal of finding experimental signatures of the biconcave structure. Taking the ^{52}Cr BEC as a test case, we show that the angular instability predicted by the BdG theory for a biconcave condensate results in angular collapse when the *s*-wave scattering length is critically lowered, and ballistic expansion of this collapsed cloud preserves the angular character, providing an indirect experimental signature of the biconcave dipolar BEC.

Chapter 6

Collapse of a Dipolar Bose-Einstein Condensate

In this chapter, we explore the structure and dynamics of rotationless ($s = 0$) dipolar BECs near their threshold for stability, paying particular attention to the biconcave structure that was introduced in section 5.2. Motivated to find an experimental signature of such interesting structure, we show that the angular roton instability associated with the presence of biconcave structure can manifest in non-trivial, time-dependent angular collapse and subsequent expansion of the dipolar BEC. We note that the original work presented in this chapter has been published in [37].

Collapse of dipolar BECs has been studied elsewhere, both experimentally [21, 22] with the ^{52}Cr BEC and theoretically [171]. Because the (magnetic) dipole moment of ^{52}Cr is effectively fixed, stability can be controlled by changing the trap geometry or by tuning the s-wave scattering length of the atoms by using a magnetic Fano-Feshbach resonance, which we discuss briefly in section 6.1. Recall from chapter 4 that the stability of the polarized dipolar BEC depends both on the magnitude of the dipole moment, the s-wave scattering length and the geometry of the trapping potential relative to the dipole polarization. Thus, for the fixed dipole system, the scattering length must be tunable to $a_s < -2a_{dd}$ and $a_s > a_{dd}$ to fully explore the stability in both prolate and oblate geometries. Indeed, this level of control was achieved in the experiment [22], and the ^{52}Cr condensate was stabilized for a variety of trap aspect ratios by tuning the s-wave scattering length to a sufficiently large value. In this experiment, instability of the condensate was triggered by reducing this scattering length below a critical value. Strikingly, the experimentally observed anisotropic density distribution of the collapsed cloud was reproduced well within mean-field theory and the

Gross-Pitaevskii equation [22]. Further, Ref. [171] has explored circumstances of local collapse in various trap geometries, contrasting approaches where the collapse is initiated by either rapid or else adiabatic changes in the scattering length. While collapse of the ^{52}Cr BEC has been observed, thus far there is no direct experimental evidence for the roton or for the local collapse of a dipolar BEC.

In this chapter we tackle head-on the prospects for observing local collapse in a dipolar BEC. In section 6.2 we analyze and extend the experimental result from Ref. [21]. We argue that, for oblate traps, the scattering length required to stabilize the condensate can be explained within mean-field theory, but only if the the theory is sensitive to local collapse phenomena. Further, the distinction between local and global collapse becomes more clear if the number of dipoles is increased. In Sec. 6.3 we develop an understanding of a more direct measurement of condensate collapse, following the experimental procedure of Ref. [22], which includes an expansion that allows for imaging of the cloud. We show that angular structure in the expanded image is a direct signature of biconcave structure. Before we proceed, we briefly discuss the physics of a Fano-Feshbach resonance, as this is the method that is used to control the s-wave scattering length in the ^{52}Cr experiments.

6.1 Fano-Feshbach Resonances

Unlike potential resonances and shape resonances, which are inherently single-channel phenomena, the Fano-Feshbach resonance is intrinsically a multi-channel phenomenon [60]. The basic idea of a Fano-Feshbach resonance can be expressed by a simplistic two-channel model. Imagine two scalar particles scattering in an open channel 1, where a closed channel 2 also exists and is higher in energy that 1. For now, let the incident scattering energy be $E = 0$ and let there be a bound state in channel 2 at energy ϵ. Such a scenario is shown schematically in figure 6.1(a). In the scattering process, this bound state may be "visited" and, if ϵ is sufficiently small, the amount of time that the particles take to exit the scattering process can be quite large.

It turns out, this phenomenon can be directly related to the s-wave scattering length of the

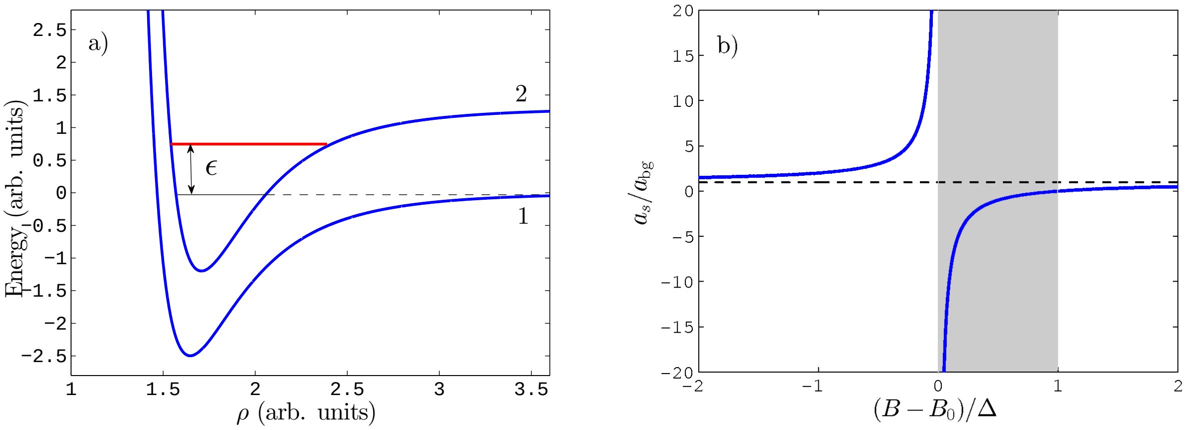

Figure 6.1: a) Schematic two-state system that is necessary for the appearance of a Fano-Feshbach resonance. Here, channel 1 is the incoming channel and a bound state at energy ϵ exists in channel 2. b) The s-wave scattering length in units of the background scattering length as a function of the applied magnetic field in units of the resonance width for a magnetic Fano-Feshbach resonance, given by Eq. (6.1).

particles. A particularly relevant case here is the magnetic Fano-Feshbach resonance (or set of resonances) in ^{52}Cr. In this case, the energy ϵ can be controlled by tuning an applied magnetic field that shifts the Zeeman levels of the atom. Thus, this magnetic Fano-Feshbach resonance allows us to map the s-wave scattering length a_s in terms of an applied field B. Where B_0 corresponds to ϵ_0 and Δ is the width of the resonance, we can write a single resonance as

$$a_s = a_{\mathrm{bg}} \left(1 - \frac{\Delta}{B - B_0} \right), \tag{6.1}$$

where a_{bg} is the “background” scattering length in the absence of an applied magnetic field. This relation is plotted in figure 6.1(b). The magnetic fields for which negative scattering lengths can be obtained are shaded in this figure. For the ^{52}Cr system in the experiment [22], the magnetic Fano-Feshbach resonance that is used occurs at $B_0 = 589\,\mathrm{G}$ and has a width of $\Delta = 1.7\,\mathrm{G}$. While this width is relatively narrow, it permits experimental control over the scattering length with an uncertainty $\Delta a_s \sim 2a_0$ [16].

6.2 Local collapse: Evidence from the Stability Diagram

Thus far only one experiment has explored the stability of a dipolar BEC as a function of the trap aspect ratio [21]. The resulting experimental stability diagram (reproduced with permission from [21]) is presented in figure 6.2 as a plot of the critical scattering length a_{crit} versus aspect ratio λ for the ^{52}Cr BEC. These results represent the measurement performed on a condensate of $N = 2 \times 10^4$ ^{52}Cr atoms. We note that the experimental results shown here are actually quite remarkable, as they demonstrate that the relatively small dipole moments of the ^{52}Cr atoms have an astounding effect on the BEC stability. In this figure, we see that the dipolar BEC in a prolate trap requires a comparatively large scattering length to achieve stability. As λ is increased, the zero-point energy in the axial direction stabilizes the dipolar BEC, and stable condensates are possible with a smaller critical scattering length. Additionally, we see that a *purely* dipolar BEC (with $a_s = 0$) is achieved near $\lambda = 10$.

This figure also shows the results of two alternative numerical calculations of the critical scattering length a_{crit}. In one, the theoretical division between stable (shaded) and unstable (unshaded) regions of parameter space is determined by solving the GPE, Eq. (3.23), and the BdG equations (5.7) and (5.8) exactly on a numeric grid, using the methods described in section 5.1. A second approach, already employed as an approximation in the experimental paper [22], shows the division between the stable and unstable regions as a dashed line. This approximation posits a Gaussian ansatz for the condensate wave function (normalized to unity),

$$\phi_0(\rho, z) = \left(\frac{1}{\pi^{3/2}\sigma_\rho^2 \sigma_z \bar{a}_{\mathrm{ho}}^3} \right)^2 \exp\left[\frac{-1}{2\bar{a}_{\mathrm{ho}}^2} \left(\frac{\rho^2}{\sigma_\rho^2} + \frac{z^2}{\sigma_z^2} \right) \right] \tag{6.2}$$

where σ_ρ and σ_z are the variational parameters and $\bar{a}_{\mathrm{ho}} = \sqrt{\hbar/M\bar{\omega}}$, where $\bar{\omega} = \sqrt[3]{\omega_\rho^2 \omega_z}$ is the geometric mean trap frequency. Using this ansatz, the GP energy functional (5.3) is calculated for a given $\bar{a}_{\mathrm{ho}}$ to determine whether the energy $E[\sigma_\rho, \sigma_z]$ has a minimum, and thus to determine if the Gaussian condensate is energetically stable. The presence of a minimum, local or global, corresponds to the presence of a stable ground state. A key feature of the Gaussian trial wave function is that it always places the maximum density in the condensate's center, i.e., it is incapable

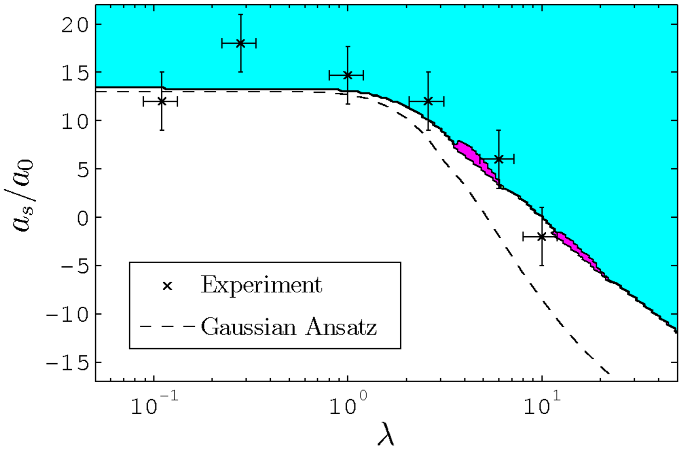

Figure 6.2: The stability diagram of a dipolar BEC of $N = 2 \times 10^4$ ^{52}Cr atoms plotted as critical scattering length versus trap aspect ratio. The points show the experimental results of [21], the shaded regions show the results of solving the GPE exactly and the dashed line shows the results of the Gaussian ansatz. The theoretical methods disagree as trap aspect ratio λ increases, and the exact results fit the experimental data with great accuracy. The pink (darker) regions are where biconcave structure is predicted on the condensate profile.

of describing local collapse. For prolate traps, the maximum density *is* in the center. In this case the Gaussian ansatz and the numerical solution to the GPE agree with each other on the critical scattering length, and they both are in good agreement with the experimental result.

Care must be taken, however, using this approximation for oblate condensates. This can be seen in the $\lambda > 1$ region of the stability diagram in figure 6.2, where the Gaussian ansatz predicts a lower critical scattering length than does the exact numeric solution of the GPE. We attribute this difference to the ability of the methods described in section 5.1 to model local collapse. Indeed, for larger aspect ratios we observe local collapse into roton-like modes, as we will discuss in the next section, and as has been reported in Ref. [171]. Further, the experimental determination of a_{crit} tends to show better agreement with the GPE prediction than with that of the Gaussian ansatz. We interpret this as experimental support for the occurrence of local collapse, albeit somewhat indirect evidence. However, the roton modes involved in collapse might have either radial or angular nodal structure. This experiment does not make this distinction.

Within the uncertainty in the experiment, the data in figure 6.2 discriminates between the

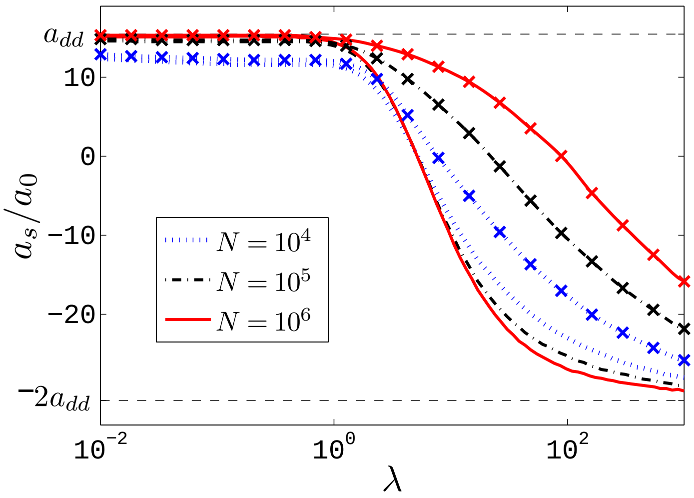

Figure 6.3: For a dipolar BEC of atomic ^{52}Cr, this figure illustrates the critical s-wave scattering length (below which the dipolar BEC is unstable) as a function of trap aspect ratio λ in units of the Bohr radius for $\bar{\omega} = 2\pi \times 700\,\text{Hz}$. The blue (dotted), black (dot-dashed) and red (solid) lines correspond to $N = 10^4$, $N = 10^5$ and $N = 10^6$, respectively. The lines without crossed symbols are the results of the Gaussian ansatz and lines with crossed symbols are the results of the exact solution of the GPE. Notice how, as N is increased, the Gaussian ansatz predicts a more stable condensate while the exact solution predicts a less stable condensate.

two methods, but one may wish for a clearer discrimination. We therefore consider cases with varying atom number N. The critical scattering length a_{crit} is shown in figure 6.3 for dipolar BECs with atom numbers of $N = 10^4$, 10^5, and 10^6. For a given trap, increasing the number of dipoles increases the relative importance of the dipole-dipole interaction (ddi), which acts to further destabilize the condensate. Thus, as predicted by our exact numeric solutions to the GPE, a_{crit} increases with increasing atom number. Vice versa, the Gaussian ansatz predicts a more stable condensate with increasing atom number. The difference between the two theoretical approaches could then be clearly distinguished in such an experiment.

Although figure 6.3 plots only the domain of aspect ratios $10^{-2} < \lambda < 10^3$, it is straightforward to obtain the stability thresholds in the $\lambda \ll 1$ and the $\lambda \gg 1$ limits for fixed $\bar{\omega}$. These limits are usefully described in terms of the characteristic dipole length a_{dd}, and correspond to the stability threshold for the 3D homogeneous dipolar BEC for $\lambda \ll 1$ and the stability threshold for the quasi-2D dipolar BEC for $\lambda \gg 1$. We see this by noting that in the limit of large ddi's, $Na_{dd}/\bar{a}_{\text{ho}} \gg 1$, the interaction-dependent term in $E[\phi_0]$ dominates over the other terms since it scales with a factor of N. Thus, in this limit, the condensate is unstable if this interaction-dependent term is negative.

Taking the limit $\lambda \to 0$ corresponds to an infinitely prolate, or cigar-shaped trap. In this geometry, the dipolar mean-field term reduces to a simple coupling to the condensate density, $d^2 \int \phi_0^\star(\rho') \frac{1-3\cos^2\theta}{|\mathbf{x}-\mathbf{x}'|^3} \phi_0(\rho') d\mathbf{x}' = -4\pi\hbar^2 a_{dd} |\phi_0(\rho)|^2/M$ because the ddi reduces to a delta-function in ρ for this geometry. Thus, in the quasi-1D geometry, the total mean-field term becomes $4\pi\hbar^2 \left(a_s - a_{dd}\right) |\phi_0(\rho)|^2$. Similarly for the limit $\lambda \to \infty$, corresponding to an infinitely oblate trap, the dipolar mean-field term reduces to $8\pi\hbar^2 a_{dd} |\phi_0(z)|^2/M$ (similar to the quasi-2D case discussed in section 4.2), giving a total mean-field term of $4\pi\hbar^2 \left(a_s + 2a_{dd}\right) |\phi_0(z)|^2$ for this geometry. Thus, in the limit $Na_{dd}/\bar{a}_{\text{ho}} \gg 1$, we find that the dipolar BEC is unstable when $a_s < a_{dd}$ for $\lambda \ll 1$ and the dipolar BEC is unstable when $a_s < -2a_{dd}$ for $\lambda \gg 1$, in agreement with the analysis given in section 4.2. These limits are indicated in figure 6.3, and the mean-field calculations are detailed in Appendix G.

6.3 Local Collapse: Evidence From the Collapsed Cloud

To take a closer look at the nature of collapse, it is necessary to track the collapse itself as a function of time. This, too, has been achieved in the ^{52}Cr BEC experiments. These experiments have not, however, focused directly on observing the consequences of local collapse. Here we discuss the prospects of making such a measurement.

Briefly, in such an experiment the s-wave scattering length is altered from a value where the condensate is stable against collapse to a somewhat lower value $a < a_{\text{crit}}$. After this transition, the atoms begin their collapse into high density regions where three-body recombination takes over, ejecting atoms from the trap. The trap is generally released after some hold time, to expand the cloud for imaging. The resulting density patterns show intricate shapes and depend on details such as whether the passage from stable to unstable is adiabatic or diabatic [171].

6.3.1 Modes of Instability

As forementioned, the underlying physics of the instability and collapse of oblate dipolar BECs is determined by the softening of a roton mode. For the case at hand, however, the roton does not emerge with increasing D, but instead emerges with decreasing a_s. Figure 6.4 illustrates the mode softening for a dipolar BEC containing $N = 10^4$ ^{52}Cr atoms in a trap with aspect ratio $\lambda = 8$. Plotted is the energy of the excitation as a function of the scattering length a_s, labeled by its azimuthal angular momentum quantum number m. The solid lines depict the real parts of these energies, while the symbols represent their imaginary parts. As a_s diminishes, the energies of these modes drop to zero, and thereafter become purely imaginary. The first such transition, at $a_s \sim -0.9a_0$, identifies the scattering length at which the dipolar BEC goes dynamically unstable, since any small perturbation is capable of exciting this mode, which then grows exponentially in time. Thus an unstable condensate quickly grows high-density peaks in regions defined by the antinodes of these modes.

Figure 6.4 is a particular example illustrating the modes that contribute to instability at a particular aspect ratio $\lambda = 8$. At this aspect ratio the condensate's density exhibits a biconcave shape, and so decay into angular rotons is expected. We reiterate, from section 5.2, that at all aspect ratios where the maximum density lies at the center rather than at the periphery, the rotons responsible for instability are always $m = 0$ modes that do not exhibit an angular structure. This connection is essential to connecting observed angular decay circumstantially to the existence of biconcave structure.

However, regardless of whether the roton is purely radial or angular in nature, it leads a dipolar BEC to instability at a fixed length scale with a wavelength $\sim 2\pi a_z$. As the trap aspect ratio λ is increased, the ratio of the axial to the radial harmonic oscillator lengths, a_z/a_ρ, is decreased, so more roton wavelengths can fit around the circumference of the condensate for larger λ. For biconcave condensates, this results in angular rotons with larger m quantum number being responsible for instability for larger λ, since more angular nodes can fit into the condensate in this

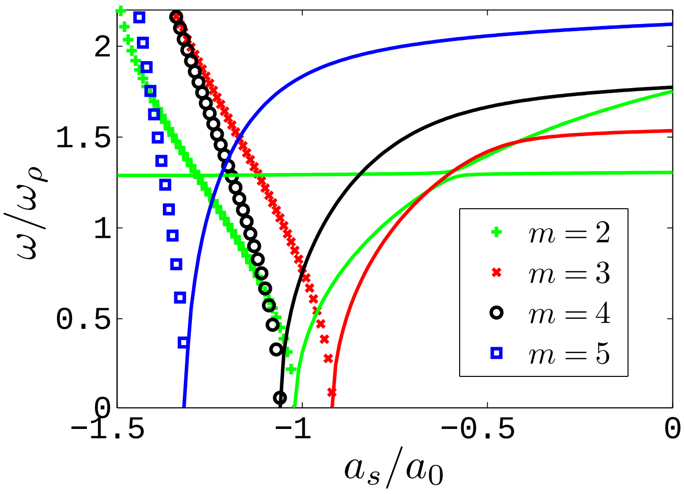

Figure 6.4: The real and imaginary parts of the low-lying BdG modes for a condensate of $N = 10^4$ ^{52}Cr atoms with mean trap frequency $\bar{\omega} = 2\pi \times 700$ Hz and trap aspect ratio $\lambda = 8$, plotted as a function of the s-wave scattering length a_s. The real parts are represented by solid lines and the imaginary parts, developing where the real parts go to zero, are represented by markers. The $m = 3$ mode, being the first to develop a nonzero imaginary energy, serves to define a_{crit} for this aspect ratio.

regime. For $N = 10^4$ ^{52}Cr atoms in a trap with $\lambda = 8$ and $\bar{\omega} = 2\pi \times 700$ Hz, this mode happens to have $m = 3$. Indeed, the circumference of the region of maximum particle density in this biconcave condensate is $\sim 6\pi a_z$, or three roton wavelengths.

6.3.2 Numerics and the “Ideal Experiment”

The mode that brings about the dynamical instability determines not only the scattering length at which the condensate will collapse, but also *how* the condensate will collapse as the stability threshold is crossed. Consider preparing a dipolar BEC of $N = 10^4$ ^{52}Cr atoms just above the stability threshold in a trap with aspect ratio $\lambda = 8$. These are the collective modes whose energies are shown in figure 6.4. A small jump in scattering length to a value just below a_{crit} would cause the condensate to go unstable by a macroscopic occupation of the $m = 3$ mode that has a nonzero imaginary energy at this scattering length. The density of the condensate during the collapse would change, on a time scale $\tau \sim 2\pi/\text{Im}[\omega]$, as the atoms macroscopically occupy three

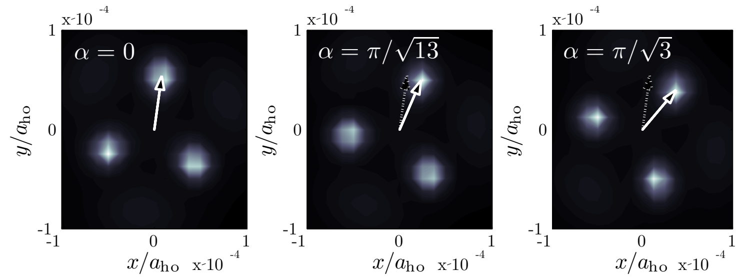

Figure 6.5: Collapsed condensate in a trap with mean frequency $\bar{\omega} = 2\pi \times 700$ Hz and aspect ratio $\lambda = 8$ after 10.5 ms. The perturbation for the collapse is controlled to have $m = 3$ symmetry and the global phases as shown in the frames. Each frame corresponds to a different value of the initial phase α. The collapsed condensates are rotated by $\alpha/3$, ensuring that the finite grid size does not influence the small length scale dynamics of the condensate collapse.

clumps that self-attract in the z-direction.

Decay of the condensate into a roton mode with $m > 0$ requires breaking the condensate's initial cylindrical symmetry by introducing fluctuations into the mode. In an experiment this is caused by thermal fluctuations, but in our calculation we must make this happen artificially. To do this, we seed the condensate wave function by adding to it a small contribution of the excited state mode:

$$\phi_0(\vec{r}) \rightarrow \phi_0(\rho, z) + 0.01 e^{2\pi i \alpha} e^{3i\phi} \bar{u}_3(\rho, z), \tag{6.3}$$

where $e^{3i\phi}$ describes the basic angular variation of the $m = 3$ roton mode, and α is an additional phase that will determine the overall rotation of the collapsed condensate. In the absence of a seed like this, the numerical solution remains at its unstable equilibrium for a time long compared to the natural lifetime $2\pi/\mathrm{Im}[\omega]$. The apparent lifetime in this case is determined by the time before roundoff error starts to affect the numerical time evolution of the GPE. However, once the wave function is seeded as above, the decay occurs on the expected time scale.

After the collapse is triggered, the condensate indeed forms the three "clumps" as expected, as seen in figure 6.5. Shown is the density of particles, as viewed in the x-y plane, i.e., looking down from the axis of the dipoles' polarization. Each peak was initially seeded by a density fluctuation at the antinode of the $m = 3$ excited state roton wave function. Thus the three peaks are uniformly equally spaced in angle, as befits the symmetry of the mode. An angular display of this sort would provide unambiguous evidence for nonlocal collapse. Moreover, the fact that the collapse occurred in an angular coordinate provides indirect evidence for the biconcave structure of the initial state.

While the relative positions of the three peaks in this experiment are well-defined by the symmetry of the roton mode, there is still an overall undetermined angle of rotation of the whole pattern. Numerically, this is set by the angle α in (6.3). Since the angular dependence of the condensate density, with this wave function, is proportional to $\cos(3\varphi + \alpha)$, we expect that, if there is no unphysical dependence on the numerical grid, the collapse will occur rotated by an angle $\alpha/3$ for any initial phase α. Indeed, we find that the collapse dynamics are unaffected by the grid, as is illustrated in figure 6.5. Here, we input the initial phases $\alpha = \pi/\sqrt{13}$ and $\alpha = \pi/\sqrt{3}$ and find that the collapsed wave function is rotated by exactly these phases times 1/3. Although not shown here, simulations for other initial phases give the same results. Based on this ability to reproduce the same angular pattern, but rotated in a predictable way, we conclude that the underlying Cartesian grid is adequate to describe this collapse.

6.3.3 A More Realistic Experiment

Figure 6.5 illustrates the kind of clean angular distribution that might be expected in the ideal experiment, where an infinitesimal change in scattering length is possible, and where only a single roton mode is excited. Thus far, neither of these circumstances is true in the ^{52}Cr experiments. Whereas figure 6.4 shows the difference in scattering length at which modes with different m quantum numbers develop imaginary energies to be a fraction of a Bohr, experimental uncertainties in the Feshbach-tuned scattering length of ^{52}Cr are $\pm 2a_0$ [21]. Additionally, imaging of a ^{52}Cr dipolar BEC was done after a time of free-expansion in this experiment, not in-trap as is described in the scenario above. We propose, with slight modification, an experiment similar to the one described by [21] that presents us with the possibility of observing angular structure in the collapse and expansion of a dipolar BEC.

Instead of making a very small jump in scattering length across the stability threshold,

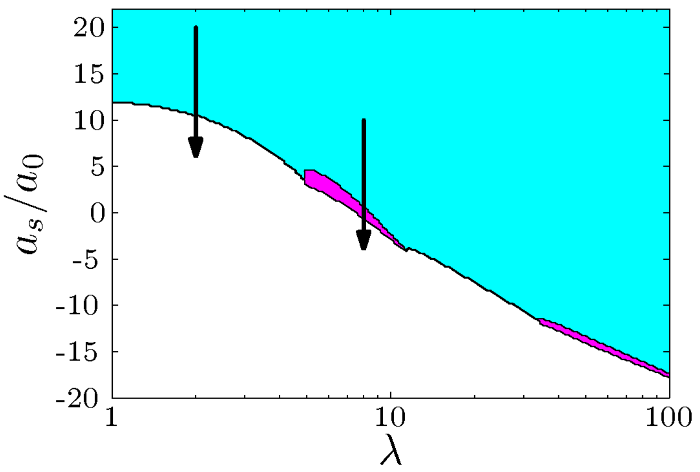

Figure 6.6: Stability diagram for $N = 10^4$ ^{52}Cr atoms. The white region is dynamically unstable, while the colored regions are stable. The pink (darker) islands are where biconcave structure is found in the ground state of the condensate. The mean trap frequency is $\bar{\omega} = 2\pi \times 700$ Hz for all aspect ratios λ. The arrows illustrate the initial and final values of scattering length in the experiment proposed in the text.

consider making a jump of $\Delta a_s = -14a_0$. For a ^{52}Cr dipolar BEC with $N = 10^4$ atoms, we numerically prepare, for $\bar{\omega} = 2\pi \times 700$ Hz, a condensate in a trap with $\lambda = 2$ and scattering length $a_s = 20a_0$ and a condensate in a trap with $\lambda = 8$ and scattering length $a_s = 10a_0$, where both scattering lengths are about $10a_0$ above a_{crit} for their respective aspect ratios. We then ramp the scattering length from its initial value to its final value over a time period of 8 ms. These scattering length ramps are illustrated by the arrows in figure 6.6. Although an 8 ms ramp time is not sufficiently slow to make the change completely adiabatic (the characteristic trap period is $2\pi/\bar{\omega} = 1.4$ ms), it is sufficiently slow to allow a biconcave shape to form during the ramp. Once this ramp has been made, we hold the collapsing condensate in the trap for $t_{\text{hold}} = 2$ ms and then turn off the trap to let the collapsed condensate propagate in free space. In an actual experiment, the expanded cloud could then be imaged to determine its density profile after expansion.

To ensure that we accurately simulate an experimental scenario and to break the cylindrical symmetry of the condensate in a physically consistent way, we seed the condensate prior to the time evolution with numerical noise. Although the non-projected GPE can only model the condensate dynamics at zero temperature, an experiment will unavoidably have a very small but finite temperature present in the gas. This means that the condensate fraction will not be exactly unity, but something slightly less. To account for this, we correct our condensate by adding excited modes (quasiparticles) with weights determined by the Bose-Einstein distribution [172],

$$n_j = \left[e^{\frac{\omega_j - \mu}{k_B T}} - 1 \right]^{-1} \tag{6.4}$$

where n_j is the number of particles occupying the quasiparticle state with energy ω_j, T is the temperature of the Bose gas, μ is the chemical potential of the condensate and k_B is the Boltzmann constant.

Using the quasiparticle spectrum given by solving the BdG equations (5.7) and (5.8) and a temperature of $T = 100$ nK, we then perturb our initial condensate by

$$\phi_0(\mathbf{x}) \to \phi_0(\rho, z) + \sum_j \sqrt{\frac{n_j}{N}}\, e^{2\pi i \alpha_j} \left[u_{m,j}(\rho, z) e^{im\varphi} + v^{\star}_{m,j}(\rho, z) e^{-im\varphi} \right], \tag{6.5}$$

where $\{\alpha_j\}$ are random numbers between 0 and 1, n_j is given by Eq. (6.4) and $u_{m,j}(\rho, z)$ and $v^{\star}_{m,j}(\rho, z)$ are BdG modes with quantum number m and energy ω_j. Also, we include the factor $\sqrt{1/N}$ in the weighting because the condensate wave function $\phi_0(\mathbf{x})$ is normalized to unity instead of being normalized to N. We impose a cutoff on the sum in Eq. (6.5) of $\omega_j < 2k_B T$, where $T = 100$ nK, simplifying the problem by ignoring higher energy modes that contribute little to the thermal excitations of the system. Indeed, $T = 100$ nK is an experimentally accessible temperature [14].

Additionally, because the condensate density becomes very large during the collapse process, a three-body loss term is required to accurately model the collapse and expansion dynamics [21]. The rate constant for three-body recombination was experimentally determined to be $L_3 = 2 \times 10^{-40}\text{m}^6/\text{s}$ for ^{52}Cr. We account for this loss in our simulations by including the term $-i\hbar N(N-1)L_3|\phi_0(\mathbf{x})|^4/2$ in the time-dependent GPE, Eq. (3.46), now given by

$$\begin{aligned} i\hbar \frac{\partial \phi_0(\mathbf{x}, t)}{\partial t} &= \Big\{ -\frac{\hbar^2}{2M}\nabla^2 + U(\mathbf{x}) + (N-1)\int d\mathbf{x}' V(\mathbf{x} - \mathbf{x}')|\phi_0(\mathbf{x}', t)|^2 \\ &\quad - N(N-1)\frac{i\hbar L_3}{2}|\phi_0(\mathbf{x}, t)|^4 \Big\} \phi_0(\mathbf{x}, t), \end{aligned} \tag{6.6}$$

where $V(\mathbf{x}-\mathbf{x}')$ is given in Eq. (3.61). To solve Eq. (6.6), we employ the 4th order Runge-Kutta algorithm with adaptive step size.[1]

Figure 6.7 illustrates the numerical time evolution of these condensates through the collapse and expansion described above. As before, these images represent integrated density profiles in the x-y plane, as viewed from the polarization axis. The top four frames illustrate the collapse and expansion of a condensate in a trap with aspect ratio $\lambda = 2$, in which there is no biconcave shape and in which, consequently, there should be no collapse to angular roton modes. During its collapse, the condensate maintains its peak density in the center. After the trap is removed and the gas is allowed to expand, its cylindrical symmetry is preserved.

By contrast, the lower four panels of figure 6.7 illustrate a representative time evolution for a condensate in a trap with aspect ratio $\lambda = 8$. In this case, by 7.5 ms the condensate has established its biconcave structure. When the condensate collapses, it does so into roton modes with angular nodal structure, leading to local collapse with angular nature. After the trap is turned off and the condensate expands for 4.5 ms, the angular structure remains in the density of the expanded cloud. The collapse is clearly dominated by a roton with $m = 3$ in this simulation. However, because several angular modes are involved, the angular pattern no longer experiences pure $m = 3$ angular symmetry. Moreover, each mode arrives with a random initial phase, meaning that there is a random asymmetry due to the interference between the unstable modes. In the experiment this will imply non-repeatability of the observed density peaks from shot to shot.

Nevertheless, once the angular pattern is established, its vestiges remain in the expanded cloud. In the final expanded picture, the clear break from cylindrical symmetry indicates that the decay modes have angular dependence, hence that the condensate went through a biconcave phase. We note here that the collapse and expansion experiment that was performed with a dipolar BEC of ^{52}Cr [173] did not probe the parameter regime for biconcave structure formation that we investigate here.

The results of simulations that are very similar to the ones described above are presented

---

[1] Available in MATLAB through the function `ode45`.

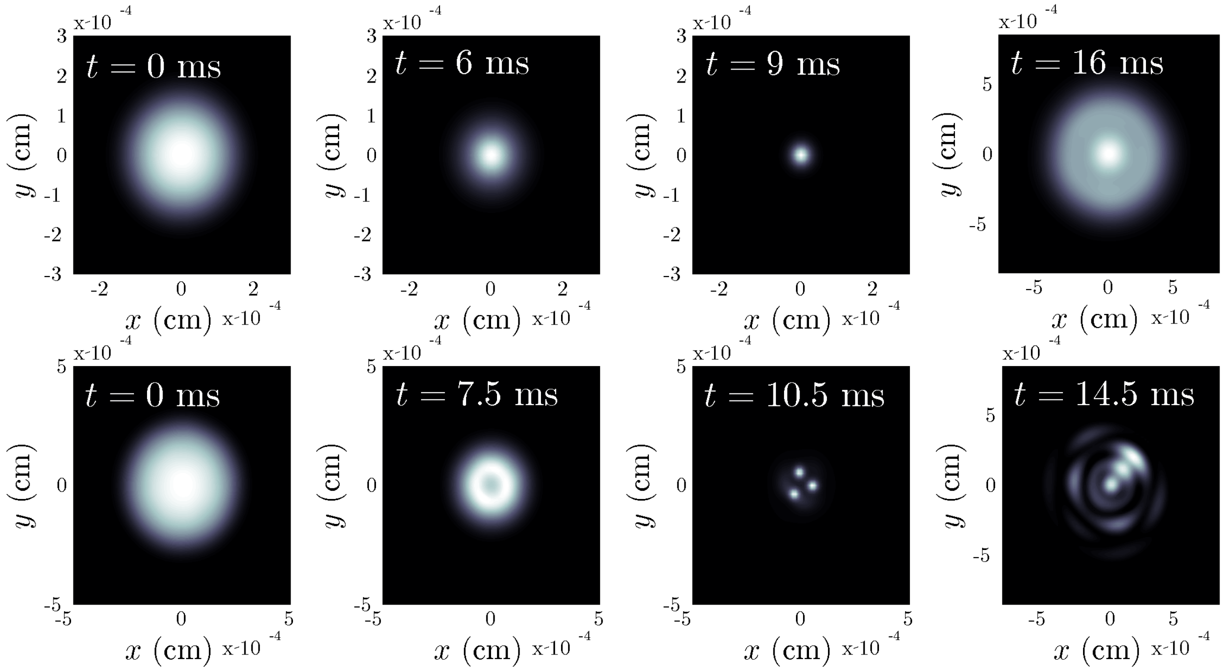

Figure 6.7: Collapse dynamics of dipolar BECs, both in harmonic traps with mean frequency $\bar{\omega} = 2\pi \times 700$ Hz, corresponding to the scattering length ramps illustrated in Figure 6.6. (a) A dipolar BEC in a trap with aspect ratio $\lambda = 2$, at $t = 0$ ms the condensate has $a_s = 20a_0$, the scattering length is ramped down to $a_s = 6a_0$ over 8 ms, the collapsed condensate is held in the trap for $t_{\text{hold}} = 2$ ms and then expanded until $t = 16$ ms. The collapse and expansion is purely radial. (b) A dipolar BEC in a trap with aspect ratio $\lambda = 8$, at $t = 0$ ms the condensate has $a_s = 10a_0$, the scattering length is ramped down to $a_s = -4a_0$ over 8 ms, the collapsed condensate is held in the trap for $t_{\text{hold}} = 2$ ms and then expanded until $t = 14.5$ ms. The condensate becomes biconcave during the ramp in scattering length and thus collapses with angular structure, preserving an angular character during expansion.

in [171], where dipolar BEC collapse is modeled in-trap and not through the expansion process and not including a three-body loss term in the simulation. Ref. [171] performs simulations of dipolar BEC collapse for both adiabatic and non-adiabatic (instantaneous) jumps in scattering length, and find very interesting results regarding the presence of global and local collapse in the condensate dynamics. For adiabatic collapse, where the change in scattering length is sufficiently slow to track the condensate across the roton softening in the BdG spectrum, Ref. [171] presents a critical trap aspect ratio above which local collapse occurs. We confirm these results, but point out that while local collapse is very interesting (and can be evidence for the presence of the roton in these systems), its manifestation in a dipolar BEC is much richer than has been discussed in previous work. A mapping of dipolar BEC collapse via the experiment proposed above can determine not only whether collapse was global or local, but whether collapse was radial or angular (including which m quantum number is responsible for the collapse) and thus provide evidence for the underlying biconcave structure.

We point out that the experiment proposed above is just one of many experimental methods that would demonstrate the angular nature of dipolar BEC collapse. Certainly, taking data for a number of additional trap aspect ratios would assist in mapping out the regions where biconcavity exists. Also, we expect that smaller and slower jumps in scattering length, which may be had with less uncertainty in the Feshbach-induced scattering length, would assist in understanding how and where collapse occurs. Slower ramping of the scattering length allows the condensate to be tracked more adiabatically and thus allows for collapse to begin when only one BdG mode has a nonzero imaginary energy, making the mapping of the collapse much more clear. Instantaneous or very fast jumps in scattering lengths across a biconcave region will miss this structure completely and thus result in a purely radial collapse. For an angular collapse to occur, the biconcave structure must manifest itself in the condensate prior to collapse.

6.4 Conclusion

In conclusion, we have shown that in order to correctly map out the stability of a dipolar BEC, a computational method that is sensitive to the local nature of dipolar BEC collapse must be used. Methods such as the gaussian ansatz that are not sensitive to such phenomenon will incorrectly predict the qualitative features of the stability. Also, we draw a connection between the BdG spectrum of a dipolar BEC and the nature of the dipolar BEC collapse. Not only can the BdG quasiparticles predict where a dipolar BEC will collapse in parameter space, they can also predict how a dipolar BEC will collapse. For dipolar BECs without biconcave structure, this collapse is purely radial while for dipolar BECs with biconcave structure, this collapse has angular structure. Performing collapse and expansion experiments on a ^{52}Cr dipolar BEC can reveal this angular structure and thus provide an experimental method for mapping biconcave structure in dipolar BECs.

Having studied the static properties of dipolar BECs in harmonic traps, including a proposed experiment that could map the rich structure seen in the parameter space of the rotationless condensate, we now proceed to investigate the superfluid properties of dipolar BECs.

Chapter 7

Superfluidity in a Dipolar Bose-Einstein Condensate

Recall from our discussion in section 2.1 that a fundamental property of a superfluid is its ability to support dissipationless flow. That is, a superfluid can move through slits or capillaries, or an object can translate through the superfluid without exciting any quasiparticle or topological (vortex) modes in the system. In this case, no energy is transferred to the fluid and the flow is dissipationless, provided the flow is sufficiently slow.

As discussed in section 2.1, liquid ^{4}He was the first experimentally accessible system to exhibit dissipationless flow at low temperature, i.e., to demonstrate the existence of superfluidity in a quantum system. However, the Bose-Einstein condensates (BECs) that have been created more recently have a distinct advantage over liquid helium in that they are dilute and hence easily characterized in terms of microscopic interactions. In particular, their superfluid critical velocity is nominally given by the speed of sound in the center of the gas, which can be easily calculated from the density and the s-wave scattering length of the constituent atoms (see section 4.1). Early experiments at MIT sought to measure v_L in a BEC of sodium atoms by stirring the condensate with a blue-detuned laser [174, 175]. However, these experiments measured a critical velocity for spinning off vortices rather than the critical velocity for shedding energy into quasiparticle excitations. This is a generic feature of such experiments in which the size of the object (in this case, the blue-detuned laser) is large compared to the healing length of the gas [176, 177, 178, 179].

In this chapter, we are concerned with the superfluid properties of dipolar BECs, in particular, those that have been produced experimentally with ^{52}Cr [14, 23] and ^{164}Dy [17]. These gases present a middle ground between atomic BECs and dense superfluid helium. Namely, the dipolar BEC is dilute enough to be understood in detail, yet its spectrum may exhibit roton features in prolate traps, as we have discussed in previous chapters. The characteristic momentum of such a roton is set by the geometry of the trap in which it is held, whereas its energy is controlled by the density of dipoles, as well as the magnitude of the dipole moment [16]. Thus, the superfluid critical velocity is completely under the control of the experimentalist. In contrast, the superfluid critical velocity in ^{4}He can be only weakly modified by changing the pressure of the liquid [48]. Thus, the dipolar BEC provides an unprecedented opportunity to explore the fundamental relationship between the roton dispersion and superfluidity.

This chapter is composed of three sections. In section 7.1, we reproduce Landau's original argument for the derivation of the superfluid critical velocity, the so-called "Landau critical velocity" v_L, in terms of the elementary quasiparticle spectrum of the superfluid. In section 7.2, we model an experiment on a purely dipolar BEC, similar to the MIT experiments. We consider a relatively weak blue-detuned laser sweeping through a dipolar BEC at a constant velocity, and compute the resulting condensate depletion due to the excitation of quasiparticles (not vortices). We find an onset of depletion at a critical velocity that is near the Landau critical velocity at low densities. At higher densities, where the roton determines v_L, the critical velocity is a decreasing function of density, a behavior unique to a dipolar BEC. Moreover, the simulations show a critical velocity that is somewhat smaller than v_L at higher densities. We attribute this to the role that the roton plays in the mechanical stability of a dipolar BEC. In section 7.3, we exploit the asymmetry of the dipole-dipole interaction (ddi) to model an experimentally realizable system that exhibits anisotropic interactions, and thus anisotropic superfluid character. By performing simulations of both weak and strong blue-detuned lasers translating through both the homogeneous quasi-two dimensional (quasi-2D) and trapped quasi-2D systems, we calculate the critical velocities for quasiparticle production and vortex formation, demonstrating the anisotropic nature of superfluidity in the dipolar BEC and illuminating the crucial role that the roton plays in this physics. Original work in this chapter has been published in [38] and [39].

7.1 Landau Critical Velocity for Superfluid Flow

Here, we derive a expression for the critical velocity for superfluid flow in terms of the quasiparticle dispersion of the superfluid, $\omega(\mathbf{p})$, as was first done by Landau in 1941 [180, 47]. To begin, we consider two inertial frames of reference, F and F', where F' is moving relative to F with velocity $\mathbf{V}$. If the superfluid has mass M, then a Galilean transformation of the momentum $\mathbf{P}$ and energy E from frame F to the frame F' is given by

$$\mathbf{P}' = \mathbf{P} - M\mathbf{V} \tag{7.1}$$

$$E' = \frac{\mathbf{P}'^2}{2M} = \frac{1}{2M}|\mathbf{P} - M\mathbf{V}|^2 = E - \mathbf{P}\cdot\mathbf{V} + \frac{1}{2}MV^2, \tag{7.2}$$

where $E = P^2/2M$ and $\mathbf{P}$ is the momentum of the superfluid in frame F.

We now consider the scenario where the fluid is moving at velocity $\mathbf{v}$ relative to an object. If the object is at rest in the frame F' and the fluid is at rest in the frame F, then the object moves with velocity $-\mathbf{v}$ relative to the fluid. If the flow dissipates, it is possible to excite a quasiparticle with, say, energy $\omega(\mathbf{p})$ and momentum $\mathbf{p}$. Then, the total energy of the fluid in the frame F is $E + \omega(\mathbf{p})$, which is just the rest energy of the fluid plus the energy of the quasiparticle, and the momentum in frame F is just $\mathbf{P} = \mathbf{p}$. Now, in the frame F', the momentum and energy of the fluid plus quasiparticle are just given by replacing $\mathbf{V}$ with $-\mathbf{v}$ and $\mathbf{P}$ with $\mathbf{p}$,

$$\mathbf{P}' = \mathbf{p} + M\mathbf{v} \tag{7.3}$$

$$E' = E + \omega(\mathbf{p}) + \mathbf{p}\cdot\mathbf{v} + \frac{1}{2}Mv^2. \tag{7.4}$$

From the results (7.3) and (7.4), we see that the quasiparticle contribution to the momentum in frame F' is just $\mathbf{p}$ and the the contribution to the energy in frame F' is $\omega(\mathbf{p}) + \mathbf{p}\cdot\mathbf{v}$. For such a process to be energetically favorable, it must then be that $\omega(\mathbf{p}) + \mathbf{p}\cdot\mathbf{v} < 0$. This is of course most easily achieved when $\mathbf{p}$ and $\mathbf{v}$ have opposing directions, which gives $\omega(\mathbf{p}) < pv$, or $v > \omega(\mathbf{p})/p$. It is the very threshold of this inequality that defines the Landau critical velocity, or the minimum relative flow velocity beyond which such a dissipative process is possible. The Landau critical velocity is thus given by

$$v_L = \min_{\mathbf{p}} \frac{\omega(\mathbf{p})}{|\mathbf{p}|}. \tag{7.5}$$

In a dispersion relation plot of the quasiparticle energy $\omega(\mathbf{k})$ as a function of momentum $\mathbf{k}$, as we see in figures 4.2 and 4.4, the Landau critical velocity is given by the minimum slope of a line that intersects both the origin $\omega(0) = 0$ and a point on the dispersion curve. For a gas with purely isotropic contact interactions, such as a dilute alkali atom BEC, v_L is set by the speed of sound in the gas. However, in superfluid ^{4}He and in trapped BECs with dipolar interactions, where rotons are present in the dispersion, v_L is set by the roton mode. While this critical velocity has been measured in the ^{4}He system [51], no such measurement has been made for a dipolar BEC. Indeed, proposing an experimentally realizable scenario in which such a measurement can be made is the main objective of the work presented in the next section.

7.2 Discrete Dipolar Superfluid

Just as we “perturbed” a dipolar BEC with a stationary blue-detuned laser in section 5.5, here we consider perturbing a dipolar BEC with a blue-detuned laser moving at constant velocity v, which results in the time-dependent potential

$$U_{\text{las}}(\mathbf{x}, t) = \frac{U_0}{\sigma} \exp\left[\frac{-2(x^2 + (y - y_{\text{ob}}(t))^2)}{\sigma \tilde{w}_0^2}\right] \tag{7.6}$$

where $\sigma = 1 + (z/z_0)^2$, $z_0 = \pi \tilde{w}_0^2/\lambda_{\text{las}}$ is the Raleigh length, $\tilde{w}_0$ is the beam waist of the laser, λ_{las} is the wavelength of the laser, $y_{\text{ob}}(t) = \Theta(t - t_0)[v(t - t_0)]$ describes the motion of the laser in the y-direction and $\Theta(t)$ is the Heaviside step function [61]. This potential describes a laser that is stationary until $t = t_0$, at which time it moves towards the edge of the condensate with velocity $\vec{v} = v\hat{y}$. The effect of this potential is taken into account by inserting it directly into the time-dependent GPE, Eq. (3.46), which we integrate using a 4th order Runge-Kutta algorithm.

The effect of this blue-detuned laser on a dipolar BEC is shown in figure 7.1 for a dipolar BEC with a trap aspect ratio $\lambda = 20$, a ddi strength $D = 124$ (where D is defined in Eq. (5.13)), and a laser with $\tilde{w}_0 = 0.4 a_\rho$ and $U_0 = 2\hbar\omega_\rho$ where we calculate the chemical potential of the unperturbed

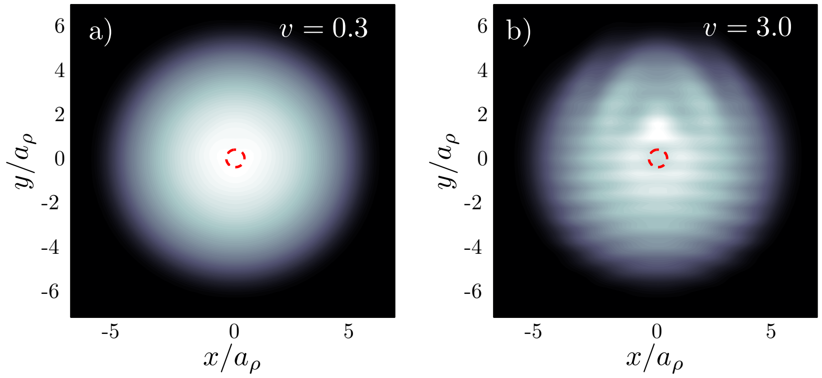

Figure 7.1: The density profiles of a dipolar BEC with $D = 124$ in a trap with aspect ratio $\lambda = 20$ after a blue-detuned laser with axis $\hat{z}$, beam waist $\tilde{w}_0 = 0.4a_\rho$, $z_0 = 1.24a_\rho$ and $U_0 = 2\hbar\omega_\rho$ has traveled through the dipolar BEC with velocity (a) $v = 0.3\ a_\rho\omega_\rho$ (b) $v = 3.0\ a_\rho\omega_\rho$. In (a), there are no visual excitations present in the system while in (b), excitations are clearly present, indicating the presence of a critical velocity for the system. The $1/e^2$ contour of the laser is shown by the red dotted lines at the center of the condensates.

condensate to be $\mu = 26.3\hbar\omega_\rho$. We estimate the Landau critical velocity for this system to be $v_L \sim 1.5\ a_\rho\omega_\rho$. For a laser velocity less than this (figure 7.1(a)), the condensate is completely unaffected whereas for a velocity larger than this (figure 7.1(b)), quasiparticles are excited and the fluid would produce a net force on the moving laser.

To determine the Landau critical velocity v_L, we first calculate the condensate's quasiparticle spectrum by solving the Bogoliubov de Gennes (BdG) equations [102]. Due to cylindrical symmetry of the system, the condensate plus BdG quasiparticles can be written as

$$\phi_0(\mathbf{x}, t) \rightarrow \phi_0(\rho, z)e^{-i\mu t} + \sum_j \left[c_j(t)u_j(\rho, z)e^{i(m\varphi - \omega_j t)} + c_j^\star(t)v_j^\star(\rho, z)e^{-i(m\varphi - \omega_j t)}\right] e^{-i\mu t} \tag{7.7}$$

where ω_j is the quasiparticle energy, m is the projection of the quasiparticle momentum onto the z-axis and μ is the chemical potential of the ground state. Here, $\phi_0(\rho, z)$ is the stationary condensate wave function, i.e., the solution of Eq. (3.23) with time-dependence $e^{-i\mu t}$, and is normalized to unity. The coefficients $c_j(t)$ must be sufficiently small so that the BdG equations can be derived by linearizing the GPE about them, as discussed in section 3.3.1. Notice that this form is identical to the usual BdG ansatz, but now the small amplitudes $c_j(t)$ have been made time dependent to describe the slowly varying quasiparticle occupations (compared to ω_j^{-1}) in out-of-equilibrium states.

In this formalism, the quasiparticles are characterized by their energies ω_j and m quantum numbers. However, in order to apply the Landau criterion to this system, the quasiparticles must be characterized by a momentum, as well. To do this, we calculate the expectation value of the momentum, or $\langle k_\rho \rangle \equiv \sqrt{\langle k_\rho^2 \rangle}$, of the quasiparticles. Using a Fourier-Hankel transform of the appropriate order (see appendix D), we transform the modes into momentum-space and compute the expectation value of the linear momentum of the j^{th} quasiparticle in momentum-space representation,

$$\langle k_\rho \rangle_j = \sqrt{\frac{\int d\mathbf{k}\, k_\rho^2 \left(|\tilde{u}_j(\mathbf{k})|^2 + |\tilde{v}_j(\mathbf{k})|^2\right)}{\int d\mathbf{k} \left(|\tilde{u}_j(\mathbf{k})|^2 + |\tilde{v}_j(\mathbf{k})|^2\right)}}, \tag{7.8}$$

where we have time-averaged cross terms $\propto \cos 2\omega_j t$ that oscillate on fast time scales [181]. By associating these momenta to the excitation energies ω_j, we determine a *discrete* dispersion relation for this system. Whereas the Landau criteria for superfluid critical velocity presented in section 7.1 is derived for a translationally invariant fluid, we apply it to this translationally *variant* system to provide a hint as to where a critical velocity for quasiparticle excitations might be and to test the application of this criterion to discrete systems.

Figure 7.2 shows the discrete dispersion relations of a dipolar BEC for various values of D. For $D = 0$ (not shown), the dispersion is given by the well known harmonic oscillator spectrum $\omega = n_\rho \omega_\rho$ with $\langle k_\rho \rangle = \sqrt{n_\rho + 1}/a_\rho$ and $n_\rho = 0, 1, 2, ...$ However, as D is increased, the spectrum changes to develop a phonon character at low-momenta and a roton character at intermediate momenta. Indeed, for $D = 175.2$, and more so for $D = 230.0$, there are some quasiparticles that branch off from the dispersion towards lower energies and approach a momentum $\langle k_\rho \rangle \sim \sqrt{20}/a_\rho$, corresponding to the characteristic roton wavelength $\lambda_{\mathrm{roton}} \simeq 2\pi a_z$, where $a_z = \sqrt{\hbar/M\omega_z}$ is the axial harmonic oscillator length [28, 35]. The modes with similar momenta but larger energy, on the upper branch of the dispersion, exist in lower-density regions of the condensate while the quasiparticles on the roton branch exist in the high density center of the condensate. Note that

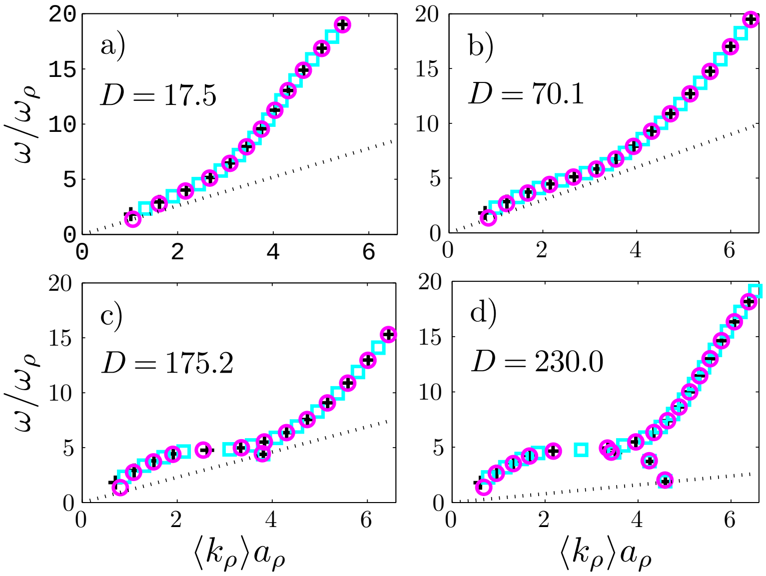

Figure 7.2: The discrete BdG quasiparticle dispersions for a dipolar BEC in a trap with aspect ratio $\lambda = 20$ for various values of D showing $m = 0$ (black + sign), $m = 1$ (teal squares) and $m = 2$ (pink circles) quasiparticles. As D is increased, the dispersion develops a phonon-like character at low momenta and a roton-like character at intermediate momenta. The slopes of the black dotted lines represent the corresponding Landau critical velocities for each D.

figure 7.2 includes only quasiparticles with $m = 0, 1, 2$.

In each case, the Landau critical velocity v_L is determined according to Eq. (7.5) as the slope of the shallowest line (or line with smallest slope) through the origin that intersects a point on the dispersion curve. These lines are indicated in the figure. For smaller D, v_L is determined by the low-momentum phonon-like modes where ω is linear in $\langle k_\rho \rangle$. By contrast, for larger D, v_L is determined by the low-lying roton mode and becomes a decreasing function of interaction strength in contrast to a BEC with only contact interactions, where v_L grows as the square root of scattering length [55, 125].

In evaluating v_L from the discrete dispersion relation, we have ignored two excitations. One is the unphysical $m = 0$ Goldstone mode [97]. A second is the $m = 1$ Kohn mode, which has eigenvalue $\omega_1 = \hbar\omega_\rho$ independent of interactions, and which corresponds to transverse sloshing of the condensate [157]. The Kohn mode moves the condensate's center of mass rather than exciting quasiparticles relative to the center of mass, which would imply the breaking of superfluidity in a translationally invariant system. We therefore ignore it here. In any event, we find that the occupation of the Kohn mode is very small compared to the total condensate depletion.

We now compare v_L as determined from the discrete dispersion relation with the onset of condensate depletion due to the laser having been moved through the dipolar BEC. To quantify the breaking of superfluidity in the simulations, we calculate the depletion of the condensate by finding the quasiparticle occupations, or the number of particles that are excited out of the condensed state. In practice, this is achieved by calculating the amplitudes $c_j(t)$ in Eq. (7.7) [182] via the orthogonality relations of the BdG modes [181] (see section 3.2) to give

$$c_j(t) = \int d\mathbf{x}' \left[u_j^\star(\mathbf{x}')\phi_0(\mathbf{x}',t) - \phi_0^\star(\mathbf{x}',t)v_j^\star(\mathbf{x}') \right] e^{i\omega_j t}, \tag{7.9}$$

where $\phi_0(\mathbf{x},t)$ is the numerical solution of the time-dependent GPE with the blue-detuned laser potential. The quasiparticle occupations are then given by $n_j(t) = |c_j(t)|^2 \int d\mathbf{x}'(|u_j(\mathbf{x}')|^2 + |v_j(\mathbf{x}')|^2)$. In the simulations, the system evolves for a time T after the laser has completely left the system. We average the quasiparticle occupations for a time T after this, giving the average excited state occupations $\bar{n}_j = \frac{1}{T}\int_0^T dt' n_j(t')$. We find that $T = 5\,\omega_\rho^{-1}$ is sufficient to converge these averages.

Figure 7.3 illustrates the total quasiparticle occupation $n_{\text{tot}} = \sum_j \bar{n}_j$ as a function of laser velocity for various values of D using the laser parameters $\tilde{w}_0 = 0.3a_\rho$, $z_0 = 0.7a_\rho$ and $U_0 = 0.4\hbar\omega_\rho$. For each D, n_{tot} stays very small until, at a certain critical velocity v_{crit}, it begins to increase significantly. Operationally, v_{crit} is determined by the intersection of linear fits below and above v_{crit}. Well above v_{crit}, the occupations decrease with velocity since the laser spends proportionally less time in the system as its velocity is increased.

Notice that the overall depletion remains small with our weak laser. We have deliberately remained in the perturbative limit with our simulations to uncover the basic physics without the complications of large laser size. Additionally, we have checked that these lasers are not sufficient to excite vortex states in the dipolar BEC. In practice, larger condensate depletion would be obtained from a repeated back-and-forth stirring, as was done in the MIT experiments, or from a wider,

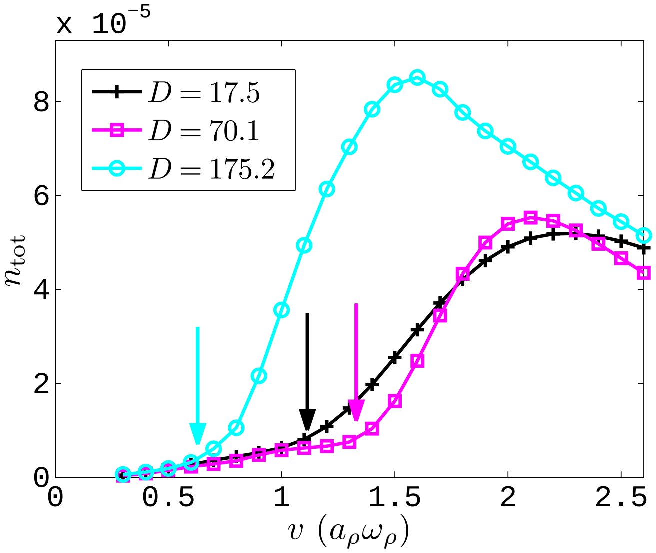

Figure 7.3: The occupations of the quasiparticles excited from a dipolar BEC with aspect ratio $\lambda = 20$ by a blue-detuned laser moving with velocity v (plotted on the horizontal axis) and with parameters $\tilde{w}_0 = 0.3a_\rho$, $U_0 = 0.4\hbar\omega_\rho$ and $z_0 = 0.7a_\rho$, for various values of D. At a critical v (indicated by the arrows), the occupations increase suddenly, indicating that the laser has excited quasiparticles in the system and superfluidity has been broken.

stronger laser. While such a laser may spin off vortices in the condensate, thus defining a critical velocity smaller than v_L, the roton, for large enough D, would still determine the critical velocity.

Critical velocities determined from numerical simulations are presented in figure 7.4 as a function of D. Results are shown for the comparatively weak ($U_0 = 0.4\hbar\omega_\rho$) and strong ($U_0 = 2\hbar\omega_\rho$) lasers. Also shown for comparison is v_L (dashed line) as determined from the discrete dispersion relations. At small D, the critical velocity grows slightly as the phonon modes stiffen and the speed of sound increases. This behavior is much like that of a BEC with purely contact interactions.

At higher density, the critical velocity instead decreases, due to the decreasing energy of the roton, and this is seen in both simulation and v_L. The agreement is less perfect than in the phonon regime, however, with the simulated result coming in lower. This is because the roton, being the collapse mechanism for dipolar BECs in traps with larger aspect ratios, softens with increasing condensate density. The presence of the laser in the dipolar BEC serves to increase the density of the system, softening the roton and thus decreasing the critical velocity of the condensate, just as

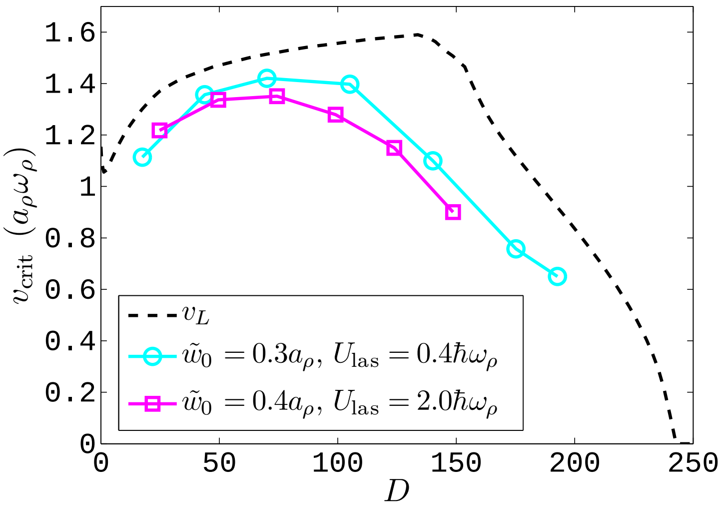

Figure 7.4: The superfluid critical velocities $v_{\rm crit}$ for dissipation due to the excitation of quasiparticles in a dipolar BEC as a function of D. The black dashed line represents the Landau critical velocity extracted from the discrete dispersion relations of the system. The teal circles represent the results of numerical simulation for a laser with parameters $\tilde{w}_0 = 0.3a_\rho$, $z_0 = 0.7a_\rho$ and $U_0 = 0.4\hbar\omega_\rho$ and the pink squares represent the results of numerical simulation for a laser with parameters $\tilde{w}_0 = 0.4a_\rho$, $z_0 = 1.24a_\rho$ and $U_0 = 2\hbar\omega_\rho$.

a stationary laser leads a dipolar BEC to instability [183]. For vanishingly small lasers, the critical velocities extracted from numerical simulation show increasingly better agreement with v_L.

Finally, it is worthwhile to consider measurements of critical velocities in experimentally accessible dipolar BECs, such as the ^{52}Cr system in Stuttgart [14]. Consider ^{52}Cr atoms whose scattering lengths have been tuned to zero in a trap with radial and axial frequencies $\omega_\rho = 2\pi \times 100$ Hz and $\omega_z = 2\pi \times 2000$ Hz, respectively. This corresponds to a radial harmonic oscillator length of $a_\rho = 1.391\,\mu$m, particle numbers of $N \sim 570D$ and critical velocities in the range of 0.11 cm/s. These circumstances suggest that it may be plausible to observe the decline of the superfluid velocity with D for $N \gtrsim 8.5 \times 10^4$ ^{52}Cr atoms, and hence to exhibit directly the roton's influence on superfluidity. This atom number corresponds to a maximum condensate density of $n_{\rm max} \simeq 9.5 \times 10^{14}$ cm^{-3}, which, given the measured 3-body loss coefficient $L_3 = 2 \times 10^{-28}$ cm^6/s [16], should not produce significant losses over the time scales considered here. Additionally, we have checked that, for sufficiently large D, the roton serves to determine v_L for ^{52}Cr dipolar BECs with non-zero

s-wave scattering lengths within the experimental uncertainty for ^{52}Cr, $-3a_0 \leq a_s \leq 3a_0$ [22], which is expected because these scattering lengths are sufficiently less than ^{52}Cr's dipole length $a_{dd} \simeq 15a_0$ [16].

Here, we have seen that the roton in the discrete dipolar BEC can play a very important role in the superfluid properties of the gas. Additionally, a measurement of the superfluid critical velocity in such a system, which is indeed within experimentally realizable limits, could provide indirect evidence of the presence of the roton in such a system. As we have discussed, the roton arises in a trapped dipolar BEC due to the anisotropy of the interactions. Interestingly, we can exploit this anisotropy further by tilting the polarization field off of the symmetry axis, in order to achieve a system where the interactions are anisotropic in-plane, and thus possess anisotropic superfluid properties.

7.3 Anisotropic Dipolar Superfluid

To simplify the problem at hand, consider a dipolar BEC in a quasi-2D, or highly pancake-shaped trapping potential with the form $U(z) = \frac{1}{2}M\omega_z^2 z^2$ and allow the dipole polarization $\hat{d}$ to be at an arbitrary angle α off of the z-axis, so $\hat{d}\cdot\hat{z} = \cos\alpha$. For sufficiently large ω_z, or for sufficiently tight trapping, we employ the separable ansatz $\phi_0(\mathbf{x},t) = \chi(z)\psi(\boldsymbol{\rho},t)$ where $\chi(z)$ is a normalized Gaussian with width l_z, which we discuss in detail in section 4.2. In such a geometry, the problem is reduced to an effectively 2D problem by integrating out the axial dependence of the relevant equations (GPE, GP energy functional). By doing this, an effective quasi-2D interaction potential is derived. For the system with dipolar and isotropic contact interactions, this potential is given by Eq. (4.23), and we derive this form explicitly in appendix C. For completeness, we write out the time-dependent GPE, Eq. (3.46), for the quasi-2D dipolar BEC here,

$$\begin{aligned} i\partial_t\psi(\boldsymbol{\rho},t) = \Big(&-\frac{1}{2}\nabla_\rho^2 + U(\boldsymbol{\rho},t) + n_{\mathrm{2D}}g|\psi(\boldsymbol{\rho},t)|^2 \\ &+ n_{\mathrm{2D}}g_d\int d\boldsymbol{\rho}' V_{\mathrm{q2D}}(\boldsymbol{\rho}-\boldsymbol{\rho}')|\psi(\boldsymbol{\rho},t)|^2\Big)\,\psi(\boldsymbol{\rho},t), \end{aligned} \tag{7.10}$$

where, in this section, we define $g = 2\sqrt{2\pi}\hbar^2 a_s/l_z M$ and $g_d = 2\sqrt{2\pi}\hbar^2 a_{dd}/l_z M$, where a_s is the 3D s-wave scattering length a_{dd} is the characteristic dipole length of the constituent dipoles, given in Eq. (2.21). Also, $n_{2\mathrm{D}}$ is the integrated density of the unperturbed (homogeneous in-plane) condensate. In (7.10), we write the trapping potential $U(\boldsymbol{\rho}, t)$ to be time-dependent to account for a moving blue-detuned laser, as discussed in the previous section. Like we do for the fully 3D case, we handle the ddi mean-field term with the convolution integral over the q2D ddi potential $V_{\mathrm{q2D}}(\boldsymbol{\rho} - \boldsymbol{\rho}')$ in momentum-space, where the momentum-space form of this potential is given by Eq. (C.8).

Additionally, in this section, we rescale energies in units of the chemical potential, given by $\mu^* = g n_{2\mathrm{D}}[1 + \epsilon_{dd}(3\cos(\alpha)^2 - 1)]$ for the unperturbed system, where $\epsilon_{dd} = g_d/g$ [148]. This leads to characteristic units of length given by the coherence length $\xi^* = \hbar/\sqrt{M\mu^*}$; time $\tau^* = \hbar/\mu^*$; and velocity $c^* = \sqrt{\mu^*/M}$. Additionally, we rescale the wave function $\psi \to \psi/\sqrt{n_{2\mathrm{D}}}$. The rescaled interaction coupling constants are then $g^* = g n_{2\mathrm{D}}/\mu^*$ and $g_d^* = g_d n_{2\mathrm{D}}/\mu^* = \epsilon_{dd} g^*$.

To begin investigating the superfluid properties of the quasi-2D dipolar BEC with anisotropic interactions, we consider the quasiparticle dispersion relation of a homogeneous quasi-2D dipolar BEC (see section 4.2),

$$\omega(\mathbf{k}) = \sqrt{\frac{k^4}{4} + k^2 g^* \left(1 + \epsilon_{dd} F\left(\frac{\mathbf{k} l_z}{\sqrt{2}}\right)\right)}, \tag{7.11}$$

where the function $F(\mathbf{q})$ is defined in appendix C. For $\alpha = 0$ (polarization along the trap axis) this dispersion does not depend on the direction of the quasiparticle propagation. However, for $\alpha \neq 0$, or for nonzero projection of $\hat{d}$ onto the x-y plane, the direction of $\mathbf{k}$ becomes important in describing the quasiparticles of the system. The Landau critical velocity is determined from the dispersion relation via Eq. (7.5), and here depends on the direction of $\mathbf{k}$ and is an anisotropic quantity when $|\cos(\alpha)| < 1$. We note that other anisotropic dispersions have been predicted for a 1D lattice system of quasi-2D dipolar BECs [184], periodically dressed BECs [185] and for dipolar gases in a 2D lattice [186]. Additionally in this vein, anisotropic solitons have been predicted for dipolar gases [187].

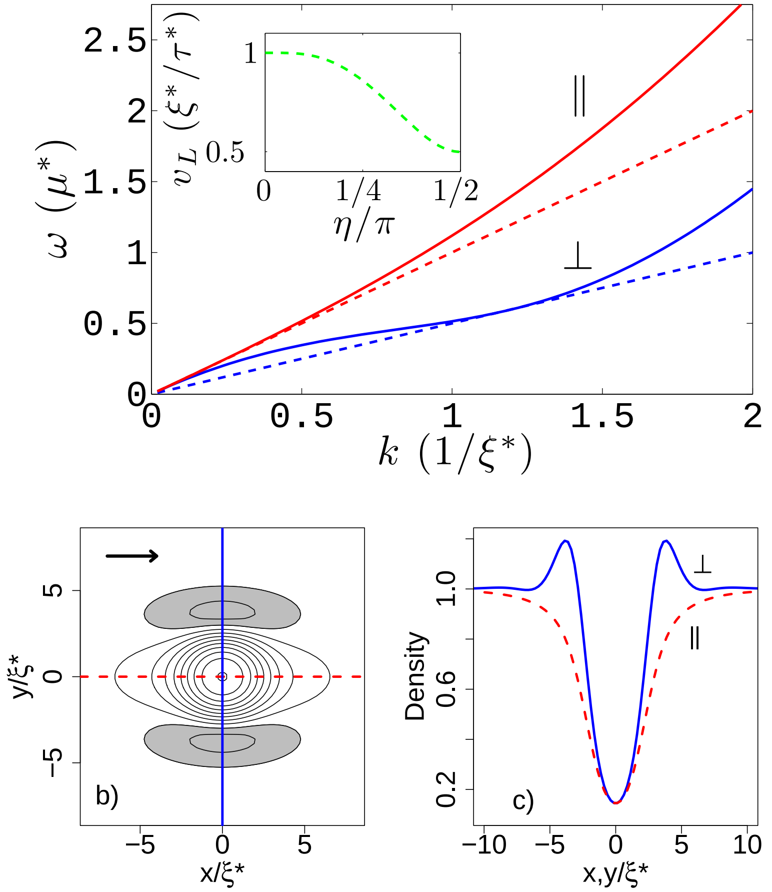

Figure 7.5: (a) The Bogoliubov dispersions for $g^* = 0.25$, $g_d^* = 1.50$, $l_z/\xi^* = 0.5$ and $\alpha = \pi/4$ for propagation perpendicular ($\perp$) to and parallel ($\parallel$) to the tilt of the dipoles, shown by the blue and red lines, respectively. The dashed lines have slopes that are the Landau critical velocities (v_L) of the dispersions, while the inset shows v_L as a smooth function of the angle η between the $\parallel$ ($\eta/\pi = 0$) and $\perp$ ($\eta/\pi = 1/2$) propagation directions. (b) A contour plot of the density for a stationary obstacle with amplitude $U_0/\mu^* = 1.0$. The shaded region indicates a density exceeding $1.05n_{2\mathrm{D}}$, and the arrow indicates the direction of polarization. (c) Density slices of (b) along the parallel (dashed red) and perpendicular (blue) directions. The density oscillation due to the roton is clear in the perpendicular case.

To illustrate the anisotropy in v_L, we use the parameters $g^* = 0.25$, $g_d^* = 1.50$, $l_z/\xi^* = 0.5$ and $\alpha = \pi/4$ ($\mu^* = 1$), which are chosen to best illustrate anisotropic effects while keeping safely away from the unstable regime; we will identify them with experimental parameters below. Figure 7.5(a) shows the dispersion calculated using these parameters for quasiparticle propagation parallel to ($\parallel$) and perpendicular to ($\perp$) the tilt of the dipoles into the plane. For parallel propagation, the dispersion resembles that of a system with contact interactions; the curve goes smoothly from the linear phonon regime at small k to the free-particle regime at large k. For this case, $v_L/c^* = 1.0$ (dashed red line), meaning that the critical velocity is identical to the speed of sound. In contrast, the perpendicular dispersion curve exhibits a roton-like feature at intermediate k, setting $v_L/c^* = 0.50$ (dashed blue line). The inset in figure 7.5(a) shows v_L as a function of the azimuthal angle, η, the angle between the polarization tilt and the direction of quasiparticle propagation. Interestingly, the speed of sound, given by $c = \lim_{k\to 0}[\omega(k)/k]$, is the same for both parallel and perpendicular propagation, $c/c^* = 1$, and is in fact isotropic. Therefore, the anisotropy in the spectrum occurs only at finite k due to the presence of an anisotropic roton.

The impact of the anisotropic roton can be directly seen in the density of the gas. In figure 7.5(b) we show a contour plot of the density in the presence of a repulsive Gaussian potential, or "probe," of the form (7.6) with $U_0/\mu^* = 1.0$ and $\sigma/\xi^* = 2.0$. We calculate this density profile by solving for the condensate wave function $\psi(\boldsymbol{\rho})$ by evolving Eq. (7.10) in imaginary time, as we discuss in chapter 5. The shaded regions indicate density above $1.05 n_{2\mathrm{D}}$, and the arrow indicates the direction of polarization. In figure 7.5(c) we plot density slices of this distribution to more clearly show the density profile in the parallel (dashed red) and perpendicular (solid blue) directions. Interestingly, the high-density regions occur in the direction perpendicular to the tilt of the dipoles, the same direction that exhibits a roton feature in the dispersion. In section 5.5, we showed that a dipolar BEC in the presence of a repulsive Gaussian can exhibit density oscillations due to the manifestation of the roton. Here, we see a manifestation of the anisotropic roton in the static structure of the quasi-2D dipolar BEC.

We now address the question of what happens to this anisotropic dipolar BEC when the probe is moved through it with velocity $\mathbf{v}$, by numerically evolving Eq. (7.10) in real time, with the repulsive Gaussian potential $U(\boldsymbol{\rho}, t) = U_{\mathrm{las}}(x - vt, y)$. For concreteness, we consider motion parallel and perpendicular to the tilt of the dipoles by tilting $\hat{d}$ into the $\hat{x}$ and $\hat{y}$ directions, respectively, while fixing the direction of the probe velocity so that $\mathbf{v} = v\hat{x}$. Figure 7.6 illustrates a schematic of this system where the polarization vector $\hat{d}$ is tilted in the x-direction. Here, the grey surface represents the condensate and the blue surface represents the blue-detuned laser. The green arrow

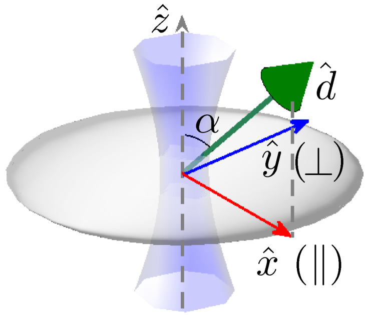

Figure 7.6: A schematic of a blue-detuned laser acting as a moving object in a dipolar BEC with anisotropic interactions. Here, the grey surface represents the condensate and the blue surface represents the blue-detuned laser. The green arrow represents the polarization vector $\hat{d}$ and the red and blue arrows show the x and y directions, respectively. In this setup, the red (x) arrow defines the parallel direction and the blue (y) arrow defines the perpendicular direction.

represents the polarization vector $\hat{d}$ and the red and blue arrows show the x and y directions, respectively. In this setup, the red (x) arrow defines the parallel direction and the blue (y) arrow defines the perpendicular direction. In this section, we identify the color red with parallel motion and the color blue with perpendicular motion.

7.3.1 Quasiparticle Production (Weak Laser)

Figure 7.7(a) shows the time-averaged drag force (averaged up to $t = 100\tau^*$) acting on a "weak" probe with parameters $U_0/\mu^* = 0.1$ and $\sigma/\xi^* = 2.0$. The force acting on the laser potential U_{las} at time t is given by [177]

$$\mathbf{F}(t) = -\int d^2\rho |\psi(\boldsymbol{\rho}, t)|^2 \vec{\nabla} U_{\text{las}}(\boldsymbol{\rho}, t). \tag{7.12}$$

In this case, the probe is sufficiently weak so that no vortices are nucleated in the fluid, and instead only quasiparticles are excited. The presence of a force on the probe signifies the excitation of quasiparticles, and thus the breakdown of superfluid flow. There is a clear anisotropic onset of force in these simulations that agrees very well with the anisotropic v_L given by the Bogoliubov dispersions in figure 7.5(a), resulting in critical velocities of $v_c/c^* = 0.90(0.46)$ for parallel (perpendicular) motion of this probe, determined by the velocity at which the drag force suddenly rises.

It has been shown that v_L is recovered as the true critical velocity only when the superfluid is perturbed by a vanishingly small object [178, 182]. Additionally, while quasiparticle excitations are a natural feature to study when considering the breakdown of superfluid flow, they may be difficult to observe experimentally. Vortices, on the other hand, are superfluid excitations in the form of topological defects that create regions of zero density and are easier to observe experimentally than quasiparticles. As forementioned, the first measurements of v_c in a BEC were from observations of the sudden onset of heating [174, 175], believed to be related to vortex production in the BECs. More recently, the Anderson group at the University of Arizona used experimental finesse to controllably create vortex pairs to observe v_c [188]. Motivated by these circumstances, we investigate the critical velocity for vortex formation in the quasi-2D dipolar BEC by using a moving probe with an amplitude that is linearly ramped from $U_0/\mu^* = 0$ to $U_0/\mu^* = 1.0$ in a time $10\tau^*$ with $\sigma/\xi^* = 2.0$. The critical velocity in this case corresponds to the probe velocity above which vortices are formed, signaling the breakdown of superfluidity.

7.3.2 Vortex Production (Strong Laser)

We observe a significant difference in the critical velocity at which vortices are formed between a probe moving parallel and perpendicular to the dipole polarization. In figure 7.7(b) we show the maximum number of vortices formed within $t/\tau^* = 100$. The critical velocities are $v_c = 0.46(0.28)$ for motion parallel (perpendicular) to the dipole tilt. These values are about half the value of the critical velocities obtained using the weaker probe, but this is not unexpected [177, 176]. As discussed previously in sections 2.1.2 and 5.3, vortices in a superfluid have quantized circulation: $\oint \mathbf{v} \cdot d\mathbf{l} = 2\pi\hbar n/m$, where $\mathbf{v}$ is the velocity field of the fluid and n is an integer, corresponding to phase winding of $2\pi n$ around the vortex core. We count vortices in our simulations by finding the phase winding on a plaquette of grid points [189].

The physical mechanism that sets the critical velocity for vortex formation is not rigorously understood. However, it is theorized that the maximum local fluid velocity about an obstacle, being larger than the background flow velocity, sets the critical velocity via the Landau criterion. This idea has been fruitful [177, 176], and we find qualitative agreement with this theory here, as

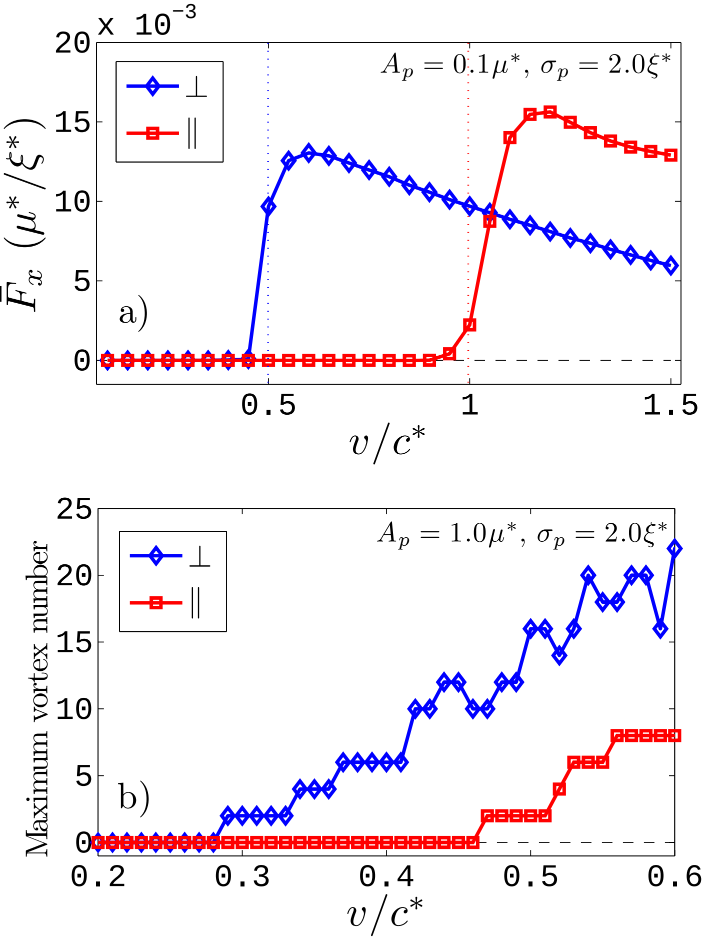

Figure 7.7: (a) The mean drag force acting on the probe with $U_0/\mu^* = 0.1$ and $\sigma/\xi^* = 2.0$ calculated up to time $t/\tau^* = 100$ for motion perpendicular to (blue diamonds) and parallel to (red squares) the dipole tilt. The dotted lines represent the corresponding v_L, in excellent agreement with the numerical simulations. (b) The maximum vortex number produced by a probe with $U_0/\mu^* = 1.0$ and $\sigma/\xi^* = 2.0$ calculated up to t/τ^*=100 for motion perpendicular to (blue diamonds) and parallel to (red squares) the dipole tilt. The corresponding critical velocities are: $v_c^{(\perp)}/c^* = 0.27$ and $v_c^{(\|)}/c^* = 0.46$.

the direction with lower v_c is also the direction of flow most likely to spawn vortices. However, we note that the ddi is anisotropic although the fully condensed (ground) state of the system is completely isotropic. The anisotropies only appear in the dispersion relation and in the ground state of the system in the presence of a perturbing potential, which is intimately related to the dispersion relation (see figures 7.5(b) and 7.5(c)) [35]. Thus, the anisotropies in the critical velocity for vortex formation are due to the anisotropy of the roton mode, just like the critical velocities for

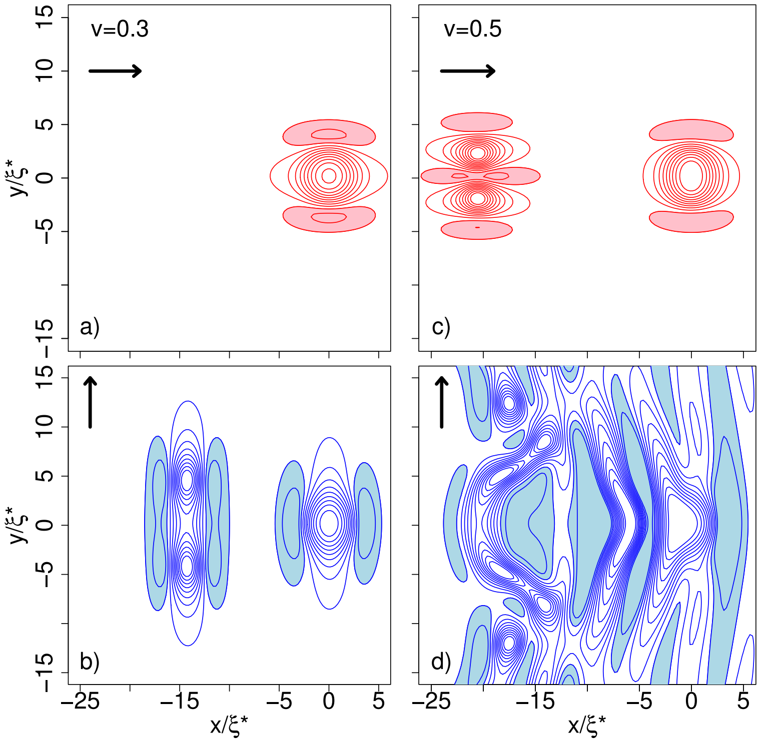

Figure 7.8: (a) and (b) The densities are shown for the $\parallel$ (top, red) and $\perp$ (bottom, blue) cases for v/c^*=0.30 and t/τ^*=125. Only the $\perp$ case has exceeded its v_c. (c) and (d) Densities for v/c^*=0.50 at t/τ^*=100. The parallel case (top, red) has exceeded its critical velocity and the perpendicular case (bottom, blue) has been wildly excited. The obstacle is at $x = y = 0$ and moving in the $+x$ direction. The shaded regions of this plot occur when the density exceeds $1.05n_{\mathrm{2D}}$, and the arrows indicate the direction of dipole tilt. An image showing the data from panel (d) made the cover of PRL **106**, Issue 6.

quasiparticle excitations.

Figure 7.8 shows contour plots of the condensate density for both parallel (red contours, top row) and perpendicular (blue contours, bottom row) motion of the probe relative to the dipole tilt for velocities $v/c^* = 0.3$ (left column) and $v/c^* = 0.5$ (right column), where the probe is moving in the $\hat{x}$ direction and is located at the origin at the time shown in figure 7.8. Recall that $v/c^* = 0.3$ is just above v_c for vortex formation for perpendicular motion, but well beneath v_c for parallel motion. This is reflected in the figure, where in (a) no vortices have been formed for parallel motion, while in (b) a vortex pair has been formed for perpendicular motion for the same probe velocity.

For the case of $v/c^* = 0.5$, we see that the parallel case in (c) has formed a vortex pair, and in

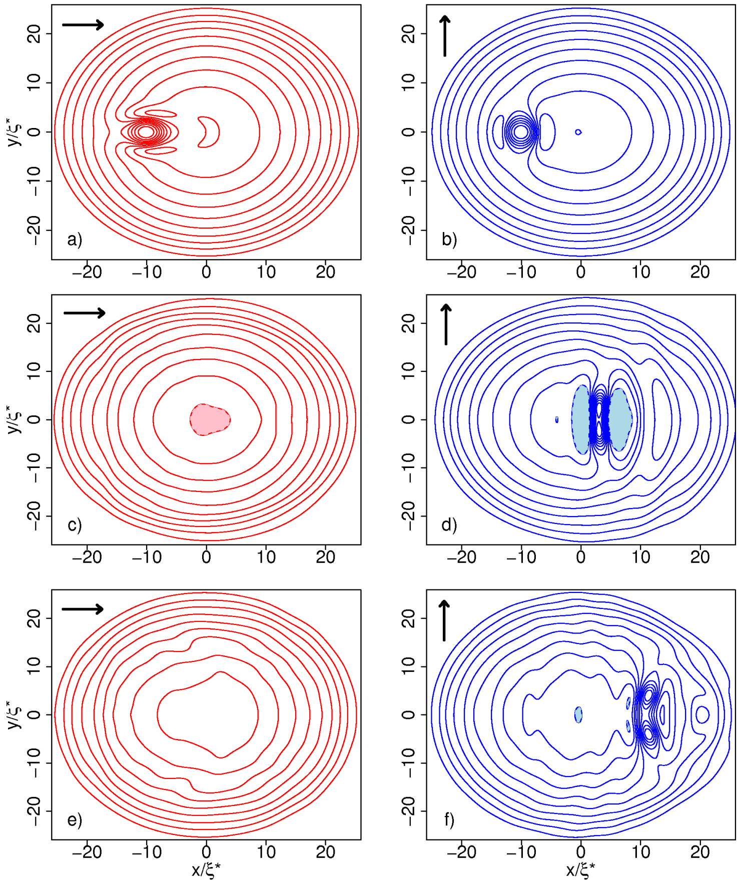

Figure 7.9: Density contours from simulations of a blue-detuned laser translating through a dipolar BEC with velocity $v/c^\star = 0.4$ in a trap with aspect ratio $\lambda = 50$, as discussed in the text. (a) and (b) are at $t/\tau^\star = 0$, (c) and (d) are taken just after the laser has left the condensate and (e) and (f) are taken well after the laser has left the condensate. The red profiles (a), (c) and (e) represent motion of the laser parallel ($\|$) to the polarization tilt and the blue profiles (b), (d) and (f) represent motion perpendicular ($\perp$) to this tilt. One clearly sees a vortex pair that has been nucleated in the perpendicular case, but not in the parallel case. Image courtesy of Chris Ticknor.

(d) the perpendicular case has been wildly excited. There is an important contrast to be made in the density profiles when there is a single vortex pair in (b) and (c). In the parallel case (c) we see that a *high* density region occurs between the vortex pair and is elongated in the polarization direction. In contrast, for the perpendicular case (b) there is a low density region between the vortex pair and high density regions on either side of the vortex pair. Both the anisotropic superfluid critical velocity for vortex pair production and these contrasting density profiles present means to observe the effects of the roton in dipolar BEC directly.

In addition to investigating the purely quasi-2D system, we have performed simulations for a quasi-2D dipolar BEC in the presence of a radial trapping potential. For a trap aspect ratio of $\lambda = 50$, we find that critical velocities for vortex production are strongly anisotropic, and the v_c are numerically similar to the free case. In these simulations, we start the probe in the center of the trap and move outwards in the parallel or perpendicular direction, linearly ramping the amplitude of the laser down to zero by the time it reaches the zero density region. Such a simulation is experimentally realizable in a dipolar BEC of atomic ^{52}Cr, for example, having a permanent magnetic dipole moment of $6\mu_B$ where μ_B is the Bohr magneton, for a dipolar BEC with particle number $N \simeq 18.5 \times 10^3$, scattering length $a_s = 5.0a_0$ where a_0 is the Bohr radius, radial trap frequency $\omega_\rho = 2\pi \times 20$Hz and a blue-detuned laser with width $\sigma = 1.76\mu$m. The speed of sound in this system is $c = 0.16\,\mathrm{cm/s}$ in the center of the trap. We plot frames from these simulations for $v/c^\star = 0.4$ in figure 7.9, where the left panel ((a), (c) and (e)) shows motion of the laser parallel to the polarization tilt and the right panel ((b), (d) and (f)) shows motion perpendicular to this tilt. The times at which these frames are sampled are $t/\tau^\star = 0$ ((a) and (b)), just after the laser leaves the condensate ((c) and (d)), and well after the laser has left the condensate ((e) and (f)). Here, one clearly sees that a vortex pair has been nucleated in the perpendicular case, but not in the parallel case, signifying the breaking of superfluidity for perpendicular flow and superfluid flow in the parallel direction.

7.4 Conclusion

In this chapter, we characterized the superfluid properties of dipolar BECs with regards to superfluid flow and the superfluid critical velocity. For the fully trapped, 3D dipolar BEC, we showed that the discrete roton plays a crucial role in the superfluidity of this system by serving to lower the critical velocity as a function of ddi strength D. By direct numerical simulations, we proposed an experiment that could provide both a measurement of the superfluid critical velocity in a dipolar BEC of ^{52}Cr and provide evidence of the roton in this system.

Additionally, we characterized the quasi-2D dipolar BEC as an anisotropic superfluid by performing numerical simulations of a blue-detuned laser moving through the system in directions parallel and perpendicular to the dipole polarization. We found a sudden onset of drag on the laser at velocities that depend strongly on the direction of motion, and attribute the anisotropy in critical velocity to the anisotropic roton so that a measurement of an anisotropic critical velocity in a dipolar BEC corresponds to a measurement of the roton in the system. Additionally, by considering a dipolar BEC that is experimentally realizable with atomic ^{52}Cr, we propose a single, stable constituent with which to study anisotropic superfluidity. As discussed in section 2.3.1, a candidate geometry for creating quasi-2D systems is a retro-reflected laser that results in a 1D lattice trapping geometry. We go on now to study the static properties of a dipolar BEC in a 1D lattice.

Chapter 8

Dipolar Bose-Einstein Condensate on a One-Dimensional Lattice

As we have seen in the previous chapters, the physics of a dipolar system depends strongly on the geometry of the trap in which it is held. For example, in section 4.2 we saw that a dipolar Bose-Einstein condensate (BEC) in a quasi-two dimensional (quasi-2D) geometry experiences a roton instability that can be suppressed by increasing the trap frequency or, equivalently, tightening the trap in the direction of polarization. Another example of such stabilization involves the inelastic scattering processes of both bosonic and fermionic species, which are predicted to be highly suppressed in tighter, quasi-two dimensional (quasi-2D) traps when the trap is applied along the polarization axis of the dipoles [133, 190, 191, 131, 130]. This suppression leads to more stable, longer-lived many-body systems of reactive molecular species. So, we see that tight trapping in the direction of polarization is necessary to obtain stable, high density dipolar quantum fluids of both atomic and molecular species.

Such a trap is realizable in a one-dimensional (1D) optical lattice, as discussed in section 2.3.1, which can be created by retro-reflecting a laser back onto itself. The presence of the lattice brings up an interesting point regarding the physics of such a system. While the dipole-dipole interaction (ddi) is anisotropic, it is also long-range, scaling as $1/r^3$, and if the lattice spacing is sufficiently small compared to the characteristic dipole length a_{dd} then the effect of the ddi is non-negligible between the lattice sites. For example, interlayer superfluidity is predicted to exist in two adjacent layers of polar fermions [9, 10, 11], and scattering in the 2D plane is predicted to be significantly modified by the presence of a weakly bound state of dipoles in adjacent layers [192]. Dramatic effects are predicted for layers of bosons, as well, for both quasi-2D [193, 184] and radially trapped [194, 195] lattice sites. The presence of the lattice is predicted to significantly alter the dispersion via the softening of a roton-like mode in the system, and thus to alter the stability properties of the Bose gas.

In this chapter, we consider a gas of bosonic dipoles in a 1D lattice with the dipoles polarized along the lattice axis, so that the system is cylindrically symmetric. Assuming that the lattice recoil is sufficiently large, we model the potentials of the individual sites as cylindrically symmetric harmonic traps. At ultracold temperatures, this leads to a lattice of non-overlapping dipolar BECs coupled by the long-range ddi. We study the stability of this system both for an infinite and finite 1D lattice. Additionally, we find regions in parameter space where biconcave structure is predicted to exist that is emergent in the lattice system, in other words, that does not exist in a single condensate. To ensure the accuracy of our results, we calculate the elementary excitations of the system and use them to determine whether our solutions are dynamically stable. In doing so, we map the structure and stability of a 1D lattice of purely dipolar BECs. Original work in this chapter has been published in [40].

8.1 Formalism for the One-Dimensional Lattice

Consider a 1D lattice with spacing d_{lat} between adjacent sites. If the lattice is sufficiently deep, it can be modeled by a series of N_{lat} harmonic traps, where each site is described by a cylindrically symmetric potential $U_j(\mathbf{x}) = \frac{1}{2}M\omega_\rho^2\left(\rho^2 + \lambda^2(z - jd_{\mathrm{lat}})^2\right)$, where M is the mass of the individual bosons and $\lambda = \omega_z/\omega_\rho$ is the trap aspect ratio of each trap. We describe this system with a coupled set of non-local Gross-Pitaevskii equations (GPEs)

$$\left\{\hat{H}_j^{(1)}(\mathbf{x}) + \sum_{j'=1}^{N_{\mathrm{lat}}} U_d^{j'}(\mathbf{x}) - \mu_j\right\}\phi_{0,j}(\mathbf{x}) = 0, \tag{8.1}$$

where $\hat{H}_j^{(1)}(\mathbf{x})$ is the non-interacting, or single-particle Hamiltonian for site j,

$$\hat{H}_j^{(1)}(\mathbf{x}) = -\frac{1}{2}\nabla^2 + U_j(\mathbf{x}), \tag{8.2}$$

$\phi_{0,j}(\mathbf{x})$ is the condensate wave function at site j, j is an integer and μ_j is the corresponding chemical potential. Without the presence of the long-range ddi, these N_{lat} equations would be independent. The ddi couples the equations through the mean-field potentials $U_d^j(\mathbf{x})$, given by the convolution

$$U_d^j(\mathbf{x}) = \int d\mathbf{x}' V_d(\mathbf{x}-\mathbf{x}')n_j(\mathbf{x}') \tag{8.3}$$

where $n_j(\mathbf{x}) = |\phi_{0,j}(\mathbf{x})|^2$ is the density of the condensate occupying the j^{th} site with norm $\int d\mathbf{x}' n_j(\mathbf{x}') = N_j$, N_j is the condensate number for site j and $V_d(\mathbf{x}-\mathbf{x}')$ is the two-body ddi potential, Eq. (3.61). A description of the fully-condensed, stationary state of this system of dipolar BECs is then given by the set of solutions $\{\phi_{0,j}(\mathbf{x}), \mu_j\}$ that minimize the energy functional corresponding to Eq. (8.1), given by

$$E[\{\phi_{0,j}(\mathbf{x})\}] = \sum_j \int d\mathbf{x}\, \phi_{0,j}^\star(\mathbf{x}) \left\{ \hat{H}_j^{(1)}(\mathbf{x}) + \frac{1}{2}\sum_{j'=1}^{N_{\mathrm{lat}}} U_d^{j'}(\mathbf{x}) \right\} \phi_{0,j}(\mathbf{x}). \tag{8.4}$$

As we have discussed, a full description of a dilute BEC of interacting atoms or molecules includes a short-range s-wave part, proportional to the s-wave scattering length. However, because this interaction is short-range, it results in the mean-field potential $U_c^j(\mathbf{x}) = g|\phi_{0,j}(\mathbf{x})|^2$. Modeling a system of non-overlapping BECs in a 1D lattice interacting only via contact interactions results in a set of uncoupled GPEs. While the interplay of contact and ddi interactions is predicted to produce interesting effects [156] that would likely be modified by the presence of the lattice, we set $a_s = 0$ in this chapter to illuminate purely dipolar effects.

As we have done previously, the dipolar mean-field is calculated in momentum-space to eliminate the problems associated with the divergence of the ddi in real-space. Here, it will prove useful to define the shifted densities $\nu_j(\mathbf{x}) = n_j(\mathbf{x}_j)$ where $\mathbf{x}_j = \{\rho, z - jd_{\mathrm{lat}}\}$, so that all $\nu_j(\mathbf{x})$ are formally centered about the origin. Then, $\nu_j(\mathbf{x}_{-j}) = n_j(\mathbf{x})$, and we can write $\tilde{n}_j(\mathbf{k}) = \mathcal{F}[\nu_j(\mathbf{x}_{-j})]$. With some simple manipulation, this expression reduces to

$$\tilde{n}_j(\mathbf{k}) = \mathcal{F}\left[\nu_j(\mathbf{x})\right] e^{ik_z d_{\mathrm{lat}} j}. \tag{8.5}$$

So, the momentum-space density of the dipolar BEC at site j can be rewritten as the Fourier transform of $n_j(\mathbf{x})$ translated into the local set of coordinates, with an additional exponential term accounting for this spatial translation. Now, by the convolution theorem (see appendix A), the mean-field contribution from the dipolar BEC at site j can be written as

$$U_d^j(\mathbf{x}) = \mathcal{F}^{-1}\left[\tilde{V}_d(\mathbf{k})\tilde{n}_j(\mathbf{k})\right] \tag{8.6}$$

where $\tilde{V}_d(\mathbf{k})$ is the Fourier transform of the ddi, given in Eq. (3.62). In this work, we calculate $\nu_j(\mathbf{x})$ directly by calculating the shifted condensate wave functions $\Phi_j(\mathbf{x})$ such that $\nu_j(\mathbf{x}) = |\Phi_j(\mathbf{x})|^2$ and account for the spatial separation of the dipolar BECs, or the presence of the lattice, with the expression given in Eq. (8.5). So, the wave functions $\phi_{0,j}(\mathbf{x})$ and $\Phi_j(\mathbf{x})$ are related by $\Phi_j(\mathbf{x}) = \phi_{0,j}(\mathbf{x}_j)$.

8.2 Wave Function Ansatz

As we have seen for a single dipolar BEC, calculating the mean-field energy on a full numeric grid has proven fruitful, however, this method is very computationally expensive when considering multiple interacting dipolar BECs, both in real- and momentum-space. In real-space, the convolution integral for the dipolar mean-field must be done directly, where there is no $1/r^3$ divergence if the condensates do not overlap. In momentum-space, the grid must be large enough to resolve the entire lattice because of the $e^{ik_z d_{\text{lat}} j}$ dependence of the momentum-space densities. To avoid these problems, we consider solutions of the form $\Phi_j(\mathbf{x}) = \psi_j(\rho)\chi_j(z)$ where

$$\chi_j(z) = \frac{1}{\sqrt{1+A_{2,j}^2}}\left(\chi_{0,j}(z) + A_{2,j}\chi_{2,j}(z)\right), \tag{8.7}$$

$$\chi_{0,j}(z) = \frac{1}{\sqrt{l_{z,j}}\pi^{\frac{1}{4}}}\exp\left[-\frac{z^2}{2{l_{z,j}}^2}\right] \tag{8.8}$$

and

$$\chi_{2,j}(z) = \frac{1}{2\sqrt{2l_{z,j}}\pi^{\frac{1}{4}}}\exp\left[-\frac{z^2}{2{l_{z,j}}^2}\right]H_2\left(\frac{z}{l_{z,j}}\right), \tag{8.9}$$

where $H_2(x) = 4x^2 - 2$ is the second Hermite polynomial [54]. This ansatz includes the zeroth and second harmonic oscillator wave functions with variable width and relative amplitude. Plugging this ansatz into the GPE and integrating out the z-dependence results in a modified GPE in the

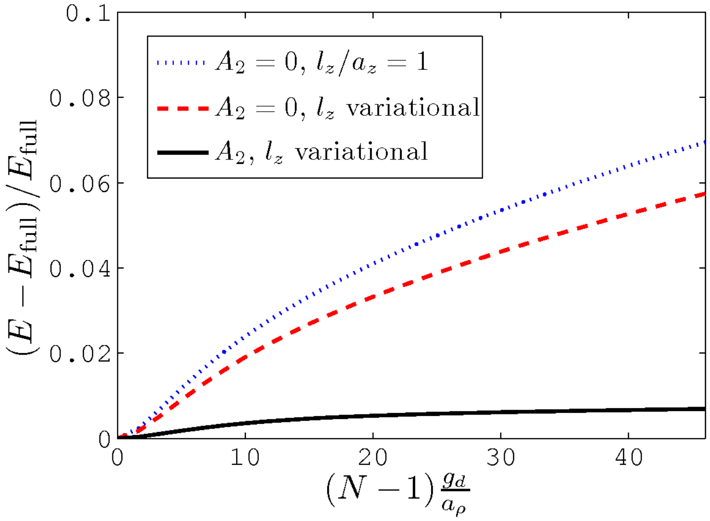

Figure 8.1: The differences in energy of a dipolar BEC in a trap with aspect ratio $\lambda = 7$ as a function of interaction strength between that calculated using the ansatz given in Eq. (8.7) and that calculated exactly on a full numeric grid. The blue dotted line shows the energy difference calculated using no 2^{nd} order h.o. wave function and a fixed axial width $l_z = a_z$, the red dashed line shows the energy difference using the same wave function but with l_z treated variational and the black solid line shows the energy difference including the 2^{nd} order h.o. wave function where the relative amplitude A_2 and l_z are treated variationally.

radial coordinate ρ that also depends on the widths $l_{z,j}$ and the relative amplitudes $A_{2,j}$ of the axial wave functions, but not the z-coordinate explicitly. We derive this modified GPE for a single dipolar BEC, given by Eq. (H.2), in Appendix H.

To test the ansatz given in Eq. (8.7), we apply it to the well known system of a single dipolar BEC in a harmonic trap. For this case, using the wave function (8.7) gives us an effectively $N_\rho + 2$ dimensional numeric problem, where we use a numeric grid in ρ with N_ρ grid points (see appendix D) and two variational parameters (for the single dipolar BEC), l_z and A_2. To minimize the corresponding energy functional, we employ the conjugate gradients (cg) algorithm (see appendix E) with fixed l_z and A_2, then minimize the resulting functional of these variational parameters between each cg iteration. Having achieved sufficient convergence in the energy minimization, we solve the corresponding Bogoliubov de Gennes (BdG) equations (3.34) in the single mode approximation, where the low-lying BdG modes are assumed to occupy the same axial wave function of the condensate.

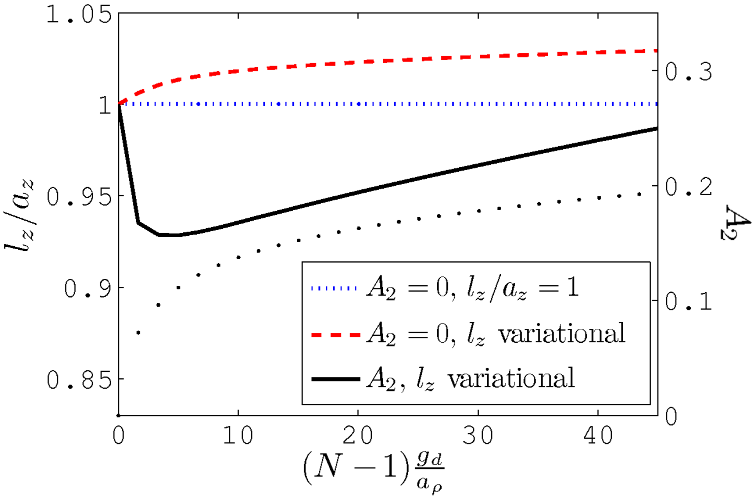

Figure 8.2: The values of the axial wave function parameters that, together with the radial wave function calculated on a grid, minimize the energy of a single dipolar BEC in a trap with aspect ratio $\lambda = 7$. The blue dotted line shows the result for $l_z = a_z$, the red dotted line shows the values of l_z when it is treated variationally and $A_2 = 0$ and the black solid line shows the values of l_z when it and A_2, the black dotted line (marked by the right vertical axis) are both treated variationally.

Figure 8.1 compares the total energies of a single dipolar BEC in a trap with $\lambda = 7$ as a function of the ddi strength $(N-1)g_d/a_{\text{ho}}$, where, in this chapter, we find it convenient to redefine $g_d = \frac{2\sqrt{2\pi}\hbar^2 a_{dd}}{M}$. Plotted is the energy difference $(E - E_{\text{full}})/E_{\text{full}}$, where E_{full} is the energy calculated by solving the GPE exactly (within strict numerical precision) on a full numeric grid in ρ and z. The blue dotted line shows the energy of the dipolar BEC when $A_2 = 0$ and l_z is fixed to be the axial harmonic oscillator length, $a_z = \sqrt{\hbar/M\omega_z}$, the red dashed line shows the energy when $A_2 = 0$ and l_z is treated variationally, and the black line shows the energy when A_2 and l_z are both treated variationally. Clearly, the full variational treatment is much more accurate than the cases where the second harmonic oscillator wave function is not included ($A_2 = 0$). Indeed, it stays within 1% of the exact energy for all values of $(N-1)g_d/a_\rho$ for which the dipolar BEC is stable. We find this to hold true for larger trap aspect ratios, as well. Figure 8.2 shows the values of the variational parameters for the same cases as in figure 8.1. In this figure, the left vertical axis labels l_z/a_z and the right vertical axis labels A_2, shown by the black dots.

Beyond energetics, this ansatz also predicts semi-quantitatively the structure and stability

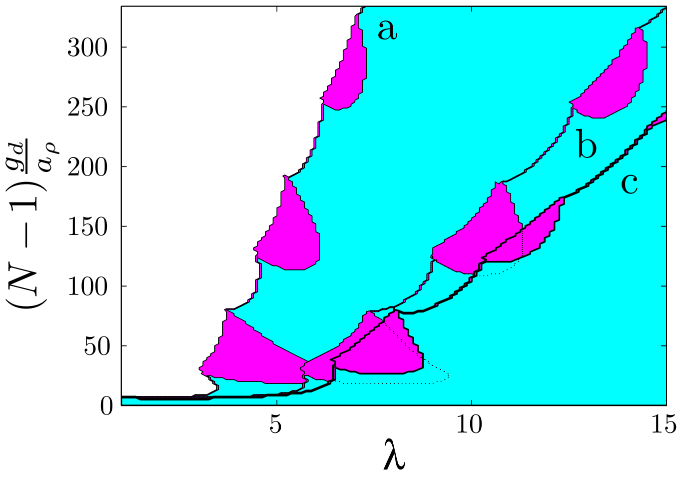

Figure 8.3: Structure/stability diagram for a single dipolar BEC. The colored regions indicate a dynamically stable condensate, and the pink (darker) regions indicate parameters for which the dipolar BEC has biconcave density. (a) and (b) are calculated using the ansatz for the axial wave function given in Eq. (8.7) and (c) is calculated using a full numeric grid. For (a), $A_2 = 0$ and $l_z/a_z = 1$, and for (b), A_2 and l_z are treated variationally.

of a single dipolar BEC. An interesting feature of the biconcave structure discussed in section 5.2 and chapter 6 is that it exists in "islands" of parameter space, defined here by $(N-1)g_d/a_\rho$ and λ. Figure 8.3 shows this structure/stability diagram for a single dipolar BEC calculated using a) $A_2 = 0$ and $l_z/a_z = 1$, b) A_2 and l_z variational and c) a full numeric grid in ρ and z. Interestingly, the biconcave islands are present in each diagram and occur for almost exactly the same values of the ddi strength $(N-1)g_d/a_\rho$. They are, however, shifted in λ, moving to smaller values as more restrictions are placed on the condensate wave function. The diagram for the full variational ansatz (b) qualitatively matches that of the full numeric grid. Thus, we expect that this ansatz will give physically meaningful results, if not quite quantitative ones. Of course, the diagram (c) in figure 8.3 is exactly that shown in figure 5.1.

As we discuss below, a key benefit of this ansatz for the 1D lattice system is that it is analytic in z. Another such ansatz that has this property is that of correlated Gaussians, which have been shown to reproduce the results of full numeric calculations for dipolar BECs quite well [196]. However, we applied this ansatz to the lattice system and found that it is numerically unstable with the minimization techniques used here.

8.3 Infinite lattice

With confidence in the ansatz given in Eq. (8.7), we now apply it to the 1D lattice system. An interesting example to consider is that of an infinite lattice, with $N_{\text{lat}} \to \infty$. This approximation introduces a discrete invariance to the system so that we can set $\Phi_j(\mathbf{x}) = \Phi_{j'}(\mathbf{x})$ for all j, j'. Thus, we can neglect, for the time being, the indexing of the wave functions and let $\Phi_j(\mathbf{x}) \to \Phi(\mathbf{x})$ for all j. Then, the mean field potential at any site is, from Eq. (8.5), given by

$$U_d(\mathbf{x}) = \sum_{j=-\infty}^{\infty} \int d\mathbf{k} \tilde{V}_d(\mathbf{k}) \tilde{n}(\mathbf{k}) e^{ik_z d_{\text{lat}} j} e^{-i\mathbf{k}\cdot\mathbf{x}} \tag{8.10}$$

where

$$\tilde{n}(\mathbf{k}) = \tilde{n}_\rho(k_\rho) \frac{e^{-\frac{1}{4}k_z^2 l_z^2}}{1+A_2^2} \left(1 + A_2 \left(A_2 - \left(\frac{1}{\sqrt{2}} + A_2\right) k_z^2 l_z^2 + \frac{1}{8} A_2 k_z^4 l_z^4\right)\right). \tag{8.11}$$

Additionally, we manipulate the infinite sum in Eq. (8.10) to give [197]

$$\sum_{j=-\infty}^{\infty} e^{ik_z d_{\text{lat}} j} = \frac{2\pi}{d_{\text{lat}}} \sum_{j=-\infty}^{\infty} \delta\left(k_z - \frac{2\pi j}{d_{\text{lat}}}\right). \tag{8.12}$$

The term that accounts for the infinite lattice can therefore be written as a Dirac comb in k_z with spacing $2\pi/d_{\text{lat}}$ between peaks. Inserting this expression into Eq. (8.10) gives the mean-field potential

$$U_d(\mathbf{x}) = 2\frac{g_d}{d_{\text{lat}}} \mathcal{F}_{2\text{D}}^{-1} \left[F_{\text{inf}}(k_\rho) \tilde{n}_\rho(k_\rho)\right], \tag{8.13}$$

where $2g_d F_{\text{inf}}(k_\rho)/d_{\text{lat}}$ is the effective momentum-space ddi for the infinite lattice and $F_{\text{inf}}(k_\rho)$ is given by

$$\begin{aligned} F_{\text{inf}}(k_\rho) = \sqrt{\frac{\pi}{2}} \sum_{j=-\infty}^{\infty} \frac{e^{-2\pi^2 j^2 \frac{l_z^2}{d_{\text{lat}}^2}}}{(1+A_2^2)^2} &\left[1 + A_2 \left(A_2 - \left(\frac{1}{\sqrt{2}} + A_2\right) 4\pi^2 j^2 \frac{l_z^2}{d_{\text{lat}}^2} + 2A_2 \pi^4 j^4 \frac{l_z^4}{d_{\text{lat}}^4}\right)\right]^2 \\ \times &\left(\frac{12\pi^2 j^2}{k_\rho^2 d_{\text{lat}}^2 + 4\pi^2 j^2} - 1\right). \end{aligned} \tag{8.14}$$

Thus, we see that the GPE for an infinite lattice of interacting dipolar BECs is reduced to a single GPE in the radial coordinate ρ where all of the axial dependence of the wave function is captured by the variational parameters A_2 and l_z.

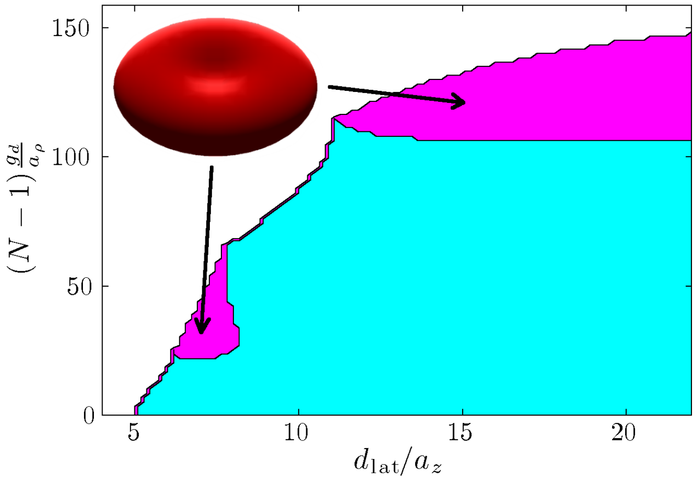

Figure 8.4: Structure/stability diagram for an infinite lattice of dipolar BECs in traps with aspect ratio $\lambda = 10$ as a function of lattice spacing d_{lat}/a_z and interaction strength $(N-1)g_d/a_\rho$. The colored region indicates dynamic stability, while the pink (darker) regions indicate parameters where the dipolar BECs have biconcave density. The inset shows an isodensity plot of a dipolar BEC with biconcave density.

We study the structure and stability of this infinite lattice of interacting dipolar BECs by solving the modified GPE for the system (again, by applying conjugate gradients to minimize the corresponding energy functional, see appendix E) and studying the BdG excitations in the single mode approximation. We find that the sum in Eq. (8.14) is sufficiently converged if a cutoff j_{cut} is applied to the index j such that $j_{\mathrm{cut}} \gg d_{\mathrm{lat}}/2\pi l_z$.

Consistent with other results [193, 184], we find that the presence of the lattice serves to destabilize the system due to the softening of a discrete roton-like mode in the system. For a single dipolar BEC in a trap, tight axial confinement aligns the dipoles so that they are predominately repulsive and, for sufficiently low densities or interactions strengths, stabilizes the condensate. In the presence of a 1D lattice, the attraction from the dipoles at other lattice sites extends the condensate in the axial direction, increasing the integrated axial density and, ultimately, making the system less stable. This destabilization is made less dramatic as d_{lat} is increased.

To study the structure and stability of the infinite lattice, we choose specific trap aspect ratios and explore the parameter space defined by $(N-1)g_d/a_\rho$ and d_{lat}. Figure 8.4 shows the

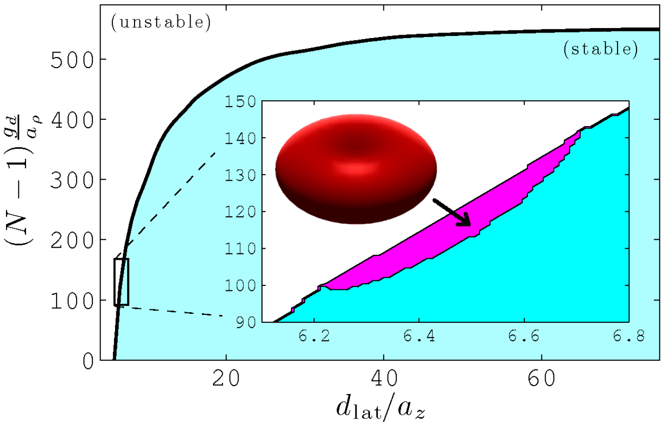

Figure 8.5: Structure/stability diagram for an infinite lattice of dipolar BECs in traps with aspect ratio $\lambda = 20$ as a function of lattice spacing d_{lat}/a_z and interaction strength $(N-1)g_d/a_\rho$. The inset shows a close-up of the diagram at the parameters indicated. The pink (darker) region in the inset indicated parameters where the dipolar BECs have biconcave density. An isodensity plot of a dipolar BEC with biconcave density is shown in this inset.

region of dynamic stability for an infinite lattice of dipolar BECs in traps with $\lambda = 10$. For lattice spacings $d_{\mathrm{lat}}/a_z \lesssim 5$, the condensate wave functions at adjacent sites overlap and the strong dipole-dipole attraction leads to complete instability. In this figure, the colored regions indicate dynamic stability and the pink (dark) regions indicate parameters at which the dipolar BECs exhibit biconcave density. As d_{lat}/a_z is increased, the diagram approaches that given by a line at $\lambda = 10$ in figure 8.3 for a single dipolar BEC. However, for smaller lattice spacings, a second biconcave island appears. Without the presence of the lattice, biconcave structure would not exist for these parameters. Thus, this structure is “emergent” in the lattice system. The inset in figure 8.4 shows an isodensity plot of a dipolar BEC with biconcave density.

Figure 8.5 shows the region of dynamic stability up to lattice spacings of $d_{\mathrm{lat}}/a_z = 80$ for a infinite lattice of dipolar BECs in harmonic traps with $\lambda = 20$. Here, the convergence of the stability line to $(N-1)g_d/a_\rho \sim 550$ is clear. The inset shows a close-up view of the diagram where a biconcave island is predicted to exist. As the aspect ratio is increased, the values of interaction strength $(N-1)g_d/a_\rho$ that the biconcave islands span becomes relatively smaller compared to the asymptotic value of the stability line. Figure 8.6 shows the stability lines for infinite lattices with

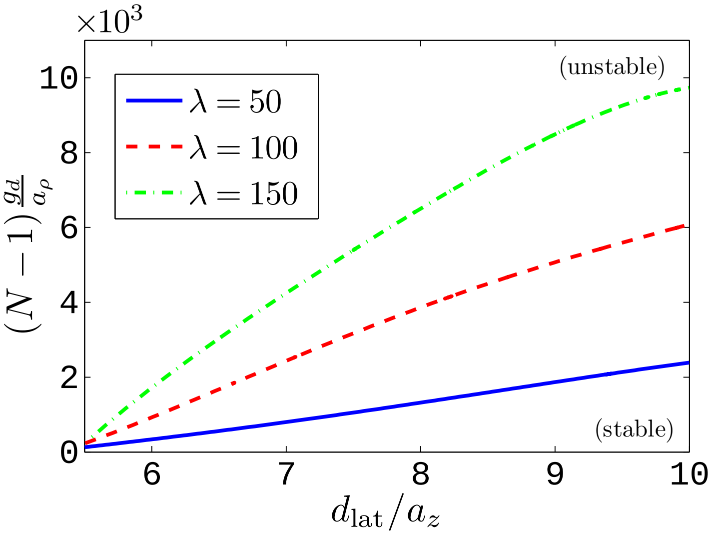

Figure 8.6: Stability lines for an infinite lattice of dipolar BECs for aspect ratios $\lambda = 50, 100, 150$ as a function of lattice spacing d_{lat}/a_z and interaction strength $(N-1)g_d/a_\rho$. The parameters beneath the lines are dynamically stable, while those above the lines are dynamically unstable.

aspect ratios $\lambda = 50, 100, 150$. We find stability islands that exist at the stability threshold within the lattice spacings $d_{\mathrm{lat}}/a_z = 6$ to 10 for all of these aspect ratios. Because they are so narrow in $(N-1)g_d/a_\rho$, though, they are not included in this plot.

By working in the ρ- and z-coordinates, a cylindrical symmetry is assumed. However, we know from chapters 5 and 6 that dipolar BECs with biconcave density profiles are dynamically unstable to angular modes, or quasiparticles. While the method used here is sensitive to dynamic instabilities that are purely radial, an extra step must be taken to detect angular instabilities. To do this, we solve the BdG equations where the BdG modes are assumed to have the form (5.6). In doing so, we treat the system as a single dipolar BEC with a modified mean-field potential due to the presence of BECs in other lattice sites, where the other BECs are stationary and are not excited. Like the single dipolar BEC in section 5.2, we find that the biconcave structures in the infinite lattice are, for some critical density or ddi, dynamically unstable to angular quasiparticles with $m \geq 2$. In chapter 6, we show that this angular instability leads to angular collapse, or collapse with angular nodes, of the biconcave dipolar BECs. A measurement of the character of collapse, whether it be radial or angular, then provides a tool to map the structure along the stability threshold of the system.

In our analysis, we found exotic ground state densities very close to the stability threshold, like those found for a finite lattice in Ref. [194]. These solutions host multiple radial density oscillations, however, we find they are dynamically unstable and are thus unlikely to be experimentally observable.

8.4 Finite Lattice

While the infinite lattice of dipolar BECs provides a clear, simple example of emergent structure in this system, it is a difficult system to realize experimentally. In a realistic experiment, the lattice has a finite extent and the occupations of the sites vary from site to site. To model this more realistic lattice system, we consider an odd number of occupied lattice sites indexed by $j \in [-j_{\text{lat}}, j_{\text{lat}}]$ where $j_{\text{lat}} = (N_{\text{lat}} - 1)/2$ with particle number given by a Gaussian distribution, $N_j = N_{\text{max}} \exp\left[-(j/j_{\text{lat}})^2\right]$, where N_{max} is the particle number in the condensate in the center of the lattice at site $j = 0$, and the outer-most sites have particle number N_{max}/e [194].

Instead of using an analytic form for the axial parts of the condensate wave functions, we solve the coupled set of GPEs given by Eq. (8.1) on a full grid (large enough to encapsulate the entire lattice) in ρ and z for each condensate. We find good convergence by using the conjugate gradients method to minimize the full energy functional of the system [102]. Additionally, to ensure numerical precision we apply a cutoff to the ddi in ρ and z so that a relatively small grid can be used while eliminating the effects of artificial "image" condensates that are present due to the use of the FFT algorithm in our calculation. We give the momentum-space form of the ddi with such a cutoff in section 5.1.1.

As an example, we consider a lattice with trap aspect ratios $\lambda = 50$, $j_{\text{lat}} = 4$ (corresponding to 9 occupied lattice sites), lattice spacing $d_{\text{lat}} = 8a_z$ and $(N_{\text{max}} - 1)g_d/a_\rho = 550$ on a numeric grid of size $[N_z, N_\rho] = [1024, 128]$. Figure 8.7 shows the density at $z = 0$ of a dipolar BEC at the center of the lattice ($j = 0$) and, for comparison, the density of a dipolar BEC with the same trap

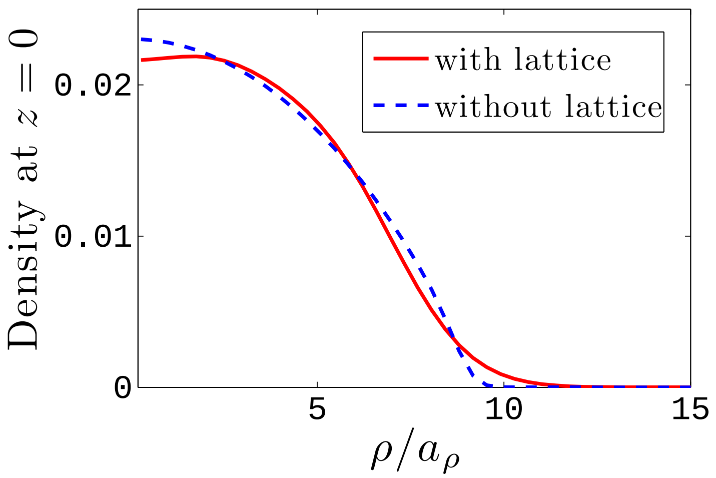

Figure 8.7: Radial densities at $z = 0$ of a dipolar BEC with $(N-1)g_d/a_\rho = 550$ in a trap with aspect ratio $\lambda = 50$. The blue dashed line shows the density of a dipolar BEC in a single harmonic trap, and the red solid line shows the density of a dipolar BEC in the center site of a 1D lattice with nine occupied sites ($j_{\text{lat}} = 4$). This dipolar BEC exhibits biconcave structure, while the single dipolar BEC does not, demonstrating the emergence of this structure in the lattice system. These densities were calculated by solving the GPE (coupled GPEs) exactly on a full numeric grid.

aspect ratio and ddi strength $(N-1)g_d/a_\rho = 550$ but without the presence of the lattice. While the dipolar BEC in the single trap does not exhibit biconcave structure, the dipolar BEC in the lattice does, showing that this emergent structure in the lattice system is present not only in the infinite lattice system, but also in the experimentally realistic system of a finite lattice with variable occupancy. Indeed, such a system is realizable with atomic ^{52}Cr, having a permanent magnetic dipole moment of $\mu = 6\mu_B$ where μ_B is the Bohr magneton, axial harmonic oscillator frequencies of $\omega_z = 2\pi \times 30$ kHz and a maximum condensate occupancy of $N_{\text{max}} \simeq 77 \times 10^3$ atoms.

The experimental observability of biconcave structure in a lattice of dipolar BECs is an important point to address. While non-destructive phase-contrast imaging techniques of trapped condensates have been successful [198], it is questionable whether such techniques can resolve the small differences in the spatial density of the biconcave condensate, especially in a 1D lattice when the other trapped condensates do not necessarily exhibit such structure. However, it was shown in chapter 6 that dipolar BECs with biconcave structure will, at a critical density, collapse anisotropically with nodal structure about the ring of maximum density. This angular character is predicted to be preserved in the expansion of the collapsed state, thereby providing an indirect signature of biconcave structure in the expanded cloud. In a system of dipolar BECs with non-zero scattering lengths, collapse of the system can be induced by decreasing the scattering length below a critical value via a Fano-Feshbach resonance, as discussed in chapter 6 [37].

8.5 Conclusion

In conclusion, we have mapped the structure and stability of a lattice of interacting, purely dipolar BECs. By asserting an analytic form for the axial part of the condensate wave functions (Eqs. (8.7)-(8.9)), we derive a simple, modified GPE for the radial part of the wave functions when the lattice is infinite. We find isolated regions ("islands") in the parameter space defined by the lattice spacing and the ddi strength where the dipolar BECs are predicted to exhibit biconcave densities. To model a more experimentally realistic system, we consider a finite lattice with varying condensate number and solve the coupled set of GPEs exactly on a full numeric grid. In doing so, we show that this emergent biconcave structure should be observable in a finite 1D lattice of dipolar BECs of atomic ^{52}Cr.

Chapter 9

Summary

This dissertation presented a number of theoretical results concerning an ultracold Bose gas, or Bose-Einstein condensate (BEC), in the presence of both isotropic short-range and dipolar interactions. This work was strongly motivated by recent experimental advances in the cooling and trapping of atomic species that possess permanent magnetic dipole moments, such as ^{52}Cr [16] and ^{164}Dy [17], which were both recently Bose-condensed in the laboratory setting. Besides these dipolar atoms, the work presented in this thesis is relevant to gases of heteronuclear polar molecules, which can achieve even larger (electric) dipole moments when polarized in an applied field, and have been produced in their absolute rovibrational ground state and cooled to near-degenerate temperatures [24, 25, 26]. While an enormous body of literature, both theoretical and experimental in nature, has been generated with regards to ultracold quantum gases with dipolar interactions [199, 16], we have focused on a particular phenomenon, being the emergence of a roton-like quasiparticle mode in the trapped dipolar BEC. This feature of dipolar BECs shares many similarities with the roton that exists in the superfluid helium system, however, the dilute BEC is much easier to control experimentally and describe theoretically. Thus, the dipolar BEC presents us with the ideal testing ground to explore the role of the roton in a superfluid system.

We have made a point to present theoretical predictions that speak to current experiments, or experiments that are realizable in the foreseeable future. Thus, much of this work is phenomenological in nature. However, after giving a short background of low-temperature physics in chapter 2, in chapter 3 we presented a detailed account of the theory that underlies our phenomenological predictions. Therein, we discussed the Bogoliubov approximation to the problem of an ultracold quantum many-body system of bosons at ultracold temperatures, out of which comes the mean-field equations that describe the condensate and the quantum fluctuations (quasiparticles) of the ultracold, dilute Bose gas, being the Gross-Pitaevskii equation and the Bogoliubov de Gennes equations, respectively. Additionally, we discussed the treatment of two-body interactions in the BEC and justified a two-body pseudopotential for both isotropic short-range and long-range, anisotropic dipole-dipole interactions. In chapter 4, we applied these theoretical results to the homogeneous (translationally invariant) three-dimensional and quasi-two-dimensional dipolar Bose gases at zero temperature. By studying the energetics and phonon modes of the fully three-dimensional system, we showed that the polarized dipolar BEC is significantly stabilized when confined along the direction of polarization, however, instability can still occur in this trapped system for sufficiently large dipole-dipole interaction strength or condensate density due to the emergence and subsequent softening of the roton. This roton instability is thus found to be both density dependent and *local*, meaning that the dipolar BEC will collapse locally on a length-scale set by the size of the confinement.

In the subsequent chapters 5-8, we proceeded to characterize the stability, quasiparticle excitations, vortex states and superfluid properties of the fully trapped dipolar BEC. Because the dipole-dipole interaction potential for polarized dipoles is cylindrically symmetric, the fully trapped dipolar BEC possesses cylindrical symmetry for trapping geometries that are cylindrically symmetric, as well. For this case, we constructed an efficient numerical algorithm for treating the kinetic energy and dipolar interaction terms in the Gross-Pitaevskii and Bogoliubov de Gennes equations that can easily be adjusted to handle condensate and quasiparticle states with well-defined vorticity. We applied this algorithm, which has its footing in the discrete Hankel transform [102] (see appendix D), to rotationless dipolar BECs and dipolar BECs with both singly- and doubly-quantized vortices. An analysis of the discrete quasiparticle spectrum of these systems revealed that the vortex states and the strange "biconcave" states of the rotationless dipolar BECs go unstable to discrete rotons with angular nodal structure. In chapter 6, we showed via explicit numeric simulation that, for example, the ^{52}Cr BEC can exhibit angular collapse and subsequent angular explosion under realistic experimental conditions. In chapter 8, we showed that a dipolar BEC loaded on a 1D lattice exhibits wildly modified stability properties and emergent biconcave structure that is not present in a single dipolar BEC in the absence of the other occupied lattice sites. Regarding the dipolar BEC with a singly-quantized vortex, we found regions in parameter space near the instability threshold where this system exhibits radial density oscillations near the vortex core. We attributed such structure to the static manifestation of the discrete radial roton in the ground state of the dipolar BEC by applying a linear perturbation theory to the Gross-Pitaevskii equation that shows the equivalence of the condensate response to a small time-independent perturbation and the discrete roton mode. In chapter 7, we examined the superfluid properties of the quasi-two-dimensional and fully trapped dipolar BECs by direct numerical simulations of an object (blue-detuned laser, in an experiment) moving through the system at varying velocity. We showed that the roton not only serves to decrease the critical velocity as a function of density in the fully trapped system, but that the dipole polarization can be tilted to create an anisotropic superfluid with anisotropic critical velocity. In both cases, we showed that a measurement of the critical velocity in the experiments proposed therein would correspond to a measurement of the roton in a dipolar BEC.

To this date, the roton has remained elusive to experimentalists. However, motivation for such a measurement and rapidly advancing experimental capabilities inspire confidence that it's presence will soon be empirically known. As forementioned, a large point in this thesis was to predict phenomena that will not only demonstrate the novel behavior of a superfluid with dipolar interactions, but also serve as indirect evidence of the presence of the roton in a dipolar BEC. In addition to the experimental work that is under active investigation, there remains a plethora of physics to explore theoretically with regards to ultracold dipolar gases. Extensions of the work presented in this thesis include, but are certainly not limited to the possibility of macroscopically occupying a roton field and the physics of roton-roton interactions. At the mean-field Bogoliubov level of the many-body field theory used in this thesis, such physics is automatically excluded as the the Bogoliubov approximation permits only perturbative occupations of quasiparticle states and does not account for interactions between quasiparticles. Additional extentions of the work presented in this thesis include the effect of temperature on the rotonization of a dipolar Bose gas, the miscibility-immiscibility transition in a two-component dipolar Bose gas and the role of the dipole-dipole interaction in spinor BECs at finite temperature. Such work is under active investigation by the author.

Bibliography

[1] M. H. Anderson, J. R. Ensher, M. R. Matthews, C. E. Wieman, and E. A. Cornell, Observation of Bose-Einstein Condensation in a Dilute Atomic Vapor, Science **269**, 198 (1995).

[2] K. B. Davis, M.-O. Mewes, M. R. Andrews, N. J. van Druten, D. S. Durfee, D. M. Kurn, and W. Ketterle, Bose-Einstein Condensation in a Gas of Sodium Atoms, Phys. Rev. Lett. **75**, 3969 (1995).

[3] C. C. Bradley, C. A. Sackett, J. J. Tollett, and R. G. Hulet, Evidence of Bose-Einstein Condensation in an Atomic Gas with Attractive Interactions, Phys. Rev. Lett. **75**, 1687 (1996).

[4] A. Einstein, Quantentheorie des einatomigen idealen Gases, Sitzungsbericht der Preussichen Akademie der Wissenschaften, Physikalisch-mathematische Klasse , 3 (1925).

[5] W. D. Phillips, Laser Cooling and Trapping of Neutral Atoms, Rev. Mod. Phys **70**, 721 (1998).

[6] O. Morsch and M. Oberthaler, Dynamics of Bose-Einstein Condensates in Optical Lattices, Rev. Mod. Phys. **78**, 179 (2006).

[7] L. D. Carr, D. DeMille, R. V. Krems, and J. Ye, Cold and Ultracold Molecules: Science, Technology and Applications, New J. Phys **11**, 055049 (2009).

[8] C. Trefzger, C. Menotti, B. Capogrosso-Sansone, and M. Lewenstein, Ultracold Dipolar Gases in Optical Lattices, J. Phys. B **44**, 193001 (2011).

[9] A. Pikovski, M. Klawunn, G. V. Shlyapnikov, and L. Santos, Interlayer Superfluidity in Bilayer Systems of Fermionic Polar Molecules, Phys. Rev. Lett. **105**, 215302 (2010).

[10] M. Baranov, A. Micheli, S. Ronen, and P. Zoller, Bilayer Superfluidity of Fermionic Polar Molecules: Many Body Effects, Phys. Rev. A **83**, 043602 (2010).

[11] A. Potter, E. Berg, D.-W. Wang, B. Halperin, and E. Demler, Superfluidity and Dimerization in a Multilayered System of Fermionic Polar Molecules, Phys. Rev. Lett. **105**, 220406 (2010).

[12] H. P. Büchler, E. Demler, M. Lukin, A. Micheli, N. Prokof'ev, G. Pupillo, and P. Zoller, Strongly Correlated 2D Quantum Phases with Cold Polar Molecules: Controlling the Shape of the Interaction Potential, Phys. Rev. Lett. **98**, 060404 (2007).

[13] G. E. Astrakharchik, J. Boronal, I. L. Kurbakov, and Y. E. Lozovik, Quantum Phase Transition in a Two-Dimensional System of Dipoles, Phys. Rev. Lett. **98**, 060405 (2007).

[14] A. Griesmaier, J. Werner, S. Hensler, J. Stuhler, and T. Pfau, Bose-Einstein Condensation of Chromium, Phys. Rev. Lett. **94**, 160401 (2005).

[15] Q. Beaufils, R. Chicireanu, T. Zanon, B. Laburthe-Tolra, E. Maréchal, L. Vernac, J.-C. Keller, and O. Gorciex, All-Optical Production of Chromium Bose-Einstein Condensates, Phys. Rev. A **77**, 061601(R) (2008).

[16] T. Lahaye, C. Menotti, L. Santos, M. Lewenstein, and T. Pfau, The Physics of Dipolar Bosonic Quantum Gases, Rep. Prog. Phys **72**, 126401 (2009).

[17] M. Lu, N. Q. Burdick, S. H. Youn, and B. L. Lev, A Strongly Dipolar Bose-Einstein Condensate of Dysprosium, (2011), arXiv:1108:5993.

[18] S. Yi and H. Pu, Spontaneous Spin Textures in Dipolar Spinor Condensates, Phys. Rev. Lett. **97**, 020401 (2006).

[19] M. Vengalattore, S. R. Leslie, J. Guzman, and D. M. Stamper-Kurn, Spontaneously Modulated Spin Textures in a Dipolar Spinor Bose-Einstein Condensate, Phys. Rev. Lett. **100**, 170403 (2008).

[20] Y. Kawaguchi, H. Saito, K. Kudo, and M. Ueda, Spontaneous Magnetic Ordering in a Ferromagnetic Spinor Dipolar Bose-Einstein Condensate, Phys. Rev. A **82**, 043627 (2010).

[21] T. Koch, T. Lahaye, J. Metz, B. Fröhlich, A. Griesmaier, and T. Pfau, Stabilization of a Purely Dipolar Quantum Gas Against Collapse, Nature Physics **4**, 218 (2008).

[22] T. Lahaye, J. Metz, B. Fröhlich, T. Koch, M. Meister, A. Griesmaier, T. Pfau, H. Saito, Y. Kawaguchi, and M. Ueda, *d*-Wave Collapse and Explosion of a Dipolar Bose-Einstein Condensate, Phys. Rev. Lett. **101**, 080401 (2008).

[23] J. Werner, A. Griesmaier, S. Hensler, A. Simoni, E. Tiesinga, J. Stuhler, and T. Pfau, Observation of Feshbach Resonances in an Ultracold Gas of ^{52}Cr.

[24] K.-K. Ni, S. Ospelkaus, M. H. G. de Miranda, A. Peer, B. Neyenhuis, J. J. Zirbel, S. Kotochigova, P. S. Julienne, J. Ye, and D. S. Jin, A High Phase-Space-Density Gas of Polar Molecules, Science **322**, 231 (2008).

[25] J. Deiglmayr, A. Grochola, M. Repp, K. Mörtlbauer, C. Glück, J. Lange, O. Dulieu, R. Wester, and M. Weidemüller, Formation of Ultracold Polar Molecules in the Rovibrational Ground State, Phys. Rev. Lett. **101**, 133004.

[26] K. Aikawa, D. Akamatsu, M. Hayashi, K. Oasa, J. Kobayashi, P. Naidon, T. Kishimoto, M. Ueda, and S. Inouye, Coherent Transfer of Photoassociated Molecules into the Rovibrational Ground State, Phys. Rev. Lett. **105**, 203001 (2010).

[27] A. Chotia, B. Neyenhuis, S. A. Moses, B. Yan, J. P. Covey, M. Foss-Feig, A. M. Rey, D. S. Jin, and J. Ye, Long-Lived Dipolar Molecules and Feshbach Molecules in a 3D Optical Lattice, (2011), arXiv:1110.4420.

[28] L. Santos, G. V. Shlyapnikov, and M. Lewenstein, Roton-Maxon Spectrum and Stability of Trapped Dipolar Bose-Einstein Condensates, Phys. Rev. Lett. **90**, 250403 (2003).

[29] U. R. Fischer, Stability of Quasi-Two-Dimensional Bose-Einstein Condensates with Dominant Dipole-Dipole Interactions, Phys. Rev. A **73**, 031602(R) (2006).

[30] S. Ronen, D. C. E. Bortolotti, and J. L. Bohn, Radial and Angular Rotons in Trapped Dipolar Gases, Phys. Rev. Lett. **98**, 030406 (2007).

[31] L. D. Landau, On the Theory of Superfluidity in Helium II, J. Phys. USSR **11**, 91 (1947).

[32] M. Cohen and R. P. Feynman, Theory of Inelastic Scattering of Cold Neutrons from Liquid Helium, Phys. Rev. **107**, 13 (1957).

[33] D. G. Henshaw and A. D. B. Woods, Modes of Atomic Motions in Liquid Helium by Inelastic Scattering of Neutrons, Phys. Rev. **121**, 1266 (1961).

[34] J. L. Bohn, R. M. Wilson, and S. Ronen, How Does a Dipolar Bose-Einstein Condensate Collapse?, Laser Physics **19**, 547 (2009).

[35] R. M. Wilson, S. Ronen, J. L. Bohn, and H. Pu, Manifestations of the Roton in Dipolar Bose-Einstein Condensates, Phys. Rev. Lett. **100**, 245302 (2008).

[36] R. M. Wilson, S. Ronen, and J. L. Bohn, Stability and Excitations of a Dipolar Bose-Einstein Condensate with a Vortex, Phys. Rev. A , 013621 (2009).

[37] R. M. Wilson, S. Ronen, and J. L. Bohn, Angular Collapse of Dipolar Bose-Einstein Condensates, Phys. Rev. A **80**, 023614 (2009).

[38] R. M. Wilson, S. Ronen, and J. L. Bohn, Critical Superfluid Velocity in a Trapped Dipolar Gas, Phys. Rev. Lett. **104**, 094501 (2010).

[39] C. Ticknor, R. M. Wilson, and J. L. Bohn, Anisotropic Superfluidity in a Dipolar Bose Gas, Phys. Rev. Lett. **106**, 065301 (2011).

[40] R. M. Wilson and J. L. Bohn, Emergent Structure in a Dipolar Bose Gas in a One-Dimensional Lattice, Phys. Rev. A **83**, 023623 (2011).

[41] P. Kapitza, Viscosity of Liquid Helium Below the λ-Point, Nature **141**, 74 (1938).

[42] J. F. Allen and A. D. Misener, Flow of Liquid Helium II, Nature **141**, 75 (1938).

[43] H. Kamerlingh-Onnes, The Superconductivity of Mercury, Comm. Phys. Lab. Univ. Leiden **120b** (1911).

[44] J. O. Wilhelm, A. D. Misener, and A. R. Clark, The Viscosity of Liquid Helium, Proc. Roy. Soc. A **151**, 342 (1935).

[45] F. London, On the Bose-Einstein Condensation, Phys. Rev. **54**, 947 (1938).

[46] L. Tisza, The Theory of Quantum Liquid Application to Liquid Helium, J. Phys. Radium **1**, 164 (1940).

[47] L. D. Landau and E. M. Lifshitz, Statistical Physics, Addison-Wesley, Reading MA, 2nd edition, 1969.

[48] O. W. Dietrich, E. H. Graf, C. H. Huang, and L. Passell, Neutron Scattering of Rotons in Liquid Helium, Phys. Rev. A **5**, 1377 (1972).

[49] O. Avenel and E. Varoquaux, Observation of Singly Quantized Dissipation Events Obeying the Josephson Frequency Relation in the Critical Flow of Superfluid ^{4}He Through an Aperature, Phys. Rev. Lett. **55**, 2704 (1985).

[50] R. P. Feynman, Progress in Low Temperature Physics, volume 1, North Holland, 1955.

[51] D. R. Allum, R. M. Bowley, and P. V. E. McClintock, Evidence for Roton Pair Creation in Superfluid ^{4}He, Phys. Rev. Lett. **36**, 1313 (1976).

[52] L. Onsager and R. Penrose, Bose-Einstein Condensation and Liquid Helium, Phys. Rev. **104**, 576 (1956).

[53] R. K. Pathria, Statistical Mechanics, Butterworth-Heinemann, 2nd edition, 1996.

[54] M. Abramowitz and I. A. Stegun, Handbook of Mathematical Functions, (1970).

[55] C. J. Pethick and H. Smith, Bose-Einstein Condensation in Dilute Gases, Cambridge University Press, 2002.

[56] W. S. Bakr, A. Peng, M. E. Tai, R. Ma, J. Simon, J. I. Gillen, S. Fölling, L. Pollet, and M. Griener, Probing the Superfluid-to-Mott Insulator Transition at the Single-Atom Level, Science **329**, 547 (2010).

[57] K. Binder, Monte Carlo Methods in Statistical Physics, (1986).

[58] W. Ketterle and N. J. van Druten, Bose-Einstein Condensation of a Finite Number of Particles Trapped in One or Three Dimensions, Phys. Rev. A **54**, 656 (1996).

[59] V. Bagnato, D. E. Pritchard, and D. Kleppner, Bose-Einstein Condensation in an External Potential, Phys. Rev. A **35**, 4354 (1987).

[60] H. Friedrich, Theoretical Atomic Physics, (2006).

[61] H. J. Metcalf and P. van der Straten, Laser Cooling and Trapping, Springer-Verlag, New York, 1999.

[62] C. E. Wieman, D. E. Pritchard, and D. J. Wineland, Atom Cooling, Trapping and Quantum Manipulation, Rev. Mod. Phys. **71**, S253 (1999).

[63] W. Ketterle and N. J. van Druten, Evaporative Cooling of Atoms, Adv. At. Mol. Phys. **37**, 181 (1996).

[64] B. H. Bransden and C. J. Joachain, Physics of Atoms and Molecules, (2003).

[65] W. H. Wing, On Neutral Particle Trapping in Quasistatic Electromagnetic Fields, Prog. Quantum Electronics **8**, 181 (1984).

[66] B. Pasquiou, E. Maréchal, G. Bismut, P. Pedri, L. Vernac, O. Gorceix, and B. Laburthe-Tolra, Spontaneous Demagnetization of a Dipolar Spinor Bose Gas in an Ultralow Magnetic Field, Phys. Rev. Lett. **106**, 255303 (2011).

[67] E. A. Cornell and C. E. Wieman, Nobel Lecture: Bose-Einstein Condensation in a Dilute Gas, the First 70 Years and some Recent Experiments, Rev. Mod. Phys **74**, 875 (2002).

[68] W. Ketterle, Nobel Lecture: When Atoms Behave as Waves: Bose-Einstein Condensation and the Atom Laser, Rev. Mod. Phys. **74**, 1131 (2002).

[69] M. R. Matthews, B. P. Anderson, P. C. Haljan, D. S. Hall, C. E. Wieman, and E. A. Cornell, Vortices in a Bose-Einstein Condensate, Phys. Rev. Lett. **83**, 2498 (1999).

[70] J. R. Abo-Shaeer, C. Raman, J. M. Vogels, and W. Ketterle, Observation of Vortex Lattices in Bose-Einstein Condensates, Science **292**, 476 (2001).

[71] P. Engels, I. Coddington, P. C. Haljan, V. Schweikhard, and E. A. Cornell, Observation of Long-Lived Vortex Aggregates in Rapidly Rotating Bose-Einstein Condensates, Phys. Rev. Lett. **90**, 170405 (2003).

[72] F. Dalfovo, S. Giorgini, L. P. Pitaevskii, and S. Stringari, Theory of Bose-Einstein Condensation in Trapped Gases, Rev. Mod. Phys. **71**, 463 (1999).

[73] J. R. Anglin and W. Ketterle, Bose-Einstein Condensation of Atomic Gases, Nature **416**, 211 (2002).

[74] D. G. Fried, T. C. Killian, L. Willmann, D. Landhuis, S. C. Moss, D. Kleppner, and T. J. Greytak, Bose-Einstein Condensation of Atomic Hydrogen, Phys. Rev. Lett. **81**, 3811 (1998).

[75] G. Modugno, G. Ferrari, G. Roati, R. J. Brecha, A. Simoni, and M. Inguscio, Bose-Einstein Condensation of Potassium Atoms by Sympathetic Cooling, Science **294**, 1320 (2001).

[76] T. Weber, J. Herbig, M. Mark, H.-C. Nagerl, and R. Grimm, Bose-Einstein Condensation of Cesium, Science **299**, 232 (2003).

[77] Y. Takasu, K. Maki, K. Komori, T. Takano, K. Honda, M. Kumakura, T. Yabuzaki, and Y. Takahashi, Spin-singlet Bose-Einstein Condensation of Two-Electron Atoms, Phys. Rev. Lett. **91**, 040404 (2003).

[78] S. Kraft, F. Vogt, O. Appel, F. Riehle, and U. Sterr, Bose-Einstein Condensation of Alkaline Earth Atoms: ^{40}Ca, Phys. Rev. Lett. **103**, 130401 (2009).

[79] S. Stellmer, M. K. Tey, B. Huang, R. Grimm, and F. Schreck, Bose-Einstein Condensation of Strontium, Phys. Rev. Lett. **103**, 200401 (2009).

[80] K.-K. Ni, A Quantum Gas of Polar Molecules, PhD thesis, University of Colorado, Boulder, 2009.

[81] M. Debatin, T. Takekoshi, R. Rameshan, L. Reichsöllner, F. Ferlaino, R. grimm, R. Vexiau, N. Vouloufa, O. Dulieu, and H.-C. Nägerl, Molecular Spectroscopy for Ground-State Transfer of Ultracold RbCs Molecules, Phys. Chem. Chem. Phys. **10**, 1039 (2011).

[82] A. V. Gorshkov, S. R. Manmana, G. Chen, E. Demler, M. D. Lukin, and A. M. Rey, Quantum Magnetism with Polar Alkali-Metal Dimers, Phys. Rev. A **84**, 033619 (2011).

[83] M. Ortner, A. Micheli, G. Pupillo, and P. Zoller, Quantum Simulations of Extented Hubbard Models with Dipolar Crystals, New J. Phys **11**, 055045 (2009).

[84] D. DeMille, Quantum Computation with Trapped Polar Molecules, Phys. Rev. Lett. **88**, 067901 (2002).

[85] N. J. Stone, Table of Nuclear Magnetic Dipole and Electric Quadrupole Moments, At. Data Nucl. Data Tables **90**, 75 (2005).

[86] G. Quéméner, J. L. Bohn, A. Petrov, and S. Kotochigova, Universalities in Ultracold Reactions of Alkali Polar Molecules, (2011), arXiv:1108.3866.

[87] C. E. Fellows, R. F. Gutterres, A. P. C. Campos, J. Vergés, and C. Amiot, The RbCs Ground Electronic State: New Spectroscopic Study, J. Mol. Spec. **197**, 19 (1999).

[88] S. Kotochigova and E. Tiesinga, Ab Initio Relativistic Calculation of the RbCs Molecule, J. Chem. Phys. **123**, 174304 (2005).

[89] C. M. Marian, U. Wahlgren, O. Gropen, and P. Pyykkö, Bonding and Electronic Structure in Diatomic ThO: Quasirelativistic Effective Core Potential Calculations, J. Mol. Struct. **169**, 339 (1988).

[90] A. A. Buchachenko, Communication: Electric Properties of the ThO Molecule, J. Chem Phys. **133**, 041102 (2010).

[91] J. D. Jackson, Classical Electrodynamics, Wiley, 3rd edition, 1998.

[92] A. A. Abrikoxov, L. P. Gorkov, and I. E. Dzyaloshinski, Methods of Quantum Field Theory in Statistical Physics, Dover Publications, Inc., New York, 1963.

[93] L. D. Landau and E. M. Lifshitz, Quantum Mechanics (Non-relativistic Theory), Butterworth-Heinemann, 3rd edition, 1977.

[94] N. N. Bogoliubov, On The Theory of Superfluidity, J. Phys. (USSR) **11**, 23 (1947).

[95] E. P. Gross, Structure of a Quantized Vortex in Boson Systems, Nuovo Cimiento **20**, 454 (1961).

[96] L. P. Pitaevskii, Vortex Lines in an Imperfect Bose Gas, Sov. Phys. JETP **13**, 451 (1961).

[97] J. Goldstone, Field Theories with Superconductor Solutions, Nuovo Cimento **19**, 154 (1961).

[98] J. Goldstone, A. Salam, and S. Weinberg, Broken Symmetries, Phys. Rev. **127**, 965 (1962).

[99] P. G. de Gennes, Superconductivity of Metals and Alloys, Westview Press, 2nd edition, 1999.

[100] K. Huang and P. Tommasini, Generalized Mean Fields for Trapped Atomic Bose-Einstein Condensates, J. Res. Natl. Inst. Stand. Technol. **101**, 435 (1996).

[101] C. Huepe, L. S. Tuckerman, S. Metens, and M. E. Brachet, Stability and Decay Rates of Nonisotropic Attractive Bose-Einstein Condensates, Phys. Rev. A **68**, 023609 (2003).

[102] S. Ronen, D. C. E. Bortolotti, and J. L. Bohn, Bogoliubov Modes of a Dipolar Condensate in a Cylindrical Trap, Phys. Rev. A **74**, 013623 (2006).

[103] T. D. Lee, K. Huang, and C. N. Yang, Eigenvalues and Eigenfunctions of a Bose System of Hard Spheres and its Low-Temperature Properties, Phys. Rev. **106**, 1135 (1957).

[104] Y. Nakamura, M. Mine, M. Okumura, and Y. Yamanaka, Condition for Emergence of Complex Eigenvalues in the Bogoliubov-de Gennes Equations, Phys. Rev. A **77**, 043601 (2008).

[105] E. Lundh and H. M. Nilsen, Dynamics of a Doubly Quantized Vortex in a Three-Dimensional Condensate, Phys. Rev. A **74**, 063620 (2006).

[106] B. D. Esry, Hartree-Fock Theory for Bose-Einstein Condensates and the Inclusion of Correlation Effects, Phys. Rev. A **55**, 1147 (1997).

[107] A. Griffin, Conserving and Gapless Approximations for an Inhomogeneous Bose Gas at Finite Temperature, Phys. Rev. B **53**, 9341 (1996).

[108] C. W. Gardiner and M. J. Davis, The Stochastic Gross-Pitaevskii Equation: II, J. Phys. B. **36**, 4731 (2003).

[109] E. Fermi, On the Pressure Displacement of Higher Terms in Spectral Series, Nuovo Cimento **11**, 157 (1934).

[110] G. F. Gribakin and V. V. Flambaum, Calculation of the Scattering Length in Atomic Collisions Using the Semiclassical Approximation, Phys. Rev. A **48**, 546 (1993).

[111] K. Huang and C. N. Yang, Quantum-Mechanical Many-Body Problem with Hard-Sphere Interaction, Phys. Rev. **105**, 767 (1957).

[112] S. T. Beliaev, Application of the Methods of Quantum Field Theory to a System of Bosons, Sov. Phys.-JETP **7**, 289 (1958).

[113] S. T. Beliaev, Energy Spectrum of a Non-Ideal Bose Gas, Sov. Phys.-JETP **7**, 299 (1958).

[114] S. Ronen, The Dispersion Relation of a Bose Gas in the Intermediate- and High-Momentum Regimes, J. Phys. B **42**, 055301 (2009).

[115] D. M. Brink and G. R. Satchler, Angular Momentum, Oxford: Clarendon, 1993.

[116] H. R. Sadeghpour, J. L. Bohn, M. J. Cavagnera, B. D. Esry, I. I. Fabrikant, J. H. Macek, and A. R. P. Rau, Collisions Near Threshold in Atomic and Molecular Physics, J. Phys. B: At. Mol. Opt. Phys. **33**, R93 (2000).

[117] J. L. Bohn, M. Cavagnero, and C. Ticknor, Quasi-Universal Dipolar Scattering in Cold and Ultracold Gases, New J. Phys. **11**, 055039 (2009).

[118] S. Yi and L. You, Trapped Atomic Condensates with Anisotropic Interactions, Phys. Rev. A **61**, 041604(R) (2000).

[119] S. Yi and L. You, Trapped Condensates of Atoms with Dipole Interactions, Phys. Rev. A **63**, 053607 (2001).

[120] A. Derevianko, Anisotropic Pseudopotential for Polarized Dilute Quantum Gases, Phys. Rev. A **67**, 033607 (2003).

[121] K. Kanjilal, J. L. Bohn, and D. Blume, Pseudopotential Treatment of Two Aligned Dipoles Under External Harmonic Confinement, Phys. Rev. A **75**, 052705 (2007).

[122] S. Ronen, D. C. E. Bortolotti, D. Blume, and J. L. Bohn, Dipolar Bose-Einstein Condensates with Dipole-Dependent Scattering Length, Phys. Rev. A **74**, 033611 (2006).

[123] D.-W. Wang, An Effective Many-Body Theory for Strongly Interacting Polar Molecules, New J. Phys. **10**, 053005 (2008).

[124] K. Góral and L. Santos, Ground State and Elementary Excitations of Single and Binary Bose-Einstein Condensates of Trapped Dipolar Gases, Phys. Rev. A **66**, 023613 (2002).

[125] L. Pitaevskii and S. Stringari, Bose-Einstein Condensation, (2003).

[126] A. R. P. Lima and A. Pelster, Quantum Fluctuations in Dipolar Bose Gases, (2011), arXiv:1103.4128.

[127] R. J. Dodd, M. Edwards, C. J. Williams, C. W. Clark, M. J. Holland, P. A. Ruprecht, and K. Burnett, Role of Attractive Interactions on Bose-Einstein Condensation, Phys. Rev. A **54**, 661 (1996).

[128] C. C. Bradley, C. A. Sackett, and R. G. Hulet, Bose-Einstein Condensation of Lithium: Observation of Limited Condensate Number, Phys. Rev. Lett. **78**, 985 (1997).

[129] Z. Li and R. V. Krems, Inelastic Collisions in an Ultracold Quasi-Two-Dimensional Gas, Phys. Rev. A **79**, 050701(R) (2009).

[130] A. Micheli, Z. Idziaszek, G. Pupillo, M. A. Baranov, P. Zoller, and P. Julienne, Universal Rates for Reactive Ultracold Polar Molecules in Reduced Dimensions, Phys. Rev. Lett. **105**, 073202 (2010).

[131] G. Quéméner and J. L. Bohn, Electric Field Suppression of Ultracold Confined Chemical Reactions, Phys. Rev. A **81**, 060701(R) (2010).

[132] C. Ticknor, Quasi-Two-Dimensional Dipolar Scattering, Phys. Rev. A **81**, 042708 (2010).

[133] G. Quéméner and J. L. Bohn, Dynamics of Ultracold Molecules in Confined Geometry and Electric Field, Phys. Rev. A **83**, 012705 (2011).

[134] K.-K. Ni, S. Ospelkaus, D. Wang, G. Quéméner, B. Neyenhuis, M. H. G. de Miranda, J. L. Bohn, and J. Ye, Dipolar Collisions of Polar Molecules in the Quantum Regime, Nature **464**, 1324 (2010).

[135] C. Ticknor and S. T. Rittenhouse, Three Body Recombination of Ultracold Dipoles to Weakly Bound Dimers, Phys. Rev. Lett. **105**, 013201 (2010).

[136] S. Müller, J. Billy, E. A. L. Henn, H. Kadau, A. Griesmaier, M. Jona-Lasinio, L. Santos, and T. Pfau, Dipolar Stabilization of an Attractive Bose Gas in a One Dimensional Lattice, (2011), arXiv:1105:5015.

[137] N. N. Bogoliubov, Quasiaverages in Problems of Statistical Physics, Dubna, 1961.

[138] V. N. Popov, On the Theory of Superfluidity of Two- and One-Dimensional Bose Systems, Theor. Math. Phys. **11**, 354 (1972).

[139] Y. Kagan, B. V. Svistunov, and G. V. Shlyapnikov, Influence on Inelastic Processes of the Phase Transition in a Weakly Collisional Two-Dimensional Bose Gas, Sov. Phys. JETP **66**, 480 (1987).

[140] A. Posazhennikova, *Colloquium*: Weakly Interacting, Dilute Bose Gases in 2D, Rev. Mod. Phys. **78** (2006).

[141] M. Schick, Two-Dimensional System of Hard-Core Bosons, Phys. Rev. A **3**, 1067 (1971).

[142] W. D. McCormick, D. L. Goodstein, and J. G. Dash, Adsorption and Specific-Heat Studies of Monolayer and Submonolayer Films of He^3 and He^4, Phys. Rev. **168**, 249 (1968).

[143] D. S. Petrov, M. Holzmann, and G. V. Shlyapnikov, Bose-Einstein Condensation in Quasi-2D Trapped Gases, Phys. Rev. Lett. **84**, 2551 (2000).

[144] U. R. Fischer, Existence of Long-Range Order for Traopped Interacting Bosons, Phys. Rev. Lett. **89**, 280402 (2002).

[145] M. Olshanii, Atomic Scattering in the Presence of an External Confinement and a Gas of Impenetrable Bosons, Phys. Rev. Lett. **81**, 938 (1998).

[146] C. Ticknor, Two-Dimensional Dipolar Scattering, Phys. Rev. A **80**, 052702 (2009).

[147] G. E. Astrakharchik, J. Boronat, J. Casulleras, I. L. Kurbakov, and Y. E. Lozovik, Weakly Interacting Two-Dimensional System of Dipoles: Limitations of the Mean-Field Theory, Phys. Rev. A **75**, 063630 (2007).

[148] R. Nath, P. Pedri, and L. Santos, Phonon Instability with Respect to Soliton Formation in Two-Dimensional Dipolar Bose-Einstein Condensates, Phys. Rev. Lett. **102**, 050401 (2009).

[149] I. E. Mazets, D. H. J. O'Dell, G. Kurizki, N. Davidson, and W. P. Schleich, Depletion of a Bose-Einstein Condensate by Laser-Induced Dipole-Dipole Interactions, J. Phys. B: At. Mol. Opt. Phys. **37**, S155 (2004).

[150] M. J. Jamieson, Adiabatically Corrected Scattering Lengths and Effective Ranges for Collisions of Helium Atoms, Chem. Phys. Lett. **310**, 222 (1999).

[151] A. Filinov, N. V. Prokof'ev, and M. Bonitz, Berezinskii-Kosterlitz-Thouless Transition in Two-Dimensional Dipole Systems, Phys. Rev. Lett. **105**, 070401 (2010).

[152] D. Hufnagl, R. Kaltseis, V. Apaja, and R. E. Zillich, Roton-Roton Crossover in Strongly Correlated Dipolar Bose-Einstein Condensates, Phys. Rev. Lett. **107**, 065303 (2011).

[153] G. B. Arfken and H. J. Weber, Mathematical Methods for Physicists, Harcourt, San Diego, 5th edition, 2001.

[154] P. A. Ruprecht, M. J. Holland, K. Burnett, and M. Edwards, Time-Dependent Solution of the Nonlinear Schrödinger Equation for Bose-Condensed Trapped Neutral Atoms, Phys. Rev. A **51**, 4704 (1995).

[155] M. Modugno, L. Pricoupenko, and Y. Castin, Bose-Einstein Condensates with a Bent Vortex in Rotating Traps, Eur. Phys. J. D **22**, 235 (2003).

[156] H.-Y. Lu, H. Lu, J.-N. Zhang, R.-Z. Qiu, H. Pu, and S. Yi, Spatial Density Oscillations in Trapped Dipolar Condensates, Phys. Rev. A **82**, 023622 (2010).

[157] W. Kohn, Cyclotron Resonance and de Hass-van Alphen Oscillations of an Interacting Electron Gas, Phys. Rev. **123**, 1242 (1961).

[158] R. A. Duine and H. T. C. Stoof, Explosion of a Collapsing Bose-Einstein Condensate, Phys. Rev. Lett. **86**, 2204 (2001).

[159] S. Yi and H. Pu, Vortex Structures in Dipolar Condensates, Phys. Rev. A **73**, 061602(R) (2006).

[160] R. M. W. van Bijnen, D. H. J. O'Dell, N. G. Parker, and A. M. Martin, Dynamical Instability of a Rotating Dipolar Bose-Einstein Condensate, Phys. Rev. Lett. **98**, 150401 (2007).

[161] M. Klawunn, R. Nath, P. Pedri, and L. Santos, Transverse Instability of Straight Vortex Lines in Dipolar Bose-Einstein Condensates, Phys. Rev. Lett. **100**, 240403 (2008).

[162] H. Saito and M. Ueda, Split Instability of a Vortex in an Attractive Bose-Einstein Condensate, Phys. Rev. Lett. **89**, 190402 (2002).

[163] H. Pu, C. K. Law, J. H. Eberly, and N. P. Bigelow, Coherent Disintegration and Stability of Vortices in Trapped Bose Condensates, Phys. Rev. A **59**, 1533 (1999).

[164] L. D. Carr and C. W. Clark, Vortices in Attractive Bose-Einstein Condensates in Two Dimensions, Phys. Rev. Lett. **97**, 010403 (2006).

[165] D. Mihalache, D. Mazilu, B. A. Malomed, and F. Lederer, Vortex Stability in Neary-Two-Dimensional Bose-Einstein Condensates with Attraction, Phys. Rev. A **73**, 043615 (2006).

[166] D. Bohm and B. Salt, Collective Treatment of Liquid Helium, Rev. Mod. Phys **39**, 894 (1967).

[167] T. Regge, Free Boundary of He II and Feynman Wave Functions, J. Low Temp. Phys. **9**, 123 (1972).

[168] F. Dalfovo, Structure of Vortices in Helium at Zero Temperature, Phys. Rev. B **46**, 5482 (1992).

[169] D. H. J. O'Dell and C. Eberlein, Vortex in a Trapped Bose-Einstein Condensate with Dipole-Dipole Interactions, Phys. Rev. A **75**, 013604 (2007).

[170] J. Sugar and C. Corliss, Atomic Energy Levels of the Iron Period Elements: Potassium Through Nickel, J. Phys. Chem. Ref. Data **14** (1985).

[171] N. G. Parker, C. Ticknor, A. M. Martin, and D. H. J. O'Dell, Structure Formation During the Collapse of a Dipolar Atomic Bose-Einstein Condensate, Phys. Rev. A **79**, 013617 (2009).

[172] C. W. Gardiner and P. Zoller, Quantum Noise, Springer, Berlin, 2nd edition, 1999.

[173] J. Metz, T. Lahaye, B. Fröhlich, A. Griesmaier, T. Pfau, H. Saito, Y. Kawaguchi, and M. Ueda, Coherent Collapses of Dipolar Bose-Einstein Condensates for Different Trap Geometries, New J. Phys. **11**, 055032 (2009).

[174] C. Raman, M. Köhl, R. Onofrio, D. S. Durfee, C. E. Kuklewica, Z. Hadzibabic, and W. Ketterle, Evidence for a Critical Velocity in a Bose-Einstein Condensed Gas, Phys. Rev. Lett. **83**, 2502 (1999).

[175] R. Onofrio, C. Raman, J. M. Vogels, J. R. Abo-Shaeer, A. P. Chikkatur, and W. Ketterle, Observation of Superfluid Flow in a Bose-Einstein Condensed Gas, Phys. Rev. Lett. **85**, 2228 (2000).

[176] T. Frisch, Y. Pomeau, and S. Rica, Transition to Dissipation in a Model of Superflow, Phys. Rev. Lett. **69**, 1644 (1992).

[177] T. Winiecki, B. Jackson, J. F. McCann, and C. S. Adams, Vortex Shedding and Drag in Dilute Bose-Einstein Condensates, J. Phys. B **33**, 4069 (2000).

[178] J. S. S. berger and W. Zwerger, Critical Velocity of Superfluid Flow Past Large Obstacles in Bose-Einstein Condensates, Phys. Rev. A **62**, 061601 (2000).

[179] B. Jackson, J. F. McCann, and C. S. Adams, Dissipation and Vortex Creation in Bose-Einstein Condensed Gases, Phys. Rev. A **61**, 051603(R) (2000).

[180] L. Landau, The Theory of Superfluidity in Helium II, J. Phys. (Moscow) **5**, 71 (1941).

[181] S. A. Morgan, S. Choi, K. Burnett, and M. Edwards, Nonlinear Mixing of Quasiparticles in an Inhomogeneous Bose Condensate, Phys. Rev. A **57**, 3818 (1998).

[182] S. Ianeselli, C. Menotti, and A. Smerzi, Beyond the Landau Criterion for Superfluidity, J. Phys. B **39**, S135 (2006).

[183] M. A. uz Zaman and D. Blume, Tuning the Structural and Dynamical Properties of a Dipolar Bose-Einstein Condensate: Ripples and Instability Islands, New J. Phys **12**, 065022 (2010).

[184] D.-W. Wang and E. Demler, Collective Excitations and Instabilities in Multi-Layer Stacks of Dipolar Condensates, (2008), arXiv:0812.1838.

[185] J. Higbie and D. M. Stamper-Kurn, Periodically Dressed Bose-Einstein Condensate: A Superfluid with an Anisotropic and Variable Critical Velocity, Phys. Rev. Lett. **88**, 090401 (2002).

[186] I. Danshita and D. Yamamoto, Critical Velocity of Flowing Supersolids of Dipolar Bose Gases in Optical Lattices, Phys. Rev. A **82**, 013645 (2010).

[187] I. Tikhonenkov, B. A. Malomed, and A. Vardi, Anisotropic Solitons in Dipolar Bose-Einstein Condensates, Phys. Rev. Lett. **100**, 090406 (2008).

[188] T. W. Neely, E. C. Samson, A. S. Bradley, M. J. Davis, and B. P. Anderson, Observation of Vortex Dipoles in an Oblate Bose-Einstein Condensate, Phys. Rev. Lett. **104**, 160401 (2010).

[189] C. J. Foster, P. B. Blakie, and M. J. Davis, Vortex Pairing in Two-Dimensional Bose Gases, Phys. Rev. A **81**, 023623 (2010).

[190] J. P. D'Incao and C. H. Greene, Collisional Aspects of Bosonic and Fermionic Dipoles in Quasi-Two-Dimensional Confining Geometries, Phys. Rev. A **83**, 030702(R) (2011).

[191] A. Micheli, G. Pupillo, H. P. Büchler, and P. Zoller, Cold Polar Molecules in Two-Dimensional Traps: Tailoring Interactions with External Fields for Novel Quantum Phases, Phys. Rev. A **76**, 043604 (2007).

[192] M. Klawunn, A. Pikovski, and L. Santos, Two-Dimensional Scattering and Bound States of Polar Molecules in Bilayers, Phys. Rev. A **82**, 044701 (2010).

[193] M. Klawunn and L. Santos, Hybrid Multisite Excitations in Dipolar Condensates in Optical Lattices, Phys. Rev. A **80**, 013611 (2009).

[194] P. Köberle and G. Wunner, Phonon Instability and Self-Organized Structures in Multilayer Stacks of Confined Dipolar Bose-Einstein Condensates in Optical Lattices, Phys. Rev. A **80**, 063601 (2009).

[195] A. Junginger, J. Main, and G. Wunner, Variational Calculations on Multilayer Stacks of Dipolar Bose-Einstein Condensates, Phys. Rev. A **82**, 023602 (2010).

[196] S. Rau, J. Main, P. Köberle, and G. Wunner, Pitchfork Bifurcations in Blood-Cell-Shaped Dipolar Bose-Einstein Condensates, Phys. Rev. A **81**, 031605 (2010).

[197] M. Jeng, Random Walks and Effective Resistances on Toroidal and Cylindrical Grids, Am. J. Phys. **68**, 37 (2000).

[198] M. R. Andrews, M. O. Mewes, N. J. vanDruten, D. S. Durfee, D. M. Kurn, and W. Ketterle, Direct, Nondestructive Observation of a Bose Condensate, Science **273**, 84 (1996).

[199] M. A. Baranov, Progress in Many-Body Physics with Ultracold Dipolar Gases, Phys. Rep. **464**, 71 (2008).

[200] A. L. Fetter and J. D. Walecka, Quantum Theory of Many-Particle Systems, Dover Publications, Inc., New York, 2003.

[201] B. Xiong, J. Gong, H. Pu, W. Bao, and B. Li, Symmetry Breaking and Self-Trapping of a Dipolar Bose-Einstein Condensate in a Double-Well Potential, Phys. Rev. A **79**, 013626 (2009).

[202] Y. Liu, S. Jung, S. Maxwell, L. D. Turner, E. Tiesinga, and P. D. Lett, Quantum Phase Transitions and Continuous Observation of Spinor Dynamics in an Antiferromagnetic Condensate, Phys. Rev. Lett. **102**, 125301 (2009).

[203] J. Burke, Theoretical Investigation of Cold Alkali Atom, PhD thesis, University of Colorado, Boulder, 1999.

[204] D. C. E. Bortolotti, S. Ronen, J. L. Bohn, and D. Blume, Scattering Length Instability in Dipolar Bose-Einstein Condensates, Phys. Rev. Lett. **97**, 160402 (2006).

[205] M. Guizar-Siciaros and J. C. Gutiérrez-Vega, Computation of Quasi-Discrete Hankel Transforms of Integer Order for Propagating Optical Wave Fields, J. Opt. Soc. Am. A **21**, 53 (2004).

[206] W. H. Press, B. P. Flannery, S. A. Teukolsky, and W. T. Vetterling, Numerical Recipes in C: The Art of Scientific Computing, Cambridge University Press, Cambridge, 2nd edition, 1992.

[207] M. C. Payne, M. P. Teter, D. C. Allan, T. A. Arias, and J. D. Joannopoulos, Iterative Minimization Techniques for Ab Initio Total-Energy Calculations: Molecular Dynamics and Conjugate Gradients, Rev. Mod. Phys. **64**, 1045 (1992).

[208] T. Lahaye, T. Koch, B. Fröhlich, M. Fattori, J. Metz, A. Griesmaier, S. Giovanazzi, and T. Pfau, Strong Dipolar Effects in a Quantum Ferrofluid, Nature **448**, 672 (2007).

Appendix A

The Convolution Theorem

The calculation of the dipolar mean-field potential (3.63) and other convolution integrals in this thesis require special treatment. Consider the integral

$$\int d\mathbf{x}' V(\mathbf{x}-\mathbf{x}')n(\mathbf{x}') \tag{A.1}$$

where $V(\mathbf{x})$ and $n(\mathbf{x})$ are both well-behaved, i.e., they have well-defined Fourier transforms. Here, $V(\mathbf{x}-\mathbf{x}')$ can be any function, though the relevant form for this work is the two-body dipole-dipole interaction (ddi) potential given in (3.61). In three-dimensions, the $1/r^3$ real-space behavior of the ddi does not present a true mathematical divergence, but can be very difficult to handle numerically when the integrals are discritized onto a real-space grid. For example, numerical sums must be taken over the entire spatial grid (corresponding to $\mathbf{x}'$) for each grid point (corresponding to $\mathbf{x}$), and the divergence corresponding to the $r = 0$ pole of the ddi can not be handled numerically.

These complications can be overcome by moving to momentum-space. We define the Fourier transform operator $\mathcal{F}$ and its inverse $\mathcal{F}^{-1}$ to move into and back from momentum-space, respectively,

$$\tilde{f}(\mathbf{k}) = \mathcal{F}\left[f(\mathbf{x})\right] = \int d\mathbf{x} f(\mathbf{x}) e^{i\mathbf{k}\cdot\mathbf{x}} \tag{A.2}$$

$$f(\mathbf{x}) = \mathcal{F}^{-1}\left[\tilde{f}(\mathbf{k})\right] = \int \frac{d\mathbf{k}}{(2\pi)^3} \tilde{f}(\mathbf{k}) e^{-i\mathbf{k}\cdot\mathbf{x}}. \tag{A.3}$$

With these operations, we can rewrite the convolution in Eq. (A.1) as

$$\begin{aligned}\int d\mathbf{x}' V(\mathbf{x}-\mathbf{x}')n(\mathbf{x}') &= \int d\mathbf{x}' \left(\int \frac{d\mathbf{k}}{(2\pi)^3}\tilde{V}(\mathbf{k})e^{-i\mathbf{k}\cdot(\mathbf{x}-\mathbf{x}')}\right)\left(\int \frac{d\mathbf{q}}{(2\pi)^3}\tilde{n}(\mathbf{q})e^{-i\mathbf{q}\cdot\mathbf{x}'}\right)\\ &= \int \frac{d\mathbf{k}}{(2\pi)^3}\int \frac{d\mathbf{q}}{(2\pi)^3}\tilde{V}(\mathbf{k})e^{-i\mathbf{k}\cdot\mathbf{x}}\tilde{n}(\mathbf{q})\int d\mathbf{x}' e^{-i(\mathbf{q}-\mathbf{k})\cdot\mathbf{x}'}\\ &= \int \frac{d\mathbf{k}}{(2\pi)^3}\int d\mathbf{q}\tilde{V}(\mathbf{k})e^{-i\mathbf{k}\cdot\mathbf{x}}\tilde{n}(\mathbf{q})\delta(\mathbf{q}-\mathbf{k})\\ &= \int \frac{d\mathbf{k}}{(2\pi)^3}\tilde{V}(\mathbf{k})\tilde{n}(\mathbf{k})e^{-i\mathbf{k}\cdot\mathbf{x}}. \qquad \text{(A.4)}\end{aligned}$$

Thus, we see that the convolution of a function $n(\mathbf{x}')$ with the function $V(\mathbf{x}-\mathbf{x}')$ is just given by the inverse Fourier transform of the product of their individual Fourier transforms,

$$\int d\mathbf{x}' V(\mathbf{x}-\mathbf{x}')n(\mathbf{x}') = \mathcal{F}^{-1}\left[\tilde{V}(\mathbf{k})\tilde{n}(\mathbf{k})\right]. \qquad \text{(A.5)}$$

Appendix B

Momentum-Space Dipole-Dipole Interaction Potential

Here we calculate the momentum-space dipole-dipole interaction potential for dipoles with arbitrary, but identical polarization. Consider the unit polarization vector $\hat{d} = \hat{x}\sin\alpha\cos\eta + \hat{y}\sin\alpha\sin\eta + \hat{z}\cos\alpha$, tilted by an angle α off of the z-axis and an angle η off of the x-axis. Then, if we say that the vector $\mathbf{x}$ separates the dipoles we can write $\hat{d}\cdot\hat{x}$ as

$$\hat{d}\cdot\hat{x} = \cos\theta\cos\alpha + \cos\phi\sin\theta\sin\alpha\cos\eta + \sin\phi\sin\theta\sin\alpha\sin\eta, \tag{B.1}$$

thus, the ddi from Eq. (2.20) takes the form

$$V_d(\mathbf{x}) = d^2\frac{1 - 3\left(\cos\theta\cos\alpha + \cos\phi\sin\theta\sin\alpha\cos\eta + \sin\phi\sin\theta\sin\alpha\sin\eta\right)^2}{x^3}. \tag{B.2}$$

To simplify the math that follows, we use the spherical harmonics $Y_{lm} \leftrightarrow Y_{lm}(\theta,\phi)$ [54] to expand (B.2),

$$\begin{aligned} V_d(\mathbf{x}) = \frac{d^2}{x^3}\Bigg\{ & \sin^2\alpha - 4\sqrt{\frac{\pi}{5}}\cos^2\alpha Y_{20} - 4\sqrt{\pi}\sin^2\alpha\cos^2\eta\left(Y_{00} - \frac{1}{\sqrt{5}}Y_{20}\right) \\ & - i\sqrt{\frac{6\pi}{5}}\sin^2\alpha\sin 2\eta\left(Y_{2-2} - Y_{22}\right) - \sqrt{\frac{6\pi}{5}}\sin 2\alpha\cos\eta\left(Y_{2-1} - Y_{21}\right) \\ & - i\sqrt{\frac{6\pi}{5}}\sin 2\alpha\sin\eta\left(Y_{2-1} - Y_{21}\right)\Bigg\}. \end{aligned} \tag{B.3}$$

We wish to compute the Fourier transform of (B.3). To do this, we use the definition of the Fourier transform (A.2) and the expansion of the spherical plane wave [91]

$$e^{i\mathbf{k}\cdot\mathbf{x}} = 4\pi\sum_{l,m} i^l Y^{\star}_{lm}(\hat{k})j_l(kx)Y_{lm}(\hat{x}), \tag{B.4}$$

where $j_l(kx)$ is the spherical Bessel function of order l, and the orthonormality relations of the spherical harmonics,

$$\int_\Omega Y_{lm}(\theta,\phi)Y^\star_{l'm'}(\theta,\phi)d\Omega = \delta_{ll'}\delta_{mm'}. \tag{B.5}$$

The resulting momentum-space ddi interaction potential is

$$\begin{aligned}\tilde{V}_d(\mathbf{k}) = \pi d^2 \big\{&2\sin^2\alpha\sin^2\theta_{\mathbf{k}}\cos\left(2\phi_{\mathbf{k}}+2\eta\right) + 2\sin 2\alpha \sin 2\theta_{\mathbf{k}}\cos\left(\phi_{\mathbf{k}}+\eta\right)\\ &+\left(\frac{4}{3}-2\sin^2\alpha\right)\left(3\cos^2\theta_{\mathbf{k}}-1\right)\Big\}.\end{aligned} \tag{B.6}$$

Note that this expression was independently derived in [201], giving a consistent result.

Appendix C

Quasi-2D Dipolar Interaction Potential

Here we calculate the effective dipole-dipole interaction (ddi) potential for the quasi-2D geometry given by Eq. (4.22) in section 4.2.2,

$$V_{\mathrm{q2D}}(\boldsymbol{\rho}-\boldsymbol{\rho}') = \int dz \int dz' \chi^{\star}(z)\chi^{\star}(z')V_d(\mathbf{x}-\mathbf{x}')\chi(z')\chi(z), \tag{C.1}$$

where $\chi(z)$ is the axial wave function in the quasi-2D geometry given in Eq. (4.19). In this work, we use the quasi-2D potential to calculate terms like $\int d\boldsymbol{\rho}' f(\boldsymbol{\rho}')V_{\mathrm{q2D}}(\boldsymbol{\rho}-\boldsymbol{\rho}')$. According to the convolution theorem (A.5), we can calculate this integral by taking the inverse Fourier transform of the product of $\tilde{f}(\mathbf{k}_\rho)$ and $\tilde{V}_{\mathrm{q2D}}(\mathbf{k}_\rho)$, so knowledge of $\tilde{V}_{\mathrm{q2D}}(\mathbf{k}_\rho)$ is sufficient to handle this calculation. This quasi-2D momentum-space interaction potential is given by the momentum-space equivalent of Eq. (C.1),

$$\tilde{V}_{\mathrm{q2D}}(\mathbf{k}_\rho) = \int dk_z \tilde{n}_z^2(k_z)\tilde{V}_d(\mathbf{k}), \tag{C.2}$$

where

$$\tilde{n}_z(k_z) = \mathcal{F}\left[\chi^2(z)\right] = \exp\left[-\frac{1}{4}k_z^2 l_z^2\right]. \tag{C.3}$$

Consider the polarization that is described in appendix B but, without loss of generality, we set $\eta = 0$ so the the polarization is tilted into the x-axis only. At the end of this calculation, we rotate the coordinates to generalize to any tilt into the x-y plane. We rewrite the result for the momentum-space ddi (B.6) as

$$\begin{aligned}\tilde{V}_d(\mathbf{k}) &= \pi d^2 \left\{2\sin^2\alpha\sin^2\theta_{\mathbf{k}}\left(\cos^2\phi_{\mathbf{k}} - \sin^2\phi_{\mathbf{k}}\right) + 4\sin 2\alpha\sin\theta_{\mathbf{k}}\cos\theta_{\mathbf{k}}\cos\phi_{\mathbf{k}}\right. \\ &\quad \left. + \,(4/3 - 2\sin^2\alpha)(3\cos^2\theta_{\mathbf{k}} - 1)\right\} \\ &= \pi d^2\left\{2\sin^2\alpha\frac{k_x^2 - k_y^2}{k^2} + 4\sin 2\alpha\frac{k_z k_x}{k^2} + \left(\frac{4}{3} - 2\sin^2\alpha\right)\left(3\frac{k_z^2}{k^2} - 1\right)\right\}. \qquad \text{(C.4)}\end{aligned}$$

We now compute the integral (C.2), where we leave out the second term in Eq. (C.4) because it is linear in k_z and therefore integrates to zero,

$$\begin{aligned}\tilde{V}_{\mathrm{q2D}}(\mathbf{k}_\rho) &= \pi d^2 \int dk_z e^{-\frac{1}{2}k_z^2 l_z^2}\left\{2\sin^2\alpha\frac{k_x^2 - k_y^2}{k^2} + \left(\frac{4}{3} - 2\sin^2\alpha\right)\left(3\frac{k_z^2}{k^2} - 1\right)\right\} \\ &= \pi d^2\left[2\sin^2\alpha\left(\pi e^{\frac{k_\rho^2 l_z^2}{2}}\frac{k_x^2 - k_y^2}{k_\rho}\mathrm{erfc}\left[\frac{k_\rho l_z}{\sqrt{2}}\right]\right)\right. \\ &\quad \left. + \left(\frac{4}{3} - 2\sin^2\alpha\right)\left(3\sqrt{2\pi}l_z - 3\pi e^{\frac{k_\rho^2 l_z^2}{2}}k_\rho\mathrm{erfc}\left[\frac{k_\rho l_z}{\sqrt{2}}\right] - 1\right)\right] \\ &\vdots \\ &= \frac{g_d}{\sqrt{2\pi}l_z}\left[\cos^2\alpha F_\perp\left(\frac{\mathbf{k}_\rho l_z}{\sqrt{2}}\right) + \sin^2\alpha F_\parallel\left(\frac{\mathbf{k}_\rho l_z}{\sqrt{2}}\right)\right], \qquad \text{(C.5)}\end{aligned}$$

where $g_d = 4\pi\hbar^2 a_{dd}/M$, a_{dd} is given by Eq. (2.21) and the dimensionless functions $F_\perp$ and $F_\parallel$ account for the projection of $\hat{d}$ onto the z-axis and onto the x axis, respectively. The function $F_\parallel$ depends explicitly on k_x, or the direction on which the dipoles are tilted. Without loss of generality, we can rotate our coordinates and replace this momentum dependence with $k_x \rightarrow k_d = \sqrt{k_x^2\cos^2\eta + k_y^2\sin^2\eta}$, giving

$$F_\perp(\mathbf{q}) = 2 - 3\sqrt{\pi}qe^{q^2}\mathrm{erfc}[q] \qquad \text{(C.6)}$$

$$F_\parallel(\mathbf{q}) = -1 + 3\sqrt{\pi}\frac{q_d^2}{q}e^{q^2}\mathrm{erfc}[q], \qquad \text{(C.7)}$$

where erfc is the complimentary error function [54]. Thus, we can write the quasi-2D momentum-space ddi as

$$\tilde{V}_{\mathrm{q2D}}(\mathbf{k}_\rho) = \frac{g_d}{\sqrt{2\pi}l_z}F\left(\frac{\mathbf{k}_\rho l_z}{\sqrt{2}}\right), \qquad \text{(C.8)}$$

where $F(\mathbf{q}) = \cos^2\alpha F_\perp(\mathbf{q}) + \sin^2\alpha F_\parallel(\mathbf{q})$.

Appendix D

Discrete Hankel Transform

Here, we give the algorithm for the discrete Hankel transform (DHT) of a function $f(\rho)e^{im\varphi}$. This algorithm is also given in [102], and is derived in detail in [205]. From Eq. (5.5) in the text, we see that the Hankel transform of such a function is given by projecting $f(\rho)$ onto the m^{th} order Bessel function $J_m(k\rho)$. Here, we assume that the function $f(\rho) = 0$ for all $\rho > R$ and its transform $\tilde{f}(k) = 0$ for all $k > K$. Additionally, we sample the real- and momentum-space functions on grids with N points that are defined in terms of the roots of the m^{th} order Bessel function α_{mj}, so that $J_m(\alpha_{mj}) = 0$ for all j,

$$\rho_{mj} = \alpha_{mj}/K \tag{D.1}$$

$$k_{mj} = \alpha_{mj}/R, \tag{D.2}$$

where $j = 1, 2, \ldots, N$. Then, the DHT of the function $f(\rho_{mj})$ is given by

$$\tilde{f}(k_{mi}) = \frac{2}{K^2} \sum_{j=1}^{N} \frac{f(\rho_{mj})}{J^2_{m+1}(\alpha_{mj})} J_m\left(\frac{\alpha_{mi}\alpha_{mj}}{RK}\right). \tag{D.3}$$

Similarly, the inverse DHT of the function $\tilde{f}(k_{mj})$ is given by

$$f(\rho_{mi}) = \frac{2}{R^2} \sum_{j=1}^{N} \frac{\tilde{f}(k_{mj})}{J^2_{m+1}(\alpha_{mj})} J_m\left(\frac{\alpha_{mj}\alpha_{mi}}{RK}\right) \tag{D.4}$$

By defining the functions

$$F(j) = \frac{R}{|J_{m+1}(\alpha_{mi})|} f\left(\frac{\alpha_{mj}}{K}\right) \tag{D.5}$$

$$\tilde{F}(j) = \frac{K}{|J_{m+1}(\alpha_{mi})|} \tilde{f}\left(\frac{\alpha_{mj}}{R}\right), \tag{D.6}$$

the DHT in Eq. (D.3) reduces to

$$\tilde{F}(i) = \sum_{j=1}^{N} T_{ij} F(j), \tag{D.7}$$

where the matrix T_{ij} is given by

$$T_{ij} = \frac{2J_m\left(\frac{\alpha_{mi}\alpha_{mj}}{RK}\right)}{|J_{m+1}(\alpha_{mi})||J_{m+1}(\alpha_{mj})|RK}. \tag{D.8}$$

We determine the cutoffs R and K by first choosing a reasonable R based on the parameters in the problem, and then K is given by $K = \alpha_{m,N+1}/R$.

Interestingly, defining the radial grids in terms of the zeros of the m^{th} order Bessel function, as in (D.1) and (D.2), and enforcing that $\tilde{f}(k) = 0$ for all $k > K$ allows us to write the radial integrals $I[f] = \int_0^\infty f(\rho)\rho d\rho$ as [102]

$$I[f] = \frac{2}{K^2} \sum_{i=1}^{\infty} \frac{f\left(\frac{\alpha_{mi}}{K}\right)}{J_{m+1}^2(\alpha_{mi})}, \tag{D.9}$$

which has a form very similar to that of Gaussian quadrature. To a very good approximation, we employ this formula on the finite grid with N points, and thus truncate the sum in Eq. (D.9) at $i = N$. The accuracy of this numeric integration is increased with increasing N and R, though we find that sufficient convergence is obtained for typical grids used in this work.

Appendix E

Energy-Functional Minimization via Conjugate Gradients

In this appendix we describe the conjugate gradients (cg) algorithm for finding the function that minimizes the Gross-Pitaevskii energy functional, Eq. (5.3) [206, 155]. We rewrite the energy functional here, representing the real-space condensate wave function $\phi(\mathbf{x})$ by the "ket" $|\phi\rangle$,

$$\frac{E[\phi]}{N} = \frac{\langle\phi|\hat{H}^{(1)}|\phi\rangle}{\langle\phi|\phi\rangle} + \frac{N-1}{2}\frac{\langle\phi|\langle\phi|\hat{V}|\phi\rangle|\phi\rangle}{\langle\phi|\phi\rangle^2}, \tag{E.1}$$

where $\hat{H}^{(1)}$ is the single particle Hamiltonian (3.16) and $\hat{V}$ represents the two-body interaction potential (3.61), so $\langle\phi|\hat{V}|\phi\rangle$ is the condensate mean-field potential. In (E.1), we explicitly normalize the terms so that the energy of a non-normalized state can be obtained.

To begin the cg algorithm, we choose a trial wave function $|\phi_1\rangle$ and modify it with the variational term $|\phi_1\rangle \to |\phi_1\rangle + \lambda|\chi_1\rangle$, where $\langle\phi_1|\chi_1\rangle = 0$ and λ is a variational scalar. This modified wave function is then substituted into the energy functional (E.1), which then becomes a 4^{th} order polynomial in λ. The minimum of this polynomial is then easily found and the λ that defines the minimum, λ_{min}, determines the modified wave function, $|\phi_2\rangle = |\phi_1\rangle + \lambda_{\text{min}}|\chi_1\rangle$, and this process is iterated until sufficient convergence is reached.

Let us adopt the notation that $|\phi_i\rangle$ and $|\chi_i\rangle$ correspond to the states used in the i^{th} iteration of the cg algorithm. To calculate $|\chi_i\rangle$ given $|\phi_i\rangle$, we simply take a gradient of the energy $E[\phi_i]/N$ and add a "preconditioning" term $P(\mathbf{k})$ by hand, which gives the Gross-Pitaveskii type expression

$$|\chi_i\rangle = \mathcal{F}^{-1}\left[P(\mathbf{k})\mathcal{F}\left[\left(\hat{H}^{(1)} + (N-1)\langle\phi_i|\hat{V}|\phi_i\rangle\right)|\phi_i\rangle\right]\right], \tag{E.2}$$

where $\mathcal{F}$ is the 3D Fourier transform operator, $P(\mathbf{k}) = 1/(k^2/2 + L)$, $L = \max(E, E_k)$, E is the total energy per particle in the state $|\phi_i\rangle$ and E_k is the kinetic energy of the state $|\phi_i\rangle$. The preconditioning function $P(\mathbf{k})$ is included to accelerate the convergence of the cg algorithm [207]. To ensure the orthogonality of $|\phi_i\rangle$ and $|\chi_i\rangle$, we operate of $|\chi_i\rangle$ with the projection operator $\hat{P}_i = 1 - |\phi_i\rangle\langle\phi_i|$, which projects a function into the space orthogonal to $|\phi_i\rangle$. We also normalize $|\chi_i\rangle$ in each iteration.

Now, the energy functional $E[\phi_i + \lambda\chi_i]/N$ takes the form

$$\frac{E[\phi_i + \lambda\chi_i]}{N} = \frac{1}{(1+\lambda^2)^2}\sum_{j=1}^{4} C_j \lambda^j, \tag{E.3}$$

where the C_j polynomial coefficients are j^{th} order in χ_i, and are given by

$$\begin{aligned}
C_0 &= \langle\phi_i|\hat{H}^{(1)}|\phi_i\rangle + \langle\phi_i|\langle\phi_i|\hat{V}|\phi_i\rangle|\phi_i\rangle \\
C_1 &= \langle\phi_i|\hat{H}^{(1)}|\chi_i\rangle + \langle\chi_i|\hat{H}^{(1)}|\phi_i\rangle + \langle\phi_i|\langle\phi_i|\hat{V}|\phi_i\rangle|\chi_i\rangle + \langle\phi_i|\langle\phi_i|\hat{V}|\chi_i\rangle|\phi_i\rangle + \langle\phi_i|\langle\chi_i|\hat{V}|\phi_i\rangle|\phi_i\rangle \\
&\quad + \langle\chi_i|\langle\phi_i|\hat{V}|\phi_i\rangle|\phi_i\rangle \\
C_2 &= \langle\phi_i|\hat{H}^{(1)}|\phi_i\rangle + \langle\chi_i|\hat{H}^{(1)}|\chi_i\rangle + \langle\chi_i|\langle\phi_i|\hat{V}|\phi_i\rangle|\chi_i\rangle + \langle\phi_i|\langle\chi_i|\hat{V}|\chi_i\rangle|\phi_i\rangle + \langle\phi_i|\langle\phi_i|\hat{V}|\chi_i\rangle|\chi_i\rangle \\
&\quad + \langle\chi_i|\langle\chi_i|\hat{V}|\phi_i\rangle|\phi_i\rangle + \langle\phi_i|\langle\chi_i|\hat{V}|\phi_i\rangle|\chi_i\rangle + \langle\chi_i|\langle\phi_i|\hat{V}|\chi_i\rangle|\phi_i\rangle \\
C_3 &= \langle\phi_i|\hat{H}^{(1)}|\chi_i\rangle + \langle\chi_i|\hat{H}^{(1)}|\phi_i\rangle + \langle\chi_i|\langle\chi_i|\hat{V}|\chi_i\rangle|\phi_i\rangle + \langle\chi_i|\langle\chi_i|\hat{V}|\phi_i\rangle|\chi_i\rangle + \langle\chi_i|\langle\phi_i|\hat{V}|\chi_i\rangle|\chi_i\rangle \\
&\quad + \langle\phi_i|\langle\chi_i|\hat{V}|\chi_i\rangle|\chi_i\rangle \\
C_4 &= \langle\chi_i|\hat{H}^{(1)}|\chi_i\rangle + \langle\chi_i|\langle\chi_i|\hat{V}|\chi_i\rangle|\chi_i\rangle.
\end{aligned} \tag{E.4}$$

We calculate λ_{min} by solving for $\partial_\lambda E[\phi_i + \lambda\chi_i]/N = 0$, where

$$\frac{\partial}{\partial\lambda}\frac{E[\phi_i + \lambda\chi_i]}{N} = \frac{1}{(1+\lambda^2)^2}\sum_{j=0}^{4} C_j \left[j\lambda^{j-1} - \frac{4\lambda^{j+1}}{1+\lambda^2}\right]. \tag{E.5}$$

The idea of the cg algorithm is to sample the shape of the Gross-Pitaevskii energy manifold on a large scale, accomplished by calculated the polynomial line (E.3) through the manifold. Finding the minimum of this line then tells us what linear combination of $|\phi_i\rangle$ and its orthogonal counterpart $|\chi_i\rangle$ minimizes the energy in the space spanned by these functions. For a purely dipolar BEC in a trap with aspect ratio $\lambda = 10$ and ddi strength $D = 50$, sampled on a grid of size $(N_\rho, N_z) = (128, 64)$, we find that convergence to a part in 10^{-14} is reached in about 4 seconds.

Appendix F

Radial Grid Interpolation

In appendix D we introduce radial grids in real and momentum-space that are defined in terms of the zeros of the m^{th} order Bessel function, and are thus termed m^{th} order grids. Such grids are constructed to properly handle the numeric integration and discrete Hankel transforms of functions with angular dependence $e^{im\varphi}$. In the methods described in section 5.1, we see that functions must be interpolated between radial grids of different orders in order to properly handle the integrals written therein. Here, we derive an accurate interpolation scheme based on the DHT.

As explained in Ref. [153], the function $f(\rho)$ may be expanded in an m^{th} order Bessel series,

$$f(\rho) = \sum_{i=1}^{N} c_{mi} J_m \left(\alpha_{mi} \frac{\rho}{R} \right) \tag{F.1}$$

where the coefficients c_{mi} are given by

$$c_{mi} = \frac{2}{R^2 \left[J_{m+1}(\alpha_{mi}) \right]^2} \int_0^R f(\rho) J_m \left(\alpha_{mi} \frac{\rho}{R} \right) \rho \, d\rho. \tag{F.2}$$

Note that the integral in Eq. (F.2) is just the Hankel transform (5.5) with $\alpha_{mi}/R = k_{mi}$, giving the transformed function $\tilde{f}(k_i)$. If ρ is discretized in Eq. (F.1), then this prescription gives exactly Eq. (D.4).

Consider the case where the function $f(\rho)$ is defined on the grid ρ_{mi} but needs to be defined on the grid ρ_{ni}, with $n \neq m$. To do this, we expand $f(\rho_{ni})$ in a Bessel series,

$$f(\rho_{ni}) = \sum_{j=1}^{N} c_{mj} J_m \left(\alpha_{mj} \frac{\rho_{ni}}{R} \right) \tag{F.3}$$

where the coefficients c_{mj} are given by Eq. (F.2) and are computed in terms of the zeros of the Bessel function of order m. However, in Eq. (F.3), the function is expanded on the grid ρ_{ni}, proportional to the zeros of the Bessel function of order n. The interpolation algorithm then simply follows by inserting the expression for the coefficients,

$$f(\rho_{ni}) = \frac{2}{R^2} \sum_{j=1}^{N} \frac{\tilde{f}(k_{mj})}{J_{m+1}^2(\alpha_{mj})} J_m\left(\frac{\alpha_{mj}\alpha_{ni}}{S}\right), \tag{F.4}$$

where $\tilde{f}(k_{mj})$ is the discrete Hankel transform of $f(\rho_{mj})$, given by Eq. (D.3).

Appendix G

Calculation of the Mean-Field Potential in Reduced Dimensions

We consider the calculation of the mean-field potential due to the dipole-dipole interaction (ddi) in two different geometries, one with $\lambda \to 0$ (a quasi-two dimensional (2D) geometry) and one with $\lambda \to \infty$ (a quasi-one dimensional (1D) geometry). In the quasi-2D geometry, we assume that the condensate wave function depends only on z and is homogeneous in the ρ-direction (or in the x- and y-directions) and in the quasi-1D geometry, we assume that the condensate wave function depends only on ρ (or on x and y) and is homogeneous in the z-direction.

We begin with the expression for the dipole-dipole interaction potential in momentum-space from Eq. (3.62)

$$\tilde{V}_d(\mathbf{k}) = \frac{4\pi}{3} d^2 \left(3\cos^2\theta_{\mathbf{k}} - 1\right), \tag{G.1}$$

where $\theta_{\mathbf{k}}$ is the angle between the direction of the dipole polarization ($\hat{z}$ or $\hat{k}_z$, for the dipolar BEC we are considering) and the vector $\mathbf{k}$. Using this momentum-space representation, the coordinate-space mean-field potential due to the dipole-dipole interaction is given by the convolution of $\tilde{V}_d(\mathbf{k})$ with the condensate density in momentum-space, $\tilde{n}(\mathbf{k})$,

$$U_d(\mathbf{r}) = \mathcal{F}^{-1}\left[\tilde{V}_d(\mathbf{k})\tilde{n}(\mathbf{k})\right], \tag{G.2}$$

where $\mathcal{F}^{-1}$ is the inverse Fourier transform operator. First, consider the quasi-2D geometry, in which the condensate density is homogeneous is x and y. The condensate density in momentum-space is then given by the Fourier transform,

$$\tilde{n}_{\mathrm{2D}}(\mathbf{k}) = \mathcal{F}\left[n_{\mathrm{2D}}(z)\right] = \tilde{n}_{\mathrm{2D}}(k_z)\delta(k_x)\delta(k_y). \tag{G.3}$$

Substituting this result and Eq. (G.1) into Eq. (G.2) and writing $\cos^2\theta_{\mathbf{k}} = k_z^2/(k_x^2+k_y^2+k_z^2)$ gives an expression for the mean-field potential in the quasi-2D geometry,

$$U_d^{\mathrm{2D}}(\mathbf{r}) = \mathcal{F}^{-1}\left[\frac{4\pi}{3}d^2\left(3\frac{k_z^2}{k_x^2+k_y^2+k_z^2}-1\right)\tilde{n}_{\mathrm{2D}}(k_z)\delta(k_x)\delta(k_y)\right]. \tag{G.4}$$

The operation of the inverse Fourier transform on this momentum-space function gives

$$U_d^{\mathrm{2D}}(\mathbf{r}) = \frac{8\pi}{3}d^2|\phi_0(z)|^2 = \frac{8\pi\hbar^2 a_{dd}}{M}|\phi_0(z)|^2, \tag{G.5}$$

where $|\phi_0(z)|^2$ is the coordinate-space condensate density in the quasi-2D geometry. We carry out the same calculation for the quasi-1D geometry, where the condensate density in momentum-space is given by

$$\tilde{n}_{\mathrm{1D}}(\mathbf{k}) = \mathcal{F}\left[n_{\mathrm{1D}}(x,y)\right] = \tilde{n}_{\mathrm{1D}}(k_x,k_y)\delta(k_z). \tag{G.6}$$

Substituting this function into Eq. (G.2) gives

$$U_d^{\mathrm{1D}}(\mathbf{r}) = -\frac{4\pi}{3}d^2|\phi_0(\rho)|^2 = -\frac{4\pi\hbar^2 a_{dd}}{M}|\phi_0(\rho)|^2, \tag{G.7}$$

where $|\phi_0(\rho)|^2$ is the coordinate-space condensate density in the quasi-1D geometry, written in terms of ρ instead of x and y.

Appendix H

Modified GPE Using 0^{th} and 2^{nd} Harmonic Oscillator Wave Functions

Consider the ansatz given by Eqs. (8.7)-(8.9) for a system with a single harmonically trapped dipolar BEC, so the indexing of the condensate wave function can be ignored and we can simply write $\phi_0(\mathbf{x}) = \psi(\rho)\chi(z)$. We derive the modified GPE by multiplying the (dimensionless) GPE,

$$\left\{-\frac{1}{2}\nabla^2 + U(\mathbf{x}) + U_d(\mathbf{x}) - \mu\right\}\phi_0(\mathbf{x}) = 0, \tag{H.1}$$

by $\chi(z)$ and integrating over z. In Eq. (H.1), $U(\mathbf{x})$ is the trapping potential, $U_d(\mathbf{x})$ is the ddi mean-field potential and μ is the chemical potential. This operation gives the modified GPE,

$$\left\{\hat{H}^{(1)}_{\text{eff}}(\rho) + 2\frac{g_d}{l_z}\mathcal{F}^{-1}_{\text{2D}}\left[\tilde{n}_\rho(k_\rho)F_{\text{eff}}\left(\frac{k_\rho l_z}{\sqrt{2}}\right)\right]\right\}\psi(\rho) = 0, \tag{H.2}$$

where $\hat{H}^{(1)}_{\text{eff}}(\rho)$ is the effective single-particle Hamiltonian,

$$\hat{H}^{(1)}_{\text{eff}}(\rho) = -\frac{1}{2}\nabla^2_\rho + \frac{1}{2}\omega^2_\rho\rho^2 - \mu + \frac{1}{1+A_2^2}\left[\left(\frac{1}{l_z^2} + \lambda^2 l_z^2\right)\left(\frac{1}{4} + \frac{5}{4}A_2^2\right) - \frac{A_2}{\sqrt{2}}\left(\frac{1}{l_z^2} - \lambda^2 l_z^2\right)\right], \tag{H.3}$$

and $F_{\text{eff}}(x)$ is given by

$$\begin{aligned}
F_{\text{eff}}(x) = {} & \frac{1}{\left(1+A_2^2\right)^2}\Bigg(1 + \sqrt{2}A_2\left(3x^2-1\right) + \frac{3}{4}A_2^2\left(3+5x^2+6x^4\right) \\
& + \frac{1}{4\sqrt{2}}A_2^3\left(1+9x^2+42x^4+12x^6\right) + \frac{1}{64}A_2^4\left(41+3x^2\left(81+134x^2+60x^4+8x^6\right)\right) \\
& - \frac{3\sqrt{\pi}}{2}\Bigg[1 + A_2\Big(A_2\left(2+A_2^2\right) + 2\left(\sqrt{2}+2A_2\right)\left(1+A_2^2\right)x^2 \\
& + A_2\left(3+4\sqrt{2}A_2+5A_2^2\right)x^4 + A_2^2\left(\sqrt{2}+2A_2\right)x^6 + \frac{1}{4}A_2^3x^8\Big)\Bigg]xe^{x^2}\text{erfc}\left[x\right]\Bigg)
\end{aligned} \tag{H.4}$$

and erfc is the complimentary error function. The corresponding dipolar mean-field energy is then

$$E_d = \frac{g_d}{l_z}\int d^2\rho\, n_\rho(\rho)\mathcal{F}^{-1}_{\text{2D}}\left[\tilde{n}_\rho(k_\rho)F_{\text{eff}}\left(\frac{k_\rho l_z}{\sqrt{2}}\right)\right]. \tag{H.5}$$